

UNIVERSITY OF THESSALY

DEPARTMENT OF MECHANICAL ENGINEERING

**Simulation of transport phenomena in conditions
far from thermodynamic equilibrium via kinetic theory
with applications in vacuum technology and MEMS**

Sarantis Pantazis

**M.Sc., Mechanical Engineer
Department of Mechanical Engineering
University of Thessaly**

A Dissertation Submitted for the Partial Fulfillment of the
Requirements for the Degree of
Doctor of Philosophy

June 2011

©2011 Sarantis Pantazis

The approval of the current dissertation by the Department of Mechanical Engineering of the University of Thessaly does not imply acceptance of the author's opinions (Law 5343/32 number 202 paragraph 2). Also, the views and opinions expressed herein do not necessarily reflect those of the European Commission.

Certified by the members of the Dissertation Committee:

1 st member (Supervisor)	Prof. Dimitris Valougeorgis Professor in the Department of Mechanical Engineering University of Thessaly
2 nd member	Prof. Nikolaos Andritsos Associate Professor in the Department of Mechanical Engineering University of Thessaly
3 rd member	Prof. Vasilis Bontozoglou Professor in the Department of Mechanical Engineering University of Thessaly
4 th member	Prof. Theodoros Karakasidis Assistant Professor in the Department of Civil Engineering University of Thessaly
5 th member	Prof. Antonis Liakopoulos Professor in the Department of Civil Engineering University of Thessaly
6 th member	Prof. Nikolaos Pelekasis Associate Professor in the Department of Mechanical Engineering University of Thessaly
7 th member	Prof. Anastasios Stamatis Assistant Professor in the Department of Mechanical Engineering University of Thessaly

Dedicated to my family

Acknowledgments

First and foremost, I would like to express my deep and sincere gratitude to my supervisor, Prof. D. Valougeorgis, for teaching and inspiring me for the whole duration of my Ph.D. Even in the most difficult situations he supported and guided me, pushing me gently to a constant improvement.

There are several other people who I feel that have contributed in the writing of this dissertation. The most important contributions, along with several helpful conversations, were made by Prof. F. Sharipov, who provided the basic concept of the channel end effect study, and Dr. Chr. Day along with the KIT personnel, who briefly introduced me in the world of experimental rarefied gas dynamics. It was also a privilege to discuss and work for a brief period of time with Prof. A. Grecos, who tirelessly discussed with me on various subjects of statistical mechanics. Moreover, I would like to acknowledge my gratitude to Prof. B. Ganapol for providing supportive material regarding the implementation of the acceleration schemes.

I take this opportunity to thank the members of my dissertation committee, Prof. N. Andritsos, Prof. V. Bontozoglou, Prof. T. Karakasidis, Prof. A. Liakopoulos, Prof. N. Pelekasis and Prof. A. Stamatis, for dedicating their time to read and correct this dissertation. I am also indebted to my colleagues, S. Misdanitis, Dr. S. Varoutis and J. Lyhnaropoulos for their easy-going collaboration in various stages, as well as for sharing the good and bad experiences of the Ph.D. studies with me.

I would also like to thank Natasa Kyriopoulou for her endless patience and encouragement throughout these years. Finally, above all, I am grateful to my parents, Spyros and Vaia Pantazi, as well as to my sister Dimitra, for their love and continuous support. This dissertation would not have been completed without their help.

Financial support for this Ph.D. has been provided by the Euratom Association - Hellenic Republic, to which I am deeply indebted. Also, partial support for conference mobility expenses has been received from the GASMEMS Marie Curie programme.

**Simulation of transport phenomena in conditions
far from thermodynamic equilibrium via kinetic theory
with applications in vacuum technology and MEMS**

Sarantis Pantazis

University of Thessaly, June 2011

Supervisor: D. Valougeorgis

In this work, non-equilibrium transport phenomena have been examined via the kinetic theory of gases. The behaviour of the gas in low pressure conditions or in low-dimensionality systems can not be captured by the usual Navier-Stokes formulation, in conjunction with the constitutive laws of Newton-Fourier-Fick. The limited number of intermolecular collisions results in departure from equilibrium and the particulate nature of the gas must be taken into account, greatly increasing the computational effort.

The problem is described by the integro-differential Boltzmann equation, which is used to determine the distribution of particles in physical and molecular velocity space, as well as in time. There are difficulties associated with the seven-dimensional nature of the distribution function, as well as with the complexity of the collision term, which is usually substituted by an appropriate model. The most widely used and successful numerical methodologies, the Discrete Velocity Method (DVM) and the Direct Simulation Monte Carlo (DSMC), are applied here in the whole range of the Knudsen number. It is important to employ approaches based on kinetic theory, since these are the only ones which are valid for any rarefaction level.

In this work, several problems including non-equilibrium phenomena are considered. The interaction of gases with solid surfaces is considered for several problems according to the Cercignani-Lampis boundary conditions. The non-linear form of this scattering kernel, which had not been pre-

viously used in the literature, is applied on the problem of heat transfer between parallel plates and coaxial cylinders. Its linearized form has also been employed for both flow and heat transfer problems and a comparison with relevant experiments has lead to surface characterization with respect to argon and helium flows.

Non-linear heat conduction phenomena are also studied for the parallel plates and coaxial cylinders geometries. Cases in a wide range of temperature differences are considered in the whole range of the Knudsen number by the Shakhov kinetic model equation. The intermolecular interaction is considered through the Inverse Power Law model. Results on heat flux, temperature and density profiles are presented and non-equilibrium phenomena, such as the non-uniform pressure distribution, are discussed.

An advanced and computationally efficient discrete velocity scheme has been developed for the numerical treatment of linear and non-linear flow and heat transfer configurations. Through this algorithm, memory and CPU time requirements have been significantly reduced. The proposed algorithm allows the effective simulation of demanding problems, such as linear and non-linear flow through orifices and tubes of finite length, where the distribution function is 5-dimensional. A comparison has also been performed with DSMC results and solid remarks about the effectiveness of the proposed discrete velocity algorithm have been drawn. In this problem, we have also developed and applied a boundary condition model for adiabatic walls, which have not been considered before in the literature.

Furthermore, we study the range of validity for linearized kinetic equations for the problems of heat transfer between parallel plates and cylinders and flow through short tubes by comparing with the non-linear results. This investigation is significant because if this range is proven to be sufficiently large, the combination of this formulation and the DSMC method can cover any possible condition and for any rarefaction level. It has been found that in the problems given here the linearized formulation results can be applied well beyond their theoretical limits with sufficient accuracy. Also, the part of this work concerning linearized flow through orifices and tubes of finite length due to small pressure

differences has not been studied previously in the literature and is very important for two reasons: first, the zero-length case is one of the few configurations that is not affected by the wall surface accommodation properties, making it an ideal problem for the benchmarking of numerical methods and kinetic models, and second the fact that other methods such as DSMC face significant difficulties in solving this problem.

The effect of the channel ends on the flow field and mass flow rate has been investigated for the geometries of rectangular channels with large aspect ratios and cylindrical tubes. A novel methodology is proposed to extend the well known fully developed flow analysis, applied in infinitely long channels, to channels of finite length. These results may be combined with a typical integration procedure to obtain the complete solution, greatly reducing the computational effort and significantly improving the accuracy of the simulation.

Finally, problems of non-linear flow through axisymmetric channel elements have been considered. Flow through a short tube has been examined by solving the Bhatnagar-Gross-Krook (BGK), Shakhov (S) and Ellipsoidal (ES) kinetic model equations by the DVM, applying an advanced numerical scheme. Results have been benchmarked by corresponding values obtained by the DSMC for a wide range of pressure differences. Also the problem of non-linear flow through an expansion/contraction pipe element, consisting of two cylindrical tubes connected in series, is studied numerically by the DSMC method and compared with experimental results. This geometry is particularly useful in the study of rarefied gas flow networks, where results concerning various components may be combined to provide a complete simulation.

Προσομοίωση φαινομένων μεταφοράς σε συνθήκες μακριά από τη θερμοδυναμική ισορροπία μέσω της κινητικής θεωρίας με εφαρμογές στην τεχνολογία κενού και τα MEMS

Σαράντης Πανταζής

Πανεπιστήμιο Θεσσαλίας, Ιούνιος 2011

Επιβλέπων: Δ. Βαλουγεώργης

Αντικείμενο της διδακτορικής διατριβής είναι η προσομοίωση ροών αερίων εκτος θερμοδυναμικής ισορροπίας μέσω της κινητικής θεωρίας. Η αραιοποιημένη κατάσταση του αερίου λόγω συνθηκών χαμηλής πίεσης ή σε συσκευές πολύ μικρών διαστάσεων δεν μπορεί να περιγραφεί από τις εξισώσεις Navier-Stokes σε συνδυασμό με τους καταστατικούς νόμους Newton-Fourier-Fick. Ο λόγος είναι ότι ο περιορισμένος αριθμός ενδομοριακών αλληλεπιδράσεων συνεπάγεται απομάκρυνση από τη θερμοδυναμική ισορροπία. Για το λόγο αυτό, πρέπει σε αυτές τις περιπτώσεις να λαμβάνεται υπ' όψιν η σωματιδιακή φύση του αερίου, με άμεση συνέπεια τη σημαντική αύξηση του υπολογιστικού κόστους.

Το πρόβλημα περιγράφεται επαρκώς για τα αραιοποιημένα αέρια μέσω της ολοκληρο-διαφορικής κινητικής εξίσωσης Boltzmann, η οποία χρησιμοποιείται για τον υπολογισμό της συνάρτησης κατανομής των μορίων στο φυσικό χώρο και τον χώρο των μοριακών ταχυτήτων, καθώς και στο χρόνο. Η επίλυση της συνήθως παρουσιάζει μεγάλες δυσκολίες λόγω της επτα-διάστατης φύσης και των ασυνεχειών της συνάρτησης κατανομής, αλλά και λόγω της περιπλοκότητας του όρου των συγκρούσεων. Οι πιο επιτυχημένες μέθοδοι αντιμετώπισης των κινητικών προβλημάτων είναι η επίλυση της εξίσωσης Boltzmann αντικαθιστώντας τον όρο των συγκρούσεων με κινητικά μοντέλα και διακριτοποιώντας και τον χώρο των μοριακών ταχυτήτων (μέθοδος των Διακριτών Ταχυτήτων, DVM), καθώς και η αντικατάσταση του αερίου από έναν αριθμό εικονικών σωματιδίων που αλληλεπιδρούν μεταξύ τους με στοχαστικούς κανόνες (μέθοδος Απευθείας Προσομοίωσης Monte Carlo, DSMC).

Είναι σημαντικό να τονισθεί ότι μόνο προσεγγίσεις που βασίζονται στην κινητική θεωρία αποδίδουν έγκυρα αποτελέσματα για κάθε επίπεδο αραιοποίησης.

Σε αυτή τη διδακτορική διατριβή αντιμετωπίζεται μια ευρεία γκάμα προβλημάτων εκτός θερμοδυναμικής ισορροπίας. Η αλληλεπίδραση του αερίου με στερεά τοιχώματα μελετάται με βάση τις συνοριακές συνθήκες Cercignani-Lampis. Η μη-γραμμική μορφή του συγκεκριμένου μοντέλου, η οποία δεν έχει χρησιμοποιηθεί στο παρελθόν στη βιβλιογραφία, εφαρμόζεται στο πρόβλημα μεταφοράς θερμότητας ανάμεσα σε παράλληλες πλάκες ή ομόκεντρους κυλίνδρους λόγω αυθαίρετα μεγάλων βαθμίδων θερμοκρασίας. Η γραμμικοποιημένη μορφή του έχει επίσης επιστρατευθεί για προβλήματα ροής και μεταφοράς θερμότητας και μέσα από τη σύγκριση με αντίστοιχα πειραματικά αποτελέσματα οδηγούμαστε στο χαρακτηρισμό επιφανειών σχετικά με τη ροή αργού και ηλίου.

Έχουν μελετηθεί μη γραμμικά φαινόμενα μεταφοράς θερμότητας για τις γεωμετρίες των παράλληλων πλακών και των ομόκεντρων κυλίνδρων. Έχουν εξετασθεί περιπτώσεις διαφοράς θερμοκρασίας σε ένα μεγάλο εύρος με βάση το κινητικό μοντέλο Shakhov. Οι ενδομοριακές αλληλεπιδράσεις προσομοιώνονται μέσω του μοντέλου Inverse Power Law. Παρουσιάζονται αποτελέσματα για τις κατανομές θερμοροής, πυκνότητας και θερμοκρασίας και σχολιάζονται φαινόμενα λόγω απομάκρυνσης από τη θερμοδυναμική ισορροπία, όπως η ανομοιόμορφη κατανομή πίεσης.

Το αριθμητικό σχήμα των διακριτών ταχυτήτων αναπτύχθηκε και η απόδοση του βελτιώθηκε για την αντιμετώπιση τόσο γραμμικών όσο και μη-γραμμικών ροών. Μέσω του αναβαθμισμένου αλγορίθμου, οι απαιτήσεις σε μνήμη και υπολογιστικό χρόνο μειώθηκαν σημαντικά. Ο προτεινόμενος αλγόριθμος επιτρέπει την αποτελεσματική προσομοίωση απαιτητικών προβλημάτων, όπως της γραμμικής και μη-γραμμικής ροής διαμέσου κυλινδρικών σχισμών και καναλιών πεπερασμένου μήκους, όπου η συνάρτηση κατανομής είναι 5-διάστατη. Η σύγκριση με αποτελέσματα της DSMC οδήγησε σε ευνοϊκά συμπεράσματα για την αποδοτικότητα του προτεινόμενου αλγορίθμου διακριτών ταχυτήτων. Επίσης, αναπτύχθηκε και εφαρμόστηκε για πρώτη φορά ένας νέος τύπος συνοριακών συνθηκών για αδιαβατικά τοιχώματα.

Σημαντική δουλειά έχει γίνει και στον προσδιορισμό του εύρους ισχύος για τις γραμμικοποιημέ-

νες κινητικές εξισώσεις, οι οποίες παράγονται για μικρές ωθούσες δυνάμεις, όπως κλίσεις πίεσης ή θερμοκρασίας, μέσω της σύγκρισης με τα αντίστοιχα μη-γραμμικά προβλήματα. Η έρευνα αυτή είναι σημαντική γιατί αν αυτό το εύρος εφαρμογής αποδειχθεί ότι είναι αρκετά μεγάλο, τότε μπορούμε να αντιμετωπίσουμε όλες τις πιθανές συνθήκες και για κάθε επίπεδο αραιοποίησης μέσω ενός κατάλληλου συνδυασμού γραμμικοποιημένων κινητικών εξισώσεων και της μεθόδου DSMC. Έχει βρεθεί ότι τα αποτελέσματα της γραμμικής θεωρίας μπορούν να εφαρμοσθούν και πέραν των αυστηρών θεωρητικών ορίων τους με ικανοποιητική ακρίβεια. Αυτή η μελέτη πραγματοποιείται για προβλήματα τόσο ροής όσο και μεταφοράς θερμότητας σε καρτεσιανή και κυλινδρική γεωμετρία. Επίσης, το κομμάτι που αφορά τη γραμμικοποιημένη ροή διαμέσου καναλιών λόγω χαμηλής βαθμίδας πίεσης δεν έχει αντιμετωπισθεί ξανά στη βιβλιογραφία και είναι σημαντικό για δύο λόγους. Ο πρώτος είναι ότι η περίπτωση μηδενικού μήκους είναι μια από τις λίγες περιπτώσεις όπου η ροή δεν επηρεάζεται από τις ιδιότητες των τοιχωμάτων, με αποτέλεσμα να θεωρείται μια ιδανική περίπτωση για την αξιολόγηση αριθμητικών μεθόδων και κινητικών μοντέλων. Ο δεύτερος λόγος είναι ότι η μέθοδος DSMC αντιμετωπίζει μεγάλες δυσκολίες στην επίλυση αυτών των γραμμικών προβλημάτων λόγω της προσέγγισης στην κατάσταση ισορροπίας.

Η επίδραση των άκρων του καναλιού σε ροή λόγω βαθμίδας πίεσης μελετάται για τις γεωμετρίες ορθογωνικών αγωγών με μεγάλους λόγους πλευρών καθώς και σε κυλινδρικά κανάλια. Μια καινοτόμος μεθοδολογία προτείνεται ούτως ώστε να επεκταθεί η τυπική ανάλυση των πλήρως ανεπτυγμένων ροών η οποία εφαρμόζεται σε κανάλια άπειρου μήκους σε κανάλια πεπερασμένου μήκους. Μέσα από αυτή τη μελέτη προκύπτει ότι η χρήση των αποτελεσμάτων αυτών μπορούν να δώσουν πολύ ακριβή αποτελέσματα χωρίς να χρειαστούν χρονοβόρες προσομοιώσεις.

Τέλος, το πρόβλημα της μη-γραμμικής ροής σε αξονοσυμμετρικά κανάλια έχει μελετηθεί. Η ροή σε αγωγό πεπερασμένου μήκους έχει εξετασθεί μέσω της επίλυσης των κινητικών μοντέλων Bhatnagar-Gross-Krook (BGK), Shakhov (S) και Ellipsoidal (ES) μέσω της DVM, εφαρμόζοντας το βελτιωμένο αριθμητικό σχήμα. Τα αποτελέσματα έχουν συγκριθεί με τις αντίστοιχες τιμές που παρέχει η μέθοδος DSMC για ένα ευρύ φάσμα διαφορών πίεσης. Επίσης, το πρόβλημα της ροής μέσα

σε ένα κανάλι με απότομη αύξηση/μείωση της διατομής του εξετάζεται αριθμητικά από τη μέθοδο DSMC και συγκρίνεται με πειραματικά αποτελέσματα. Η προσομοίωση καναλιών αυτού του τύπου είναι ωφέλιμη στη μελέτη δικτύων αραιοποιημένων ροών, όπου αποτελέσματα που αφορούν διάφορες γεωμετρίες μπορούν να συνδυαστούν ώστε να μελετηθεί το πλήρες πρόβλημα.

Table of Contents

Chapter 1. Introduction	1
1.1 General concepts	1
1.2 Dissertation structure and contents	2
1.3 Novelty and scientific contributions	4
Chapter 2. Literature review	7
2.1 Introduction	7
2.2 Brief historical overview and fundamental principles of kinetic theory	8
2.3 Kinetic models	14
2.4 Numerical methods	16
2.5 Boundary conditions	19
2.6 Flow through channels	22
2.7 Non-linear heat transfer	26
Chapter 3. Gas-surface scattering effect in flow and heat transfer problems	29
3.1 Boundary condition models	29
3.2 Application of the CL kernel	35
3.2.1 Introduction	35
3.2.2 Linearized flow through a rectangular duct	36
3.2.3 Linearized and non-linear heat transfer between parallel plates	40
3.2.3.1 Linearized heat transfer	41
3.2.3.2 Non-linear heat transfer	43
3.2.4 Non-linear heat transfer between concentric cylinders	45
3.3 Results and discussion	48
3.3.1 Flow through a rectangular duct	48
3.3.2 Heat transfer between parallel plates	51
3.3.3 Non-linear heat transfer between two concentric cylinders	52
3.4 Concluding remarks	53
Chapter 4. Linear flows driven by pressure gradients	67
4.1 Introduction	67
4.2 Linearized flow in short channels	68
4.2.1 Introduction	68
4.2.2 Governing equations for small pressure differences	69
4.2.3 Boundary conditions	71
4.3 Formulation of the end effect problem	75
4.3.1 Introduction	75
4.3.2 Governing equations	75
4.3.3 Boundary conditions	78
4.3.4 Dimensionless flow rate derivation including the channel end effect	79
4.4 Numerical scheme	81
4.4.1 Introduction	81
4.4.2 Discretization and description of algorithm	81
4.4.3 Description of the marching step and related benefits	82
4.4.4 Numerical and domain parameters	84

4.5	Results	85
4.5.1	Introduction	85
4.5.2	Linearized flow	86
4.5.3	Investigation of the end effect	90
4.6	Concluding remarks	93
Chapter 5.	Non linear heat transfer	125
5.1	Introduction	125
5.2	Formulation of the two problems	126
5.2.1	Introduction	126
5.2.2	Heat transfer between parallel plates	126
5.2.3	Heat transfer between coaxial cylinders	130
5.3	Numerical scheme	136
5.4	Results and discussion	140
5.4.1	Introduction	140
5.4.2	Heat transfer between parallel plates	141
5.4.3	Heat transfer between coaxial cylinders	143
5.4.3.1	Bulk quantities for hard sphere molecules with diffuse boundary conditions	143
5.4.3.2	Influence of intermolecular interaction law	146
5.4.3.3	Range of validity of linear analysis	147
5.5	Concluding remarks	148
Chapter 6.	Non linear flows	167
6.1	Introduction	167
6.2	Kinetic formulation - Short tube flow	168
6.2.1	Introduction	168
6.2.2	Governing equations	168
6.2.3	Macroscopic quantity moments	171
6.2.4	Boundary conditions	172
6.3	The Discrete Velocity numerical method and its optimization	175
6.3.1	Introduction	175
6.3.2	Numerical scheme	175
6.3.3	Further improvements in the numerical algorithm	177
6.4	DSMC formulation - Flow through an expansion/contraction element	178
6.4.1	Introduction and problem description	178
6.4.2	The DSMC method	179
6.4.3	Numerical details	181
6.5	Results	182
6.5.1	Introduction	182
6.5.2	Flow through a tube	183
6.5.2.1	Flow rates and field distributions	183
6.5.2.2	Computational performance	186
6.5.2.3	Qualitative comparison with DSMC	189
6.5.3	Flow through an expansion/contraction element	191
6.6	Concluding remarks	193
Chapter 7.	Concluding remarks	233
7.1	Summary and contributions	233
7.2	Future work	237

Bibliography	239
Appendices	259
Appendix 1. Derivation of boundary conditions	261
1.1 Impermeability condition	261
1.2 Fully developed flow boundary conditions	262
1.3 Adiabatic wall condition	262
Appendix 2. Derivation of mass flow rate equation	265
2.1 Linearized flow	265
2.2 Non-linear flow	266
Appendix 3. Derivation of discretized equations	269
Appendix 4. Grid description	271
Appendix 5. Conservation principles	273
5.1 Introduction	273
5.2 Non-linear heat transfer	273
5.3 Linearized flow through a channel	274
5.4 Non-linear flow through an axisymmetric channel element	275
Appendix 6. Analytical solutions	277
6.1 Introduction	277
6.2 Free molecular regime	277
6.3 Hydrodynamic regime	281

List of Tables

3.1	Reduced flow rate G for flow through a duct	55
3.2	Conductance C [l/sec] dependence on the accommodation coefficients for N_2 flow through a duct ($H = W = 16\text{mm}$, $L = 1277\text{mm}$) into vacuum at 296K	56
3.3	Heat flux for the parallel plate problem, obtained by the linear formulation	57
3.4	Heat flux for the parallel plate problem, obtained by the non-linear formulation for $\beta = 0.05$	58
3.5	Heat flux for the parallel plate problem, obtained by the non-linear formulation for $\beta = 0.5$	58
3.6	Radial heat flow $q(r = \gamma)$ with CL boundary conditions for $\beta = 0.1$ and $\gamma = 1/65$	59
3.7	Results for the radial heat flow $q(r = \gamma)$ with CL boundary conditions, obtained by the linearized model and reproduced from [113] for $\beta = 0.1$ and $\gamma = 1/65$	59
4.1	Discretized equation for the tube end geometry problem	95
4.2	Geometric parameters for the end geometry	96
4.3	Numerical parameters used in the simulations	96
4.4	Dimensionless flow rate W for plate geometry and several δ and L/H values	97
4.5	Dimensionless flow rate W for tube geometry and several δ and L/R values	97
4.6	Dimensionless flow rate W with incomplete accommodation for the linearized tube problem	97
4.7	Dimensionless flow rate W obtained by DSMC in previous works	98
4.8	Effective length increment values for the two geometries	99
4.9	Flow rate ratio for linear flow	99
4.10	Flow rate ratio for non-linear flow ($\hat{P}_{out}/\hat{P}_{in} = 0.5$)	99
5.1	Number and range of discrete velocity magnitudes	150
5.2	Non-linear dimensionless heat fluxes for the parallel plate geometry and various values of δ_0 , T_A/T_B	150
5.3	Linearized dimensionless heat fluxes for the parallel plate geometry and various values of δ_0 , T_A/T_B	150
5.4	Number of iterations needed for some indicative cases with diffuse reflection	151
5.5	Radial heat flow $q_r(r = \gamma)$ for hard sphere molecules with diffuse boundary conditions	152
5.6	Radial heat flow $q_r(r = \gamma)$ for Maxwell molecules with diffuse boundary conditions	153
6.1	Discretized equation for the problem of non-linear flow through a tube	194
6.2	Discrete velocity algorithm numerical parameters	195
6.3	DSMC numerical parameters	195
6.4	Dimensionless flow rate W for the ES model	196
6.5	Dimensionless flow rate W obtained by the DSMC method in previous works [149, 152]	196
6.6	Dimensionless flow rate W for the BGK and S models	197
6.7	Dimensionless flow rate W for the BGK model and $P_{out} = 0.99$	197
6.8	Dimensionless flow rate W for the ES model and adiabatic walls	197
6.9	Effect of grid refinement and the Wynn- ε scheme on the number of iterations	198
6.10	Total CPU time [h] for various algorithm improvements	199
6.11	CPU time analysis [%] of the average time allocation for a typical run	199
6.12	Memory requirements for the non-linear DVM code	199
6.13	DSMC expanding/contracting tube geometrical cases	200

6.14 DSMC expanding/contracting tube flow rate W	200
--	-----

List of Figures

3.1	Specular reflection for the impinging angles $\theta = -\pi/6$ (blue) and $\theta = -\pi/3$ (green)	60
3.2	Diffuse reflection for the impinging angle $\theta = -\pi/6$	60
3.3	Diffuse-specular reflection with $\alpha_M = 0.8$ for the impinging angle $\theta = -\pi/6$	60
3.4	Cercignani-Lampis reflection with $\alpha_n = 0.50$, $\alpha_t = 1.00$ (green) and $\alpha_n = 1.00$, $\alpha_t = 0.50$ (red) for the impinging angle $\theta = -\pi/6$	61
3.5	Nearly specular reflection ($\alpha_t = \alpha_n = 10^{-4}$) for the impinging angles $\theta = -\pi/6$ (blue) and $\theta = -\pi/3$ (green)	61
3.6	Nearly back-scattering reflection ($\alpha_t = 1.9999$, $\alpha_n = 10^{-4}$) for the impinging angles $\theta = -\pi/6$ (blue) and $\theta = -\pi/3$ (green)	61
3.7	Comparison between experimental and numerical results for conductance (nitrogen, 296K)	62
3.8	Comparison between experimental and numerical mass flow rates for argon (up) and helium (below), for high (left) and low (right) δ values	63
3.9	Dependence of the dimensionless radial heat flow on the CL accommodation coefficient α_t while keeping $\alpha_n = 1$ constant for $\gamma = 0.5$ and $\beta = 1$.	64
3.10	Dependence of the dimensionless radial heat flow on the CL accommodation coefficient α_n while keeping $\alpha_t = 1$ constant for $\gamma = 0.5$ and $\beta = 1$.	65
3.11	Dependence of the dimensionless radial heat flow on the Maxwell accommodation coefficient α_M for $\gamma = 0.5$ with $\beta = 1$.	66
4.1	Flow configuration and coordinate system	100
4.2	Velocity coordinate system for the parallel plates (left) and the tube (right)	101
4.3	Division of the channel geometry into three parts	102
4.4	Indicative pressure distribution along the central axis at the outlet part to justify constant density perturbation	103
4.5	Flow configuration and coordinate system	104
4.6	Schematical representation of the marching scheme for the channel (up) and tube (down)	105
4.7	Non-uniform grid used in the numerical solution	106
4.8	Pressure perturbation for the plate (up) and tube (down) geometry with $L/L_0 = 0$ and $\delta = 1$	107
4.9	Axial velocity for the plate (up) and tube (down) geometry with $L/L_0 = 0$ and $\delta = 1$	108
4.10	Streamlines for the plate (up) and tube (down) geometry with $L/L_0 = 0$ and $\delta = 1$	109
4.11	Pressure perturbation for the plate (up) and tube (down) geometry with $L/L_0 = 10$ and $\delta = 10$	110
4.12	Axial velocity for the plate (up) and tube (down) geometry with $L/L_0 = 10$ and $\delta = 10$	111
4.13	Streamlines for the plate (up) and tube (down) geometry with $L/L_0 = 10$ and $\delta = 10$	112
4.14	Pressure perturbation (up) and axial velocity (down) for the plate geometry with $L/H = 2$ and $\delta = 1$	113
4.15	Pressure perturbation (up) and axial velocity (down) for the plate geometry with $L/H = 10$ and $\delta = 1$	114
4.16	Pressure perturbation for the tube geometry with $L/L_0 = 2$ and $\delta = 0.1$ (up), $\delta = 1$ (middle), $\delta = 10$ (down)	115
4.17	Axial velocity for the tube geometry with $L/L_0 = 2$ and $\delta = 0.1$ (up), $\delta = 1$ (middle), $\delta = 10$ (down)	116
4.18	Pressure perturbation for the tube geometry with $L/L_0 = 5$ and $\delta = 0.1$ (up), $\delta = 1$ (middle), $\delta = 10$ (down)	117

4.19	Axial velocity for the tube geometry with $L/L_0 = 5$ and $\delta = 0.1$ (up), $\delta = 1$ (middle), $\delta = 10$ (down)	118
4.20	Pressure perturbation distribution at the symmetry axis for the plate (left) and tube (right) geometry with $L/L_0 = 0$ (up), $L/L_0 = 2$ (middle), $L/L_0 = 10$ (down)	119
4.21	Density perturbation along the symmetry axis for the plate geometry and $\delta = 0.2$ (top), $\delta = 1$ (middle), $\delta = 10$ (bottom)	120
4.22	Density (left) and horizontal velocity (right) perturbation distributions for $\delta = 0.2$ (up), $\delta = 1$ (middle) and $\delta = 10$ (below)	121
4.23	Comparison of results obtained by the end geometry formulation with linearized results for $\delta = 1$ (up) and $\delta = 10$ (down)	122
4.24	Comparison of results obtained by the end geometry formulation with non-linear results for $\delta = 1$ (up) and $\delta = 10$ (down)	123
5.1	Geometry and coordinate system for the parallel plate (up) and coaxial cylinders (down) problems	154
5.2	Flow diagram of the typical iteration algorithm	155
5.3	Flow diagram of the upgraded iteration algorithm	156
5.4	Linear (empty symbols) and non-linear (filled symbols) temperature profiles for various δ_0 with $T_A/T_B = 3$ ($\beta = 0.5$)	157
5.5	Reduced distribution functions φ (left) and ψ (right) in terms of the molecular velocity c_y at several locations between the plates for $\delta_0 = 1.5$ and $T_A/T_B = 3$ ($\beta = 0.5$)	158
5.6	Dimensionless radial heat flow q_r at $r = \gamma$ in terms of δ_0 for various γ , with $\beta = 0.1$ (up) and $\beta = 10$ (down)	159
5.7	Dimensionless temperature profiles $\tau(r)$ for $\beta = 0.1$ (up), $\beta = 1$ (middle) and $\beta = 10$ (down), with $\gamma = 0.5$ (left) and $\gamma = 0.1$ (right)	160
5.8	Dimensionless density profiles $\rho(r)$ for $\beta = 0.1$ (up), $\beta = 1$ (middle) and $\beta = 10$ (down), with $\gamma = 0.5$	161
5.9	Dimensionless pressure profiles $p(r)$ for $\beta = 0.1$ (up), $\beta = 1$ (middle) and $\beta = 10$ (down), with $\gamma = 0.5$ (left) and $\gamma = 0.1$ (right)	162
5.10	Dependence of the dimensionless radial heat flow and temperature distributions on the IPL coefficient ω for $\beta = 1$ (up) and $\beta = 10$ (down). Hard spheres ($\omega = 0.5$) are denoted with filled symbols and Maxwell molecules ($\omega = 1$) with empty symbols	163
5.11	Dimensional radial heat flow through various gases in terms of the reference pressure P_B for $\gamma = 0.1$, with $\beta = 0.1$ (up) and $\beta = 1$ (down)	164
5.12	Relative error between nonlinear and linearized radial heat flow in terms of β for various δ_0 , with $\gamma = 0.5$ (up) and $\gamma = 0.1$ (down)	165
5.13	Dimensionless radial heat flow and temperature profiles using linearized (empty symbols) and nonlinear (filled symbols) analysis for $\beta = 0.1$ (up), $\beta = 1$ (middle) and $\beta = 10$ (down)	166
6.1	Cylindrical tube geometry	201
6.2	Expansion/contraction channel geometry	202
6.3	Expansion/contraction channel computational cell grid	203
6.4	Density contour for the short tube geometry and $L/R = 0$, $P_{out} = 0.1$ with $\delta = 0.1$ (up), $\delta = 1$ (middle) and $\delta_0 = 10$ (down)	204
6.5	Axial velocity contour for the short tube geometry and $L/R = 0$, $P_{out} = 0.1$ with $\delta = 0.1$ (up), $\delta = 1$ (middle) and $\delta_0 = 10$ (down)	205
6.6	Streamlines for the short tube geometry and $L/R = 0$, $P_{out} = 0.1$ with $\delta = 0.1$ (up), $\delta = 1$ (middle) and $\delta_0 = 10$ (down)	206
6.7	Density contour for the short tube geometry and $L/R = 10$, $P_{out} = 0.9$ with $\delta = 0.1$ (up), $\delta = 1$ (middle) and $\delta_0 = 10$ (down)	207

6.8	Axial velocity contour for the short tube geometry and $L/R = 10$, $P_{out} = 0.9$ with $\delta = 0.1$ (up), $\delta = 1$ (middle) and $\delta_0 = 10$ (down)	208
6.9	Streamlines for the short tube geometry and $L/R = 10$, $P_{out} = 0.9$ with $\delta = 0.1$ (up), $\delta = 1$ (middle) and $\delta_0 = 10$ (down)	209
6.10	Density (up) and axial velocity (middle) contours, as well as streamlines (down) for the short tube geometry and $L/R = 0$, $P_{out} = 0.5$, $\delta_0 = 10$	210
6.11	Density (up) and axial velocity (middle) contours, as well as streamlines (down) for the short tube geometry and $L/R = 5$, $P_{out} = 0.5$, $\delta_0 = 10$	211
6.12	Density (up) and axial velocity (middle) contours, as well as streamlines (down) for the short tube geometry and $L/R = 10$, $P_{out} = 0.5$, $\delta_0 = 10$	212
6.13	Density contour for the short tube geometry and $L/R = 1$, $\delta_0 = 2$ with $P_{out} = 0.1$ (up), $P_{out} = 0.5$ (middle) and $P_{out} = 0.9$ (down)	213
6.14	Axial velocity contour for the short tube geometry and $L/R = 1$, $\delta_0 = 2$ with $P_{out} = 0.1$ (up), $P_{out} = 0.5$ (middle) and $P_{out} = 0.9$ (down)	214
6.15	Streamlines for the short tube geometry and $L/R = 1$, $\delta_0 = 2$ with $P_{out} = 0.1$ (up), $P_{out} = 0.5$ (middle) and $P_{out} = 0.9$ (down)	215
6.16	Heat flux in the direction normal to the wall for adiabatic and isothermal walls, with $L/R = 1$, $\delta_0 = 20$, $P_{out} = 0.5$	216
6.17	Density (up) and axial velocity (middle) contours, as well as streamlines (bottom) for flow through an adiabatic tube with $L/R = 1$, $P_{out} = 0.5$ with $\delta_0 = 20$	217
6.18	Density (up) and axial velocity (middle) contours, as well as streamlines (bottom) for flow through an isothermal tube with $L/R = 1$, $P_{out} = 0.5$ with $\delta_0 = 20$	218
6.19	Speed up due to parallelization for various δ_0 and $P_{out} = 0.1$	219
6.20	Wynn- ε effect on the residual for $\delta_0 = 10$, $P_{out} = 0.1$	219
6.21	Iterations for various grid levels with $L/R = 1$ (up) and $L/R = 10$ (down) and for $\delta_0 = 0.1$ (square), $\delta_0 = 1$ (triangle), $\delta_0 = 10$ (circle)	220
6.22	Evolution of the dimensionless flow rate W from DSMC against CPU time at the inlet and outlet cross-sections of a tube with $L/R = 1$, for $\delta_0 = 1$ (left), $\delta_0 = 10$ (right) and for $P_{out} = 0.1$ (up), $P_{out} = 0.5$ (middle), $P_{out} = 0.9$ (down)	221
6.23	Evolution of the dimensionless flow rate W from DVM against CPU time at the inlet and outlet cross-sections of a tube with $L/R = 1$, for $\delta_0 = 1$ (left), $\delta_0 = 10$ (right) and for $P_{out} = 0.1$ (up), $P_{out} = 0.5$ (middle), $P_{out} = 0.9$ (down)	222
6.24	Density (up) and axial velocity (middle) contour, as well as streamlines (down) for the expanding tube geometry (Case 1) with $P_{out} = 0.1$, $\delta = 0.1$	223
6.25	Density (up) and axial velocity (middle) contour, as well as streamlines (down) for the expanding tube geometry (Case 1) with $P_{out} = 0.1$, $\delta = 10$	224
6.26	Density (up) and axial velocity (middle) contour, as well as streamlines (down) for the expanding tube geometry (Case 2) with $P_{out} = 0.1$, $\delta = 0.1$	225
6.27	Density (up) and axial velocity (middle) contour, as well as streamlines (down) for the expanding tube geometry (Case 2) with $P_{out} = 0.1$, $\delta = 10$	226
6.28	Density (up) and axial velocity (middle) contour, as well as streamlines (down) for the contracting tube geometry (Case 3) with $P_{out} = 0.1$, $\delta = 0.1$	227
6.29	Density (up) and axial velocity (middle) contour, as well as streamlines (down) for the contracting tube geometry (Case 3) with $P_{out} = 0.1$, $\delta = 10$	228
6.30	Density (up) and axial velocity (middle) contour, as well as streamlines (down) for the contracting tube geometry (Case 4) with $P_{out} = 0.1$, $\delta = 0.1$	229
6.31	Density (up) and axial velocity (middle) contour, as well as streamlines (down) for the contracting tube geometry (Case 4) with $P_{out} = 0.1$, $\delta = 10$	230
6.32	Numerical and experimental conductances for the contraction (up) and expansion (down) elements	231

Nomenclature

α_M	Maxwell accommodation coefficient
α_n	Cercignani-Lampis normal kinetic energy accommodation coefficient
α_t	Cercignani-Lampis tangential momentum accommodation coefficient
β	Dimensionless temperature difference parameter
\hat{q}	Dimensional heat flux vector
\hat{u}	Dimensional macroscopic velocity vector
\hat{u}_w	Velocity vector of the wall
\hat{x}	Dimensional position vector
ξ	Dimensional molecular velocity vector
c	Dimensionless molecular velocity vector
q	Dimensionless heat flux vector (or perturbation)
u	Dimensionless macroscopic velocity vector (or perturbation)
x	Dimensionless position vector
ΔL	Effective length increment
ΔP	Pressure difference
ΔT	Temperature difference

Δt	DSMC time step
δ	Rarefaction parameter
δ_D	Dirac delta function
δ_{ij}	Kronecker delta
γ	Radius ratio of the two cylinders
\hat{P}_{ij}	Dimensional stress tensor
$\hat{\bar{P}}_{ij}$	Dimensionless stress tensor
λ	Molecular mean free path
μ	Dynamic viscosity
ν	Collision frequency
ω	Inverse Power Law parameter
ρ	Dimensionless number density (or perturbation)
ρ_w	Impermeability constant
σ_T	Collision cross section
τ	Adsorption time
τ	Dimensionless temperature (or perturbation)
τ_w	Adiabatic boundary condition constant
Kn	Knudsen number
Ma	Mach number

Pr	Prandtl number
Re	Reynolds number
v_0	Most probable molecular velocity
C	Channel conductance
f	Molecular distribution function
f^M	Maxwellian distribution function
F_N	Number of real molecules per computational particle
G	Reduced flow rate
g	Source term for the channel end effect problem
H	Distance between plates / Height of rectangular channel
h	Perturbation of the distribution function
h_w	Perturbation term of the wall Maxwellian
I_0	Modified Bessel function of the 1 st kind and 0 th order
k_B	Boltzmann constant
L	Channel length
L_1, L_2, R_1, R_2	Contraction/expansion channel element geometrical parameters
L_0	Reference length
L_{dev}	Development length
L_{left}	Left container size

L_{right}	Right container size
M	Molecular velocity discrete magnitudes
m	Molar mass
$N(\theta, \phi)$	Number of molecules scattered per unit solid angle
n	Dimensional number density
N_0	Total amount of scattered molecules
n_0	Reference number density
N_r	Radial direction nodes
N_x	Axial/horizontal direction nodes
N_y	Vertical direction nodes
N_θ	Molecular velocity discrete angles
N_{free}	Number of computational particles entering from free surfaces
P	Dimensional pressure
P_0	Reference pressure
P_{coll}	Probability of collision for a given pair of molecules
P_{in}	Upstream pressure
P_{out}	Downstream pressure
$Q(f, f')$	Collision operator of the Boltzmann equation
$R(\xi' \rightarrow \xi)$	Scattering kernel

R_A	Inner cylinder radius
R_B	Outer cylinder radius
R_D	Diffuse scattering kernel
R_g	Ideal gas law constant (specific for each gas)
R_S	Specular scattering kernel
R_u	Universal gas constant
R_{CL}	Cercignani-Lampis scattering kernel
R_{DS}	Diffuse-specular scattering kernel
S	Speed-up of numerical calculations due to parallelization
T	Dimensional temperature
T_0	Reference temperature
T_w	Temperature of the wall
$V, X, Y, Z, \varphi, \psi$	Projections of the distribution function
V_{cell}	Cell volume
W	Dimensionless flow rate
W	Width of rectangular channel
X_P	Dimensionless pressure gradient
\dot{M}_{FM}	Free molecular solution for zero length channel

Chapter 1

Introduction

1.1 General concepts

Gas flows are very important in a wide variety of applications encountered in our every day life. In most cases, the equations of mass, momentum and energy equilibrium, combined by the Newton-Fourier-Fick constitutive equations, describe their behaviour very well and have been applied successfully for many years. However, this formulation is subject to certain limitations due to the underlying assumption that the gas must be considered as a continuum medium. Even though this is a reasonable assumption for many cases, there are situations where this hypothesis fails: the mean free path between inter-molecular collisions may become comparable to a characteristic length, due to conditions of low pressure or if the gas is confined in a region of very small dimensions.

Beyond a certain limit, it is not possible to investigate such phenomena accurately without taking into account the molecular nature of the gas. In this case, we may say that the gas is in a *rarefied* state, for which the departure from thermodynamic equilibrium leads to a failure of the macroscopic equations. In order to properly describe such flows, concepts derived from statistical mechanics and kinetic theory of gases need to be involved. Our purpose is to provide a description of the macroscopic behaviour, starting from the microscopic equations which govern the motion of molecules from which the gas is constituted [1]. The governing equation in this regime is the Boltzmann equation, described and commented briefly in Chapter 2. This equation concerns the distribution function of particles, a 7-dimensional probability density distribution of molecules in physical space, molecular velocity space and time. The Boltzmann equation is quite complex and can be solved analytically only for very specific situations. Therefore, we are often lead to the pursuit of numerical solutions, since the experimental investigation is usually very costly.

There are important reasons to extend our studies to such cases, since many emerging technologies would benefit from this: The creation of micro- and nanometer-sized devices is very important since they offer increased reliability, low cost and high efficiency [2, 3] in comparison to their normal-sized counterparts. Vacuum flows are encountered in many applications, ranging from a simple pressure sensor [4] to the vacuum systems of fusion reactors [5]. High altitude aerodynamics need to be investigated very carefully for the correct operation of spacecrafts [6] and satellites [7]. Thus, the accuracy and efficiency of simulations is of high importance for the design, manufacturing and optimization of these devices.

1.2 Dissertation structure and contents

The aim of this dissertation is to study numerically several flow and heat transfer configurations in the whole range of the Knudsen number to upgrade and advance certain numerical simulations techniques and provide new insight on the physical laws far from local equilibrium. The next chapters may be outlined as follows:

- A literature review is presented in Chapter 2. The most important concepts, quantities and equations are introduced and discussed.
- The simulation of boundary conditions is described in Chapter 3. After a brief overview of the main principles in gas-surface interaction, the Cercignani-Lampis boundary conditions are applied in several problems, involving flow and heat transfer. Among these problems, both linearized and non-linear formulations are used and the corresponding differences are denoted. These results may serve for surface characterization, since the Cercignani-Lampis accommodation coefficients can only be found by using at least two experiments. A comparison with experiments is also included.
- Linear (i.e. slow speed) flows through channels are examined in Chapter 4 for two cross-sections: a rectangular one with very low aspect ratio (approximated as a “parallel plate” channel) and a

circular one. The flow may be linear due to a low pressure difference between the upstream and downstream ends but also due to a very large channel length, leading to a small local pressure gradient. In the first case, the complete field is simulated, while in the second case only the channel ends are considered and solutions are joined together by a well known integration procedure. The solution for the channel ends and the combination procedure are not trivial, since they require a new type of boundary conditions for fully developed flow and the utilization of the effective length concept. Some cases are considered by both methods and a comparison takes place between them, as well as with earlier results obtained by the simple integration procedure without taking into account the end effects.

- Non-linear heat transfer phenomena are studied in Chapter 5. Heat conduction through a rarefied gas confined between two parallel plates or two concentric cylinders is considered for any temperature difference and in the whole range of the Knudsen number by the Shakhov kinetic model equation. The range of applicability of the linearized formulation is also discussed through a demonstration of results on heat flux, temperature and density profiles. The intermolecular interaction is also considered through the Inverse Power Law model.
- Non-linear flows, driven by arbitrarily large pressure differences for small to moderate length ratios, are studied in Chapter 6. The problems of flow through a short cylindrical tube and a contraction/expansion element are investigated by the most popular numerical methods: the Discrete Velocity Method and the Direct Simulation Monte Carlo. Various acceleration methods are considered for the non-linear kinetic algorithm and a qualitative comparison is given for the two formulations. Three kinetic models have been applied, namely the BGK, S and ES, and a new type of boundary conditions for adiabatic walls have also been developed and applied.
- The dissertation is completed with the concluding remarks, given in Chapter 7. This chapter also points out several fields where this work could be extended in the near future, as well as various remarks on the value of the current contributions made here.

1.3 Novelty and scientific contributions

In this dissertation, results have been obtained by reliable numerical methods in the whole range of the Knudsen number and for various problems of practical interest. Moreover, further development of algorithms and models has been achieved and comparisons with experimental data and other numerical methods have been performed.

Gas-surface interaction in heat transfer configurations has been studied by the non-linear form of the Cercignani-Lampis scattering kernel, which has not been applied before in the literature. The linearized form of this kernel has also been employed for both flow and heat transfer problems and a comparison with relevant experiments has lead to surface characterization with respect to argon and helium flows.

The problems of linearized and non-linear heat transfer between parallel plates and concentric cylinders have been solved numerically by the Discrete Velocity Method. The effect of the radius ratio, the rarefaction levels, the temperature difference, the surface accommodation properties and the intermolecular interaction law has been investigated.

The effect of the channel ends on the flow field and mass flow rate has been investigated for the geometries of rectangular channels with low aspect ratios and cylindrical tubes. A novel methodology is proposed to extend the well known fully developed flow analysis, applied in infinitely long channels, to channels of finite length. These results may be used to avoid the complete numerical solution, greatly reducing the computational effort.

Linearized flow through short rectangular channels with low aspect ratio and short cylindrical pipe elements due to small pressure differences has been studied, providing results for the first time in the literature. The corresponding non-linear flow configuration for the cylindrical geometry has also been simulated and compared with DSMC results. A boundary condition model has been developed for adiabatic walls, which have not been considered before in the literature, and applied on the latter problem. Through the study of the above linear and non-linear flow problems, as well as from the previously mentioned heat transfer problems, the validity range of linearized theory has been

investigated. It has been found that the linearized formulation results can be applied well beyond their theoretical limits with sufficient accuracy.

An advanced and computationally efficient discrete velocity scheme has been developed for the numerical treatment of linear and non-linear flow and heat transfer configurations. Through this algorithm, memory and CPU time requirements have been significantly reduced. A qualitative comparison with the DSMC has been performed and solid remarks about the effectiveness of the proposed discrete velocity algorithm have been drawn.

Non-linear flow through a contraction/expansion pipe element, consisting of two cylindrical tubes connected in series, has been simulated via the DSMC method. The influence of the governing parameters has been examined and results are given for flow rates and other macroscopic quantities. This is an important configuration for practical engineering purposes and this numerical treatment may be extended in more complex geometries for the modelling of rarefied gas flow networks.

Chapter 2

Literature review

2.1 Introduction

The simulation of rarefied gas flows is a challenging task of high importance for several fields, such as the vacuum industry [5, 8], high altitude aerodynamics [9, 6] and the Micro Electronic Mechanical Systems (MEMS) industry [2, 3]. During the last few years, there is an increased need for research and development in these fields since the comprehension of related phenomena is in many cases quite limited. Some indicative applications are given below.

Hypersonic flows around space vehicles [10, 6] and satellites [7, 11] during re-entry is frequently encountered in rarefied atmospheres. The reentry angle for large Mach number is the most important parameter in this case. The DSMC numerical method is frequently employed in such cases and large organizations, including NASA [12], develop their own code versions of this numerical algorithm. The numerical study of such phenomena is a very important factor for the development of new technologies [13, 14]. The construction of microscale propulsion devices such as mono- and bi-propellant thrusters and resistojets, has also increased the needs for the accurate simulation and measurement of rarefied flows [15].

The detailed modelling of vacuum pumps [16, 17, 18] and gas separators [19] is very important to obtain the maximum efficiency. Multi-layer insulation (MLI) blankets, extensively used in space vehicles, consists of several layers of thin sheets with vacuum conditions between them to ensure that heat is transferred only through radiation. A large factor in the performance of the insulation is its behaviour in the case of degraded vacuum [20]. Vacuum deposition systems are used for the fabrication of thin-film materials in the manufacture of integrated circuits, MEMS and nanocomposites [21]. The scientific branch of cryogenics [22] requires extended usage of vacuum facilities.

Moreover, vacuum is employed in several scientific experiments that have to be conducted in rarefied conditions. The aim of the Karlsruhe Tritium Neutrino Experiment (KATRIN) [23, 24] is to measure the neutrino particle mass. Particle accelerators [25] require ultra-high-vacuum (UHV) conditions that can only be achieved by careful design and optimization of the vacuum equipment. The thermonuclear fusion reactor ITER, that is currently under construction in Cadarache, France, is a promising international programme for covering future energy needs. Due to the high requirements for pumping [5] (insulation vacuum, low pressure to maintain plasma, fuel pumping), flow conditions usually correspond to the transitional or free molecular ranges. The AIA prototype [26] is a robotic long reach carrier, able to move inside a fusion reactor and perform various tasks without deconditioning the torus vessel. One of its most promising features is leak sniffing, in which it is important to know the characteristics of the rarefied gas mixture sample flow in the umbilicus connecting the sensor tip with the detector.

Several applications also exist in the emerging field of microfluidics. In the case of MEMS with moving parts, such as microresonators [27] and comb drive sensors [28], the damping forces induced by the rarefied gas ambient can significantly alter performance and sensitivity characteristics. The flow field around micro heat flux sensors [29] plays an important role in the accuracy of the device. Flows are also rarefied in flows through porous media [30]. Read-head sliders in hard disk drives can be designed optimally only if the air flow in the microgap is simulated properly [31].

Other applications include the field of aerosols [32], chemical vapor deposition [33] and vacuum metrology [34]. More information on applications and various aspects of rarefied gas dynamics may be found in [35, 36, 37].

2.2 Brief historical overview and fundamental principles of kinetic theory

The beginning of the statistical approach to the physical description of gases is attributed to Maxwell [38] and Boltzmann [39]. In his works, Maxwell pointed out that not all molecules move with the same velocity, but in a random manner. Then he proceeded to calculate the distribution of molec-

ular velocities and his findings were corrected by Boltzmann. This *Maxwellian* (or, more correctly, Maxwell-Boltzmann) distribution, is Gaussian according to the local conditions

$$f^M(\mathbf{x}, \boldsymbol{\xi}, t) = n(\mathbf{x}, t) \left[\frac{m}{2\pi k_B T(\mathbf{x}, t)} \right]^{3/2} \exp \left\{ -\frac{m [\boldsymbol{\xi} - \mathbf{u}(\mathbf{x}, t)]^2}{2k_B T(\mathbf{x}, t)} \right\} \quad (2.1)$$

The interpretation of this expression is that the probability density function of molecular velocities f can be described at the physical point \mathbf{x} , time t and for the molecular velocity vector $\boldsymbol{\xi}$ by a Gaussian distribution connected to the local properties: the gas number density $n(\mathbf{x}, t)$, the gas velocity $\mathbf{u}(\mathbf{x}, t)$ and the gas temperature $T(\mathbf{x}, t)$. The parameter m denotes the molar mass and $k_B = 1.38065 \times 10^{-23}(\text{kg m}^2)(\text{K sec}^2)$ is a constant named after Boltzmann.

Boltzmann further investigated these phenomena and managed to derive an integro-differential equation describing the evolution of molecular velocity distribution in time and space. The most important assumptions during its derivation were that only binary collisions take place (which is true for low densities) and the hypothesis of *molecular chaos* (“stosszahlansatz”, “assumption about the collision number”), which allows the substitution of a two-particle distribution function with a product of two one-particle distribution functions. Thus, the term molecular chaos refers to the statistical independence of molecules [40]. The Boltzmann equation is

$$\frac{\partial f}{\partial t} + \boldsymbol{\xi} \cdot \frac{\partial f}{\partial \mathbf{x}} + \mathbf{F} \cdot \frac{\partial f}{\partial \boldsymbol{\xi}} = Q(f, f') \quad (2.2)$$

where the collision operator is given by

$$Q(f, f') = \int \int \int (f' f'_* - f f_*) g b db d\epsilon d\boldsymbol{\xi}_* \quad (2.3)$$

Here, $g = |\boldsymbol{\xi} - \boldsymbol{\xi}_*|$ represents the relative velocity, b is the impact parameter and ϵ determines the azimuthal angle, as defined in [41]. The operator of (2.3) contains the contribution of particles obtaining a velocity in $\boldsymbol{\xi} + d\boldsymbol{\xi}$ after a collision (the “gain” part) and of particles with pre-collisional velocities in $\boldsymbol{\xi} + d\boldsymbol{\xi}$ but scattering to other velocity vectors after the collision (the “loss” part). Boltzmann also proved that the Maxwellian distribution is a solution of this equation. The existence and uniqueness of the solution for the Boltzmann equation were confirmed for Hard Sphere molecules in 1910 by

Hilbert [42]. Grad [43] also proved the equivalence of solving the Boltzmann equation with the Euler and Navier-Stokes equations, with the main difference being the time and space scale. It can be easily seen that the Boltzmann equation also leads to the conservation principles when appropriate projections are made.

In the case of hydrodynamic equations, the constitutive equations, such as Newton's law of viscosity and Fourier's law of heat conduction, are required to obtain a closed system. These expressions rely on knowing the values of the transport coefficients, namely the viscosity, heat conductivity and diffusion coefficient. Similarly, an undetermined part in the Boltzmann equation is the intermolecular potential. If this is specified, the complete solution of the problem can be obtained without the need for the determination of the transport coefficients.

In the same works, Boltzmann further investigated these phenomena and formulated the H-Theorem, which practically expresses the irreversibility of physical processes. The quantity

$$\mathcal{H} = \int_{-\infty}^{\infty} f \log f d\xi \quad (2.4)$$

if integrated in the physical space, must always decrease (or remain constant in the special case of a Maxwellian distribution function). It is well known now that this principle is directly connected to entropy increase, as expressed by the second law of thermodynamics. At all times, molecules tend to approach the equilibrium state, where molecular velocities follow the local Maxwell distribution, since this is the state of maximum entropy.

Solving the Boltzmann equation for the unknown distribution function leads to the determination of any quantity of practical interest. In particular, the macroscopic quantities are found by appropriate moments of the distribution function, such as the following:

- Number density

$$n(\mathbf{x}, t) = \int_{-\infty}^{\infty} f d\xi \quad (2.5)$$

- Gas velocity vector

$$\hat{\mathbf{u}}(\mathbf{x}, t) = \frac{1}{n(\mathbf{x}, t)} \int_{-\infty}^{\infty} \boldsymbol{\xi} f d\boldsymbol{\xi} \quad (2.6)$$

- Pressure

$$P(\mathbf{x}, t) = \frac{m}{3} \int_{-\infty}^{\infty} (\boldsymbol{\xi} - \mathbf{u})^2 f d\boldsymbol{\xi} \quad (2.7)$$

- Stress tensor

$$\hat{P}_{ij}(\mathbf{x}, t) = m \int_{-\infty}^{\infty} (\xi_i - u_i)(\xi_j - u_j) f d\boldsymbol{\xi} \quad (2.8)$$

- Temperature

$$T(\mathbf{x}, t) = \frac{m}{3k_B n(\mathbf{x}, t)} \int_{-\infty}^{\infty} (\boldsymbol{\xi} - \mathbf{u})^2 f d\boldsymbol{\xi} \quad (2.9)$$

- Heat flux vector

$$\hat{\mathbf{q}}(\mathbf{x}, t) = \frac{m}{2} \int_{-\infty}^{\infty} (\boldsymbol{\xi} - \mathbf{u})^2 (\boldsymbol{\xi} - \mathbf{u}) f d\boldsymbol{\xi} \quad (2.10)$$

From Equations (2.7) and (2.9) we may see that the ideal law of gases

$$P(\mathbf{x}, t) = n(\mathbf{x}, t) k_B T(\mathbf{x}, t) \quad (2.11)$$

is valid even in non-equilibrium systems.

Around 1909, Knudsen defined a dimensionless number [44], nowadays named after himself, describing the rarefaction condition of a gas

$$\text{Kn} = \frac{\lambda}{L} \quad (2.12)$$

where L is a characteristic dimension of the geometry under consideration or the length scale of a macroscopic gradient, such as the density, found by $L = \rho / (\partial \rho / \partial x)$. The mean free path of gas molecules λ is defined as the mean distance travelled by a molecule between two successive collisions.

If molecules are considered as hard spheres, the mean free path is given by

$$\lambda = \frac{1}{\sqrt{2} \pi d^2 n} \quad (2.13)$$

where d is the molecular diameter and n is the number density. In terms of macroscopic quantities, it can also be expressed as

$$\lambda = \frac{\sqrt{\pi}}{2} \frac{\mu v_0}{P} \quad (2.14)$$

with μ being the dynamic viscosity of the gas in temperature T and P is the pressure. The most probable molecular velocity is defined as

$$v_0 = \sqrt{\frac{2k_B T}{m}} \quad (2.15)$$

An alternative rarefaction parameter δ is also commonly used, given by

$$\delta = \frac{\sqrt{\pi}}{2} \frac{L}{\lambda} = \frac{\sqrt{\pi}}{2} \frac{1}{\text{Kn}} \quad (2.16)$$

These dimensionless numbers are frequently associated with practical quantities as follows

$$\delta = \frac{LP}{\mu v_0} \quad (2.17)$$

$$\text{Kn} = \sqrt{\frac{\gamma\pi}{2}} \frac{\text{Ma}}{\text{Re}} \quad (2.18)$$

where γ is the specific heat ratio of the gas and Ma, Re are the Mach and Reynolds numbers. These numbers are until today the prevalent measure of rarefaction, classifying the rarefaction levels in four (rather loosely distinct) regimes: the hydrodynamic, slip, transitional and free molecular regime. Their most widely acceptable definition is given below

- $\text{Kn} < 10^{-3}$ (or $\delta > 1000$): Hydrodynamic regime. The gas may be considered as a continuum medium and the Navier-Stokes equations are applicable.
- $10^{-3} < \text{Kn} < 10^{-1}$ (or $1000 > \delta > 10$): Slip regime. Non-equilibrium phenomena start manifesting in the boundary regions of the domain. In particular, velocity slip and temperature jump are observed on the walls.
- $10^{-1} < \text{Kn} < 100$ (or $10 > \delta > 10^{-2}$): Transition regime. A kinetic description of the gas is necessary, since intermolecular collisions are reduced and the distribution function is not of Maxwellian type.

- $\text{Kn} > 100$ (or $\delta < 10^{-2}$): Free molecular regime. The molecules undergo ballistic motion and remain unaffected by other molecules. No intermolecular collisions take place.

As we depart from the hydrodynamic regime, non-equilibrium phenomena appear: the gas and the wall surface do not have the same velocity or temperature, secondary flows are induced by temperature gradients (or concentration gradients for mixtures) and so on. These phenomena can not be captured by the classical hydrodynamic equation systems.

The applicability of Euler/Navier-Stokes equations can be extended up to the slip regime by using appropriate velocity slip and temperature jump boundary conditions [45]. In this way, existing CFD methodologies can be extended up to the slip regime with minimal further computational load and problems of mixed density flow fields and complicated geometries can be tackled [3]. However, only a limited range of rarefaction ($\text{Kn} \leq 0.1$) can be simulated in this way. There have been some attempts of extending the applicability of this approach with higher-order boundary conditions [31, 46] or by changing the constitutive relations [47]. The most successful treatment is attributed to Sone with a development of a hydrodynamic system of equations for rarefied gas flows, generated by an asymptotic expansion of kinetic equations [48].

Also, higher order equation systems have been considered. Chapman [49] and Enskog [50] independently described the distribution function f of molecules in terms of a deviation series from the equilibrium Maxwell distribution, according to

$$f = f^{(0)} + \text{Kn}f^{(1)} + \text{Kn}^2f^{(2)} + \dots \quad (2.19)$$

By replacing this expression in the Boltzmann equation, we obtain a system of integro-differential equations. The zeroth, first and second order terms lead to the Euler, Navier-Stokes and Burnett equations respectively [51]. This was a very important point in the history of statistical mechanics, since the Chapman-Enskog analysis allowed the calculation of the viscosity and thermal conductivity transport coefficients from first principles [41]. The solution of Burnett equations is still considerably limited since they face severe difficulties with numerical stability [52].

2.3 Kinetic models

In order to deal with the analytical barriers and immense computational requirements associated with the solution of the Boltzmann equation, several models have been proposed to substitute the collision term. The description of the complete behaviour of molecular interaction contains a lot of information which is not needed for many purposes. Thus, the loss and gain terms are modified according to the assumption that the molecules attain a Maxwellian distribution after a single inter-molecular collision, while simultaneously matching the first moments of Equation (2.3) with the ones of the model. In more detail, the basic requirements for the construction of a kinetic model are the following:

- The laws of conservation must be satisfied, i.e.

$$\int \phi(\boldsymbol{\xi}) Q(f, f') d\boldsymbol{\xi} = 0 \quad (2.20)$$

where $\phi(\boldsymbol{\xi}) = 1, m\boldsymbol{\xi}, m\xi^2/2$ are the five collision invariants of mass, momentum and energy.

- The distribution function should approach the Maxwellian distribution in equilibrium.
- Results near the hydrodynamic regime should agree with exact results known for that case.
- The H-Theorem must be satisfied.

The BGK model, proposed in [53] and independently in [54], was the first model to appear and has been widely applied, mostly due to its simplicity

$$Q(f, f^M) = \nu (f^M - f) \quad (2.21)$$

with ν being the collision frequency, assumed to be independent of the molecular velocity, and f^M is the local Maxwellian, calculated with the local number density, temperature and velocity according to Equation (2.1). The Maxwellian and local distribution parts represent the gain and loss terms of the Boltzmann collision operator, respectively. This model is closely related to the Maxwell diffuse type

of reflection for interaction with walls, since molecules relax to the local Maxwellian distribution with a uniform angular distribution around the point of collision after a single collision.

The BGK model has provided satisfying results in the whole range of the Knudsen number. In fact, it has been seen in many works that the results provided by this model are reasonably close to the ones provided by the Boltzmann equation (e.g. within 1-2%) [45]. However, there are some well known limitations of the model. In particular, the collision frequency must be adjusted according to the flow needs. For an isothermal flow, a Chapman-Enskog expansion method is used to obtain the correct value of viscosity, while for non-isothermal transport phenomena the heat conductivity is matched to the value provided by the full collision integral by the same method. It is impossible to have simultaneously both transport coefficients correctly determined by this model and therefore yields a Prandtl number equal to unity for monatomic gases (the correct value is 2/3). In BGK model, the collision frequency must be multiplied by 3/2 for the solution of heat transfer problems and therefore it is not appropriate for the simulation of coupled flow and heat transfer phenomena.

Two more models were produced in the same manner but also keeping higher moments of the collision term, namely the Shakhov model [55]

$$Q(f, f^M) = \nu \left\{ f^M \left[1 + \frac{2}{5} \frac{m}{n (k_B T)^2} (1 - \text{Pr}) \mathbf{q} \cdot (\boldsymbol{\xi} - \hat{\mathbf{u}}) \left(\frac{m(\boldsymbol{\xi} - \hat{\mathbf{u}})^2}{2k_B T} - \frac{5}{2} \right) \right] - f \right\} \quad (2.22)$$

and the Ellipsoidal model [56]

$$Q(f, f^M) = \nu \text{Pr} \left\{ \frac{n}{\pi^{3/2}} \sqrt{|A|} \exp \left[- \sum_{i,j=1}^3 (\xi_i - \hat{u}_i) A_{ij} (\xi_j - \hat{u}_j) \right] - f \right\} \quad (2.23)$$

where

$$A_{ij} = \left[\frac{2k_B T \delta_{ij}}{m \text{Pr}} - \frac{2(1 - \text{Pr}) \hat{P}_{ij}}{nm \text{Pr}} \right]^{-1} \quad (2.24)$$

Pr is the Prandtl number, k_B is the Boltzmann constant, m is the molar mass and δ_{ij} the Kronecker delta. The ellipsoidal model is derived to further satisfy the expression

$$\int (\xi_i - \hat{u}_i) (\xi_j - \hat{u}_j) f_{ES}^M d\xi = \frac{nk_B T}{\text{Pr}} \delta_{ij} - \frac{(1 - \text{Pr}) \hat{P}_{ij}}{\text{Pr}} \quad (2.25)$$

It can be seen that by substituting $Pr = 1$ in (2.22) and (2.23) the BGK expression is retrieved. In the simulations of the following Chapters, the characteristic value for monatomic gases, $Pr = 2/3$, has been used to obtain correct values for all physical quantities.

A shortcoming of the Shakhov model is that the H-theorem has not been proven for its non-linear form. However, since it was shown that the H-theorem holds for the ES model [57], it is believed that it also holds for the S model since they have been produced in the same manner. Furthermore, we have not observed any unphysical findings in our numerical simulations and therefore conclude that the Shakhov model is reliable even in its non-linear form.

Other models have been proposed in [58, 59, 60]. In the case of mixtures, kinetic models have been derived by Morse [61], Hamel [62], McCormack [63] and Kosuge [64]. Their application is more complicated [65, 66] and additional mixture-dependent information may be required [67, 68].

It is also important to note that it is sometimes possible to linearize the distribution function in terms of a small quantity depending on the problem at hand (e.g. a small temperature difference in a heat transfer problem or a small pressure gradient in a pressure driven flow). In this case, the resulting equations are easier to handle and possess favourable mathematical properties. Furthermore, similar equations have been widely used in the past in neutron transport problems and this leads to an exchange of concepts and methods. The linearized formulation is a particularly popular approach for kinetic model equations and has been employed in several problems of Chapters 3 and 4.

2.4 Numerical methods

The numerical solution of the Boltzmann transport equation still remains a formidable task due to the seven dimensions of the distribution function and the complicated collision integral. Some numerical solutions have appeared in the last decades [69, 70, 71]. However, they mostly concern the linearized form of the Boltzmann equation or are limited to hard sphere interaction. Another physically realistic method of simulation would be to consider the interaction of all molecules located inside the domain and apply the laws of motion. This is the method of Molecular Dynamics. No approximations

are made, except the form of the intermolecular potential, and therefore it can capture the largest possible variety of phenomena. It is one of the few methods that can also deal not only with rarefied gases but also with dense gases, liquids and two phase flows. However, due to the enormous amount of molecules in real conditions, the method is only applicable for problems of very small dimensions, of the order of a few nanometers, and for very small times. Thus, it is used only sparingly in the field of rarefied gas dynamics.

For reasons of computational efficiency and memory availability, the kinetic model equations are more frequently used for the simulation of rarefied gases. This approach has been studied systematically for decades and a robust theoretical background is now available. The Discrete Velocity (or Discrete Ordinates) Method (DVM) [72] is one of the most widely used methods. It is applied in Chapters 3-6 of this work for various conditions, for both linearized and non-linear kinetic formulations. It is completely deterministic and its basic principle is that only a discrete set of molecular velocities is examined, carefully chosen so that the integration of the distribution function during the calculation of the bulk quantities is performed with good accuracy. Thus, we can discretize the kinetic equations in the physical and molecular velocity space and solve only for these specific discrete velocities in an iterative manner. This method has been used extensively in several works [73, 74, 75] and is particularly suitable when the distribution function can be linearized in terms of a small parameter [76, 77]. It can also be employed when the form of kinetic models is non-linear [78, 79] but this approach has not received equally wide attention due to the inherent difficulties in the corresponding problems.

The Direct Simulation Monte Carlo (DSMC) method was formulated by Bird [80, 81] in 1963 and is of statistical nature. It is based on the direct simulation of the interaction between computational particles, each one representing a large number of real molecules. The simulated gas is composed of these particles which move and interact among themselves, as well as with solid walls. The collisions are performed in a stochastic manner, i.e. collision pairs are chosen randomly according to certain laws, while their motion is deterministic. The underlying assumptions are the same as in the Boltzmann equation and it has been proven [82] that for a large number of computational particles the

method is equivalent to solving the Boltzmann equation itself. The DSMC method is well known for its simplicity, as well as its accuracy and efficiency in highly non-equilibrium systems. It is also relatively easy to consider various phenomena such as ionization and flows with chemical reactions. Its most important drawback is the strong statistical noise appearing for transport phenomena close to the equilibrium state. This problem can be alleviated if appropriate techniques are used [83, 84] but the proposed modifications are not implemented easily.

In practice, the gas may be close to or far from equilibrium in different positions of the same apparatus and approaches capable of dealing with multiple levels of rarefaction are often required. An approach based on kinetic principles is imperative, since it is the only way to describe the whole range of the Knudsen number. As the complexity increases for high-dimensional problems, the DSMC method is usually preferred over the use of kinetic equations. However, this method is associated with certain difficulties in the parallelization of the code [85] and statistical noise for low speed flows, while in the solution of high speed flows its performance is excellent. On the other hand, deterministic methods are more appropriate for low Mach numbers, where the transport equations are simplified due to linearization and their solution is obtained very efficiently due to the proposed acceleration schemes [76, 66, 86].

There are also schemes where the phase space is discretized and treated similarly to the DVM but the collision integral is obtained by employing particle methods. These approaches belong in the family of semi-regular methods [87] and may offer significant advantages.

There are numerous other methods that have not been used in this work, such as the Lattice Boltzmann method [88, 89], the Information Preservation method [90, 51], the Analytical Discrete Ordinate method [91, 92], moment methods [93, 94], variational methods [95], extended hydrodynamic equation systems [48] etc. Even though these methods can also be very effective, limitations related to applicability range, generality, accuracy or complexity usually lead us to the selection of DVM or DSMC.

Finally, it is noted that micro-/mesoscopic numerical methods are now solved much faster than

in the past, not only due to the larger computational power and availability but also due to the possibility of extended parallelization programming techniques in Graphics Processing Units (GPUs) by the CUDA technology [96, 97]. It is expected that these computational techniques will receive more attention in the near future.

2.5 Boundary conditions

Special attention must be given for the boundary conditions required for the solution of the Boltzmann equation. The boundary conditions are a very important part for the solution of any problem and many non-equilibrium phenomena may develop near the domain boundaries. The interaction of rarefied gases with a solid surface is the most challenging aspect of this scientific branch and deserves the dedication of extra effort. There has been significant effort in modelling the boundary conditions in several works [98, 99], even though only the Maxwell scattering kernel has been used. Nevertheless, there are many arguments against its use in most cases. Another kernel was proposed by Epstein [100], where the accommodation coefficient depends on the particle velocity, but it is also an empirical approach and has not been widely accepted.

The application of the Cercignani-Lampis (CL) kernel, first seen in [101] and re-derived by different approaches in [102, 103, 104], is recommended instead. Some of the facts that establish the superiority of this model are the distinction between the accommodation of energy and momentum through the coefficients α_n and α_t and the possibility of adjusting them to obtain diffuse, specular or backscattering reflection. It is widely accepted that this approach seems to be more physical and its linear form has been used successfully in the past in several papers concerning various flow problems [105, 106, 107, 108]. It was also easily adapted to the DSMC method [109, 110] after some extensions by Lord [111, 112]. However, very limited work has been done in linear heat transfer [113] and none so far involving non-linear kinetic equations.

An alternative approach in modelling gas-surface interaction is to move this effect from the boundary conditions to the Boltzmann equation. In [114] the interaction between wall and gas molecules

is split in two parts: the long range attractive forces are modelled as a force field on the streaming part of the Boltzmann equation, while the short range repulsive potential is included in an additional collisional term. This method is derived from Enskog's theory of dense fluids and a Monte Carlo collisional procedure similar to the one used for the gas molecules can be employed for interaction with walls as well. This model is able to predict accommodation coefficients qualitatively (and in some cases quantitatively) close to those provided by MD simulations.

The study of roughness is also another subject of a lot of research currently, such as [115]. In this work, direct simulation Monte Carlo is used along with rough walls, derived by a statistical approach, and a mathematical formulation is introduced to deal with difficulties associated with the complexity of calculating the intersection of the surface with the molecular trajectory in an efficient manner.

The work of Lord is also well known in the literature for the extensions of the Cercignani-Lampis kernel and its application in the DSMC method [111, 112]. The original Cercignani-Lampis kernel does not include the case of diffuse reflection with incomplete energy accommodation, i.e. the reflection of molecules with equal probability at each direction at a partially accommodated energy level. In this case, the kernel is independent of the tangential velocity orientation and therefore the coefficient of tangential momentum is unity. However, the accommodation coefficients of energy, equal for the tangential and normal directions, can be different than unity. This case is considered in these works, also including the case of partially diffuse scattering. Lord also points out that the CL model may be used to describe internal degrees of freedom but fails to provide a realistic description of vibrational states because of its classical (instead of quantum) derivation and modifies the scattering kernel accordingly.

Three methods have been used to derive the accommodation coefficients of the diffuse-specular or CL models:

- Derivation through molecular beam experiments

Molecular beams can be used to determine the angular distribution of reemitted molecules

and obtain information on the validity of theoretical models and the accommodation coefficients. A beam of molecules of any species (but preferably of small molecular mass, such as helium) is concentrated on a point of the surface under consideration, while a movable detector is used to determine the pattern of departing molecules. The beam must be as nearly monoenergetic as possible and properly focused on the point under investigation. The surface should be a single crystal of known orientation and its surface should be clean, or at least, contaminated in a known way. The actual measurement is the ratio of the molecules scattered for each particular solid angle to the number of impinging molecules, without distinguishing the molecules according to their speed. The experimental setup and basic principles are very well described in [116] and some experiments can be seen in [117, 118].

It can be seen [101] that the departing distributions have a totally different shape than the one produced by the diffuse-specular kernel, while the CL kernel provides satisfactory results. The agreement is not simply due to a best fitting, since the values of α_n and α_t are the same in all cases.

- Derivation through bulk quantity comparison between experiments and numerical results

The most popular method of determining gas-surface interaction details is via the fitting of the accommodation coefficients through the comparison of macroscopic quantities between reliable experimental and numerical data. There are several works employing this principle [119, 120, 121]. A measurable quantity, such as the flow rate through a channel or the heat flux in a geometry with different surface temperatures, is compared with simulation results or already tabulated numerical values for different accommodation coefficients in the literature. In this manner, the very costly examination of gas-surface interaction in the micro-/nanoscale and the corresponding limitations are avoided.

- Derivation through Monte Carlo / Molecular Dynamics simulations of gas-surface interaction

The accommodation coefficients can also be found by comparison with Monte Carlo [122, 118] or Molecular Dynamics [123, 124] calculations. The surface data may be imported via atomic force microscopy on a real surface [125] or may be generated according to the wall characteristics [124, 123]. This type of study may receive more attention in the following years due to the high accuracy and increasing availability of computational resources. Furthermore, in this manner deviations from currently available theoretical models, that are due to approximations such as the independence of the accommodation coefficients on the impinging particle conditions (i.e. energy, internal state, direction of incidence), can be observed [123] and mostly phenomenological modifications have been proposed [124].

Further information on various scattering kernels, their application and comparison with experiments may be found in Chapter 3.

2.6 Flow through channels

The problem of flow through channels of various cross-sections is very important for the rarefied gas dynamics community. The flow configuration can be described as follows: Two infinitely large reservoirs, containing a single, monatomic, rarefied gas, are connected via a channel. The reservoirs are maintained at different pressures $\hat{P}_{in}, \hat{P}_{out}$, inducing gas motion through the channel. The temperature of both vessels and all walls remains constant and equal to T_0 . Our aim is to calculate practical quantities, such as the mass flow rate, in the steady state. Problems of this type are investigated for different conditions and channel cross-sections in Chapters 3, 4 and 6.

There are significant applications for such flows and particularly for flow through cylindrical tubes. In the case of an orifice (i.e. a tube of negligible length), the configuration can be used for comparison with experimental data without the influence of gas-surface interaction, since results are practically independent of the wall accommodation properties [126, 45]. Thus, the apparatus can be realized experimentally and used as a test for kinetic models, numerical methods and intermolecular interaction models. Furthermore, orifices and finite length channels are commonly encountered in

many practical applications in aerospace [15], vacuum [127], microfluidics [128] and other applications [129, 130, 131], while long channels are also common in vacuum and MEMS networks.

Flow through long channels has been considered by many researchers [132, 133, 86] and for various geometries [73, 134, 135, 136, 74, 137], both numerically and experimentally. The wide availability of results stems from the simplifications occurring because of the fully developed flow conditions. Due to this hypothesis, the channel end effects are considered to be negligible. In order to further increase accuracy, some authors have applied the effective length concept [45] to take into account the finite length. This effect has also been considered in this work and the corresponding analysis is given in Chapter 4.

The study of short channels poses large difficulties due to the increased dimensionality of the problem: the distribution function is four- or five-dimensional and the complete flow field, including part of the upstream/downstream containers, must be included in the simulation. In this case, the methodology is differentiated depending on the size of the pressure difference.

When large pressure differences are considered, the flow is non-linear. There are several experimental investigations regarding flow through finite (or zero) length channels [126, 138, 127]. Results include mass flow rates, discharge coefficients and interpolating formulas. Tubes of small length-to-radius ratios have also been studied experimentally by Sreekanth [139], Fujimoto and Usami [140] and Marino [141] and Varoutis et al. [142] for a wide range of pressure ratios in the transition regime.

Numerical works during the 60's investigate slit and orifice flows near the free molecular regime [143, 144, 145], with particular emphasis on flow into vacuum, but their range of applicability is small. In order to obtain the behaviour of the flow for any rarefaction regime, the most successful approaches rely on the Direct Simulation Monte Carlo (DSMC) method and the discrete velocity method (DVM). For large pressure differences, DSMC has been used in the whole range of rarefaction, due to its simplicity and high accuracy for high speed flows, for the solution of slit [146, 147, 148], orifice [149, 15, 150] and short channel flow [151, 152, 147]. These works have limitations on the pressure ratio range, up to 0.7-0.9 [149, 152] due to the increased noise in this regime. It is also worth

mentioning that some authors [146] derive interpolating formulas for the mass flow rate, covering up to the whole range of rarefaction.

Non-linear kinetic model equations have also been tackled by the DVM for problems of plane and axisymmetric geometry. Early works [153, 154, 155] may contain some inaccuracy due to the high computational cost of these calculations and the low-order schemes. More recent works [79, 78] show that this approach could be used alternatively for any value of pressure ratio in a unified manner, as an alternative to DSMC. This type of treatment is applied in Chapter 6 for the solution of flow through a tube of finite length, driven by large gradients of pressure. An enhanced algorithm is proposed by applying certain computational techniques. In particular, the total number of iterations is significantly reduced by the Wynn-epsilon acceleration [156, 157], the code is parallelized and memory demands are reduced by proper handling of the allocated arrays. The efficiency of the algorithm is described and a preliminary comparison with recently obtained DSMC results [152] is provided. Our objective is to provide a fully deterministic algorithm for solving non-linear kinetic equations and obtain results with computational efficiency similar to that of the DSMC method.

In the case of small pressure differences, the literature is rather limited. Very few experimental works deal with low pressure differences [158, 159]. Regarding numerical works, Akin'shin et al [160] have solved the linearized non-isothermal slit problem by the integral moment method employing the Shakhov kinetic model. Flow through a slit has also been examined by Hasegawa and Sone [161] for small pressure differences with the BGK model. Sharipov has applied the Discrete Velocity method to solve the linearized isothermal [162] and non-isothermal [163] slit problem, where the satisfaction of the Onsager theorem is verified.

In Chapter 4 of this dissertation, we apply the Discrete Velocity method to investigate flows driven by small pressure differences in the whole length of the Knudsen number. The channel geometry length ratio ranges from zero up to 10 and the channel end effects are considered by including a part of the upstream and downstream containers. Low pressure differences have not been examined in the past and a study of this problem is important, since it provides reliable and efficient solutions

for conditions where the computational cost of DSMC is very high. The range of applicability of linearized theory is examined via a comparison with DSMC results in the literature, in order to cover all possible conditions of flow, along with the high-velocity flow in short tubes and the linearized, fully developed flow through long tubes. This is a continuation of previous work [156] where it was shown that linearized theory was valid not only for infinitesimally small but also for finite differences and can be used in a range beyond the strict mathematical limits. Results include distributions of all important macroscopic quantities (number density, temperature, velocity) as well as the mass flow rate in dimensionless form.

Besides the case of straight pipes, channel elements with different geometrical configurations of short length, such as contraction/expansion elements [164, 165, 166, 167] and turns [168], have been investigated in the literature. Numerical results are usually limited in the hydrodynamic, slip or free molecular regime or do not take into account the fact that the distribution function is not Maxwellian at the channel ends [169]. The simulation of gas flows in short channel components is very important for practical applications. Results for such geometries are necessary for numerical codes simulating rarefied flows in networks in a very efficient manner, based on kinetic principles [170]. The objective in this case is not to obtain a complete, highly accurate solution, which in most cases can only be achieved by extremely demanding kinetic simulations of the whole network, but to make reliable estimations on the flow rate and pressure drop in vacuum systems and MEMS. This information is particularly helpful during the designing phase of such devices. Furthermore, it can assist in optimization and inverse engineering studies. For this purpose, the contraction/expansion channel element, consisting of two cylindrical tubes of different diameters connected in series, is examined in Chapter 6 via the DSMC method. The pressure difference is large and various geometrical configurations are considered.

2.7 Non-linear heat transfer

In many occasions the design and optimization of high vacuum equipment, micro-devices or applications of high altitude aerodynamics include the study of heat transfer effects through rarefied gases. The problem of heat transfer between parallel plates has been studied extensively, both for single gases [171, 172, 173, 174, 175] and mixtures [176] in the whole range of the Knudsen number. Even more, it has been used to benchmark the efficiency of several semi-analytical and numerical methods solving kinetic equations [177, 99, 178]. In the case of heat transfer in a rarefied gas between coaxial cylinders, it is commonly found in various technological applications, such as the Pirani gauge [4] for monitoring pressure in vacuum technology. The Pirani sensor is composed of a cylindrical vessel in the center of which a filament is heated and its electrical resistance is checked. As the gas pressure inside the vessel drops, the heat transferred from the filament to the gas is reduced, the filament temperature is increased and the resistance of the wire is modified. It is also used in the area of low/medium vacuum and its applications are found in the semi-conductor industry, in leak detection and food processing. Furthermore, this geometry is found in multilayer insulation blankets for cryogenic equipment [20] and micro heat exchangers in microfluidics. Also, it has been used for a long time to determine the thermal conductivity of gases and to study temperature jump and energy accommodation at the inner cylinder.

Most of this work is based on linearized kinetic solutions of the BGK kinetic model equation under the restrictive assumption of small temperature differences between the two walls. Only few results exist in the literature for the more general case of arbitrary large temperature ratios between the plates and most of them are based on the BGK model with purely diffuse reflection at the walls [179]. Some of the well known drawbacks of this approach are that it can not predict the correct value of the transport coefficients and simulate non-isothermal flows.

Another important factor that is often neglected in kinetic theory analyses is the influence of the intermolecular potential. There are several models to apply in this case, such as Hard Spheres, Variable Hard Spheres, Variable Soft Spheres, Inverse Power Law, Lennard-Jones and realistic potential [68,

80]. Differences among them lie in the modelling or not of both attractive and repulsive intermolecular forces, as well as the shape of the potential. The effect of the intermolecular potential is very important for non-linear heat transfer phenomena, since the differences in the properties of the two colliding partners become larger. In this work, the Inverse Power Law (IPL) model is used due to its simplicity and flexibility. The repulsive contribution is taken into account and the viscosity is related to the temperature via the simple expression $\mu \propto T^\omega$. The two limiting values $\omega = 0.5$ and $\omega = 1$ correspond to the cases of Hard Spheres and Maxwell Molecules respectively, while the intermediate values are related to the Variable Hard Spheres model of specific gases [80].

Chapter 3

Gas-surface scattering effect in flow and heat transfer problems

3.1 Boundary condition models

The laws of interaction between a gas and a solid surface need to be taken into account in the vast majority of practical situations, since both internal and external flows usually include some interaction with walls. These laws are very important from an engineering point of view because the phenomena of lift and drag, friction, heat transfer, etc. highly depend on them. This interaction, however, is not easily described theoretically due to the large number of factors of influence, such as the solid surface structure, its roughness and cleanliness, and the high complexity involved in the process. In reality, the particle is adsorbed at the impact point and may form chemical bonds, dissociate and become ionized before being re-emitted after a small time interval back to the main volume of the gas from a different point of the surface. A complete simulation can not be realized easily since the departing velocity ξ can only be determined if the full path of the molecule within the wall is computed exactly by the method of molecular dynamics, leading to a very high computational cost. Fortunately, the simulation of the detailed interaction process is not needed in many cases. An adequate description of the scattering phenomena is obtained by employing simplified but reliable models, correlating the distribution functions of molecules approaching and leaving the wall surface. Even though this approach has some limitations, it provides good results for a wide variety of conditions.

At this point, some fundamental notation conventions used throughout the following analysis need to be explained. In the following, the superscripts $-$, $+$ are used to distinguish between the distributions before and after the interaction with the wall. Furthermore, the apostrophe ($'$) superscript is attached to the molecular velocity vector of particles before interaction with the wall. Finally, the subscripts n , t denote the normal and tangential directions relative to the wall. Thus, for example, the

distributions of incident and departing molecules are $f^-(\xi')$ and $f^+(\xi)$ respectively, while the departing molecular velocity vector consists of a normal and two tangential components $\xi = (\xi_n, \xi_{t1}, \xi_{t2})$.

A scattering kernel $R(\mathbf{x} \rightarrow \mathbf{x} + d\mathbf{x}, \xi' \rightarrow \xi, t \rightarrow t + \tau)$ is defined as the probability density function of the reflected state of the molecule, when it reaches the wall with velocity ξ' , becomes adsorbed on the wall at point \mathbf{x} at time t and departs from it after a time interval τ at the surface point $\mathbf{x} + d\mathbf{x}$ with velocity ξ . For certain conditions, the scattering kernel may also depend on the impinging distribution [180] but this case is excluded from this work. Furthermore, in order to make this study more tractable, some assumptions are in order. First off, the adsorption time τ and the distance to the point of re-emergence $d\mathbf{x}$ are taken to be negligibly small. Moreover, we assume that the wall molecules remain relatively unaffected by collisions and are in local thermal equilibrium with each other at the wall temperature T_0 , which may vary on a macroscopic scale. These hypotheses allow us to assume that $R = R(\xi' \rightarrow \xi)$ and that the dependence on the surface point \mathbf{x} is only a function of the temperature T_0 and the chemical composition of the wall. Finally, all kinds of chemical reactions and alterations of the molecule are also excluded from this study.

An obvious property of the scattering process is that, if the wall is non-porous and non-absorbing, all molecules will be re-emitted with some velocity. Thus the total scattering probability must be equal to unity

$$\int_{\xi_n > 0} R(\xi' \rightarrow \xi) d\xi = 1 \quad (3.1)$$

It is clear that this property is directly connected to the condition of no wall penetration ($u_n = 0$). It is also noted that in some specialized applications, such as interaction with the surface of a vacuum pump cryo-panel, this condition may not be valid.

The total number of molecules impinging on a wall surface unit area per unit time interval is

$$f^-(\xi') \big|_{\xi'_n} d\xi' \quad (3.2)$$

If we multiply Equation (3.2) with $R(\xi' \rightarrow \xi)$ and due to the kernel properties, we derive the general

expression for the boundary conditions

$$|\xi_n| f^+ (\xi) = \int_{\xi'_n < 0} |\xi'_n| R(\xi' \rightarrow \xi) f^- (\xi') d\xi' \quad (3.3)$$

In essence, this simply expresses the principle of mass flux equilibrium on the wall.

The scattering kernel must also be non-negative

$$R(\xi' \rightarrow \xi) \geq 0 \quad (3.4)$$

for all ξ, ξ' due to its definition as a probability density.

Another property that the scattering kernel should satisfy is the so-called reciprocity law (or detailed balance)

$$|\xi'_n \cdot \mathbf{n}| f_0(\xi') R(\xi' \rightarrow \xi) = |\xi_n| f_0(\xi) R(-\xi \rightarrow -\xi') \quad (3.5)$$

The physical meaning is that if a gas is at equilibrium at the temperature T_0 of the wall and hence has distribution function f_0 , the number of molecules scattered from a velocity range $(\xi', \xi' + d\xi')$ to a velocity range $(\xi, \xi + d\xi)$ is equal to the number of molecules scattered from $(-\xi, -\xi - d\xi)$ to $(-\xi', -\xi' - d\xi')$. Thus, if the impinging distribution is the Maxwellian at the wall conditions f_0 and mass is conserved at the wall, then the distribution function of the emerging molecules is again f_0 , or in other words, the wall Maxwellian is preserved and satisfies the boundary conditions. It is a consequence of time reversal invariance and of thermal equilibrium of the medium.

It is also important to note that, when the problem in question is linearized, we obtain

$$h^+ = Ah^- + h_w - Ah_w \quad (3.6)$$

where h_w is the Maxwellian perturbation term of each particular wall and the operator A is defined by

$$\begin{aligned} Ah^- &= \frac{1}{\xi_n} \int_{\xi'_n < 0} |\xi'_n| R(\xi' \rightarrow \xi) \exp(\xi^2 - \xi'^2) h^-(\xi') d\xi' \\ &= \frac{1}{\xi_n} \int_{\xi'_n < 0} |\xi'_n| R(-\xi \rightarrow -\xi') h^-(\xi') d\xi' \end{aligned} \quad (3.7)$$

This can be derived by substituting the linearization expression, in the form $f^+ = f_0(1 + h^+ - h_w)$, in Equation (3.3).

Before moving on to the description of various scattering kernels found in the literature, we must make a note on the visual representation of the boundary conditions in the microscopic level. The most usual practice is to plot the scattering patterns occurring from a monoenergetic collimated beam (or, in practice, from a collimated thermal beam) impinging on the surface with a known angle [180]. The quantity

$$N(\theta, \phi) = \frac{1}{N_0} \int_0^\infty f(\xi) |\xi \cdot \mathbf{n}| \xi^2 d\xi \quad (3.8)$$

is the number of molecules scattered per unit solid angle (regardless of their velocity magnitude), normalized by the total amount of scattered molecules

$$N_0 = \int_{\xi \cdot \mathbf{n} > 0} f(\xi) |\xi \cdot \mathbf{n}| d\xi \quad (3.9)$$

The quantity N is plotted at the plane of incidence in Figures 3.1-3.6 for various models, in order to get a more direct sense of the phenomena. In the cases shown here, a monoenergetic beam has been simulated for these plots and the incidence angle is noted below each figure.

The simplest scattering model is the specular kernel, proposed in the early papers of Maxwell

$$R_S(\xi' \rightarrow \xi) = \delta_D[\xi' - \xi + 2\mathbf{n}(\mathbf{n} \cdot \xi)] \quad (3.10)$$

where \mathbf{n} is the unit vector normal to the surface at point \mathbf{r} and $\delta_D(\mathbf{r}) = \delta_D(x) \delta_D(y) \delta_D(z)$ is the Dirac function. In this model, the molecules are assumed to reflect specularly, i.e. the normal velocity component is reversed (Figure 3.1). This model is not realistic in most practical situations, since it cannot predict the appearance of non-normal stresses exerted from the gas on the surface.

Maxwell also proposed another kernel for the diffuse type of reflection, which has become the most well known and widely used model

$$R_D(\xi' \rightarrow \xi) = \frac{m^2 \xi_n}{2\pi(k_B T_w)^2} \exp\left(-\frac{m(\xi - \hat{\mathbf{u}}_w)^2}{2k_B T_w}\right) \quad (3.11)$$

In this case, the velocity magnitudes of re-emitted molecules follow a Maxwellian distribution, determined by the temperature and velocity of the wall, while the angular distribution is uniform. The scattering pattern occurring from Equation (3.11) is plotted in Figure 3.2. As stated in [180], the probability of any particular magnitude and direction of the velocity will be the same as in a gas in thermal and mechanical equilibrium with the solid. This is due to the fact that during the adsorption of the gas molecule, it interacts multiple times with the nearby wall molecules, coming to a local thermodynamic equilibrium with wall particles before returning to the flow domain. The popularity of this approach is based on the fact that the model is simple, easily understood at both microscopic and macroscopic level, while the associated numerical effort for its implementation is minimal. For this purpose, it has been used in a variety of physical systems, providing good results in agreement with corresponding experimental findings [74, 121]. However, in some cases, the gas may behave much differently. In particular, exceptionally rough or smooth walls may display different scattering patterns, while light molecules also tend to reflect more specularly than heavy ones.

In order to achieve a better agreement with practical results, Maxwell had to resort to qualitative arguments and introduce a phenomenological parameter α_M which is not directly related to the structure of the surface

$$\alpha_M(\phi) = \frac{\int_{\xi'_n < 0} \phi(\xi') |\xi'_n| f^-(\xi') d\xi' - \int_{\xi_n > 0} \phi(\xi) |\xi_n| f^+(\xi) d\xi}{\int_{\xi'_n < 0} \phi(\xi') |\xi'_n| f^-(\xi') d\xi' - \int_{\xi_n > 0} \phi(\xi) |\xi_n| f_w(\xi) d\xi} \quad (3.12)$$

It is used to express in which degree have the properties $\phi(\xi)$ accommodated to the wall conditions. The pre-collision property fluxes are the terms containing f^- , the post-collision fluxes is the one with f^+ and the wall conditioned flux is the integral containing f_w , which is the Maxwellian at the wall conditions. The diffuse-specular kernel is then expressed by

$$R_{DS}(\xi' \rightarrow \xi) = \alpha_M R_D(\xi' \rightarrow \xi) + (1 - \alpha_M) R_S(\xi' \rightarrow \xi) \quad (3.13)$$

The main assumption is that a portion of every surface element absorbs all the incident molecules and afterwards allows them to re-emit diffusely, while the remaining portion reflects all the molecules

incident upon it specularly [180] (Figure 3.3). Another, more commonly used, definition of α_M is that it represents the fraction of diffusively evaporated molecules, while the remaining molecules reflect specularly. This parameter is called the accommodation coefficient because it expresses the tendency of the gas to accommodate to the state of the wall. However, it is well known that momentum and energy accommodate at a different rate: momentum is changed much faster than energy and thus one coefficient is not enough to describe this process in a realistic manner. Also, as stated in [105, 106, 107], discrepancies are found in other cases between numerical and experimental data [159]. In particular, the mass flow rate is in reality lower than it was expected by numerical calculations and the required value of the Maxwell accommodation coefficient $0 < \alpha_M \leq 1$ would be outside of its physical range. Also, it has been reported that the value of α_M may depend on the rarefaction degree [159, 181]. Therefore, an attempt to examine a variety of gases and surfaces and store the corresponding values of α_M in tables would not be effective. It seems that trying to integrate all types of interaction mechanisms in only one free parameter is not correct and cannot be physically justified.

A more realistic model was presented by Cercignani and Lampis in [101], defined by

$$R_{CL} = R_{t1} R_{t2} R_n \quad (3.14)$$

consisting of two tangential

$$R_t \left(\xi'_t \rightarrow \xi_t \right) = \frac{1}{\sqrt{\pi \alpha_t (2 - \alpha_t) (2k_B T_w / m)}} \times \exp \left\{ -\frac{[\xi_t - (1 - \alpha_t) \xi'_t]^2}{(2k_B T_w / m) \alpha_t (2 - \alpha_t)} \right\} \quad (3.15)$$

and a normal part

$$R_n \left(\xi'_n \rightarrow \xi_n \right) = \frac{\xi_n}{\alpha_n (k_B T_w / m)} \times \exp \left\{ -\frac{[\xi_n^2 + (1 - \alpha_n) \xi_n'^2]}{(2k_B T_w / m) \alpha_n} \right\} I_0 \left(\frac{\sqrt{1 - \alpha_n} \xi_n \xi'_n}{\alpha_n (k_B T_w / m)} \right) \quad (3.16)$$

where $I_0(x) = (1/2\pi) \int_0^{2\pi} \exp(x \cos \psi) d\psi$ is the modified Bessel function of the first kind and zeroth order. The most apparent indication of the CL superiority in comparison to the diffuse-specular kernel

is the fact that continuous, physically reasonable, lobular shaped distributions of direction and energy are produced for the re-emitted molecules (Figure 3.4). By combining (3.3) with the CL kernel (3.14) - (3.16) and defining α_n, α_t similarly to (3.12), it can be seen that the two accommodation coefficients $\alpha_n \in [0, 1]$ and $\alpha_t \in [0, 2]$ correspond to the properties of normal kinetic energy ($\phi(\xi) = (m\xi_n^2)/2$) and tangential momentum ($\phi(\xi) = m\xi_{ti}, i = 1, 2$) respectively. According to the model assumptions, their values depend only upon the physical nature of the gas and the wall, as well as on the temperature of the latter. Furthermore, the reciprocity property is satisfied and the whole spectrum of scattering behaviour is described continuously. Some of the previously mentioned scattering behaviours can be reproduced by an appropriate selection of the accommodation coefficients. In particular, specular interaction can be reproduced for $\alpha_t = \alpha_n \rightarrow 0$, which leads to $R_{CL} \rightarrow R_S$ (Figure 3.5), and diffuse interaction for $\alpha_t = \alpha_n = 1$ with $R_{CL} = R_D$. Back-scattering can also be modelled by $\alpha_t \rightarrow 2, \alpha_n \rightarrow 0$ with $R_{CL} = \delta_D(\xi_n + \xi'_n) \delta_D(\xi_{t1} + \xi'_{t1}) \delta_D(\xi_{t2} + \xi'_{t2})$ (Figure 3.6). The dependence on two coefficients is an advantage, since as mentioned before momentum and energy are accommodated at a different rate. This kernel has been used in many recent works [110, 113, 156]. For rough physical surfaces, a value of α_t rather close to unity or slightly larger is to be expected. Finally, the thermomolecular pressure difference (TPD) exponent is dependent on the accommodation coefficients and does not remain equal to 0.5 as in the Maxwell diffuse-specular model [105].

3.2 Application of the CL kernel

3.2.1 Introduction

The procedure of the CL kernel application has been validated by reproducing previous works in the literature, including both flow [105, 107] and heat transfer [113] problems. This work is an extension to more demanding problems. In particular, the problems of linearized pressure-driven flow through a rectangular duct, linear and non-linear heat transfer between parallel plates, as well as non-linear heat transfer between concentric cylinders are treated in the next subsections. Similar methodology may be followed for any scattering kernel, if an even more realistic model is proposed.

3.2.2 Linearized flow through a rectangular duct

The application of the CL scattering kernel is studied here for the well known problem of rarefied gas flow through a long duct of rectangular cross-section with height H and width W [75]. The flow is fully developed, driven by a small pressure gradient along the longitudinal direction z , while the rectangular cross section lies in the $x - y$ plane. Isothermal wall conditions at reference temperature T_0 are assumed. This problem is more challenging than previous works due to the large number of boundary surface points and the two-dimensional nature of the molecular velocity vector. Detailed results for the conductance and dimensionless flow rate are tabulated in terms of the channel aspect ratio and certain values of the CL accommodation coefficients to use for practical engineering purposes. Finally, a comparison with experimental results is also performed.

The problem can be described in the whole range of the Knudsen number by the Boltzmann equation, where the collision term is substituted by the BGK model. After a well-known mathematical procedure [182, 77], involving linearization, non-dimensionalization and projection, we get the governing equation

$$c_x \frac{\partial \varphi}{\partial x} + c_y \frac{\partial \varphi}{\partial y} + \delta \varphi = \delta u_z - \frac{1}{2} \quad (3.17)$$

where

$$\varphi = \frac{1}{\sqrt{\pi}} \int h c_z \exp(-c_z^2) dc_z \quad (3.18)$$

is the projection of the distribution function, $c_i, i = x, y, z$ are the components of the molecular velocity (instead of $\xi_i, i = x, y, z$ due to the non-dimensionalization) and u_z is the macroscopic velocity along the duct. All quantities in (3.17) are in dimensionless form. The rarefaction parameter δ is defined as

$$\delta = \frac{PH}{\mu v_0} \quad (3.19)$$

with $P = P(z)$ being the pressure along the channel, μ the dynamic viscosity at reference temperature T_0 and $v_0 = \sqrt{2RT_0}$ the most probable molecular velocity, where R is the gas constant. The

macroscopic velocity is calculated through

$$u_z(x, y) = \frac{1}{\pi} \int_{-\infty}^{\infty} \int_{-\infty}^{\infty} \varphi \exp(-c_x^2 - c_y^2) dc_x dc_y \quad (3.20)$$

For simplicity, the methodology is presented for just the lower boundary, i.e. $y = -1/2$, but can be easily extended for the other three walls. The departing velocity components (c_n, c_{t1}, c_{t2}) are (c_y, c_x, c_z) , while the components of the impinging velocity (c'_n, c'_{t1}, c'_{t2}) are (c'_y, c'_x, c'_z) . Since linearization has taken place, Equation (3.6) is the starting point here, with terms containing h_0 vanishing because the walls are maintained stationary and isothermal at the reference temperature, leading to a zero perturbation from the reference Maxwellian. Acting accordingly on (3.6) in order to form the projection of the distribution function, given by (3.18), it is reduced that

$$\begin{aligned} \varphi^+ \left(x, -\frac{1}{2}, c_x, c_y \right) &= \frac{1}{\sqrt{\pi}} \int_{-\infty}^{\infty} A h^- \left(x, -\frac{1}{2}, c'_x, c'_y, c'_z \right) c_z \exp(-c_z^2) dc_z \\ &= \frac{1}{c_y \sqrt{\pi}} \int_{-\infty}^{\infty} \int_{-\infty}^{\infty} \int_{-\infty}^0 \left[\int_{-\infty}^{\infty} |c'_y| R(-c \rightarrow -c') c_z \exp(-c_z^2) h^- \left(x, -\frac{1}{2}, c'_x, c'_y, c'_z \right) dc_z \right] dc'_y dc'_x dc'_z \end{aligned} \quad (3.21)$$

for $c_y > 0$. This expression can be simplified by calculating the integral

$$\begin{aligned} E(c' \rightarrow c) &= \int_{-\infty}^{\infty} R(-c \rightarrow -c') c_z \exp(-c_z^2) dc_z \\ &= R_t(-c_x \rightarrow -c'_x) R_n(-c_y \rightarrow -c'_y) \int_{-\infty}^{\infty} R_t(-c_z \rightarrow -c'_z) c_z \exp(-c_z^2) dc_z \end{aligned} \quad (3.22)$$

The tangential Cercignani-Lampis component must be substituted in this expression. Taking into account the non-dimensionalization, Equations (3.15) and (3.16) become

$$R_t(c'_t \rightarrow c_t) = \frac{1}{\sqrt{\pi \alpha_t (2 - \alpha_t)}} \exp \left\{ -\frac{[c_t - (1 - \alpha_t) c'_t]^2}{\alpha_t (2 - \alpha_t)} \right\} \quad (3.23)$$

$$R_n(c'_n \rightarrow c_n) = \frac{2c_n}{\alpha_n} \exp \left\{ -\frac{[c_n^2 + (1 - \alpha_n) c_n'^2]}{\alpha_n} \right\} I_0 \left(\frac{2\sqrt{1 - \alpha_n} c_n c'_n}{\alpha_n} \right) \quad (3.24)$$

and we obtain

$$\int_{-\infty}^{\infty} R_t \left(-c_z \rightarrow -c'_z \right) c_z \exp \left(-c_z^2 \right) dc_z = (1 - \alpha_t) c'_z \exp \left(-c'^2_z \right) \quad (3.25)$$

Then, we substitute this result in Equations (3.22) and (3.21) to get

$$\begin{aligned} \varphi^+ \left(x, -\frac{1}{2}, c_x, c_y \right) &= \frac{1 - \alpha_t}{c_y \sqrt{\pi}} \int_{-\infty}^{\infty} \int_{-\infty}^{\infty} \int_{-\infty}^0 |c'_y| R_n \left(-c_y \rightarrow -c'_y \right) R_t \left(-c_x \rightarrow -c'_x \right) \\ &\quad \times c'_z \exp \left(-c'^2_z \right) h^- \left(x, -\frac{1}{2}, c'_x, c'_y, c'_z \right) dc'_y dc'_x dc'_z \end{aligned} \quad (3.26)$$

Finally, after rearranging this expression to get the φ^- projection according to (3.18) with c'_z and substituting the rest of the scattering kernel components from (3.23) and (3.24), the CL boundary conditions read as

$$\begin{aligned} \varphi^+ \left(x, -\frac{1}{2}, c_x, c_y \right) &= -\frac{2(1 - \alpha_t)}{\alpha_n \sqrt{\pi \alpha_t} (2 - \alpha_t)} \int_{-\infty}^{\infty} \int_{-\infty}^0 \varphi^- \left(x, -\frac{1}{2}, c'_x, c'_y \right) c'_y \\ &\quad \times \exp \left\{ -\frac{c'^2_y + (1 - \alpha_n) c_y^2}{\alpha_n} - \frac{[(1 - \alpha_t) c_x - c'_x]^2}{\alpha_t (2 - \alpha_t)} \right\} I_0 \left(\frac{2\sqrt{1 - \alpha_n} c_y c'_y}{\alpha_n} \right) dc'_y dc'_x \end{aligned} \quad (3.27)$$

for the lower horizontal wall and $c_y > 0$. In terms of the polar molecular velocity coordinates, it is expressed as

$$\begin{aligned} \varphi^+ \left(x, -\frac{1}{2}, c_p, \theta \right) &= -\frac{2(1 - \alpha_t)}{\alpha_n \sqrt{\pi \alpha_t} (2 - \alpha_t)} \int_{-\pi}^0 \int_0^{\infty} \varphi^- \left(x, -\frac{1}{2}, c'_p, \theta' \right) c'^2_p \sin \theta' \\ &\quad \times \exp \left\{ -\frac{(c'_p \sin \theta')^2 + (1 - \alpha_n) (c_p \sin \theta)^2}{\alpha_n} - \frac{[(1 - \alpha_t) (c_p \cos \theta) - (c'_p \cos \theta')]^2}{\alpha_t (2 - \alpha_t)} \right\} \\ &\quad \times I_0 \left(\frac{2\sqrt{1 - \alpha_n} (c_p \sin \theta) (c'_p \sin \theta')}{\alpha_n} \right) dc'_p d\theta' \end{aligned} \quad (3.28)$$

for $\theta \in [0, \pi]$. Following the same procedure at the upper horizontal wall ($y = 1/2$) leads to

$$\varphi^+ \left(x, \frac{1}{2}, c_p, \theta \right) = \frac{2(1 - \alpha_t)}{\alpha_n \sqrt{\pi \alpha_t} (2 - \alpha_t)} \int_0^{\pi} \int_0^{\infty} \varphi^- \left(x, \frac{1}{2}, c'_p, \theta' \right) c'^2_p \sin \theta'$$

$$\begin{aligned} & \times \exp \left\{ -\frac{(c'_p \sin \theta')^2 + (1 - \alpha_n)(c_p \sin \theta)^2}{\alpha_n} - \frac{[(1 - \alpha_t)(c_p \cos \theta) - (c'_p \cos \theta')]^2}{\alpha_t(2 - \alpha_t)} \right\} \\ & \times I_0 \left(\frac{2\sqrt{1 - \alpha_n}(c_p \sin \theta)(c'_p \sin \theta')}{\alpha_n} \right) dc'_p d\theta' \end{aligned} \quad (3.29)$$

and $\theta \in [-\pi, 0]$. The procedure is similar for the vertical walls. For the left wall we get

$$\begin{aligned} \varphi^+ \left(-\frac{1}{2}, y, c_p, \theta \right) &= -\frac{2(1 - \alpha_t)}{\alpha_n \sqrt{\pi \alpha_t(2 - \alpha_t)}} \int_{\pi/2}^{3\pi/2} \int_0^\infty \varphi^- \left(-\frac{1}{2}, y, c'_p, \theta' \right) c_p'^2 \cos \theta' \\ & \times \exp \left\{ -\frac{(c'_p \cos \theta')^2 + (1 - \alpha_n)(c_p \cos \theta)^2}{\alpha_n} - \frac{[(1 - \alpha_t)(c_p \sin \theta) - (c'_p \sin \theta')]^2}{\alpha_t(2 - \alpha_t)} \right\} \\ & \times I_0 \left(\frac{2\sqrt{1 - \alpha_n}(c_p \cos \theta)(c'_p \cos \theta')}{\alpha_n} \right) dc'_p d\theta' \end{aligned} \quad (3.30)$$

for $\theta \in [-\pi/2, \pi/2]$ and for the right wall

$$\begin{aligned} \varphi^+ \left(\frac{1}{2}, y, c_p, \theta \right) &= \frac{2(1 - \alpha_t)}{\alpha_n \sqrt{\pi \alpha_t(2 - \alpha_t)}} \int_{-\pi/2}^{\pi/2} \int_0^\infty \varphi^- \left(\frac{1}{2}, y, c'_p, \theta' \right) c_p'^2 \cos \theta' \\ & \times \exp \left\{ -\frac{(c'_p \cos \theta')^2 + (1 - \alpha_n)(c_p \cos \theta)^2}{\alpha_n} - \frac{[(1 - \alpha_t)(c_p \sin \theta) - (c'_p \sin \theta')]^2}{\alpha_t(2 - \alpha_t)} \right\} \\ & \times I_0 \left(\frac{2\sqrt{1 - \alpha_n}(c_p \cos \theta)(c'_p \cos \theta')}{\alpha_n} \right) dc'_p d\theta' \end{aligned} \quad (3.31)$$

for $\theta \in [\pi/2, 3\pi/2]$.

The final integrals (3.28)-(3.31) are calculated numerically at each iteration of the numerical scheme and take up the largest part of the simulation. Some common terms can be grouped and stored in an array to reduce the computational effort but this may result in high memory demands. Also, the impinging and departing distributions must be stored. These factors pose significant computational difficulties in the application of CL boundary conditions for high dimensional problems.

For practical calculations, the reduced flow rate is estimated by

$$G(\delta) = 2 \frac{H}{W} \int_{-W/(2H)}^{W/(2H)} \int_{-1/2}^{1/2} u_z(x, y) dy dx \quad (3.32)$$

Once the kinetic problem is solved, the dimensionless kinetic quantities are converted to dimensionalized bulk quantities following a standard procedure based on mass conservation along the channel [45]. The conductance of the flow is obtained by [74]

$$C = \frac{4(H \times W)^2}{2(H + W)} \frac{R_u T_0}{v_0 m} G^* \quad (3.33)$$

where

$$G^* = \frac{1}{\delta_1 - \delta_2} \int_{\delta_2}^{\delta_1} G(\delta) d\delta \quad (3.34)$$

Here δ_1 and δ_2 correspond to the inlet and outlet conditions, R_u is the universal gas constant, while m denotes the molar mass. The integrodifferential system of (3.17) and (3.20), along with the boundary conditions (3.28)-(3.31), may be discretized by the discrete velocity method and solved in an iterative manner, presented here briefly:

1. The gas velocity $u(x, y)$ is initially assumed
2. The discretized version of Equation (3.17) is solved using a marching scheme
3. The departing distribution φ^+ is calculated by the Cercignani-Lampis final expressions
4. The gas velocity is re-calculated from the new values of φ via Equation (3.20)
5. Steps 2 - 4 are repeated until convergence has been reached for the bulk velocity $u(x, y)$.

This procedure is given in detail in later chapters, along with various modifications.

3.2.3 Linearized and non-linear heat transfer between parallel plates

The examination of an isothermal flow problem, such as the one presented in the previous section, allows the determination of the tangential momentum accommodation coefficient α_t with good accuracy, since in that case the flow rate is practically independent of the normal energy accommodation coefficient α_n . In order to determine the latter coefficient, a second experiment may be performed for the same combination of gas and surface type, involving heat transfer. In this subsection, the problem of heat conduction in a rarefied gas confined between two parallel plates of infinite dimensions is

presented briefly for small and arbitrary temperature differences. The reader is referred to Chapter 5 for more details on the non-linearized formulation. The consideration of arbitrary temperature differences here also sheds some light in the application of the CL scattering kernel on the non-linear form of kinetic equations and the differences in the corresponding results.

3.2.3.1 Linearized heat transfer

Two parallel plates are maintained at different temperatures $T|_{y=\pm\frac{1}{2}} = T_0 \mp \Delta T/2$, where T_0 is the average temperature of the two walls. A rarefied gas is confined between them and we are interested in calculating heat conduction in the whole range of the Knudsen number. When the temperature difference ΔT is small, the distribution function can be linearized around the Maxwellian in the equilibrium conditions f_0 , i.e.

$$f = f_0 \left(1 + h \frac{\Delta T}{T_0} \right) \quad (3.35)$$

After non-dimensionalizing and applying the projections

$$\varphi = \frac{1}{\pi} \int \int h \exp(-c_x^2 - c_z^2) dc_x dc_z \quad (3.36)$$

$$\psi = \frac{1}{\pi} \int \int h (c_x^2 + c_z^2 - 1) \exp(-c_x^2 - c_z^2) dc_x dc_z \quad (3.37)$$

on the Shakhov kinetic model equation, we obtain the system

$$c_y \frac{\partial \varphi}{\partial y} + \delta \varphi = \delta \left[\rho + \tau \left(c_y^2 - \frac{1}{2} \right) + \frac{4}{15} q c_y \left(c_y^2 - \frac{3}{2} \right) \right] \quad (3.38)$$

$$c_y \frac{\partial \psi}{\partial y} + \delta \psi = \delta \left[\tau + \frac{4}{15} q c_y \right] \quad (3.39)$$

where the perturbations of number density, temperature and heat flux are defined as

$$\rho = \frac{n - n_0}{n_0} \frac{T_0}{\Delta T} = \frac{1}{\sqrt{\pi}} \int \varphi \exp(-c_y^2) dc_y \quad (3.40)$$

$$\tau = \frac{T - T_0}{\Delta T} = \frac{1}{3\sqrt{\pi}} \int [2\psi + \varphi (2c_y^2 - 1)] \exp(-c_y^2) dc_y \quad (3.41)$$

$$q = \frac{\hat{q}}{P_0 v_0} \frac{T_0}{\Delta T} = \frac{1}{\sqrt{\pi}} \int \left[\psi + \varphi \left(c_y^2 - \frac{3}{2} \right) \right] c_y \exp(-c_y^2) dc_y \quad (3.42)$$

Once again, we start from Equation (3.6), with the perturbation from the reference Maxwellian being

$$h_w|_{y=\pm\frac{1}{2}} = \rho_w|_{y=\pm\frac{1}{2}} \mp \frac{1}{2} \left(c^2 - \frac{1}{2} \right) \quad (3.43)$$

The presence of the impermeability constants ρ_w may seem a little odd here but they are eliminated further below in the process. We operate on (3.6) accordingly so that we get the boundary conditions in terms of the projections (3.36) and (3.37)

$$\varphi^+ = \frac{1}{\pi} \int_{-\infty}^{\infty} \int_{-\infty}^{\infty} \exp(-c_x^2 - c_z^2) (Ah^- + h_w - Ah_w) dc_x dc_z = B_\varphi + C_\varphi - D_\varphi \quad (3.44)$$

$$\psi^+ = \frac{1}{\pi} \int_{-\infty}^{\infty} \int_{-\infty}^{\infty} (c_x^2 + c_z^2 - 1) \exp(-c_x^2 - c_z^2) (Ah^- + h_w - Ah_w) dc_x dc_z = B_\psi + C_\psi - D_\psi \quad (3.45)$$

where A is defined in Equation (3.7) and $B_i, C_i, D_i, i = \varphi, \psi$ are the three parts of the corresponding integrals. The latter terms are calculated for each wall in the same way as in Section 3.2.2, that is, by separating the variables and carrying out analytically some of the integrals. The intermediate quantities B_i, C_i, D_i are found to be equal to

$$B_\varphi = -\frac{2}{\alpha_n} \int_{c'_n < 0} c'_n \exp \left[-\frac{c_n'^2 + (1 - \alpha_n) c_n^2}{\alpha_n} \right] I_0 \left(\frac{2\sqrt{1 - \alpha_n} c_n c'_n}{\alpha_n} \right) \varphi^-(c'_n) dc'_n \quad (3.46)$$

$$B_\psi = -\frac{2(1 - \alpha_t)^2}{\alpha_n} \int_{c'_n < 0} c'_n \exp \left[-\frac{c_n'^2 + (1 - \alpha_n) c_n^2}{\alpha_n} \right] I_0 \left(\frac{2\sqrt{1 - \alpha_n} c_n c'_n}{\alpha_n} \right) \psi^-(c'_n) dc'_n \quad (3.47)$$

$$C_\varphi|_{y=\pm\frac{1}{2}} = \rho_w|_{y=\pm\frac{1}{2}} \mp \frac{1}{2} \left(c_y^2 - \frac{1}{2} \right) \quad (3.48)$$

$$C_\psi|_{y=\pm\frac{1}{2}} = \mp \frac{1}{2} \quad (3.49)$$

$$D_\varphi|_{y=\pm\frac{1}{2}} = \rho_w|_{y=\pm\frac{1}{2}} \pm \frac{1}{2} [(\alpha_n - 1) c_n^2 - \alpha_n] \pm \frac{1}{4} \quad (3.50)$$

$$D_\psi|_{y=\pm\frac{1}{2}} = \mp \frac{(1 - \alpha_t)^2}{2} \quad (3.51)$$

where c_n are the positive c_y values and c'_n are the negative c_y values for the lower wall, while c_n, c'_n are the negative and positive c_y values for the upper wall. Therefore, from Equations (3.44)-(3.51), we obtain the final expressions

$$\varphi^+|_{y=\pm\frac{1}{2}} = B_\varphi \pm \frac{\alpha_n}{2} (1 - c_y^2) \quad (3.52)$$

$$\psi^+|_{y=\pm\frac{1}{2}} = B_\psi \pm \frac{\alpha_t (\alpha_t - 2)}{2} \quad (3.53)$$

3.2.3.2 Non-linear heat transfer

When the temperature difference ΔT takes large values, the non-linear form of the kinetic equation must be used. The Shakhov model kinetic equation, after non-dimensionalization and projection of the distribution function, leads to the system

$$c_y \frac{\partial \varphi}{\partial y} = \delta_0 \rho \sqrt{\tau} \left\{ \varphi^M \left[1 + \frac{4}{15} \frac{q c_y}{\rho \tau^2} \left(\frac{c_y^2}{\tau} - \frac{3}{2} \right) \right] - \varphi \right\} \quad (3.54)$$

$$c_y \frac{\partial \psi}{\partial y} = \delta_0 \rho \sqrt{\tau} \left\{ \psi^M \left[1 + \frac{4}{15} \frac{q c_y}{\rho \tau^2} \left(\frac{c_y^2}{\tau} - \frac{1}{2} \right) \right] - \psi \right\} \quad (3.55)$$

where the projections φ, ψ are defined as

$$\varphi(y, c_y) = \int \int g(y, \mathbf{c}) dc_x dc_z \quad (3.56)$$

$$\psi(y, c_y) = \int \int (c_x^2 + c_z^2) g(y, \mathbf{c}) dc_x dc_z \quad (3.57)$$

and the dimensionless number density ρ , temperature τ and heat flux q are given by

$$\rho(y) = \int \varphi dc_y \quad (3.58)$$

$$\tau(y) = \frac{2}{3\rho} \int (\psi + c_y^2 \varphi) dc_y \quad (3.59)$$

$$q(y) = q_y(y) = \int c_y (\psi + c_y^2 \varphi) dc_y \quad (3.60)$$

The reader is referred to Section 5.2.2 for further information on the formulation and the numerical simulation of the problem.

The general expression for the application of boundary conditions, Equation (3.3), is employed in its non-dimensional form

$$|c_n| g^+ (\mathbf{c}) = \int_{c'_n < 0} |c'_n| R(\mathbf{c}' \rightarrow \mathbf{c}) g^- (\mathbf{c}') d\mathbf{c}' \quad (3.61)$$

and we operate on it with $\int \int (\cdot) dc_x dc_z$ and $\int \int (\cdot) (c_x^2 + c_z^2) dc_x dc_z$ to obtain

$$|c_n| \varphi^+ (\mathbf{c}) = \int \int \left[\int_{c'_n < 0} |c'_n| R(\mathbf{c}' \rightarrow \mathbf{c}) g^- (\mathbf{c}') d\mathbf{c}' \right] dc_x dc_z \quad (3.62)$$

$$|c_n| \varphi^+ (\mathbf{c}) = \int \int \left[\int_{c'_n < 0} |c'_n| R(\mathbf{c}' \rightarrow \mathbf{c}) g^- (\mathbf{c}') d\mathbf{c}' \right] (c_x^2 + c_z^2) dc_x dc_z \quad (3.63)$$

with c_n, c'_n being the positive and negative c_y values respectively for the lower wall and vice versa for the upper wall. We may substitute the Cercignani-Lampis kernel here, including the temperature variation

$$R_t(c'_t \rightarrow c_t) = \frac{1}{\sqrt{\pi\tau\alpha_t(2-\alpha_t)}} \exp \left\{ -\frac{[c_t - (1-\alpha_t)c'_t]^2}{\tau\alpha_t(2-\alpha_t)} \right\} \quad (3.64)$$

$$R_n(c'_n \rightarrow c_n) = \frac{2c_n}{\tau\alpha_n} \exp \left\{ -\frac{[c_n^2 + (1-\alpha_n)c_n'^2]}{\tau\alpha_n} \right\} I_0 \left(\frac{2\sqrt{1-\alpha_n}c_nc'_n}{\tau\alpha_n} \right) \quad (3.65)$$

Similarly to the previous examples, some integrals of Equations (3.62) and (3.63) can be calculated analytically, such as

$$\int_{-\infty}^{\infty} \int_{-\infty}^{\infty} R_t(c'_z \rightarrow c_z) R_t(c'_x \rightarrow c_x) dc_x dc_z = 1 \quad (3.66)$$

$$\int_{-\infty}^{\infty} \int_{-\infty}^{\infty} R_t(c'_z \rightarrow c_z) R_t(c'_x \rightarrow c_x) (c_x^2 + c_z^2) dc_x dc_z = (1-\alpha_t)^2 (c_x'^2 + c_z'^2) + \tau\alpha_t(2-\alpha_t) \quad (3.67)$$

Finally, Equations (3.62) and (3.63) lead to the boundary conditions

$$\varphi^+ = -\frac{2}{\alpha_n\tau} \int_{c'_n < 0} \varphi^- c'_n \exp \left(-\frac{c_n^2 + (1-\alpha_n)c_n'^2}{\tau\alpha_n} \right) I_0 \left(\frac{2\sqrt{1-\alpha_n}c_nc'_n}{\tau\alpha_n} \right) dc'_n \quad (3.68)$$

$$\begin{aligned} \psi^+ = & -\frac{2}{\alpha_n \tau} \int_{c'_n < 0} [(1 - \alpha_t)^2 \psi^- + \tau \alpha_t (2 - \alpha_t) \varphi^-] c'_n \\ & \times \exp \left(-\frac{c_n^2 + (1 - \alpha_n) c_n'^2}{\tau \alpha_n} \right) I_0 \left(\frac{2\sqrt{1 - \alpha_n} c_n c'_n}{\tau \alpha_n} \right) dc'_n \end{aligned} \quad (3.69)$$

It can be confirmed that for $\alpha_t = \alpha_n = 1$ the diffuse reflection expressions are obtained. The φ^- part in Equation (3.69) may seem counter-intuitive at first but it provides the impermeability constant for diffuse reflection.

3.2.4 Non-linear heat transfer between concentric cylinders

Another problem of involving heat transfer, namely heat conduction between concentric cylinders, has been used for many years to determine the Maxwell accommodation coefficient and can also be used for our purposes. A rarefied gas is confined between two concentric stationary cylinders of infinite length. An arbitrarily large temperature difference is imposed between them, causing radial heat flow through the gas from the hot towards the cold cylinder. The main parameters are the reference rarefaction parameter δ_0 , the ratio of the inner to the outer cylinder radius γ and the ratio of the temperature difference to the outer wall reference temperature β . The kinetic equation is non-dimensionalized and projected to express the dimensionless distribution function g in terms of

$$\varphi(r, c_p, \theta) = \int g dc_z \quad (3.70)$$

$$\psi(r, c_p, \theta) = \int c_z^2 g dc_z \quad (3.71)$$

The molecular velocity has two components, namely $c_r = c_p \cos \theta$ and $c_\theta = c_p \sin \theta$, and the governing equations for the reduced distribution functions φ, ψ read as

$$c_p \cos \theta \frac{\partial \varphi}{\partial r} - \frac{c_p \sin \theta}{r} \frac{\partial \varphi}{\partial \theta} = \delta_0 \rho \sqrt{\tau} (\varphi^S - \varphi) \quad (3.72)$$

$$c_p \cos \theta \frac{\partial \psi}{\partial r} - \frac{c_p \sin \theta}{r} \frac{\partial \psi}{\partial \theta} = \delta_0 \rho \sqrt{\tau} (\psi^S - \psi) \quad (3.73)$$

where the Shakhov terms are

$$\varphi^S = \varphi^M \left[1 + \frac{4}{15} \frac{1}{\rho \tau^2} q c_p \cos \theta \left(\frac{c_p^2}{\tau} - 2 \right) \right] \quad (3.74)$$

$$\psi^S = \psi^M \left[1 + \frac{4}{15} \frac{1}{\rho \tau^2} q c_p \cos \theta \left(\frac{c_p^2}{\tau} - 1 \right) \right] \quad (3.75)$$

and the Maxwellian distribution is

$$\varphi^M = \frac{\rho}{\pi \tau} \exp \left(-\frac{c_p^2}{\tau} \right) \quad (3.76)$$

$$\psi^M = \frac{\rho}{2\pi} \exp \left(-\frac{c_p^2}{\tau} \right) \quad (3.77)$$

The symbols ρ , τ , q denote the dimensionless number density, temperature and heat flux respectively, calculated by

$$\rho(r) = \int_0^{2\pi} \int_0^\infty \varphi c_p d c_p d \theta \quad (3.78)$$

$$\tau(r) = \frac{2}{3\rho(r)} \int_0^{2\pi} \int_0^\infty (c_p^2 \varphi + \psi) c_p d c_p d \theta \quad (3.79)$$

$$q(r) = \int_0^{2\pi} \int_0^\infty (c_p \cos \theta) (c_p^2 \varphi + \psi) c_p d c_p d \theta \quad (3.80)$$

The most important quantity for practical calculations is the radial heat flux at the inner cylinder wall $q(\gamma)$, where γ is the inner to outer wall radius. The problem is axially symmetric and therefore becomes one-dimensional in physical space. Thus, the boundary conditions are only imposed in two points. It is noted that, even though gas-surface interaction is correctly described with the CL model, the involved computational effort is significantly increased. Thus, for the present heat transfer problem, only purely diffuse boundary conditions are applied on the outer wall ($r = 1$). This choice is also justified by the fact that one of the main purposes of this heat transfer configuration is to provide a methodology for determining the accommodation coefficients of the inner cylinder. Thus, a technical surface with no exceptional treatment would suffice for the outer cylinder and, as a result, purely diffuse boundary conditions should be adequate. Moreover, a larger impact of the scattering kernel is expected on the inner cylinder due to temperature variation. Based on the above, the following boundary conditions are applied for the reduced distribution functions at the outer wall ($r = 1$)

$$\varphi^+(1, c_p, \theta) = \frac{1}{\pi} \exp(-c_p^2) \quad (3.81)$$

$$\psi^+(1, c_p, \theta) = \frac{1}{2\pi} \exp(-c_p^2) \quad (3.82)$$

The above expressions are valid for $\theta \in [\pi/2, 3\pi/2]$. At the inner wall ($r = \gamma$), we choose to impose the Cercignani-Lampis scattering kernel for $\theta \in [-\pi/2, \pi/2]$.

Even though the governing equations are quite different, the procedure is similar for the case of non-linear heat transfer. The starting point is the general equation (3.3), expressed in dimensionless form

$$|c_n| g^+(\mathbf{c}) = \int_{c'_n < 0} |c'_n| R(\mathbf{c}' \rightarrow \mathbf{c}) g^-(\mathbf{c}') d\mathbf{c}' \quad (3.83)$$

Acting accordingly on (3.83) to form the projections φ, ψ on the left hand side, we get

$$|c_n| \varphi^+(\mathbf{c}) = \int \left[\int_{c'_n < 0} |c'_n| R(\mathbf{c}' \rightarrow \mathbf{c}) g^-(\mathbf{c}') d\mathbf{c}' \right] dc_z \quad (3.84)$$

$$|c_n| \psi^+(\mathbf{c}) = \int \left[\int_{c'_n < 0} |c'_n| R(\mathbf{c}' \rightarrow \mathbf{c}) g^-(\mathbf{c}') d\mathbf{c}' \right] c_z^2 dc_z \quad (3.85)$$

We may substitute the Cercignani-Lampis kernel here, including the temperature variation on the inner (hot) wall

$$R_t(c'_t \rightarrow c_t) = \frac{1}{\sqrt{\pi\tau\alpha_t(2-\alpha_t)}} \exp\left\{-\frac{[c_t - (1-\alpha_t)c'_t]^2}{\tau\alpha_t(2-\alpha_t)}\right\} \quad (3.86)$$

$$R_n(c'_n \rightarrow c_n) = \frac{2c_n}{\tau\alpha_n} \exp\left\{-\frac{[c_n^2 + (1-\alpha_n)c_n'^2]}{\tau\alpha_n}\right\} I_0\left(\frac{2\sqrt{1-\alpha_n}c_nc'_n}{\tau\alpha_n}\right) \quad (3.87)$$

At the inner boundary we have $(c_n, c_{t1}, c_{t2}) = (c_r, c_\vartheta, c_z)$ and $(c'_n, c'_{t1}, c'_{t2}) = (c'_r, c'_\vartheta, c'_z)$. Similarly to the previous subsection, the following integrals are calculated

$$\int_{-\infty}^{\infty} R_t(c'_z \rightarrow c_z) dc_z = 1 \quad (3.88)$$

$$\int_{-\infty}^{\infty} R_t(c'_z \rightarrow c_z) c_z^2 dc_z = (1-\alpha_t)^2 c_z'^2 + \frac{\tau}{2} \alpha_t (2-\alpha_t) \quad (3.89)$$

and Equations (3.84) and (3.85) lead to the final expressions

$$\begin{aligned} \varphi^+(\gamma, c_p, \theta) = & -\frac{2}{\alpha_n(1+\beta)^{3/2}\sqrt{\pi\alpha_t(2-\alpha_t)}} \int_{\pi/2}^{3\pi/2} \int_0^\infty \left(c'_p \cos \theta'\right) \varphi^-(\gamma, c'_p, \theta') \times \\ & \exp\left[-\frac{(c_p \cos \theta)^2 + (1-\alpha_n)(c'_p \cos \theta')^2}{(1+\beta)\alpha_n}\right] \exp\left[-\frac{[(c_p \sin \theta) - (1-\alpha_t)(c'_p \sin \theta')]^2}{(1+\beta)\alpha_t(2-\alpha_t)}\right] \times \\ & I_0\left[\frac{2\sqrt{1-\alpha_n}(c'_p \cos \theta)(c'_p \cos \theta')}{(1+\beta)\alpha_n}\right] c'_p dc'_p d\theta' \end{aligned} \quad (3.90)$$

$$\begin{aligned} \psi^+(\gamma, c_p, \theta) = & -\frac{2}{\alpha_n(1+\beta)^{3/2}\sqrt{\pi\alpha_t(2-\alpha_t)}} \int_{\pi/2}^{3\pi/2} \int_0^\infty \left(c'_p \cos \theta'\right) \times \\ & \left[(1-\alpha_t)^2 \psi^-(\gamma, c'_p, \theta') + \frac{1+\beta}{2} \alpha_t(2-\alpha_t) \varphi^-(\gamma, c'_p, \theta')\right] \times \\ & \exp\left[-\frac{(c_p \cos \theta)^2 + (1-\alpha_n)(c'_p \cos \theta')^2}{(1+\beta)\alpha_n}\right] \exp\left[-\frac{[(c_p \sin \theta) - (1-\alpha_t)(c'_p \sin \theta')]^2}{(1+\beta)\alpha_t(2-\alpha_t)}\right] \times \\ & I_0\left[\frac{2\sqrt{1-\alpha_n}(c_p \cos \theta)(c'_p \cos \theta')}{(1+\beta)\alpha_n}\right] c'_p dc'_p d\theta' \end{aligned} \quad (3.91)$$

It can be confirmed that for $\alpha_t = \alpha_n = 1$ the diffuse reflection expressions are obtained. As in the case of non-linear heat transfer between parallel plates, the φ^- part in Equation (3.91) provides the impermeability constant for diffuse reflection.

3.3 Results and discussion

3.3.1 Flow through a rectangular duct

The numerical results have been obtained using a uniform grid of 200 intervals in both the x and y directions, 20 magnitudes, distributed in $[0, c_{max}]$ according to the Legendre polynomial roots, and 120 polar angles, uniformly distributed in $[0, 2\pi]$. The validity of the code has been benchmarked for $\alpha_t = \alpha_n = 1$ by comparing with corresponding results in the literature [182] obtained using Maxwell diffuse boundary conditions and good agreement has been found. Also, the qualitative behaviour of

the CL results resembles the one observed in other geometrical configurations, such as flow through a cylindrical tube [107].

In Table 3.1 the reduced flow rate G is shown for three aspect ratios H/W in the whole range of the rarefaction parameter δ . It is seen that it highly depends on the value of the tangential momentum accommodation coefficient. Lower values of conductance are observed for higher α_t , occurring due to a higher probability of bouncing-back molecular behaviour. Furthermore, the variation of α_n does not play a significant role. In more detail, the influence of α_n on G depends on the degree of tangential accommodation: for $\alpha_t < 1$ an increase in α_n causes a decrease in the flow rate, while for $\alpha_t > 1$ the opposite tendency is demonstrated. The flow rate is also highly dependent on the aspect ratio of the orthogonal cross section and increases as the ratio decreases. Finally, it is noted that in every case, the Knudsen minimum occurs for values of δ around unity.

It would be useful to compare the current numerical simulations with relevant experimental data in order to obtain the accommodation coefficients, thereby characterizing the specific gas-surface combinations. For this purpose, the TRANSFLOW (Transitional Flow Range Experiments) test facility [74], set up by the KIT research team, has been employed. The basic principle of the TRANSFLOW test rig is the measurement of the conductance of different channels in the transitional and near transitional flow regime at isothermal conditions, based on the direct dynamic approach: a constant flow is adjusted and the pressure difference is measured. The constant flow into the test rig is provided by a dosing unit. The temperature and pressure of the injected gas can be measured in the dosing dome, which is directly connected to the dosing unit. The test channel follows the dosing dome in the flow direction. At the downstream end it is connected with the pump dome. The pump dome serves to measure temperatures and pressures at the outlet side of the test channel. It is also equipped with turbomolecular pumps, which are further connected to the forepumps, to maintain the vacuum conditions inside the system. A complete description can be found in several previous works, such as [74, 183]. In this work, a long duct of square cross-section with length $L = 1277\text{mm}$ and $H = W = 16\text{mm}$ has been used [75]. The inner surface of the channel was of standard clean technical quality without

special treatment. Gas nitrogen (N_2) has been used in average temperature $T_0 = 296\text{K}$.

Based on the dimensionless results, in Table 3.2, the conductance is provided for nitrogen flow through a square duct used in the experimental part of this work. It is seen that the dependency of the conductance on the CL accommodation coefficients is similar to the one observed for the reduced flow rate. In Figure 3.7, the computational results based on the CL and Maxwell diffuse boundary conditions have been compared with the corresponding experimental data [74]. In order to obtain the values of the CL accommodation coefficients, it is observed that in Tables 3.1 and 3.2 the dependence of the flow rates on α_n , for this pressure driven flow, is negligible. Therefore, it is safely assumed that $\alpha_n = 1$, while the value of α_t is varied to reduce the discrepancies with the experimental results. It is found that, by setting $\alpha_t = 1.06$, excellent agreement is obtained with the corresponding experimental results in the whole range of δ . The previously implemented Maxwell diffuse boundary conditions slightly overestimate the experimental results [74]. It can be thus stated that for the specific combination of nitrogen and technically clean steel surface the back-scattering phenomenon may occur, producing flow rates relatively lower than the ones predicted by the Maxwell diffuse kernel.

This comparison has been performed for a vacuum apparatus and a corresponding experiment in the microscale is required to examine possible similarities and differences in the scattering behaviour for both scales. The experimental results of [121] for the mass flow rate have been reproduced in Figure 3.8, concerning flow of He and Ar through a microduct of dimensions $H = 1.88 \times 10^{-6}\text{m}$, $W = 21.2 \times 10^{-6}\text{m}$ and $L = 5 \times 10^{-3}\text{m}$. The corresponding numerical values for diffuse reflection and for CL interaction have been plotted along the same figure. The tangential accommodation coefficient has been adjusted to $\alpha_t = 1.02$ for argon and $\alpha_t = 1.04$ for helium in the whole range of the Knudsen number. The small deviations between the diffuse numerical and experimental results are also within the experimental uncertainty and therefore we may argue that the non-diffuse accommodation effect is practically negligible for this apparatus. The tangential accommodation coefficient is very close for the two gases and in fact a little larger for the light gas, as also seen in recent studies [184]. The curves shown here do not display qualitative differences with corresponding ones concerning vacuum flow

and thus we conclude that, for technical surfaces, some back-scattering may occur but the tangential momentum accommodation coefficient remains close to unity, as stated before.

3.3.2 Heat transfer between parallel plates

For the heat conduction problem between parallel plates, the heat flux is displayed in Tables 3.3 - 3.5 for a variety of physical situations, characterized by different rarefaction levels, temperature differences and accommodation coefficients. In particular, the linearized results are given in Table 3.3, the non-linear for a low temperature difference ($T_A/T_B = 1.1$, $\beta = 0.05$) in Table 3.4 and the non-linear for a high temperature difference ($T_A/T_B = 3$, $\beta = 0.5$) in Table 3.5. The values $1 < \alpha_t < 2$ are not displayed due to the symmetrical properties of Equations (3.52)-(3.53) and (3.68)-(3.69), as far as α_t is concerned: results for $\alpha_t > 1$ are equal to the ones for $\alpha'_t = \alpha_t - 1$. At all cases, the heat flux is reduced when the accommodation coefficients are not equal to unity. This is particularly visible as the normal kinetic energy coefficient α_n is decreased, since the boundary conditions approach the specular law. The value of α_t plays a minor role in the phenomenon compared to α_n , since it only affects one of the two projections for each problem and only as a multiplier, while α_n appears in the denominator of various involved fractions in all projections.

The three tables become comparable if we divide the non-linear results with 2β (or if we multiply the linearized results by the same constant). A very good agreement is then found between the linearized heat fluxes (Table 3.3) and the non-linear ones for $\beta = 0.05$ (Table 3.4); however, there are tangible differences with the results of case $\beta = 0.5$ (Table 3.5). It is seen that, if we compare diffuse results of high and low temperature differences, large discrepancies are observed. On the contrary, if we examine the values for lower accommodation coefficients and particularly for smaller α_n , the agreement is always relatively good. This may be explained by an extension of the considerations given in Section 5.4.2: in the extreme case of nearly free molecular conditions and very large temperature differences, most molecules move with very low velocities within a very narrow velocity magnitude range, with a direction from the cold wall to the hot one, while very few of them move fast in the opposite direction. As a result, the temperature (variance of molecular velocity) is quite low and

higher moments involving the difference $(\mathbf{c} - \mathbf{u})^2$, such as the heat flux, are also reduced. This is the reason that diffuse reflection results for large β differ so much from the other two tables. However, as the accommodation coefficients drop and approach specular interaction, molecules moving fast are affected in a smaller degree by the cold wall and retain their large velocities. Therefore, the temperature is closer to the corresponding linear profile and the heat flux remains linearly proportional to the temperature difference.

3.3.3 Non-linear heat transfer between two concentric cylinders

The influence of the gas-surface interaction law on the radial heat flow for the cylindrical heat transfer problem is studied in Figures 3.9-3.11 by providing numerical results for $q(r = \gamma)$ in terms of the parameters $0 < \alpha_t < 2$ and $0 < \alpha_n < 1$ and for various values of β , γ and δ_0 . In Figures 3.9 and 3.10, the radial heat flow $q(r = \gamma)$ is plotted for $\beta = 1$ and $\gamma = 0.5$ in terms of each accommodation coefficient while keeping each time the other one constant and equal to unity. It is clearly observed that the dependency of q on α_t is relatively weak, while, on the contrary, its dependency on α_n is significant. Even more, as expected in both cases, as δ_0 is decreased the effect of the accommodation coefficients becomes stronger. It is also noted that the radial heat flow in terms of α_t is symmetric around $\alpha_t = 1$. This property is inherent in the form of the boundary conditions (3.90) and (3.91). Values of $\alpha_t > 1$ correspond to a large number of bouncing-back molecules, which occur at rough surfaces. In terms of α_n , q is monotonically increased. It is found that α_n is more important than α_t in pure heat transfer problems. The same features are observed for other values of β . Furthermore, the behaviour of the macroscopic quantities in terms of the two accommodation coefficients is qualitatively similar in linear and nonlinear configurations.

Since the implementation of the CL boundary conditions is demanding in terms of formulation and numerical implementation and in order to increase our confidence on the accuracy of the present numerical solution based on the nonlinear Shakhov model, the results reported here are compared with previously reported results for the same heat transfer configuration based on the linearized Shakhov model [113]. The values of the heat flow provided in Table 3.6 for $\beta = 0.1$ and $\gamma = 1/65$ and

for a wide range of α_t and α_n may be directly compared with the corresponding results of Table IV in Reference [113], reproduced in Table 3.7 including the appropriate transformations. Since the normalized temperature difference is small ($\beta = 0.1$), it is expected to have good agreement between the present nonlinear results and the corresponding linearized ones. In fact, for $\delta_0\gamma = 0.1$ there is agreement to all three significant figures for many cases. For $\delta_0\gamma = 1$ the agreement is still very good since 2-3 significant figures are the same. Finally, for $\delta_0\gamma = 10$ the agreement is reduced to 1-2 significant figures. This is reasonable since, even though $\beta = 0.1$ is a relatively small normalized temperature difference, it is not small enough to have very accurate linearized results at large δ_0 . It is clear that nonlinear effects become important in dense atmospheres, even for small temperature differences.

For completeness purposes, corresponding results are provided by imposing the well known Maxwell diffuse-specular scattering law at the inner wall. In Figure 3.11, the radial heat flow $q(r = \gamma)$ is plotted for $\beta = 1$ and $\gamma = 0.5$ in terms of the accommodation coefficient $0 < \alpha_M \leq 1$. As expected, the corresponding results in Figures 3.9 and 3.10 for the specific values of $\alpha_n = \alpha_t = 1$ and $\alpha_M = 1$ respectively are identical. Furthermore, a qualitative remark on the comparison with these figures can be made: it is seen that the heat flows of Figure 3.11 for $\delta_0 = 0$ and $\delta_0 = 20$ are similar to the corresponding ones in Figures 3.9 and 3.10 for $\alpha_t = 1$, $0 < \alpha_n \leq 1$ and $0 < \alpha_t \leq 1$, $\alpha_n = 1$ respectively, while for the intermediate values of $\delta_0 = 2$ and $\delta_0 = 10$ the heat flows in Figure 3.11 are similar to the resulting ones obtained by a combination of the corresponding heat flows presented in Figures 3.9 and 3.10.

3.4 Concluding remarks

In this Chapter, the Cercignani-Lampis scattering kernel, known to describe the behaviour of the gas more realistically in comparison to previous models, has been applied in one flow and three heat transfer problems. In particular, linearized flow through a long rectangular duct has been examined on the basis of the BGK model and results have been compared with experimental data, provid-

ing a tangential momentum accommodation coefficient of around 1.02-1.06 and indicating a slight back-scattering behaviour for technical surfaces and Argon/Helium gases. This coefficient has been found to be slightly larger for the lighter gas, in accordance with recent studies [184]. Linearized and non-linear heat conduction between parallel plates, as well as non-linear heat conduction between concentric cylinders have been investigated by the Shakhov model. It is seen that the normal kinetic energy accommodation coefficient is in this case more important than the tangential momentum accommodation coefficient. The linear and non-linear models provide nearly identical results in their common range of applicability, while an unusual agreement is observed as the interaction becomes more specular and is interpreted as being due to the fact that the molecules are only partially affected by the scattering properties of the wall. The complete behaviour of the most significant quantities in practical applications, i.e. the flow rate and heat flux, have been tabulated for all possible scattering patterns, various geometrical configurations and a wide range of the Knudsen number. These simulations can be used to determine the accommodation coefficients and characterize specific gas-surface interactions. In this manner, the effect of the wall boundary conditions may be accurately taken into account.

Table 3.1: Reduced flow rate G' for flow through a duct

δ	α_t	H/W=1				H/W=0.5				H/W=0.25			
		$\alpha_n = 0.50$	0.75	1.00	0.50	0.75	1.00	0.50	0.75	1.00	0.50	0.75	1.00
0.00	0.50	1.738	1.721	1.708	2.363	2.335	2.316	2.983	2.936	2.905			
	0.75	1.142	1.136	1.131	1.562	1.551	1.543	2.004	1.985	1.972			
	1.00	0.839	0.839	0.839	1.152	1.152	1.152	1.500	1.500	1.500			
	1.25	0.645	0.651	0.656	0.892	0.901	0.908	1.180	1.196	1.208			
	1.50	0.497	0.508	0.517	0.693	0.710	0.725	0.940	0.968	0.991			
0.10	0.50	1.686	1.672	1.662	2.271	2.251	2.236	2.817	2.781	2.757			
	0.75	1.095	1.090	1.085	1.479	1.470	1.464	1.851	1.837	1.826			
	1.00	0.793	0.793	0.793	1.073	1.073	1.073	1.354	1.354	1.354			
	1.25	0.602	0.606	0.610	0.816	0.823	0.829	1.041	1.053	1.063			
	1.50	0.456	0.464	0.473	0.622	0.636	0.648	0.809	0.832	0.851			
0.50	0.50	1.640	1.634	1.629	2.206	2.197	2.190	2.696	2.681	2.669			
	0.75	1.059	1.057	1.055	1.426	1.423	1.420	1.748	1.741	1.735			
	1.00	0.762	0.762	0.762	1.028	1.028	1.028	1.261	1.261	1.261			
	1.25	0.574	0.576	0.578	0.776	0.780	0.783	0.957	0.963	0.969			
	1.50	0.434	0.438	0.442	0.592	0.599	0.605	0.740	0.752	0.763			
1.00	0.50	1.639	1.637	1.635	2.215	2.212	2.209	2.695	2.689	2.683			
	0.75	1.063	1.062	1.061	1.440	1.438	1.437	1.749	1.746	1.743			
	1.00	0.768	0.768	0.768	1.043	1.043	1.043	1.265	1.265	1.265			
	1.25	0.582	0.583	0.584	0.794	0.795	0.797	0.965	0.967	0.970			
	1.50	0.445	0.447	0.449	0.615	0.618	0.621	0.755	0.761	0.766			
5.00	0.50	1.870	1.869	1.868	2.624	2.622	2.620	3.171	3.169	3.167			
	0.75	1.288	1.287	1.287	1.826	1.825	1.825	2.195	2.194	2.194			
	1.00	0.987	0.987	0.987	1.416	1.416	1.416	1.698	1.698	1.698			
	1.25	0.800	0.800	0.800	1.162	1.163	1.163	1.395	1.396	1.397			
	1.50	0.668	0.669	0.669	0.987	0.988	0.989	1.189	1.191	1.192			
10.00	0.50	2.221	2.219	2.216	3.202	3.197	3.193	3.863	3.857	3.852			
	0.75	1.626	1.625	1.624	2.382	2.379	2.377	2.868	2.865	2.862			
	1.00	1.317	1.317	1.317	1.959	1.959	1.959	2.360	2.360	2.360			
	1.25	1.126	1.127	1.128	1.698	1.701	1.703	2.051	2.053	2.056			
	1.50	0.993	0.996	0.998	1.520	1.524	1.528	1.841	1.846	1.851			

Table 3.2: Conductance C [l/sec] dependence on the accommodation coefficients for N_2 flow through a duct ($H = W = 16\text{mm}$, $L = 1277\text{mm}$) into vacuum at 296K

δ	α_t	$\alpha_n=0.50$	0.75	1.00
0.00	0.50	1.065	1.055	1.047
	0.75	0.700	0.696	0.693
	1.00	0.514	0.514	0.514
	1.25	0.395	0.399	0.402
	1.50	0.305	0.311	0.317
0.10	0.50	1.033	1.025	1.019
	0.75	0.671	0.668	0.665
	1.00	0.486	0.486	0.486
	1.25	0.369	0.371	0.374
	1.50	0.279	0.285	0.290
0.50	0.50	1.005	1.002	0.998
	0.75	0.649	0.648	0.647
	1.00	0.467	0.467	0.467
	1.25	0.352	0.353	0.354
	1.50	0.266	0.269	0.271
1.00	0.50	1.005	1.003	1.002
	0.75	0.652	0.651	0.650
	1.00	0.471	0.471	0.471
	1.25	0.357	0.357	0.358
	1.50	0.273	0.274	0.275
5.00	0.50	1.146	1.146	1.145
	0.75	0.790	0.789	0.789
	1.00	0.605	0.605	0.605
	1.25	0.490	0.490	0.490
	1.50	0.409	0.410	0.410
10.00	0.50	1.362	1.360	1.358
	0.75	0.997	0.996	0.996
	1.00	0.808	0.808	0.808
	1.25	0.690	0.691	0.691
	1.50	0.609	0.610	0.612

Table 3.3: Heat flux for the parallel plate problem, obtained by the linear formulation

δ	α_t	α_n		
		0.50	0.75	1.00
0.00	0.50	2.63×10^{-1}	3.39×10^{-1}	4.51×10^{-1}
	0.75	3.43×10^{-1}	4.18×10^{-1}	5.31×10^{-1}
	1.00	3.76×10^{-1}	4.51×10^{-1}	5.64×10^{-1}
0.15	0.50	2.52×10^{-1}	3.23×10^{-1}	4.25×10^{-1}
	0.75	3.21×10^{-1}	3.93×10^{-1}	4.95×10^{-1}
	1.00	3.49×10^{-1}	4.21×10^{-1}	5.23×10^{-1}
1.5	0.50	1.99×10^{-1}	2.50×10^{-1}	3.10×10^{-1}
	0.75	2.33×10^{-1}	2.85×10^{-1}	3.45×10^{-1}
	1.00	2.45×10^{-1}	2.97×10^{-1}	3.57×10^{-1}
15	0.50	8.03×10^{-2}	8.86×10^{-2}	9.53×10^{-2}
	0.75	8.49×10^{-2}	9.22×10^{-2}	9.83×10^{-2}
	1.00	8.62×10^{-2}	9.33×10^{-2}	9.92×10^{-2}
150	0.50	1.18×10^{-2}	1.20×10^{-2}	1.21×10^{-2}
	0.75	1.19×10^{-2}	1.21×10^{-2}	1.22×10^{-2}
	1.00	1.20×10^{-2}	1.21×10^{-2}	1.22×10^{-2}

Table 3.4: Heat flux for the parallel plate problem, obtained by the non-linear formulation for $\beta = 0.05$

δ_0	α_t	α_n		
		0.50	0.75	1.00
0.00	0.50	2.63×10^{-2}	3.38×10^{-2}	4.51×10^{-2}
	0.75	3.43×10^{-2}	4.18×10^{-2}	5.30×10^{-2}
	1.00	3.76×10^{-2}	4.51×10^{-2}	5.64×10^{-2}
0.15	0.50	2.52×10^{-2}	3.23×10^{-2}	4.25×10^{-2}
	0.75	3.21×10^{-2}	3.93×10^{-2}	4.95×10^{-2}
	1.00	3.49×10^{-2}	4.20×10^{-2}	5.23×10^{-2}
1.5	0.50	1.99×10^{-2}	2.50×10^{-2}	3.10×10^{-2}
	0.75	2.33×10^{-2}	2.85×10^{-2}	3.45×10^{-2}
	1.00	2.45×10^{-2}	2.97×10^{-2}	3.57×10^{-2}
15	0.50	8.03×10^{-3}	8.85×10^{-3}	9.53×10^{-3}
	0.75	8.48×10^{-3}	9.22×10^{-3}	9.83×10^{-3}
	1.00	8.62×10^{-3}	9.33×10^{-3}	9.92×10^{-3}
150	0.50	1.20×10^{-3}	1.22×10^{-3}	1.23×10^{-3}
	0.75	1.21×10^{-3}	1.22×10^{-3}	1.23×10^{-3}
	1.00	1.21×10^{-3}	1.23×10^{-3}	1.24×10^{-3}

Table 3.5: Heat flux for the parallel plate problem, obtained by the non-linear formulation for $\beta = 0.5$

δ_0	α_t	α_n		
		0.50	0.75	1.00
0.00	0.50	2.60×10^{-1}	3.24×10^{-1}	4.05×10^{-1}
	0.75	3.39×10^{-1}	4.00×10^{-1}	4.76×10^{-1}
	1.00	3.71×10^{-1}	4.32×10^{-1}	5.06×10^{-1}
0.15	0.50	2.49×10^{-1}	3.12×10^{-1}	3.86×10^{-1}
	0.75	3.17×10^{-1}	3.78×10^{-1}	4.49×10^{-1}
	1.00	3.44×10^{-1}	4.05×10^{-1}	4.74×10^{-1}
1.5	0.50	1.94×10^{-1}	2.41×10^{-1}	2.90×10^{-1}
	0.75	2.27×10^{-1}	2.73×10^{-1}	3.22×10^{-1}
	1.00	2.39×10^{-1}	2.84×10^{-1}	3.32×10^{-1}
15	0.50	7.84×10^{-2}	8.64×10^{-2}	9.30×10^{-2}
	0.75	8.28×10^{-2}	8.99×10^{-2}	9.59×10^{-2}
	1.00	8.41×10^{-2}	9.10×10^{-2}	9.68×10^{-2}
150	0.50	1.17×10^{-2}	1.19×10^{-2}	1.20×10^{-2}
	0.75	1.18×10^{-2}	1.20×10^{-2}	1.21×10^{-2}
	1.00	1.18×10^{-2}	1.20×10^{-2}	1.21×10^{-2}

Table 3.6: Radial heat flow $q(r = \gamma)$ with CL boundary conditions for $\beta = 0.1$ and $\gamma = 1/65$

$\delta_0\gamma$	α_t	$\alpha_n=0.25$	0.50	0.75	1.00
0.1	0.50	2.69×10^{-2}	3.33×10^{-2}	3.96×10^{-2}	4.58×10^{-2}
	0.75	3.17×10^{-2}	3.80×10^{-2}	4.42×10^{-2}	5.03×10^{-2}
	0.90	3.30×10^{-2}	3.93×10^{-2}	4.55×10^{-2}	5.16×10^{-2}
	1.00	3.32×10^{-2}	3.95×10^{-2}	4.57×10^{-2}	5.18×10^{-2}
1	0.50	1.80×10^{-2}	2.09×10^{-2}	2.33×10^{-2}	2.55×10^{-2}
	0.75	2.01×10^{-2}	2.26×10^{-2}	2.48×10^{-2}	2.68×10^{-2}
	0.90	2.06×10^{-2}	2.31×10^{-2}	2.52×10^{-2}	2.71×10^{-2}
	1.00	2.07×10^{-2}	2.32×10^{-2}	2.53×10^{-2}	2.72×10^{-2}
10	0.50	4.02×10^{-3}	4.16×10^{-3}	4.26×10^{-3}	4.34×10^{-3}
	0.75	4.11×10^{-3}	4.22×10^{-3}	4.31×10^{-3}	4.37×10^{-3}
	0.90	4.13×10^{-3}	4.24×10^{-3}	4.32×10^{-3}	4.38×10^{-3}
	1.00	4.14×10^{-3}	4.24×10^{-3}	4.32×10^{-3}	4.40×10^{-3}

Table 3.7: Results for the radial heat flow $q(r = \gamma)$ with CL boundary conditions, obtained by the linearized model and reproduced from [113] for $\beta = 0.1$ and $\gamma = 1/65$

$\delta_0\gamma$	α_t	$\alpha_n=0.25$	0.50	0.75	1.00
0.1	0.50	2.69×10^{-2}	3.34×10^{-2}	3.97×10^{-2}	4.59×10^{-2}
	0.75	3.17×10^{-2}	3.81×10^{-2}	4.43×10^{-2}	5.04×10^{-2}
	0.90	3.30×10^{-2}	3.93×10^{-2}	4.55×10^{-2}	5.16×10^{-2}
	1.00	3.33×10^{-2}	3.96×10^{-2}	4.58×10^{-2}	5.19×10^{-2}
1	0.50	1.82×10^{-2}	2.10×10^{-2}	2.34×10^{-2}	2.55×10^{-2}
	0.75	2.02×10^{-2}	2.27×10^{-2}	2.49×10^{-2}	2.68×10^{-2}
	0.90	2.08×10^{-2}	2.32×10^{-2}	2.53×10^{-2}	2.72×10^{-2}
	1.00	2.09×10^{-2}	2.33×10^{-2}	2.54×10^{-2}	2.72×10^{-2}
10	0.50	3.99×10^{-3}	4.08×10^{-3}	4.17×10^{-3}	4.24×10^{-3}
	0.75	4.06×10^{-3}	4.14×10^{-3}	4.21×10^{-3}	4.27×10^{-3}
	0.90	4.08×10^{-3}	4.15×10^{-3}	4.22×10^{-3}	4.27×10^{-3}
	1.00	4.09×10^{-3}	4.15×10^{-3}	4.22×10^{-3}	4.28×10^{-3}

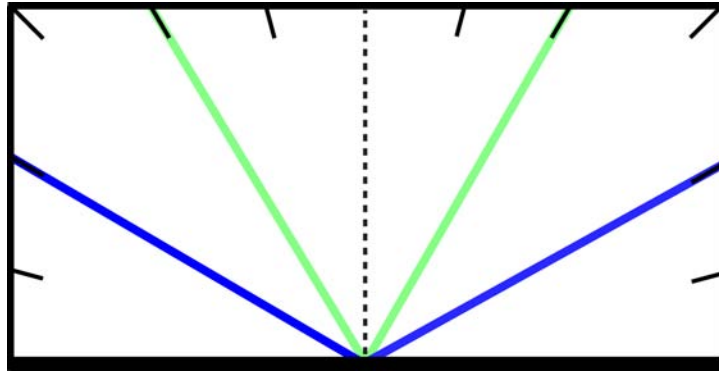


Figure 3.1: Specular reflection for the impinging angles $\theta = -\pi/6$ (blue) and $\theta = -\pi/3$ (green)

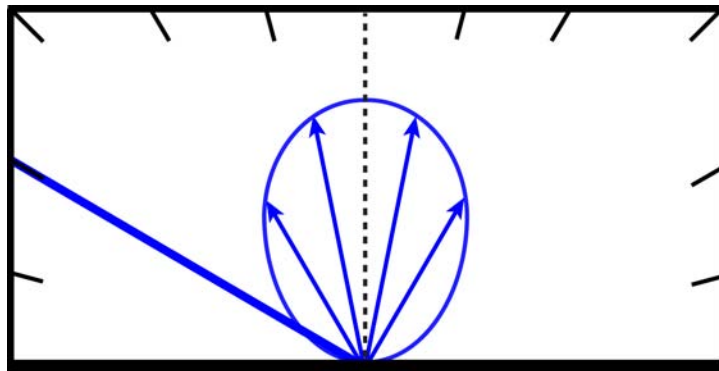


Figure 3.2: Diffuse reflection for the impinging angle $\theta = -\pi/6$

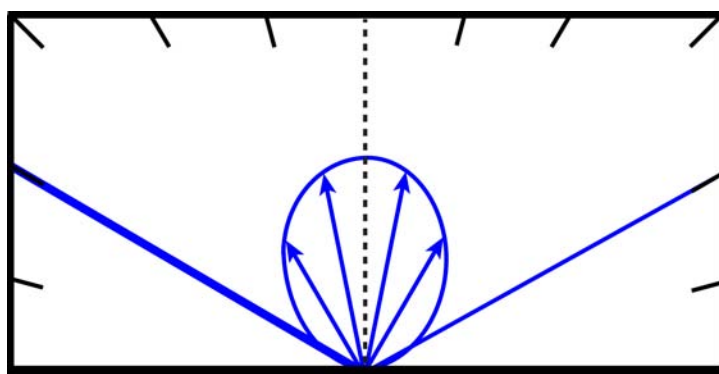


Figure 3.3: Diffuse-specular reflection with $\alpha_M = 0.8$ for the impinging angle $\theta = -\pi/6$

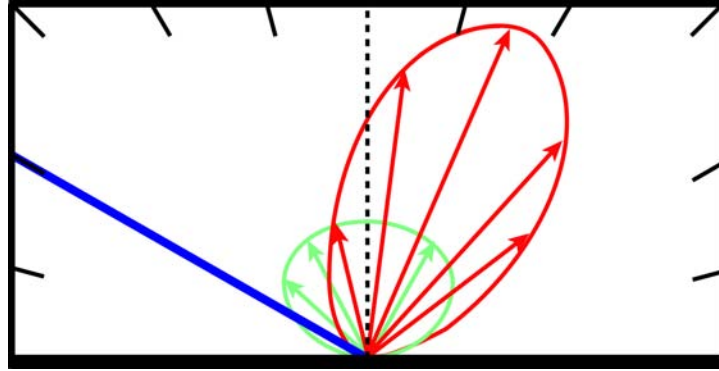


Figure 3.4: Cercignani-Lampis reflection with $\alpha_n = 0.50, \alpha_t = 1.00$ (green) and $\alpha_n = 1.00, \alpha_t = 0.50$ (red) for the impinging angle $\theta = -\pi/6$

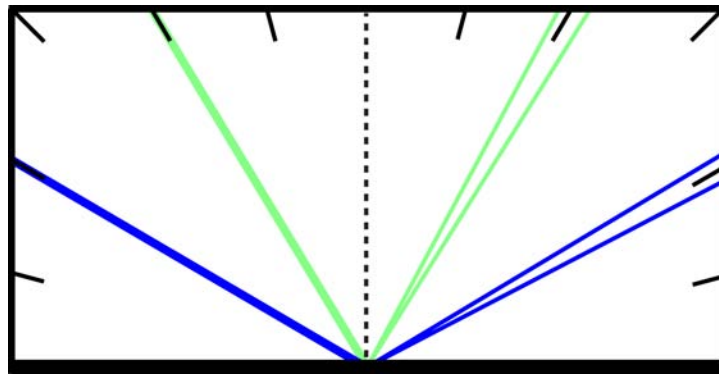


Figure 3.5: Nearly specular reflection ($\alpha_t = \alpha_n = 10^{-4}$) for the impinging angles $\theta = -\pi/6$ (blue) and $\theta = -\pi/3$ (green)

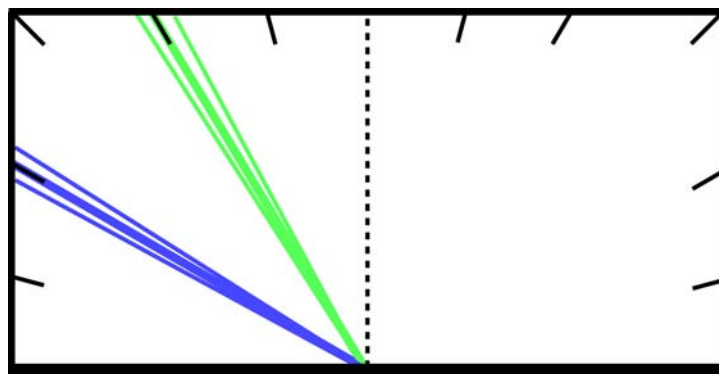


Figure 3.6: Nearly back-scattering reflection ($\alpha_t = 1.9999, \alpha_n = 10^{-4}$) for the impinging angles $\theta = -\pi/6$ (blue) and $\theta = -\pi/3$ (green)

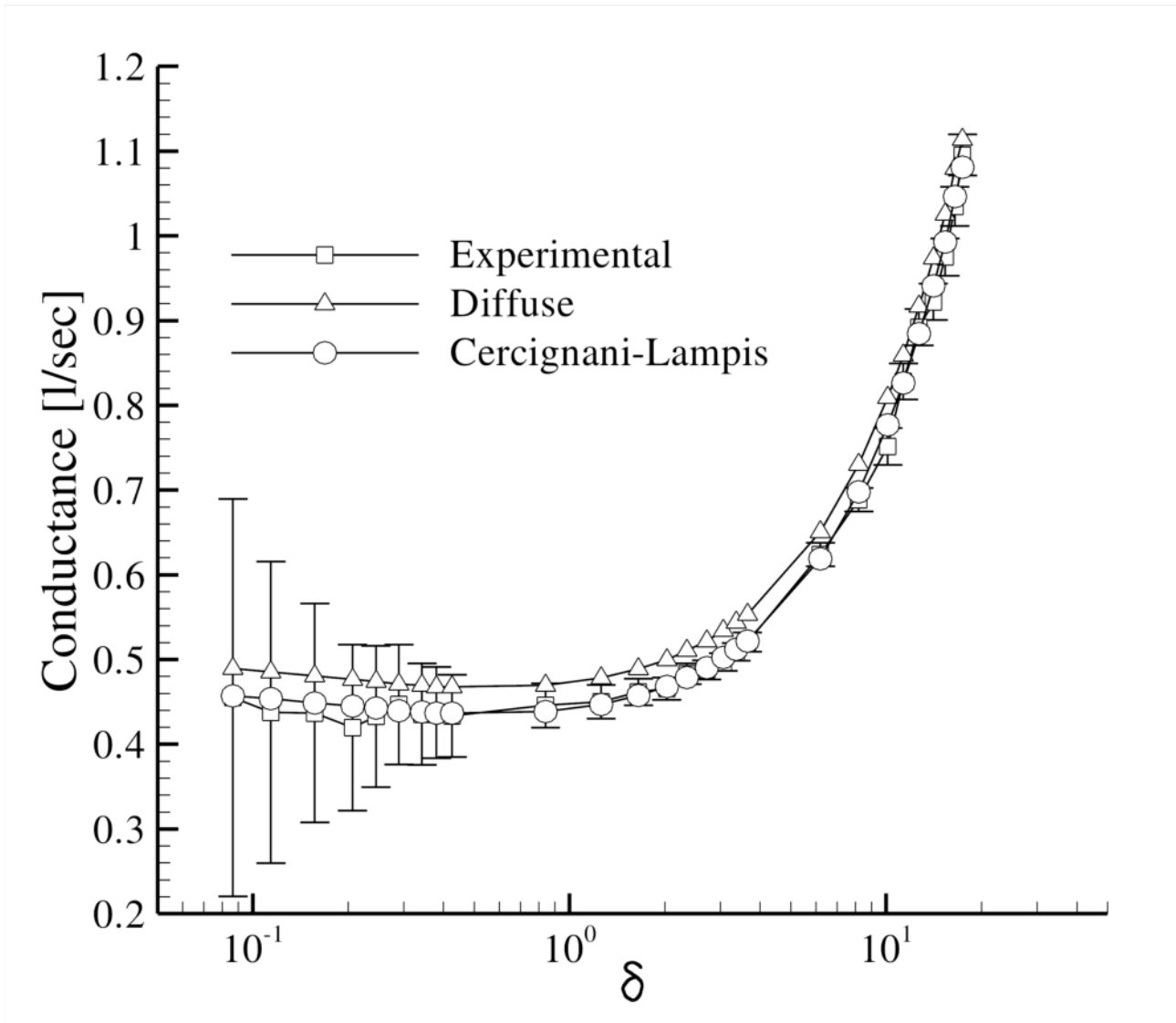


Figure 3.7: Comparison between experimental and numerical results for conductance (nitrogen, 296K)

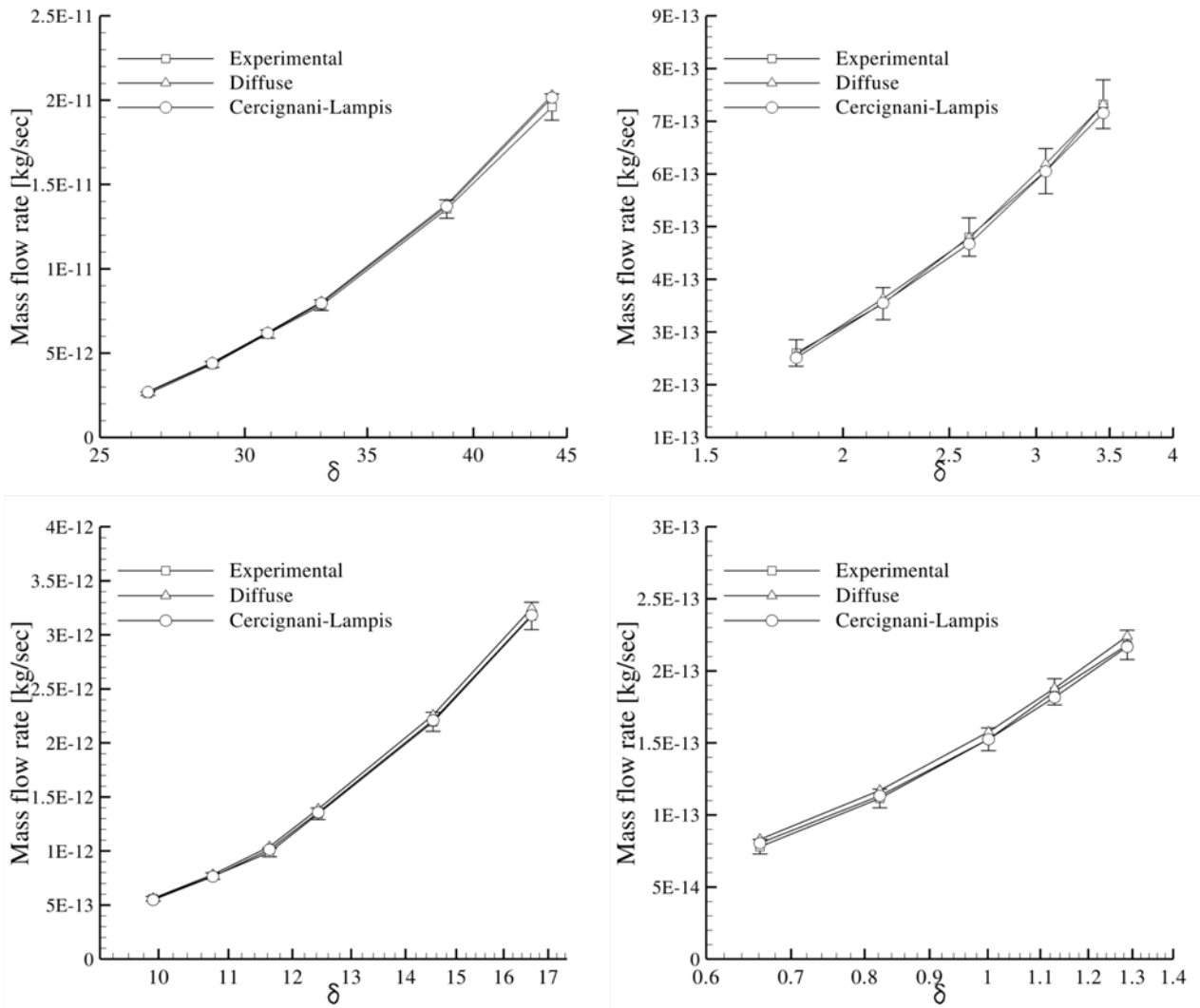


Figure 3.8: Comparison between experimental and numerical mass flow rates for argon (up) and helium (below), for high (left) and low (right) δ values

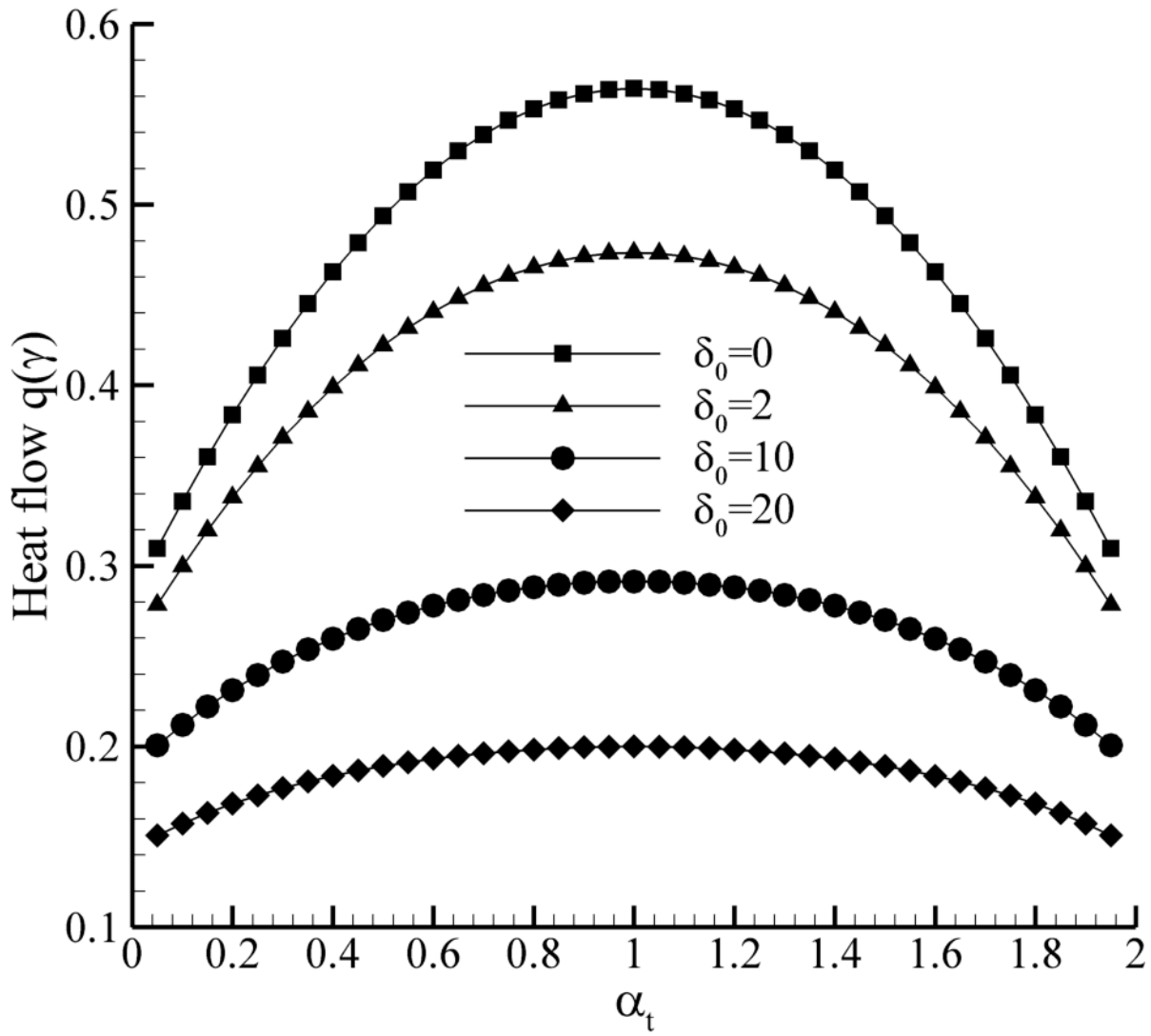


Figure 3.9: Dependence of the dimensionless radial heat flow on the CL accommodation coefficient α_t while keeping $\alpha_n = 1$ constant for $\gamma = 0.5$ and $\beta = 1$.

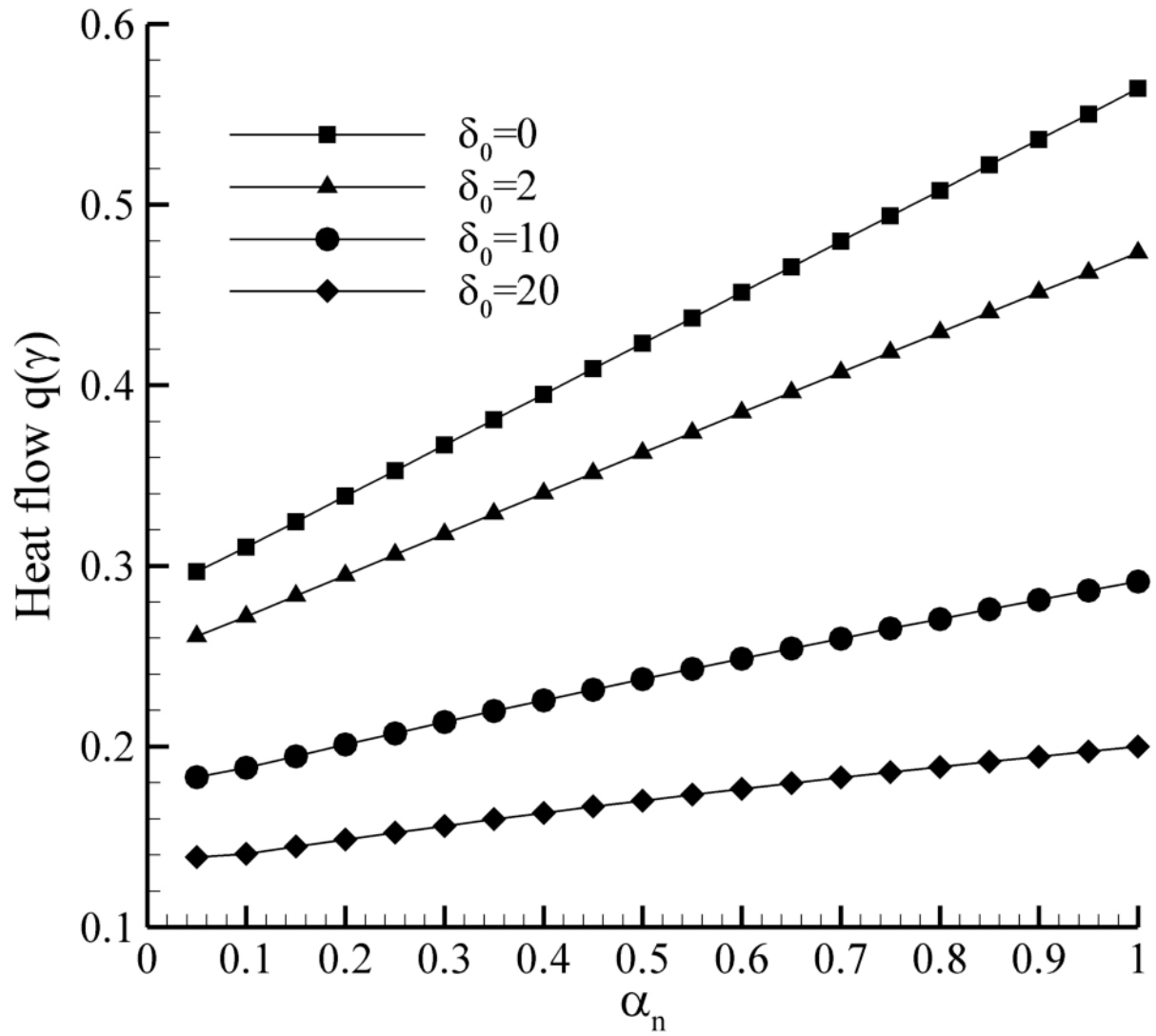


Figure 3.10: Dependence of the dimensionless radial heat flow on the CL accommodation coefficient α_n while keeping $\alpha_t = 1$ constant for $\gamma = 0.5$ and $\beta = 1$.

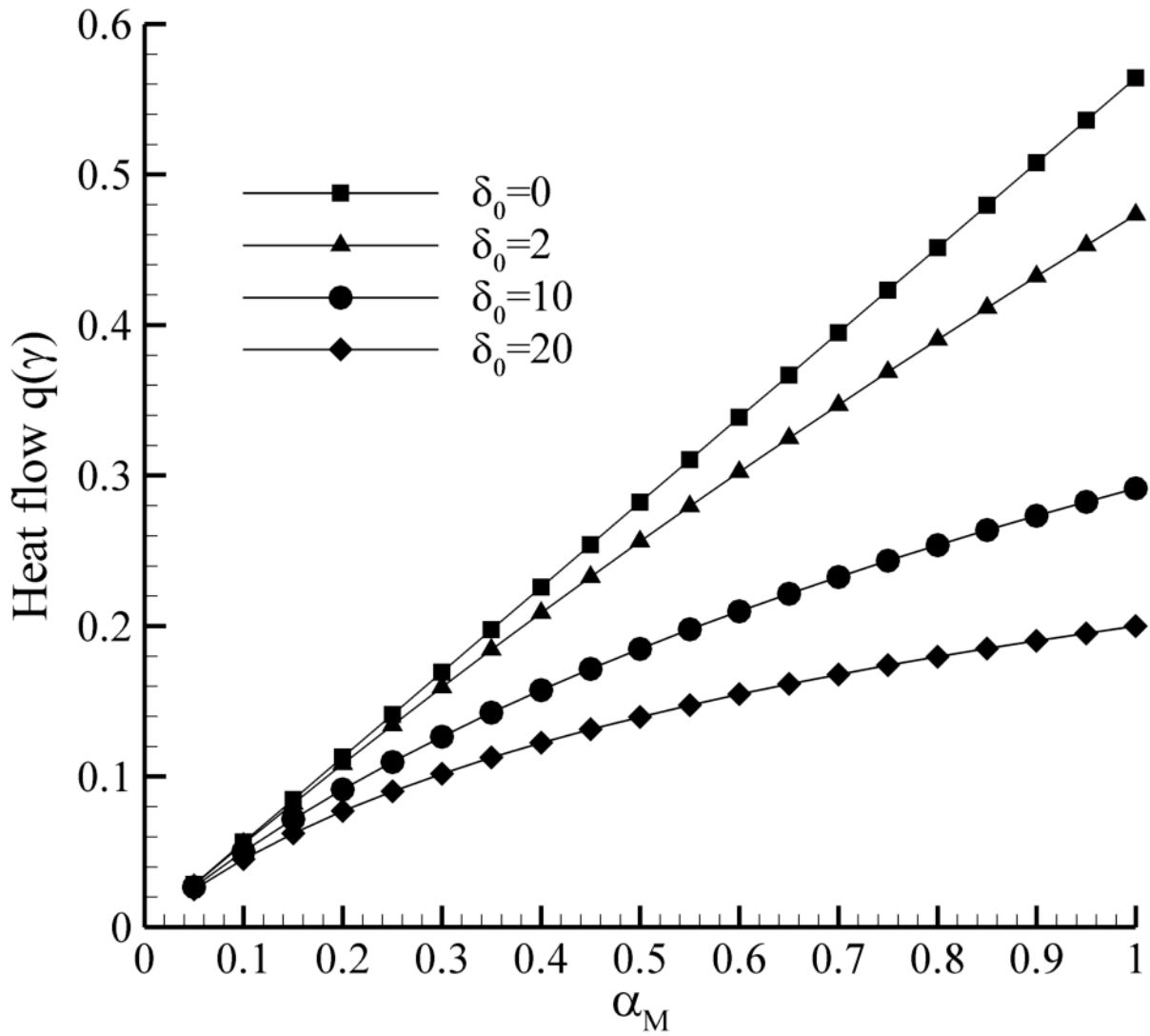


Figure 3.11: Dependence of the dimensionless radial heat flow on the Maxwell accommodation coefficient α_M for $\gamma = 0.5$ with $\beta = 1$.

Chapter 4

Linear flows driven by pressure gradients

4.1 Introduction

The linear, fully developed flow of a rarefied gas through channels of various cross sections has been studied extensively by several deterministic methods, as seen in Chapter 2. This state is characterized by zero velocity in the transversal directions and constant density at each cross-section, based on the underlying assumption that the channel is sufficiently long. However, in many practical situations there are significant deviations from this behaviour near the channel ends, where the assumption of constant density at each cross-section is not valid and the flow becomes two- or three-dimensional. This effect is particularly apparent in short channels, even for linear flows, and the fully developed profile may not be observed at all. Furthermore, even when the channel is long, the channel end effect may be significant in applications where high accuracy is required.

For the case of short channels with low pressure difference, the complete geometry must be simulated, including a part of the containers before and after the channel [152]. This type of investigation is possible for short to moderately long channels and has been realized here for two geometries: a rectangular channel of very low aspect ratio (i.e. Height / Width < 0.01), simplified to a parallel plate geometry, and a cylindrical tube. Flow due to low pressure differences is examined for the complete problem in the following sections, since the corresponding calculations have not been realized before in the literature, while the investigation of large pressure differences will be dealt with in Chapter 6. The channel length ranges from zero (the terms “slit” and “orifice” are widely used in the literature for this special case of parallel plate channel and cylindrical tube respectively) up to ten or twenty times the plate distance or tube radius.

An alternative methodology is also proposed to calculate the influence of the two ends for mod-

erately long to very long channels. The inlet and outlet parts of the channel are considered separately and the deviation from the fully developed profile is expressed via the effective length concept. This quantity has been calculated in the past using the integro-moment method [185] and in this manner the solution can be obtained by properly combining results with the fully developed flow field. The most important advantage of this approach is that the results of this work may be used to obtain the complete profiles with a very low computational cost in comparison to the full simulation. The same geometries have been considered and the results are applicable for any pressure ratio and for sufficiently long channels, as long as the local gradient of pressure is small.

It is noted that, since the formulations for the plane and axisymmetric geometries have many common elements, they are presented in a unified manner. The geometrical description of the complete geometry is shown in Figure 4.1. Two reservoirs containing a rarefied gas at pressures \hat{P}_{in} and \hat{P}_{out} and maintained at temperature T_0 are connected via a channel through which the gas flows. The reservoirs are infinitely large and only a fraction of their real size is shown here. The position vector $\mathbf{x} = (x_1, x_2, x_3)$ may refer to (x, y, z) with a characteristic length $L_0 = H$ or (x, r, ϑ) with $L_0 = R$, where H is the distance between the plates and R is the tube radius. The flow is oriented towards the positive direction of the x coordinate for both cases. Due to the geometrical properties of the flow, the dependence on the component x_3 will also be omitted in most cases. Finally, the velocity vector is denoted by $\mathbf{c} = (c_1, c_2, c_3)$ and the component orientations are identical to the ones of corresponding coordinates in the physical space.

4.2 Linearized flow in short channels

4.2.1 Introduction

In this section, we examine the case of flow due to small pressure differences between the upstream and the downstream vessel, i.e. $\Delta P/P_0 \ll 1$ with $\Delta P = \hat{P}_{out} - \hat{P}_{in}$ and the right container conditions as reference quantities, i.e. $P_0 = \hat{P}_{out}$. The derivation of the governing equations, boundary conditions and macroscopic quantities, including linearization of the distribution function,

non-dimensionalization and projection, is presented for the two geometries in a unified manner.

4.2.2 Governing equations for small pressure differences

Due to the small pressure difference, we may linearize the distribution function according to

$$f(\hat{\mathbf{x}}, \boldsymbol{\xi}) = f_0 [1 + h(\hat{\mathbf{x}}, \boldsymbol{\xi}) \Delta P / P_0] \quad (4.1)$$

where $h(\hat{\mathbf{x}}, \mathbf{c})$ is the perturbation of the distribution function $f(\hat{\mathbf{x}}, \mathbf{c})$ from the Maxwellian distribution at the reference conditions

$$f_0 = n_0 / (2\pi k_B T_0)^{3/2} \exp [-(\boldsymbol{\xi} - \hat{\mathbf{u}})^2 / (2RT_0)] \quad (4.2)$$

caused by the pressure difference. All quantities are then expressed in dimensionless form as follows:

$$\begin{aligned} \mathbf{x} &= \frac{\hat{\mathbf{x}}}{L_0}, \quad \mathbf{c} = \frac{\boldsymbol{\xi}}{v_0}, \quad v_0 = \sqrt{2 \frac{k_B}{m} T_0}, \\ \rho(\mathbf{x}) &= \frac{n(\mathbf{x}) - n_0}{n_0} \frac{P_0}{\Delta P}, \quad \tau(\mathbf{x}) = \frac{T(\mathbf{x}) - T_0}{T_0} \frac{P_0}{\Delta P}, \\ p(\mathbf{x}) &= \frac{\hat{P}(\mathbf{x}) - P_0}{P_0} \frac{P_0}{\Delta P}, \quad \mathbf{u}(\mathbf{x}) = \frac{\hat{\mathbf{u}}(\mathbf{x})}{v_0} \frac{P_0}{\Delta P} \end{aligned} \quad (4.3)$$

with v_0 being the most probable molecular velocity, k_B is the Boltzmann constant and $\rho, \tau, \mathbf{u}, p$ are the perturbations of density, temperature, velocity and pressure and $n_0 = P_0 / (k_B T_0)$. The degree of rarefaction is described by the rarefaction parameter δ , defined here as

$$\delta = \frac{P_0 L_0}{\mu_0 v_0} \quad (4.4)$$

where μ_0 is the gas viscosity at reference temperature T_0 .

The BGK model (2.21) substitutes the collision term due to its simplicity and the nearly isothermal properties of this flow. The kinetic equation becomes

$$\mathbf{c} \cdot \frac{\partial h}{\partial \mathbf{x}} = \delta \left[\rho + \tau \left(c^2 - \frac{3}{2} \right) + 2\mathbf{c} \cdot \mathbf{u} - h \right] \quad (4.5)$$

Similarly, the macroscopic quantity perturbations are expressed in terms of the perturbation h as

$$\begin{aligned}\rho &= \frac{1}{\pi^{3/2}} \int_{-\infty}^{\infty} \int_{-\infty}^{\infty} \int_{-\infty}^{\infty} h \exp(-c^2) dc_1 dc_2 dc_3 \\ \mathbf{u} &= \frac{1}{\pi^{3/2}} \int_{-\infty}^{\infty} \int_{-\infty}^{\infty} \int_{-\infty}^{\infty} h \mathbf{c} \exp(-c^2) dc_1 dc_2 dc_3 \\ \tau &= \frac{1}{\pi^{3/2}} \int_{-\infty}^{\infty} \int_{-\infty}^{\infty} \int_{-\infty}^{\infty} h \left(\frac{2}{3} c^2 - 1 \right) \exp(-c^2) dc_1 dc_2 dc_3\end{aligned}\quad (4.6)$$

The pressure perturbation is calculated by the ideal gas law, we get $p(\mathbf{x}) = \rho(\mathbf{x}) + \tau(\mathbf{x})$.

The molecular velocity vector is transformed to cylindrical coordinates, (c_p, θ, c_z) for the parallel plates and (c_p, θ, c_x) for the tube, as seen in Figure 4.2. In the case of flow through parallel plates, it is further possible to eliminate the c_z component of the distribution function by introducing appropriate projections, as explained in Chapter 1, expressed by the following moments

$$V(x, y, c_p, \theta) = \frac{1}{\sqrt{\pi}} \int_{-\infty}^{\infty} h(x, y, c_p, \theta, c_z) \exp(-c_z^2) dc_z \quad (4.7)$$

$$X(x, y, c_p, \theta) = \frac{1}{\sqrt{\pi}} \int_{-\infty}^{\infty} h(x, y, c_p, \theta, c_z) \left(c_z^2 - \frac{1}{2} \right) \exp(-c_z^2) dc_z \quad (4.8)$$

Thus, by properly acting on the governing equation, we finally obtain the final system, consisting of two equations for the parallel plates

$$c_p \cos \theta \frac{\partial V}{\partial x} + c_p \sin \theta \frac{\partial V}{\partial y} + \delta V = \delta \left[\rho + \tau (c_p^2 - 1) + 2 (c_p \cos \theta u_x + c_p \sin \theta u_y) \right] \quad (4.9)$$

$$c_p \cos \theta \frac{\partial X}{\partial x} + c_p \sin \theta \frac{\partial X}{\partial y} + \delta X = \delta \frac{\tau}{2} \quad (4.10)$$

and one for the tube

$$c_p \cos \theta \frac{\partial h}{\partial r} - \frac{c_p \sin \theta}{r} \frac{\partial h}{\partial \theta} + c_x \frac{\partial h}{\partial x} + \delta h = \delta \left[\rho + \tau \left(c^2 - \frac{3}{2} \right) + 2 \mathbf{c} \cdot \mathbf{u} \right] \quad (4.11)$$

The macroscopic perturbations are expressed by

$$\rho = \frac{1}{\pi} \int_0^{2\pi} \int_0^\infty V c_p \exp(-c_p^2) dc_p d\theta \quad (4.12)$$

$$u_x = \frac{1}{\pi} \int_0^{2\pi} \int_0^\infty V c_p^2 \cos \theta \exp(-c_p^2) dc_p d\theta \quad (4.13)$$

$$u_y = \frac{1}{\pi} \int_0^{2\pi} \int_0^\infty V c_p^2 \sin \theta \exp(-c_p^2) dc_p d\theta \quad (4.14)$$

$$\tau = \frac{2}{3\pi} \int_0^{2\pi} \int_0^\infty [(c_p^2 - 1) V + X] c_p \exp(-c_p^2) dc_p d\theta \quad (4.15)$$

for the 4D parallel plates problem and by

$$\rho = \frac{1}{\pi^{3/2}} \int_{-\infty}^\infty \int_0^{2\pi} \int_0^\infty h c_p \exp(-c^2) dc_p d\theta dc_x \quad (4.16)$$

$$u_r = \frac{1}{\pi^{3/2}} \int_{-\infty}^\infty \int_0^{2\pi} \int_0^\infty h (c_p \cos \theta) c_p \exp(-c^2) dc_p d\theta dc_x \quad (4.17)$$

$$u_x = \frac{1}{\pi^{3/2}} \int_{-\infty}^\infty \int_0^{2\pi} \int_0^\infty h c_x c_p \exp(-c^2) dc_p d\theta dc_x \quad (4.18)$$

$$\tau = \frac{1}{\pi^{3/2}} \int_{-\infty}^\infty \int_0^{2\pi} \int_0^\infty h \left(\frac{2}{3} c^2 - 1 \right) c_p \exp(-c^2) dc_p d\theta dc_x \quad (4.19)$$

for the 5D cylindrical tube problem.

4.2.3 Boundary conditions

The formulation is completed by providing the boundary conditions for h and V, X , corresponding to the plate and tube problems respectively. Molecules entering from the free surfaces (A),(B),(F),(G) (as shown in Figure 4.1) conform to a Maxwellian distribution according to the conditions of the corresponding vessel. Thus, for the left vessel, we have $n = n_{in}$, $T = T_0$ and $\hat{u} = 0$ and

therefore the perturbation from the equilibrium distribution is

$$\begin{aligned} h^+ &= \rho_{in} = \frac{n_{in} - n_0}{n_0 (\Delta P / P_0)} = \frac{(P_0 + \Delta P) - P_0}{P_0 (\Delta P / P_0)} = 1 \\ V^+ &= 1 \\ X^+ &= 0 \end{aligned} \quad (4.20)$$

Similarly, it is found that in downstream free surfaces (F),(G), where $n = n_{out}$, $T = T_0$ and $\hat{\mathbf{u}} = 0$, the perturbation of the incoming distribution is $h^+ = V^+ = X^+ = 0$.

For the walls (C),(D),(E), the diffuse boundary conditions are imposed according to the impermeability condition (the velocity component normal to the wall must be equal to zero) and the velocity integrals (4.13)-(4.14) and (4.17)-(4.18). Thus, we have

$$\rho_w = -\frac{I_{impinging}}{I_{departing}} \quad (4.21)$$

with

$$I_{departing}|_a = \int_{\theta_{1a}}^{\theta_{2a}} \int_0^\infty [c_p^2 \phi_a(\theta)] \exp(-c_p^2) dc_p d\theta \quad (4.22)$$

$$I_{impinging}|_a = \int_{\pi+\theta_{1a}}^{\pi+\theta_{2a}} \int_0^\infty V^- [c_p^2 \phi_a(\theta)] \exp(-c_p^2) dc_p d\theta \quad (4.23)$$

and the possible values of the above quantites for $a = C, D, E$ are

$$\begin{aligned} C : \theta_{1C} &= -\pi/2, \theta_{2C} = \pi/2, \phi_C(\theta) = \cos \theta \\ D : \theta_{1D} &= 0, \theta_{2D} = \pi, \phi_D(\theta) = \sin \theta \\ E : \theta_{1E} &= \pi/2, \theta_{2E} = 3\pi/2, \phi_E(\theta) = \cos \theta \end{aligned} \quad (4.24)$$

for the parallel plates and

$$I_{departing}|_a = \int_{c_{x1a}}^{c_{x2a}} \int_{\pi-\theta_{2a}}^{\pi-\theta_{1a}} \int_0^\infty [c_p \phi_a(\theta, c_p, c_x)] \exp(-c_p^2 - c_x^2) dc_p d\theta dc_x \quad (4.25)$$

$$I_{impinging}|_a = \int_{-c_{x2a}}^{-c_{x1a}} \int_{\theta_{1a}}^{\theta_{2a}} \int_0^\infty h^- [c_p \phi_a(\theta, c_p, c_x)] \exp(-c_p^2 - c_x^2) dc_p d\theta dc_x \quad (4.26)$$

$$C : \theta_{1C} = 0, \theta_{2C} = \pi, c_{x1a} = -\infty, c_{x2a} = 0, \phi_C(\theta, c_p, c_x) = c_x$$

$$D : \theta_{1D} = 0, \theta_{2D} = \pi/2, c_{x1a} = -\infty, c_{x2a} = \infty, \phi_D(\theta, c_p, c_x) = c_p \cos \theta \quad (4.27)$$

$$E : \theta_{1E} = 0, \theta_{2E} = \pi, c_{x1a} = 0, c_{x2a} = \infty, \phi_E(\theta, c_p, c_x) = c_x$$

for the cylindrical tube. An example of this derivation for the wall (C) in a parallel plate geometry is shown in Appendix 1. It is noted that the integrals of departing velocities (4.22) and (4.25) are also calculated numerically for consistency reasons: since the macroscopic velocity is calculated completely numerically, integration errors may lead to the appearance of non-zero normal macroscopic velocities if $I_{departing}$ is calculated analytically. These velocity components may be quite small if the discretization is sufficient, but may have a significant impact on the conservation of mass for long channels. The boundary condition finally reads as

$$\begin{aligned} h^+ &= \rho_w \\ V^+ &= \rho_w \\ X^+ &= 0 \end{aligned} \quad (4.28)$$

Diffuse-specular boundary conditions can also be taken into account by adjusting the accommodation coefficient α_M . For the cylindrical tube, the boundary conditions at the walls read as:

$$h^+ = \alpha_M \rho_w + (1 - \alpha_M) h^-$$

and the ρ_w constants are given by

$$\rho_w = -\frac{I_{impinging} + (1 - \alpha_M) I_{specular}}{\alpha_M I_{departing}} \quad (4.29)$$

The integrals of Equation (4.29) are

$$I_{departing}|_a = \int_{c_{x1a}}^{c_{x2a}} \int_{\pi-\theta_{2a}}^{\pi-\theta_{1a}} \int_0^\infty [c_p \phi_a(\theta, c_p, c_x)] \exp(-c_p^2 - c_x^2) dc_p d\theta dc_x \quad (4.30)$$

$$I_{impinging}|_a = \int_{-c_{x2a}}^{-c_{x1a}} \int_{\theta_{1a}}^{\theta_{2a}} \int_0^{\infty} h^- [c_p \phi_a (\theta, c_p, c_x)] \exp (-c_p^2 - c_x^2) dc_p d\theta dc_x \quad (4.31)$$

$$I_{specular}|_a = \int_{c_{x1a}}^{c_{x2a}} \int_{\pi-\theta_{2a}}^{\pi-\theta_{1a}} \int_0^{\infty} h_{specular} [c_p \phi_a (\theta, c_p, c_x)] \exp (-c_p^2 - c_x^2) dc_p d\theta dc_x \quad (4.32)$$

$$C : \theta_{1C} = 0, \theta_{2C} = \pi, c_{x1a} = -\infty, c_{x2a} = 0, \phi_C (\theta, c_p, c_x) = c_x$$

$$D : \theta_{1D} = 0, \theta_{2D} = \pi/2, c_{x1a} = -\infty, c_{x2a} = \infty, \phi_D (\theta, c_p, c_x) = c_p \cos \theta \quad (4.33)$$

$$E : \theta_{1E} = 0, \theta_{2E} = \pi, c_{x1a} = 0, c_{x2a} = \infty, \phi_E (\theta, c_p, c_x) = c_x$$

Finally, at the axis of symmetry ($x_2 = 0$) the molecules are reflected specularly

$$h^+ (x, 0, c_p, \theta, c_x) = h^- (x, 0, c_p, \pi - \theta, c_x)$$

$$V^+ (x, 0, c_p, \theta) = V^- (x, 0, c_p, -\theta) \quad (4.34)$$

$$X^+ (x, 0, c_p, \theta) = X^- (x, 0, c_p, -\theta)$$

The most important quantity for the practical applications is the mass flow rate through the channel, defined by

$$\dot{M} = \int [mn(\hat{\mathbf{x}})] \hat{u}_x(\hat{\mathbf{x}}) d\hat{A} \quad (4.35)$$

with \hat{A} being the channel cross-section. In both cases, the flow rate is non-dimensionalized by the analytical free molecular solution ($\delta_{in} = \delta_{out} = 0$) for flow through a channel of zero length. This solution can be easily extracted by the method of characteristics and yields $\dot{M}_{FM,i} = A_i \Delta P / v_0$ with $A_{pl} = H / \sqrt{\pi}$ for the plates and $A_{tb} = R^2 \sqrt{\pi}$ for the tube. Results are presented for the dimensionless flow rate

$$W_i = \frac{\dot{M}_i}{\dot{M}_{FM,i}} = 4\sqrt{\pi} G_i \quad (4.36)$$

where

$$G_{pl}|_x = \int_0^{1/2} u_x(x, y) dy$$

$$G_{tb}|_x = \int_0^1 u_x(x, r) r dr \quad (4.37)$$

are the reduced flow rates obtained by the simulations. The analytical derivation of these expressions is found in Appendix 2.

4.3 Formulation of the end effect problem

4.3.1 Introduction

In the alternative formulation, the channel is divided into three segments as seen in Figure 4.3, denoted here by the terms “inlet part”, “middle part” and “outlet part”. These are distinguished by the transformation of the flow field, which is two-dimensional for the two channel end parts but gradually turns into one-dimensional at the middle part, which is characterized by fully developed flow conditions. By studying the areas of flow entrance/exit, we can determine the perturbation of pressure far from the channel ends and then apply a well known integration procedure to obtain the pressure profile in the middle part. In this manner, the solution of the complete problem is avoided, greatly reducing the computational effort. In fact, if the pressure perturbation values are tabulated for each geometry and δ , the integration step can provide the pressure profile within a few minutes.

4.3.2 Governing equations

The most challenging task is the application of appropriate boundary conditions at the interfaces between the three parts of the channel. In the middle area, pressure and density are constant at each cross-section, varying linearly in the x –direction, with a constant gradient. Thus, it would be preferable to use a reference pressure varying linearly inside the channel with the same gradient, as seen in Figure 4.4 for the outlet problem, in order to obtain a constant perturbation term as the interface is approached.

Since the geometries of the channel entrance and exit are exactly the same, the study of only one of them is required. The outlet end geometry considered here is displayed in Figure 4.5, where the region $\hat{x}_1 > 0$ represents the container, while $\hat{x}_1 < 0$ corresponds to the channel. The gas flows from

the long channel into the infinitely large container, where it is maintained at pressure $P_0 \left(= \hat{P}_{out} \right)$ and temperature $T_0 \left(= \hat{T}_{out} \right)$ far from the channel exit. Inside the fully developed region of the channel, a constant pressure gradient $|X_P| \ll 1$ is maintained far from the channel end

$$X_P = \frac{L_0}{P_0} \frac{\partial \hat{P}}{\partial \hat{x}_1} \quad (4.38)$$

Thus, it would be preferable to use a linearly varying reference pressure inside the channel, such as

$$P_R = \begin{cases} P_0 & , \hat{x}_1 > 0 \\ P_0 [1 + X_P(\hat{x}_1/L_0)] & , \hat{x}_1 \leq 0 \end{cases} \quad (4.39)$$

in order to approach the linear trend of the real pressure at large distances from the channel exit, that is when $\hat{x}_1 \ll -L_0$, and obtain a constant pressure perturbation term, as seen in Figure 4.4. The reference number density is defined by

$$n_R = \begin{cases} P_0 / (k_B T_0) & , \hat{x}_1 > 0 \\ P_0 [1 + X_P(\hat{x}_1/L_0)] / (k_B T_0) & , \hat{x}_1 \leq 0 \end{cases} \quad (4.40)$$

A linearization can then be performed in terms of X_P , according to

$$f = f_R (1 + h X_P) \quad (4.41)$$

with f_R being a Maxwellian at reference conditions

$$f_R = \frac{n_R}{(2\pi R_g T_0)^{3/2}} \exp \left(-\frac{\xi^2}{2 R_g T_0} \right) \quad (4.42)$$

All quantities are expressed in dimensionless form as follows:

$$\begin{aligned} \mathbf{x} &= \frac{\hat{\mathbf{x}}}{L_0}, \quad \mathbf{c} = \frac{\boldsymbol{\xi}}{v_0}, \quad v_0 = \sqrt{2 \frac{k_B}{m} T_0}, \\ \rho(\mathbf{x}) &= \frac{n(\mathbf{x}) - n_R}{n_R X_P}, \quad \tau(\mathbf{x}) = \frac{T(\mathbf{x}) - T_0}{T_0 X_P}, \\ p(\mathbf{x}) &= \frac{\hat{P}(\mathbf{x}) - P_R}{P_R X_P}, \quad \mathbf{u}(\mathbf{x}) = \frac{\hat{\mathbf{u}}(\mathbf{x})}{v_0 X_P} \end{aligned} \quad (4.43)$$

with $v_0 = \sqrt{2 k_B T_0 / m}$ being the most probable molecular velocity, k_B is the Boltzmann constant and $\rho, \tau, \mathbf{u}, p$ are the perturbations of density, temperature, velocity and pressure. The degree of rarefaction is described by the rarefaction parameter δ , defined in (4.4).

The BGK model substitutes the collision term and the same projections as in the previous section, given by Equations (4.7) and (4.8), are also used here. Therefore, after expressing the velocity vector in polar and cylindrical coordinates as before, the final equations are

$$c_p \cos \theta \frac{\partial V}{\partial x} + c_p \sin \theta \frac{\partial V}{\partial y} + \delta V = \delta [\rho + \tau (c_p^2 - 1) + 2 (c_p \cos \theta u_x + c_p \sin \theta u_y)] + g(x, c_p, \theta) \quad (4.44)$$

$$c_p \cos \theta \frac{\partial X}{\partial x} + c_p \sin \theta \frac{\partial X}{\partial y} + \delta X = \delta \frac{\tau}{2} \quad (4.45)$$

for the channel and

$$c_p \cos \theta \frac{\partial h}{\partial r} - \frac{c_p \sin \theta}{r} \frac{\partial h}{\partial \theta} + c_x \frac{\partial h}{\partial x} + \delta h = \delta \left[\rho + \tau \left(c^2 - \frac{3}{2} \right) + 2 \mathbf{c} \cdot \mathbf{u} \right] + g(x, c_x) \quad (4.46)$$

for the tube. It can be seen that the only differences with Equations (4.9) - (4.11) are the source terms, given by

$$g_{ch}(x, c_p, \theta) = \begin{cases} 0 & , \quad x > 0 \\ -c_p \cos \theta & , \quad x \leq 0 \end{cases} \quad (4.47)$$

$$g_{tb}(x, c_x) = \begin{cases} 0 & , \quad x > 0 \\ -c_x & , \quad x \leq 0 \end{cases} \quad (4.48)$$

These terms are obtained during the linearization of the streaming part due to the physical space dependence of the reference pressure. For example, for the tube case we have

$$\xi_x \frac{\partial [f_R (1 + hX_P)]}{\partial \hat{x}} = \xi_x f_R X_P \frac{\partial h}{\partial \hat{x}} + \xi_x (1 + hX_P) \frac{\partial f_R}{\partial \hat{x}} \quad (4.49)$$

and the second part of the right hand side eventually leads to the source term.

The macroscopic moments are found by exactly the same expressions as before, Equations (4.12) - (4.15) for the plates and (4.16)-(4.19) for the tube. Moreover, the pressure perturbation is calculated by $p(\mathbf{x}) = \rho(\mathbf{x}) + \tau(\mathbf{x})$ from the ideal gas law.

Even though this formulation is valid for the outlet part of the channel, it can also be used to model the inlet part by noting that the dimensionless pressure gradient X_P has the opposite sign and thus the flow direction is reversed. The final objective of this study is to calculate the pressure perturbation at the fully developed cross-section of the end geometry, which will finally serve for the correct connection at the interfaces between the middle and the end parts.

4.3.3 Boundary conditions

All boundary conditions except the one imposed on surface (A) (Figure 4.5) are also similar to the ones employed in the full problems of the previous section. At the free surfaces (D),(E) incoming molecules conform to the Maxwellian distribution at the local reference values and therefore the perturbation of the distribution function is zero ($h^+ = 0$). The impermeability condition ($u_n = 0$) is imposed at the walls (D),(E), i.e. $h^+ = \rho_w$, $V^+ = \rho_w$, $X^+ = 0$ where ρ_w is found again by equations (4.21) - (4.27). At the axis of symmetry ($x_2 = 0$) molecules are reflected specularly, as in Eq. (4.34).

At the incoming surface of the channel (A), the distribution function conforms to the condition

$$\lim_{x \rightarrow -\infty} \frac{\partial h_{in}}{\partial x} = \lim_{x \rightarrow -\infty} \frac{\partial V_{in}}{\partial x} = \lim_{x \rightarrow -\infty} \frac{\partial X_{in}}{\partial x} = 0 \quad (4.50)$$

since that cross-section is characterized by fully developed flow conditions and thus the perturbations should remain constant. After substituting (4.50) in equations (4.44) and (4.46) and taking into account that $\tau_{in} = u_{y,in} = 0$ due to the fully developed conditions

$$c_y \frac{\partial V_{in}}{\partial y} + \delta V_{in} = \delta [\rho_{in} + 2c_x u_{x,in}] + g(x, c_x) \quad (4.51)$$

$$c_p \cos \theta \frac{\partial h_{in}}{\partial r} - \frac{c_p \sin \theta}{r} \frac{\partial h_{in}}{\partial \theta} + \delta h_{in} = \delta [\rho_{in} + 2c_x u_{x,in}] + g(x, c_x) \quad (4.52)$$

it may be seen that we can further project the equations with

$$Y(y, c_y) = \frac{1}{\sqrt{\pi}} \int_{-\infty}^{\infty} V_{in}(-L_{dev}, y, c_x, c_y) c_x \exp(-c_x^2) dc_x \quad (4.53)$$

$$Z(r, c_p, \theta) = \frac{1}{\sqrt{\pi}} \int_{-\infty}^{\infty} h_{in}(-L_{dev}, r, c_p, \theta, c_x) c_x \exp(-c_x^2) dc_x \quad (4.54)$$

and obtain the well-known, fully developed flow problems, described by the equations

$$c_y \frac{\partial Y(y, c_y)}{\partial y} + \delta Y(y, c_y) = \delta u_{x,in}(y) - \frac{1}{2} \quad (4.55)$$

$$c_p \cos \theta \frac{\partial Z(r, c_p, \theta)}{\partial r} - \frac{c_p \sin \theta}{r} \frac{\partial Z(r, c_p, \theta)}{\partial \theta} + \delta Z(r, c_p, \theta) = \delta u_{x,in}(r) - \frac{1}{2} \quad (4.56)$$

As a final step, the unprojected distribution at the incoming surface (A) can be retrieved by the expressions

$$V_{in}(y, c_p, \theta) = 2(c_p \cos \theta) Y(y, c_p \sin \theta) + \rho_{in}(y) \quad (4.57)$$

$$h_{in}(r, c_p, \theta, c_x) = 2c_x Z(r, c_p, \theta) + \rho_{in}(r) \quad (4.58)$$

and used as incoming boundary conditions. The corresponding projection to X leads to $X_{in} = 0$ and therefore is omitted.

To summarize, the boundary distributions, denoted by the “plus” superscript, are equal to

$$\begin{array}{llll} h_{wall}^+ = \rho_w & h_{container}^+ = 0 & h_{channel}^+ = h_{in} & h_{center}^+ = h_{specular} \\ V_{wall}^+ = \rho_w & V_{container}^+ = 0 & V_{channel}^+ = V_{in} & V_{center}^+ = V_{specular} \\ X_{wall}^+ = 0 & X_{container}^+ = 0 & X_{channel}^+ = 0 & X_{center}^+ = X_{specular} \end{array} \quad (4.59)$$

Before the presentation of the numerical algorithm, it is important to discuss the application of the boundary conditions (4.50) and (4.57) - (4.58) on surface A. In order to use (4.57) - (4.58), the distribution functions Y and Z need to be calculated by the solution of (4.55) - (4.56) with the corresponding boundary conditions. This step is performed once at the beginning of the numerical solution and Y, Z are stored to be used at each iteration. This type of incoming boundary condition is preferred here over the use of (4.50) since it provides an estimation of the error of the scheme: the distribution of molecules arriving at surface A from the exhaust must also conform to (4.57) - (4.58) with a relatively good accuracy, something which is not enforced in the iteration process. Furthermore, it provides a better representation of the physical conditions.

4.3.4 Dimensionless flow rate derivation including the channel end effect

The pressure perturbation at cross-section (A) is the main quantity of interest here. Its value can be used to determine the entrance/exit pressure and, along with a well known integration procedure for the fully developed part of the flow [186], the complete pressure profile along a channel can be obtained. From Figure 4.4 and Equations (4.43),(4.39), it can be seen that

$$\delta P = P - P_R = p(-L_{dev}, x_2) P_R X_P \quad (4.60)$$

and

$$\tan \phi = -X_P P_R \quad (4.61)$$

leading to

$$\Delta L_{out} = -p(-L_{dev}, x_2) \quad (4.62)$$

Similarly, when the geometry represents an inlet part ($X_P > 0, \delta P < 0$) we get

$$\Delta L_{in} = -p(-L_{dev}, x_2) \quad (4.63)$$

Thus, we may obtain a very good agreement for the middle part of the complete channel (which usually is the largest part), if we apply the integration procedure at a “modified” geometry, where L has been increased by a fictional ΔL_{in} at the inlet and ΔL_{out} at the outlet. Alternatively, we may get the complete pressure profile by properly combining fully developed and end results during the dimensionalization.

The integration procedure is performed according to

$$\dot{M} = -G_{FD}(\delta) \frac{\pi R^3}{v_0} \frac{dP}{dx_1} = -G \frac{\pi R^3}{v_0} \frac{\Delta P}{L} \quad (4.64)$$

where the x_1 coordinate takes values in $[0, L]$ and G_{FD} is the fully developed solution for a channel of infinite length. The quantity G is a constant, adjusted to obtain this equality. From (4.64) we get

$$G_{FD}(\delta) \frac{dP}{dx_1} = G \frac{\Delta P}{L} \quad (4.65)$$

and using the definition of the rarefaction parameter (4.4)

$$G_{FD}(\delta) \frac{d\delta}{dx_1} = G \frac{\delta_{in} - \delta_{out}}{L} \quad (4.66)$$

If we separate the variables and integrate, we get

$$\frac{1}{\delta_{in} - \delta_{out}} \int_{\delta_{in}}^{\delta_{out}} G_{FD}(\delta) d\delta = \frac{G}{L} \int_0^L dx_1 \quad (4.67)$$

and therefore the expression for G is obtained

$$G = \frac{1}{\delta_{in} - \delta_{out}} \int_{\delta_{in}}^{\delta_{out}} G_{FD}(\delta) d\delta \quad (4.68)$$

Finally, if we repeat the same procedure taking the end effect into account (by changing the integration limits in the right hand side of Equation (4.67) to $-\Delta L_{in}$ and $L + \Delta L_{in}$) we deduce that

$$G = \frac{L}{L + \Delta L_{in} + \Delta L_{out}} \frac{1}{\delta_{in} - \delta_{out}} \int_{\delta_{in}}^{\delta_{out}} G_{FD}(\delta) d\delta \quad (4.69)$$

For the tube geometry, we can further simplify to get [45]

$$G(L, \delta) = \frac{L}{L + \Delta L_{in} + \Delta L_{out}} G_{FD}\left(\frac{\delta_{in} + \delta_{out}}{2}\right) \quad (4.70)$$

4.4 Numerical scheme

4.4.1 Introduction

In this subsection, we derive the discretized equation and describe the typical numerical algorithm. Furthermore, we highlight various improvements in the computational scheme, which allow us to consider larger domains in order to impose the boundary conditions at their appropriate locations. Finally, the numerical parameters and some information on their selection are given. It must be noted that the computational resources of the supercomputing facility in Juelich research center, Germany have been used for all the simulations discussed here.

4.4.2 Discretization and description of algorithm

The main characteristics of the numerical scheme are similar to the ones found in previously formulated discrete velocity schemes. The continuum spectrum of the molecular velocity magnitudes c_p and c_x are discretized to M values, their values being chosen according to the roots of the M th order Legendre polynomial mapped in $[0, c_{p,max}]$ and $[0, c_{x,max}]$ respectively, while the molecular velocity angles N_θ are uniformly distributed in $[0, 2\pi]$ ($[0, \pi]$ for the tube due to the axisymmetrical proper-

ties of the flow). The distribution functions, bulk quantity fields and governing equations are further discretized by a finite volume scheme in the physical space to $N_x \times N_y$ or $N_x \times N_r$ points.

The discrete velocity method algorithm is then applied, consisting of the following steps:

1. Bulk quantity perturbations ρ , \mathbf{u} and τ are initially assumed.
2. If the end geometry is considered, incoming distributions in cross-section (A) are estimated from Equations (4.57) with $\cos \theta > 0$ for the channel and (4.58) with $c_x > 0$ for the tube.
3. The discretized equations are solved using a marching scheme.
4. New estimations for the bulk quantities are calculated.
5. Steps 2 - 4 are repeated until convergence has been reached for the macroscopic quantities.

Kinetic equations (4.9) - (4.11) and (4.44) - (4.46) are discretized according to the second-order finite volume scheme. The procedure is presented for Eq. (4.46), since this is the most complicated case: at each interval $\Delta r_i, \Delta \theta_j, \Delta x_k$ around r_i, θ_j, x_k , we act upon the governing equation with

$$A = \int_{x_k - \frac{\Delta x_k}{2}}^{x_k + \frac{\Delta x_k}{2}} \int_{\theta_j - \frac{\Delta \theta_j}{2}}^{\theta_j + \frac{\Delta \theta_j}{2}} \int_{r_i - \frac{\Delta r_i}{2}}^{r_i + \frac{\Delta r_i}{2}} (\cdot) dr d\theta dx \quad (4.71)$$

to eliminate all derivatives [156]. Then, all integrations can either be carried out analytically or substituted by the trapezoidal rule, causing the second-order error. The detailed derivations are shown in Appendix 3, while the final discretized equation is seen in Table 4.1, where for example $h_{i+,j+,k+}^{l,m} = h\left(r_i + \frac{\Delta r_i}{2}, x_k + \frac{\Delta x_k}{2}, c_p^l, \theta_j + \frac{\Delta \theta_j}{2}, c_x^m\right)$ and so on. This expression is applied for any interval, regardless of the grid distances and the angular discretization, and is also usable as $r \rightarrow 0$ after the application of the l'Hospital rule on the indeterminate fractions.

4.4.3 Description of the marching step and related benefits

The kinetic equations are solved independently for each velocity component (c_p, θ) or (c_p, c_x) (the angles θ are not independent with each other in the cylindrical case) if the macroscopic quan-

tities are known. A marching scheme is applied to solve these equations to avoid solving a system, maximizing efficiency and reducing memory consumption. This is highly desirable since the problems of channel and tube are 4- and 5-dimensional respectively and therefore subject to significant computational limitations. A brief explanation is given here for the channel problem (see also Figure 4.6, up). At each node column, the distribution function is calculated by solving for the corresponding unknown component in the discretized equation, properly substituting the boundary conditions (blue arrows) and the previous column values (green arrows). The first component to be calculated is the one moving downwards from the physical node right below the upper boundary (component 1 in the same figure), since all values of distribution required for this calculation are known, followed by the one below it for the same angle (component 2) and so on, until the lowermost component is reached (component 3). Due to the symmetry conditions, this procedure also returns the upward moving counterpart (component 4), without the need for storage in memory. Finally, we keep on solving in the positive y direction to component 5 and further above, until all values are known. When the whole distribution column in x is completed, all information on the macroscopic conditions and impermeability variables is stored and we move on by Δx to the next column. The calculated distribution function is then moved to another temporary array to store the "previous" values and the whole procedure is repeated for the rest of the columns (and overall for each velocity vector).

The description for the cylindrical geometry marching scheme is quite similar (Figure 4.6, below). The discretized equation is solved for the unknown values (white nodes) using the known quantities (dark nodes) from the previous column (green arrows) or the boundary conditions (blue arrows). However, we must also take into account the additional complexity of the angular velocity component. The angles are calculated starting from $\theta = \pi$, where a simplified version of the discretized equation can be applied, solving all the way until the lower boundary. Then, angles starting from $\theta = \pi - \Delta\theta$ down to $\theta = \pi/2$ are calculated in this sequence (as the purple arrow indicates) while moving downwards. The symmetry condition is applied at the center and thus the boundary values for $\theta = \pi/2$ down to $\theta = 0$. Finally, we solve for these distributions until we reach the upper surface. Angles in

$(\pi, 2\pi)$ are symmetric and do not need to be calculated again. By taking the discretized version of the moments (4.12) - (4.19), employing Gauss-Legendre quadrature for the velocity magnitudes and the trapezoidal rule for the angles, macroscopic quantities are calculated and this procedure is repeated for all columns and each combination of c_p, c_x until the complete macroscopic field has been found.

The application of this algorithm has two important consequences: First, memory requirements are dramatically reduced, since two temporary arrays of dimensions $(N_y, 2)$ for the channel and (N_r, N_θ) for the tube can be used for the distribution function in the current and the previous column instead of one large with dimensions (N_x, N_y, M, N_θ) and $(N_x, N_r, M, N_\theta, M)$ (which would also be more costly to access in memory due to the multiple dimensions). Storing the distribution only in parts of the domain needed by the marching scheme allows the simulation of much larger and denser grids. Second, the velocity magnitude independency leads to a straightforward parallelization of the code. Each processor solves the kinetic equation for a group of velocities and information on macroscopic quantities and impermeability constants is exchanged between the processors at the end of each iteration. In this manner, the transmission of the distribution function is circumvented, greatly reducing the cost of parallel communication. A large number of processors, namely $M \times N_\theta/2$ and M^2 , can be used for the channel and tube problems respectively.

It has also been seen that the convergence rate benefits significantly by adjusting the initial assumption for the macroscopic variables to reasonable values. For example, in the problems of linearized flow through channel or tube, the density perturbation is chosen equal to unity in the left vessel, zero in the right and varies linearly inside the channel. In the same context, velocities are set to zero everywhere in the field. This selection is quite close to the final expected distribution of macroscopic variables and significantly reduces the number of iterations.

4.4.4 Numerical and domain parameters

These steps of the algorithm are repeated, using the new values for the bulk quantities again for the solution of the kinetic equations and the new estimation of incoming distributions in surface (A) for the end effect geometry. The iteration scheme is completed when all macroscopic quantities have

converged, satisfying a predetermined criterion: in our calculations the average residual per node has been chosen

$$\text{residual} = \frac{1}{4N_{total}} \sum_{i=1}^{N_{total}} [|\rho_i - \rho_i^{pr}| + |\tau_i - \tau_i^{pr}| + |u_{x1,i} - u_{x1,i}^{pr}| + |u_{x2,i} - u_{x2,i}^{pr}|] \quad (4.72)$$

where the pr superscript denotes the corresponding quantities in the previous iteration and N_{total} is the total number of nodes. The solution is repeated for different values of L_{left}/L_0 , L_{right}/L_0 , L_{dev}/L_0 to ensure the correct application of boundary conditions by checking the convergence of the quantities of interest (flow rate and pressure perturbation). For the complete geometry, the values $L_{left}/L_0 = L_{right}/L_0 = 15$ are found to provide accuracy levels higher than 1%, while regions up to $L_{left}/L_0 = L_{right}/L_0 = 50$ have been tested. The corresponding domain parameters for the end geometry are given in Table 4.2. In order to ensure that the accuracy would be sufficient in areas of large gradients, a non-uniform grid has been used in the physical space, described in Appendix 4. It is displayed in Figure 4.7 in an exaggerated form in order to clarify the areas of high/low discretization. At all times, the maximum interval is kept low, even if the field appears to be quite smooth, in order to avoid the appearance of discretization error. An analysis has also been performed for the numerical parameters through several runs, resulting in the values given in Table 4.3 in order to obtain grid independent results. These values depend on δ and the channel geometry (cross-section, L/L_0).

4.5 Results

4.5.1 Introduction

The results shown in this section are divided in two sections, corresponding to the solution of the complete problem and the end effect problem, respectively. In the first case we focus on the flow rate values and the field characteristics, while in the second one we compare the results obtained by the end effect approach in comparison to the fully developed flow simulations and the complete channel simulation for moderately long channels.

4.5.2 Linearized flow

The code has been benchmarked with previous results for the slit case [162], showing good agreement for $\delta < 5$. There are discrepancies for larger δ but since there is a very good agreement with the non-linear BGK model flow rate values for the parallel plate channel with $\hat{P}_{out}/\hat{P}_{in} = 0.9$ [79] and for the cylindrical tube with $\hat{P}_{out}/\hat{P}_{in} = 0.9, 0.99$ (Chapter 6), we conclude that the present values are correct. Furthermore, the free molecular solution (Appendix 6) is obtained with very good accuracy and the principle of mass conservation (Appendix 5) is fulfilled in the whole domain with an error less than 0.1%.

Results include flow rates for the parallel plate channel in Table 4.4 and for the cylindrical tube in Table 4.5. It is observed that the flow rate is relatively close for both geometries for small L/L_0 ratios and small δ . This is just a consequence of the non-dimensionalization with the analytical solution for $L/L_0 = 0$ and $\delta = 0$. Furthermore, the flow rate increases monotonically along with the rarefaction parameter for all geometrical cases except $L/H = 10$. In the latter case, the onset of the Knudsen minimum phenomenon is observed for the plate channel. The flow rate obtains a minimum value between $\delta = 0.5$ and $\delta = 1$, due to a small percentage of molecules moving almost axially along the channel, having a very small transversal velocity component. When the Knudsen number is high, their contribution to the mass flow becomes very important, while as the Knudsen drops, the mass flow rate is also decreased due to the appearance of intermolecular collisions, interrupting these long axial trajectories. On the other hand, very large collision frequencies induce an overall drift velocity which increases the mass flow through the channel. The Knudsen minimum phenomenon is not observed in the case of the tube for the length-over-radius ratios shown here and it seems that a longer tube is required. Furthermore, the flow rate is significantly reduced for all cases as the channel length is increased due to the lower pressure gradient and the wall friction.

Indicative results for incomplete accommodation are also presented in Table 4.6. It is seen that, in comparison to the fully accommodated results of Table 4.5, the flow rate remains constant for orifice flow. This is one of the favorable properties of orifice flow, making it an ideal configuration for

the evaluation of numerical schemes, kinetic models and intermolecular potentials, since the factor of gas-surface interaction can be neglected in this case. It has been found in the past [162] that the slit also possesses similar properties, which have not been investigated in this work. For a tube of finite length, it increases significantly, especially for small δ . In particular, the deviation is up to 21% for $L/R = 1, \delta \leq 1$, 15 % for $L/R = 1, \delta = 10$, 93 % for $L/R = 10, \delta \leq 1$ and 42% $L/R = 10, \delta = 10$. This trend is to be expected since surface accommodation properties play a more important role for highly rarefied atmospheres and longer channels.

A comparison of the flow rate values with previously obtained DSMC results ($\hat{P}_{out}/\hat{P}_{in} = 0.9$ [149] and $\hat{P}_{out}/\hat{P}_{in} = 0.7$ [152]), reproduced in Table 4.7 modified by the expression $W_{Lin} = W_{DSMC} / (1 - \hat{P}_{out}/\hat{P}_{in})$, shows good agreement, especially near the free molecular regime. These similarities for $\delta \rightarrow 0$ are explained by the fact that the Reynolds number also approaches zero and thus the flow field becomes symmetrical. The same trend appears for small ΔP and large L/R , also leading to small Mach and Reynolds. The low pressure difference value in [149] acts beneficially for this comparison and the maximum error observed here for orifice flow is about 7.7 % at $\delta = 10$. Thus, since the orifice is the most non-linear case, it is expected that this value is the maximum deviation between the two methods for $\hat{P}_{out}/\hat{P}_{in} \leq 0.9, \delta \leq 10$ and any tube length. Comparing with [152] confirms that discrepancies are reduced when the tube becomes longer due to the lower pressure gradient.

It would not be easy to make a direct comparison between linearized and DSMC results because of the inherent difficulties of both formulations to deal with flows far from or near equilibrium, respectively. However, it can be seen that at a pressure ratio value of about $\hat{P}_{out}/\hat{P}_{in} = 0.9$, both formulations give satisfactory results in good agreement with each other. This conclusion has two implications: First, linearized equations provide correct results at a wider range than expected from the mathematical derivation, i.e. up to $\Delta P/P_0 = 0.1$ or even more for low δ . Thus, the results shown here are useful for a considerable range of pressure ratios, for which another computational method is not available in the whole range of the Knudsen number. Secondly, practically all physical conditions for these two problems can be simulated by applying either DSMC or linearized kinetic equations in

the respective range of each method. Therefore, problems driven by forces of any magnitude can be considered using the linearized and DSMC formulations and in a wide range of the Knudsen number.

For all cases considered here, the field is symmetric around $x = L/(2L_0)$ for any channel length and in the whole range of the Knudsen number, as expected. Furthermore, the macroscopic quantity fields for both geometries are found to be quite similar. This characteristic is observed in Figures 4.8 - 4.13, where the pressure perturbation, the dimensionless axial velocity and the streamlines are plotted for both the plate and cylindrical channels, with $L/L_0 = 0, \delta = 1$ and $L/L_0 = 10, \delta = 10$. Besides the differences caused by the different reference length, leading to a larger dimensionless opening for the tube, there are many similarities between the two flow fields. The pressure ranges between the two reservoir values inside the channel and around its ends, while a region of higher and lower density than the container values is also observed just above the channel opening. The velocity field values are also quite close to each other. The velocity is nearly zero as we approach the upstream container incoming surface, it increases until the center of the channel, where the maximum value is attained, and then gradually drops back to zero in a symmetrical fashion. Finally, the streamlines are nearly identical for both cases. Structures appearing in non-linear flows, such as vortices, are absent here for all cases. It is confirmed that the impermeability condition is always satisfied, producing completely horizontal lines inside the channel even for the demanding case of the relatively long channel with $L/L_0 = 10$. Since the streamlines are nearly identical for all cases considered here, they are not shown in the comparisons further below. Due to these common characteristics, conclusions on the dependence of the flow field on various characteristics are the same for both geometries and are presented below for just one of them each time.

The effect of changing the plate channel length is examined for a constant rarefaction parameter $\delta = 1$ by comparing Figures 4.8 - 4.10 (up) for $L/L_0 = 0$, Figure 4.14 for $L/L_0 = 2$, and Figure 4.15 for $L/L_0 = 10$. The pressure distribution around the channel ends gradually becomes closer to the container values as the length increases, i.e. the pressure contour coloring at each container is more uniform in Figure 4.15. This happens because the area of the reservoirs affected by the channel

flow is smaller for longer channels, due to the smaller induced gas velocities. The axial velocity is significantly reduced for longer tubes and seems to obtain a developed profile as we move inside the channel away from its ends. The end influence on the velocity profile seems to fade away around one unit of dimensionless length inside the channel for $L/L_0 = 10$ and $\delta = 1$.

The influence of δ is shown in Figures 4.16 and 4.17 for a cylindrical tube of $L/L_0 = 2$ and $\delta = 0.1, 1$ and 10 . No significant changes occur for pressure for this length, besides a slightly larger deviation of pressure in the containers from the equilibrium values as δ is increased. The axial velocity values are also increased along with δ but no other significant differences occur. Similar conclusions can be drawn for a cylindrical tube of $L/L_0 = 5$ and the same δ values, shown in Figures 4.18 and 4.19. The velocity profile in this case seems to develop to a nearly constant profile inside the channel for $\delta = 10$, which implies that the end effect treatment, discussed in detail in the next subsection, may be applied under these conditions to provide results with decent accuracy while avoiding the complete solution of the problem. For smaller δ or shorter channels, the fully developed flow characteristics are not so strong.

The axial distribution of pressure is shown in Figure 4.20 for several values of L/L_0 and δ and for both geometries. It is seen that the profiles are quite similar at all cases shown here and nearly linear inside the channel. This is reasonable since the pressure gradient is small and the hypotheses of fully developed flow are practically fulfilled. The differences are mostly located in the gradient of pressure, determining the flow rate. There are larger discrepancies for the parallel plate channel and qualitative differences appear for large length ratios: it can be observed that for a small value of the rarefaction parameter ($\delta = 0.1$), the profile is not linear due to the channel end effect, in contrast to $\delta = 10$ where the effect of the finite length fades away in short distance from the channel ends.

4.5.3 Investigation of the end effect

The fictional length increments ΔL , which are equal to the pressure perturbation found in the end geometry as shown before, provide the extra “effective” length and are shown in Table 4.8 for various rarefaction levels. It is seen that its value becomes smaller for larger δ , showing that the end effect is more important for highly rarefied flows. The decrease in ΔL is also steeper for small δ . Furthermore, we observe that the effective length decreases with a smaller slope for the cylindrical case, in comparison to the parallel plate geometry. A comparison to the values previously obtained by an approximate solution in reference [45] is also provided. The authors consider the complete channel geometry by an integral method and match the ΔL constant to fit their results. However, there are significant deviations due to the different formulation of the two problems and different discretization/geometric parameters L_{dev} , L_{right} used in the reference.

The absolute value of the density perturbation at the center of the channel ($x_2 = 0$) is shown in Figure 4.21 for $\delta = 0.2, 1$ and 10 . The most striking feature is the fact that the density perturbation is practically constant along the x_1 axis as $x_1 \rightarrow -L_{dev}$. Since the temperature variation is very small in this isothermal problem, it is seen that $\rho \simeq p$. Therefore, the constant trend of the density perturbation obtained after some point in the channel is a direct consequence of the linearity of the pressure profile for long channels and our reference pressure selection. A larger developing length is observed when the rarefaction parameter is low. It is also seen that density and temperature perturbations are nearly zero at the reservoir boundaries, since the reference conditions prevail there.

A part of the density perturbation field is also plotted in Figure 4.22 for some representative values of δ , namely $\delta = 0.2, 1, 10$. In this two-dimensional plot, it can be seen that the density perturbation progressively becomes constant along each cross section as we move far from the channel end. Furthermore, for highly rarefied conditions the expansion structure spans to a larger area inside the container in fact in the longitudinal direction. This seems to have some connection with the molecular beaming phenomenon, since the number of particles arriving at the outlet container with an almost completely axial velocity should increase when fewer inter-molecular collisions occur. As δ increases,

this phenomenon is reduced and the number density field is affected in a smaller area of the container, also producing more round isolines. The dimensionless horizontal velocity u_x also displays a nearly developed velocity profile at the left end of the channel, which coincides with the solution of the fully developed problem at the inlet cross-section. The maximum value of the macroscopic velocity also seems to behave according to the Knudsen minimum, taking its smallest value around $\delta = 1$. Comments on the expansion structure given before are also valid here: a smaller area is influenced for flows near the hydrodynamic regime.

An application of the end geometry results is presented here for the case of flow through a moderately long cylindrical tube. An identical procedure may be applied for the plane geometry if needed. According to Equations (4.68) and (4.64), the mass flow rate using fully developed flow results is

$$\dot{M}_{FD} = -\frac{\pi R^3}{v_0} \frac{\Delta P}{L} G_{FD} \left(\frac{\delta_{in} + \delta_{out}}{2} \right) \quad (4.73)$$

and using the end effect treatment (4.70), it becomes

$$\dot{M}_{EE} = -\frac{\pi R^3}{v_0} \frac{\Delta P}{L + \Delta L_{in} + \Delta L_{out}} G_{FD} \left(\frac{\delta_{in} + \delta_{out}}{2} \right) \quad (4.74)$$

When the complete geometry is considered in the simulation, the mass flow rate is found by Equation (4.36)

$$\dot{M}_{LIN} = \Delta P \frac{4\pi R^2}{v_0} G_{LIN} \quad (4.75)$$

for the linearized formulation and

$$\dot{M}_{NL} = P_0 \frac{4\pi R^2}{v_0} G_{NL} \quad (4.76)$$

for the non-linear one, given in detail in Chapter 6. It is expected that the ratio of mass flow rates, using complete simulation and typical integration with/without end effects, should approach unity as the tube length increases. These ratio values are given in Table 4.9 for a variety of flow conditions. It is seen that the maximum discrepancy for the end effect treatment (1%) occurs for highly rarefied conditions ($\delta = 0.2$). This is due to the fact that the tube is quite short in comparison to the development length required to achieve a constant pressure perturbation, as seen in Figure 4.21. However, as δ obtains

values over unity, we observe that the discrepancies drop significantly for the end effect treatment (less than 1 % at all cases examined here), in comparison to the fully developed flow simulation (up to 7-19 %). The lowest discrepancies are found for the extra cases of $L/R = 20$, executed in the complete geometry to enhance our trust on this methodology. It is seen that discrepancies in this case drop for both methods and we reach the conclusion that errors below 1% may be obtained by the end effect simulation if $\delta \geq 1$ and $L/R \geq 20$ are considered. Finally, some non-linear runs with $L/R = 20$ and a pressure ratio $\hat{P}_{out}/\hat{P}_{in} = 0.5$ are included in Table 4.10. Since the values $\delta = 0.5, 5$, needed for the outlet part fictional length ΔL_{out} are not included in our calculations, a simple linear interpolation is used in the values of Table 4.8. Even though this approach contains some error, it is seen that the agreement is still much better than the corresponding value obtained by fully developed flow simulations.

A comparison in terms of the axial pressure distribution is also shown in Figure 4.23 for the linearized and in Figure 4.24 for the non-linear formulation and $\hat{P}_{out}/\hat{P}_{in} = 0.5$. These have been obtained by adjusting the channel length according to the fictional “effective length” increments, before and after the real channel, and applying the integration procedure. It is seen that at all cases, the curves of the complete and end effect simulations are very close to each other except the areas very close to the channel ends. On the other hand, the typical integration curve always provides a larger pressure gradient.

At all cases examined here, the end effect approach seems to provide results of higher accuracy. Furthermore, from Figures 4.23 and 4.24, it is reasonable to infer that discrepancies are greatly reduced as the length is increased, since the gradients of all three solutions must become indistinguishable as the length tends to infinity. Thus, we can conclude that including the effective length in the typical integration scheme should greatly enhance the accuracy of results for relatively short to moderately long channels, especially for large δ , and it could also benefit highly rarefied flows for long channels.

4.6 Concluding remarks

In this Chapter, we have investigated flow through two channel geometries, namely a rectangular and a cylindrical channel, due to a small pressure difference by the linearized BGK model. A highly efficient memory storage scheme and the algorithm parallelization have been described. We have found very good agreement with non-linear results and some disagreement with DSMC due to its computational restrictions in the low pressure difference regime. The corresponding fields of pressure, axial velocity, streamlines, as well as the axial distributions of pressure have been discussed. Moreover, the end effect for channels of moderate to large length ratios has been considered and compared with fully developed flow simulations and the complete simulation. It has been found that this approach offers significant improvements over previous methodologies, allowing the usage of the typical integration scheme to model short to moderately long channels with a maximum error of 2% instead of simulating the complete channel, and the corresponding values given here can be used in practical applications with minimal computational effort.

Table 4.1: Discretized equation for the tube end geometry problem

$$\begin{aligned}
& \frac{c_p^l \cos \theta_j}{4\Delta r_i} \left(h_{i+,j+,k+}^{(l,m)} + h_{i+,j-,k+}^{(l,m)} - h_{i-,j+,k+}^{(l,m)} - h_{i-,j-,k+}^{(l,m)} \right. \\
& \quad \left. + h_{i+,j+,k-}^{(l,m)} + h_{i+,j-,k-}^{(l,m)} - h_{i-,j+,k-}^{(l,m)} - h_{i-,j-,k-}^{(l,m)} \right) \\
& - \frac{c_p^l \sin \theta_j}{4\Delta \theta_j} \left[\frac{1}{r_{i+}} \left(h_{i+,j+,k+}^{(l,m)} - h_{i+,j-,k+}^{(l,m)} + h_{i+,j+,k-}^{(l,m)} - h_{i+,j-,k-}^{(l,m)} \right) \right. \\
& \quad \left. + \frac{1}{r_{i-}} \left(h_{i-,j+,k+}^{(l,m)} - h_{i-,j-,k+}^{(l,m)} + h_{i-,j+,k-}^{(l,m)} - h_{i-,j-,k-}^{(l,m)} \right) \right] \\
& + \frac{c_x^m}{4\Delta x_k} \left(h_{i+,j+,k+}^{(l,m)} + h_{i+,j-,k+}^{(l,m)} + h_{i-,j+,k+}^{(l,m)} + h_{i-,j-,k+}^{(l,m)} \right. \\
& \quad \left. - h_{i+,j+,k-}^{(l,m)} - h_{i+,j-,k-}^{(l,m)} - h_{i-,j+,k-}^{(l,m)} - h_{i-,j-,k-}^{(l,m)} \right) \\
& + \frac{\delta}{8} \left(h_{i+,j+,k+}^{(l,m)} + h_{i+,j-,k+}^{(l,m)} + h_{i-,j+,k+}^{(l,m)} + h_{i-,j-,k+}^{(l,m)} \right. \\
& \quad \left. + h_{i+,j+,k-}^{(l,m)} + h_{i+,j-,k-}^{(l,m)} + h_{i-,j+,k-}^{(l,m)} + h_{i-,j-,k-}^{(l,m)} \right) \\
& = \frac{\delta}{4} \{ (\rho_{i+,k+} + \rho_{i-,k+} + \rho_{i+,k-} + \rho_{i-,k-}) \\
& + \left[(c_p^l)^2 + (c_z^m)^2 - \frac{3}{2} \right] (\tau_{i+,k+} + \tau_{i-,k+} + \tau_{i+,k-} + \tau_{i-,k-}) \\
& + 2c_p^l \cos \theta_j (u_{r,i+,k+} + u_{r,i-,k+} + u_{r,i+,k-} + u_{r,i-,k-}) \\
& + 2c_x^m (u_{x,i+,k+} + u_{x,i-,k+} + u_{x,i+,k-} + u_{x,i-,k-}) \} - g_{tb}(x_k, c_x^m)
\end{aligned}$$

Table 4.2: Geometric parameters for the end geometry

δ	0.2	0.4	1	2	4	8	10
L_{dev}/L_0	60	50	40	30	30	20	20
L_{right}/L_0	10	10	12	12	15	15	15

Table 4.3: Numerical parameters used in the simulations

Parameters	Channel	Tube
Nodes / unit length in dense areas ($N_x = N_y = N_r$)	150 – 200	150 – 200
Grid non-uniformity parameter (η)	10^{-2} - 10^{-3}	10^{-2} - 10^{-3}
Discrete angles (N_θ) in $(0, 2\pi)$	250 – 400	300 – 400
Discrete magnitudes M	16 – 20	16×16
Max. value of velocity magnitude (c_{max})	4 – 5	5
Convergence criterion	10^{-8} - 10^{-9}	10^{-8} - 10^{-9}

Table 4.4: Dimensionless flow rate W for plate geometry and several δ and L/H values

		L/H					
		0	0.5	1	2	5	10
δ	0	0.999	0.802	0.682	0.541	0.356	0.240
	0.01	1.00	0.805	0.685	0.542	0.356	0.239
	0.1	1.05	0.837	0.709	0.556	0.356	0.231
	0.5	1.21	0.957	0.798	0.609	0.366	0.222
	1	1.40	1.09	0.894	0.666	0.383	0.225
	2	1.73	1.32	1.07	0.772	0.424	0.242
	5	2.67	1.97	1.54	1.07	0.561	0.313
	10	3.97	2.90	2.24	1.54	0.792	0.438

Table 4.5: Dimensionless flow rate W for tube geometry and several δ and L/R values

		L/R					
		0	0.5	1	2	5	10
δ	0	0.999	0.801	0.672	0.514	0.311	0.191
	0.01	1.00	0.805	0.675	0.516	0.311	0.191
	0.1	1.04	0.833	0.696	0.530	0.316	0.192
	0.5	1.19	0.947	0.786	0.589	0.341	0.201
	1	1.37	1.08	0.892	0.660	0.373	0.217
	2	1.72	1.35	1.10	0.799	0.440	0.251
	5	2.77	2.13	1.70	1.20	0.642	0.362
	10	4.35	3.32	2.63	1.86	0.988	0.554

Table 4.6: Dimensionless flow rate W with incomplete accommodation for the linearized tube problem

		L/R					
		0		1		10	
		$\alpha = 0.5$	$\alpha = 0.8$	$\alpha = 0.5$	$\alpha = 0.8$	$\alpha = 0.5$	$\alpha = 0.8$
δ	0	1.00	0.999	0.814	0.726	0.368	0.247
	0.1	1.04	1.04	0.840	0.751	0.368	0.247
	1	1.37	1.37	1.07	0.955	0.402	0.271
	10	4.35	4.35	3.03	2.76	0.786	0.617

Table 4.7: Dimensionless flow rate W obtained by DSMC in previous works

$\hat{P}_{out}/\hat{P}_{in}$		0.9 [149]	0.7 [152]				
L/R		0	0.5	1	2	5	10
δ	0	-	0.803	0.670	0.510	0.310	0.181
	0.1	1.03	0.820	0.683	0.520	0.310	-
	0.5	-	0.900	0.747	0.567	0.333	0.202
	1	1.30	1.00	0.830	0.633	0.353	-
	2	-	1.21	0.993	0.733	0.410	0.233
	5	-	1.80	1.47	1.06	0.580	-
	10	4.02	2.54	2.13	1.57	0.877	0.487

Table 4.8: Effective length increment values for the two geometries

δ		0.2	0.4	1	2	4	8	10
$\Delta L_{channel}$	Present work	2.15	1.55	1.05	0.827	0.654	0.574	0.556
	Table 35 in [45]	1.76	1.34	1.01	0.820	0.715	0.720	0.665
ΔL_{tube}	Present work	1.33	1.16	0.964	0.841	0.735	0.688	0.682

Table 4.9: Flow rate ratio for linear flow

	L/R	$\dot{M}_{FD}/\dot{M}_{LIN}$	$\dot{M}_{EE}/\dot{M}_{LIN}$	$\dot{M}_{FD}/\dot{M}_{EE}$
$\delta = 0.2$	10	1.28	1.01	1.27
$\delta = 1$	10	1.19	1.00	1.19
$\delta = 2$	10	1.17	1.00	1.17
$\delta = 10$	10	1.14	1.00	1.14
$\delta = 1$	20	1.10	1.00	1.10
$\delta = 10$	20	1.07	1.00	1.07

Table 4.10: Flow rate ratio for non-linear flow ($\hat{P}_{out}/\hat{P}_{in} = 0.5$)

	L/R	$\dot{M}_{FD}/\dot{M}_{NL}$	$\dot{M}_{EE}/\dot{M}_{NL}$	$\dot{M}_{FD}/\dot{M}_{EE}$
$\delta = 1$	20	1.08	0.978	1.10
$\delta = 10$	20	1.07	1.00	1.07

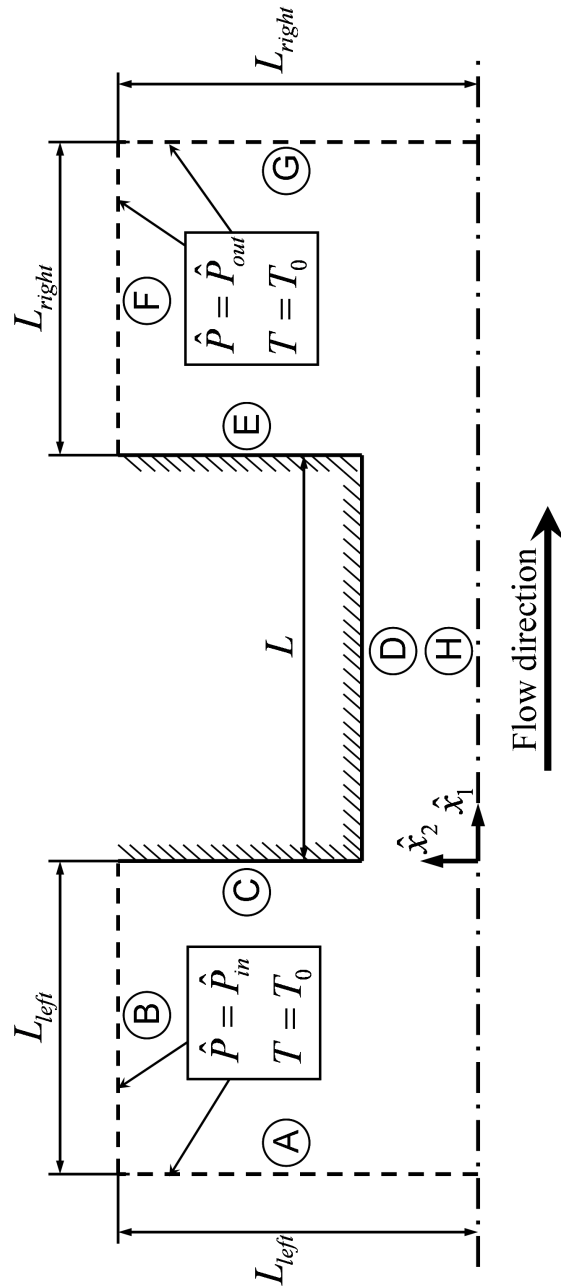


Figure 4.1: Flow configuration and coordinate system

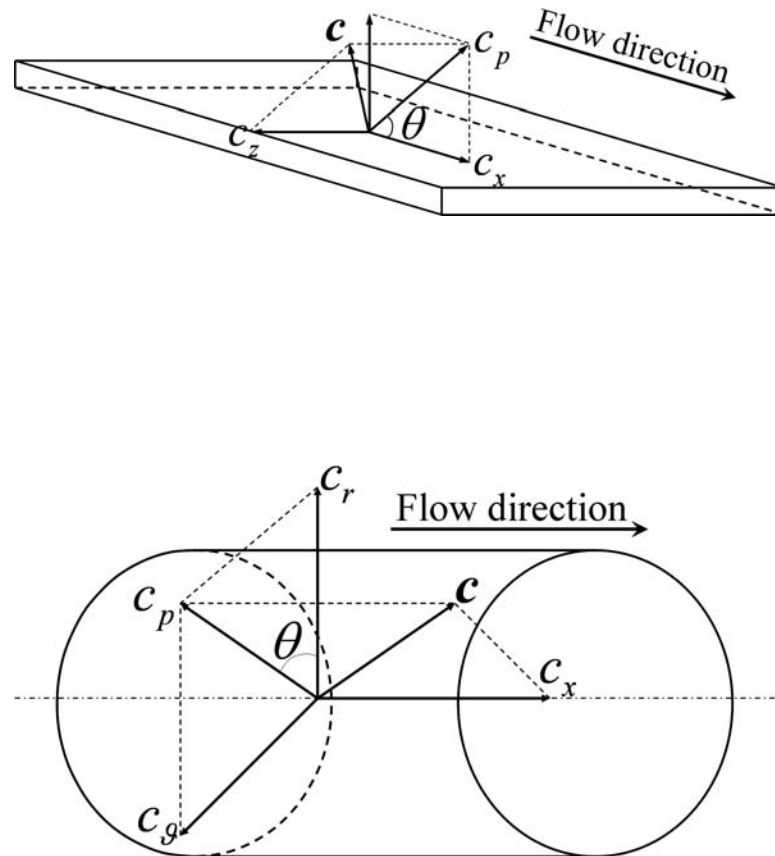


Figure 4.2: Velocity coordinate system for the parallel plates (left) and the tube (right)

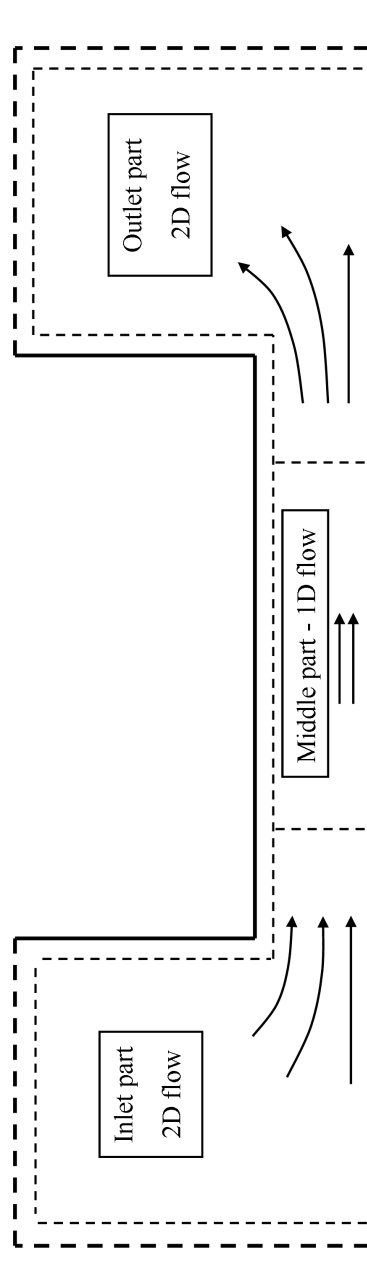


Figure 4.3: Division of the channel geometry into three parts

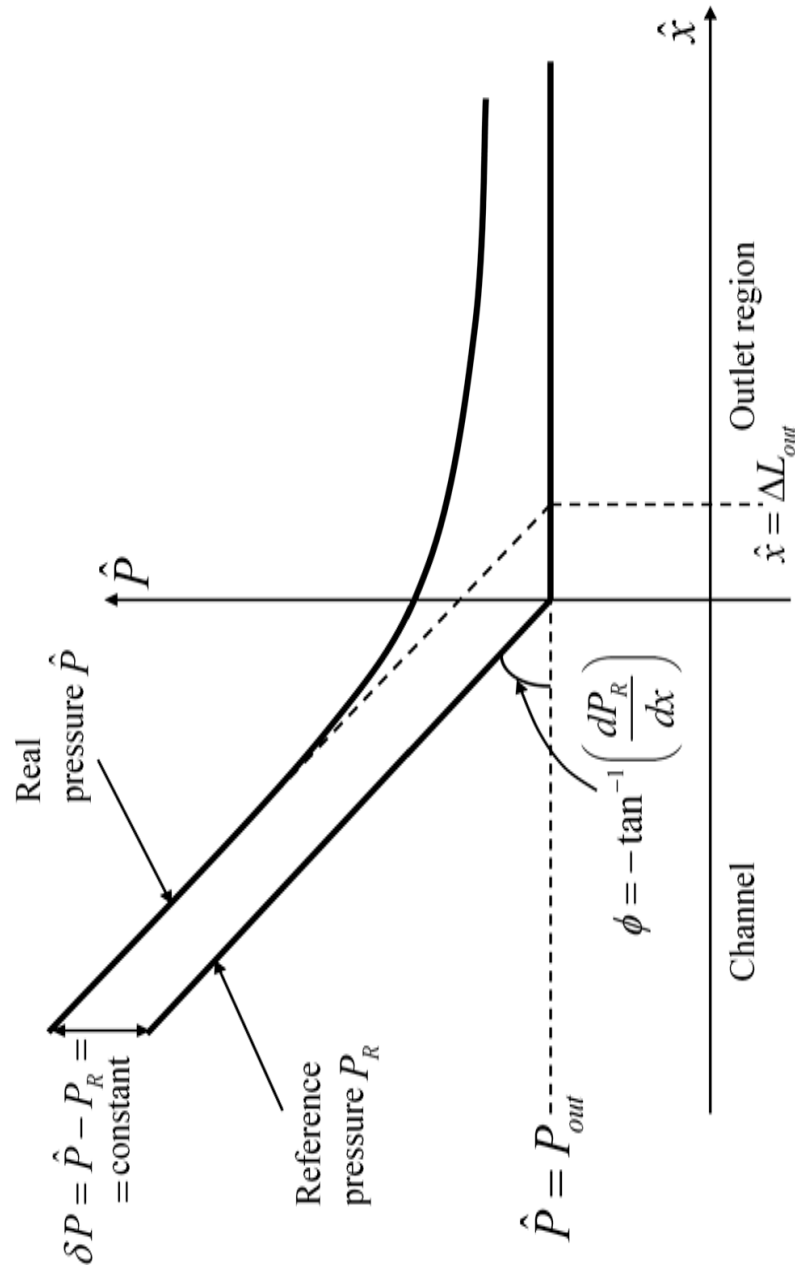


Figure 4.4: Indicative pressure distribution along the central axis at the outlet part to justify constant density perturbation

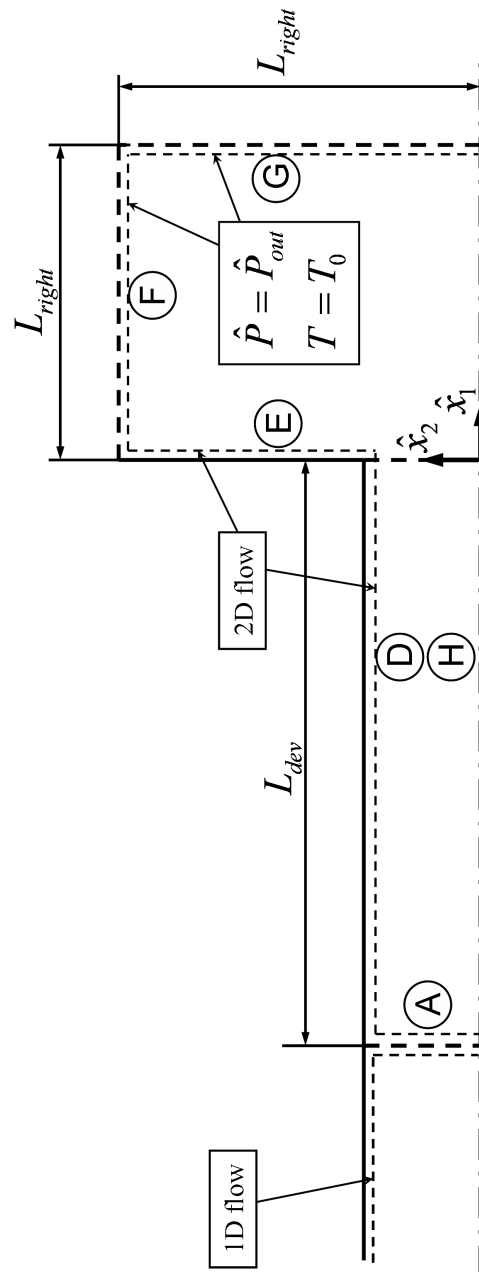


Figure 4.5: Flow configuration and coordinate system

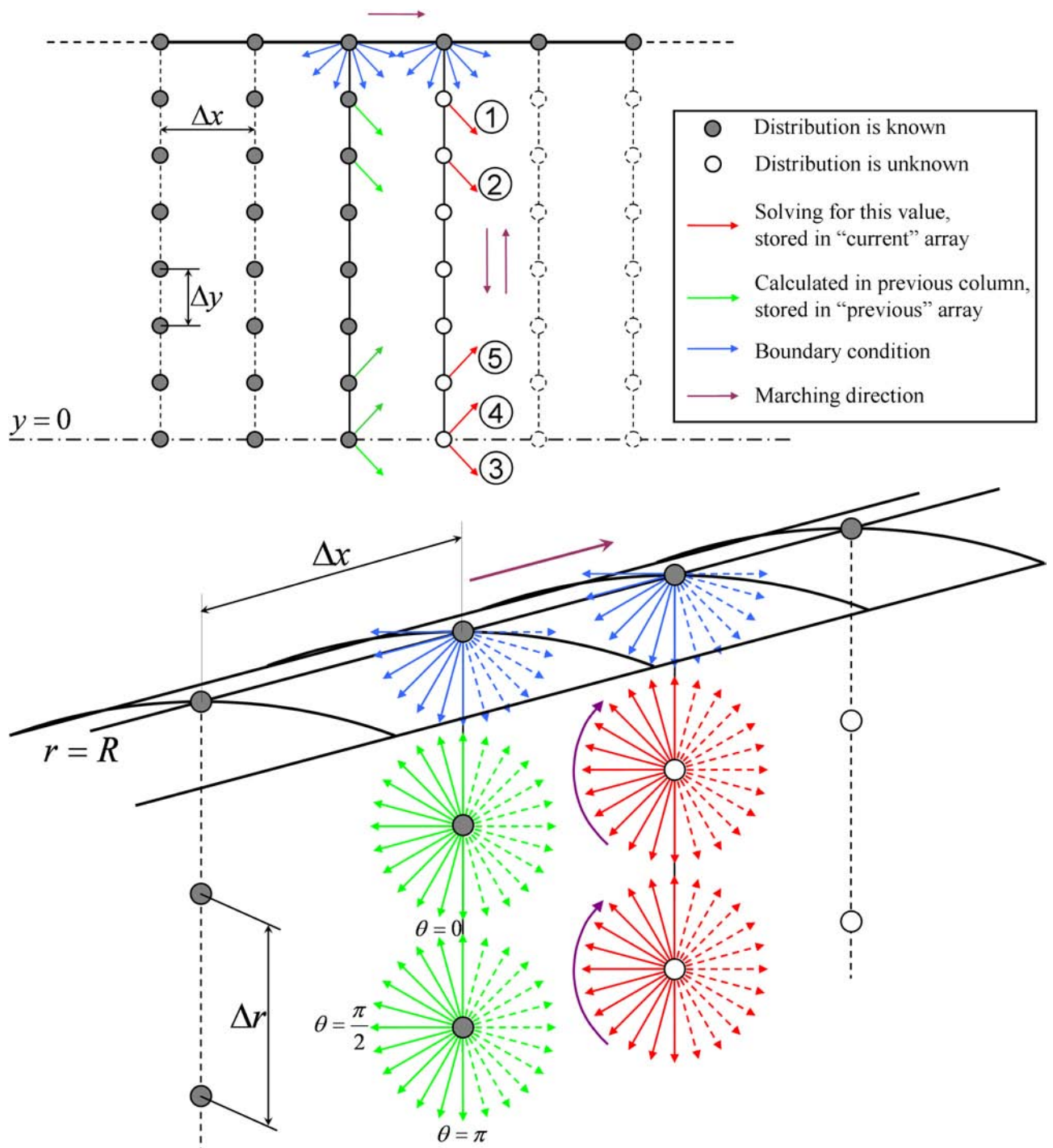


Figure 4.6: Schematic representation of the marching scheme for the channel (up) and tube (down)

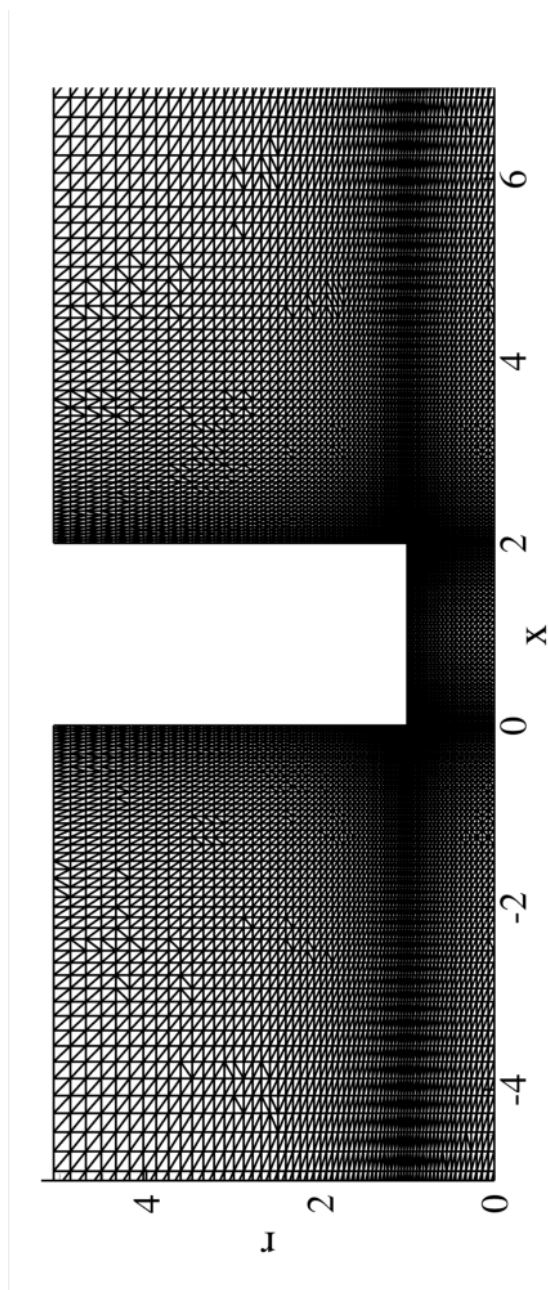


Figure 4.7: Non-uniform grid used in the numerical solution

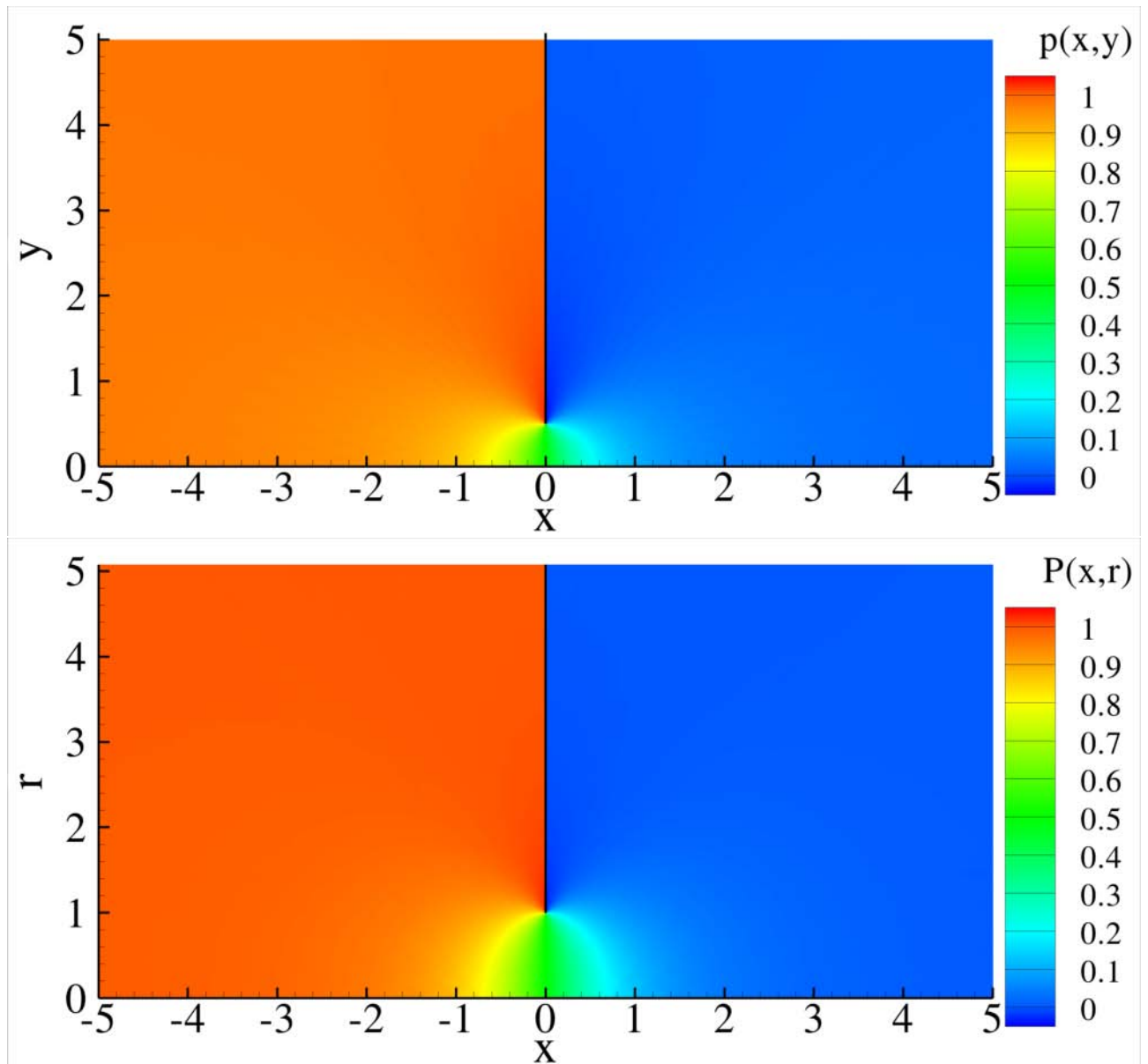


Figure 4.8: Pressure perturbation for the plate (up) and tube (down) geometry with $L/L_0 = 0$ and $\delta = 1$

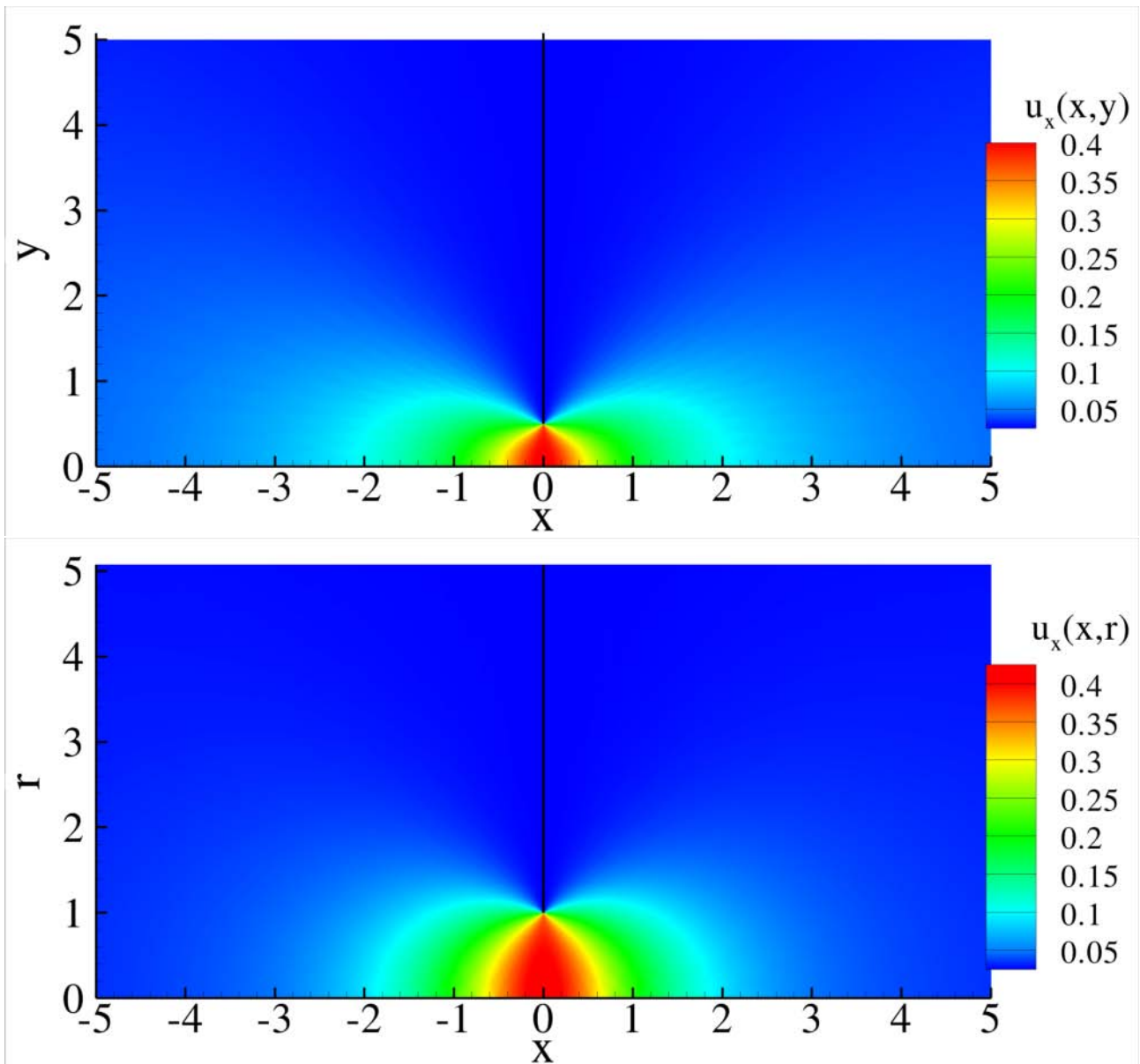


Figure 4.9: Axial velocity for the plate (up) and tube (down) geometry with $L/L_0 = 0$ and $\delta = 1$

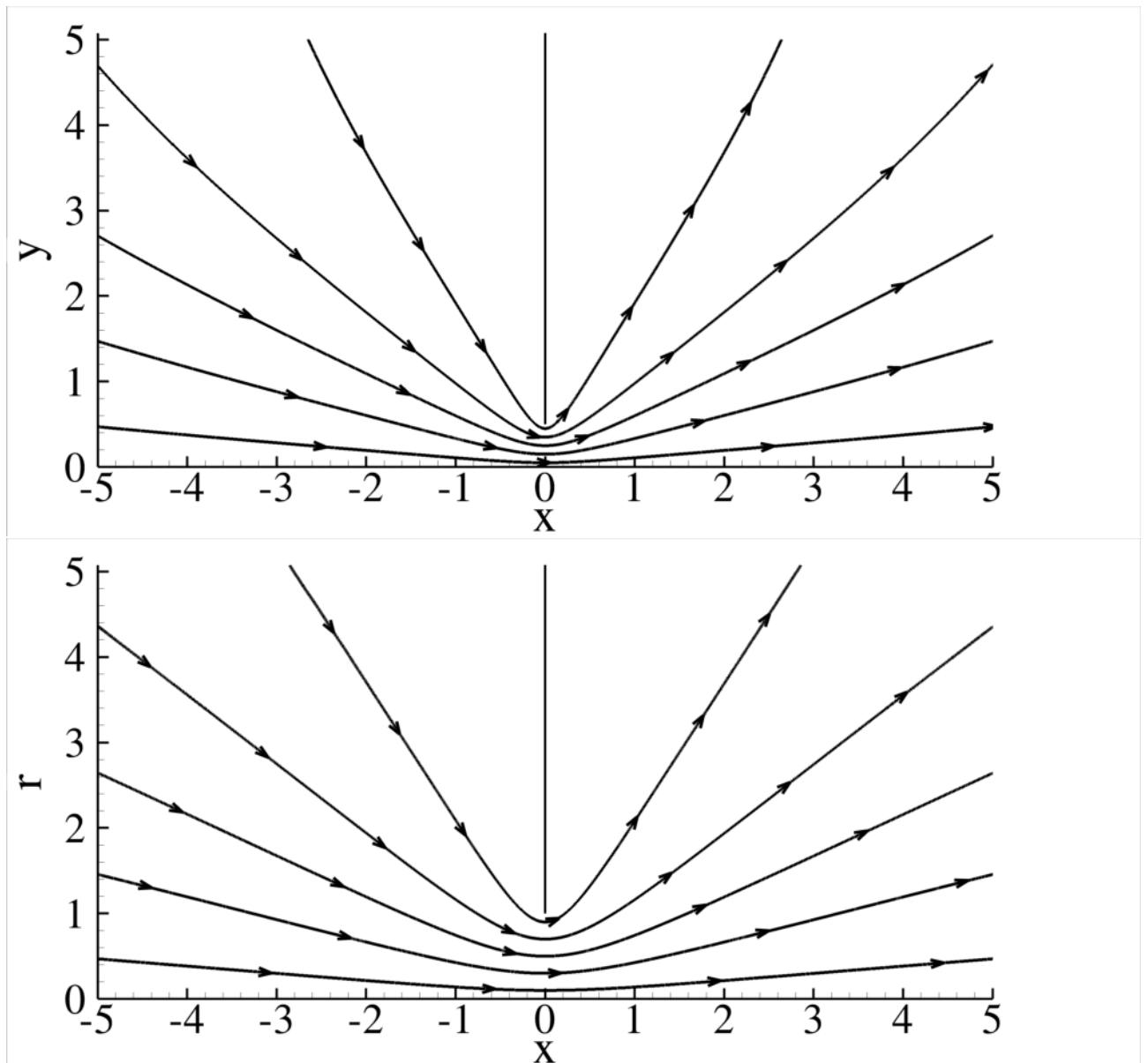


Figure 4.10: Streamlines for the plate (up) and tube (down) geometry with $L/L_0 = 0$ and $\delta = 1$

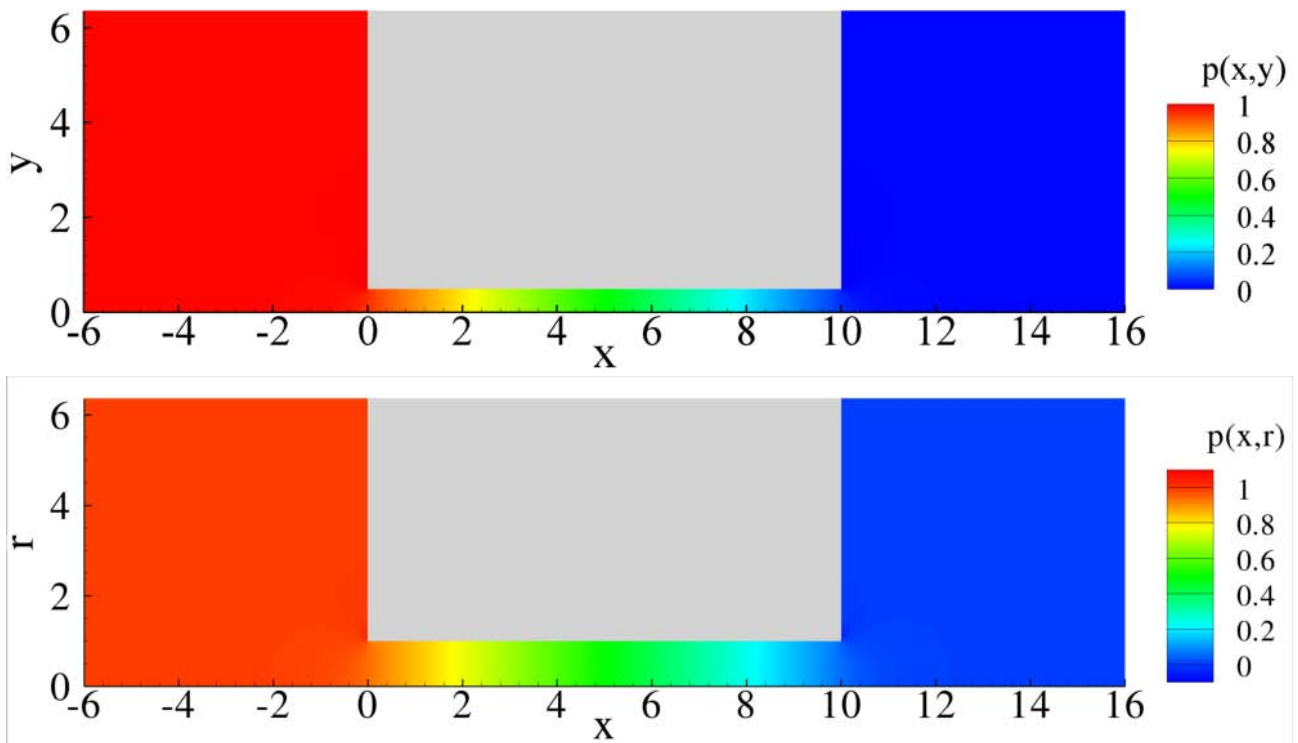


Figure 4.11: Pressure perturbation for the plate (up) and tube (down) geometry with $L/L_0 = 10$ and $\delta = 10$

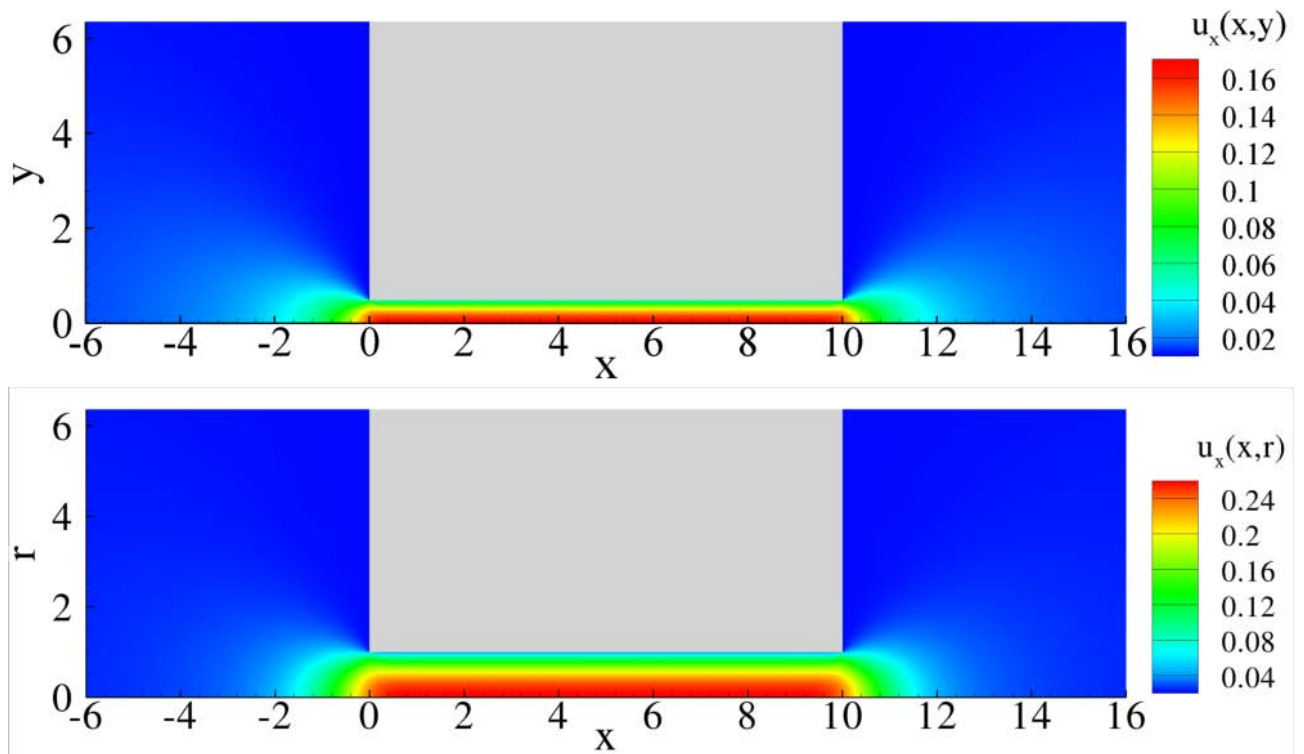


Figure 4.12: Axial velocity for the plate (up) and tube (down) geometry with $L/L_0 = 10$ and $\delta = 10$

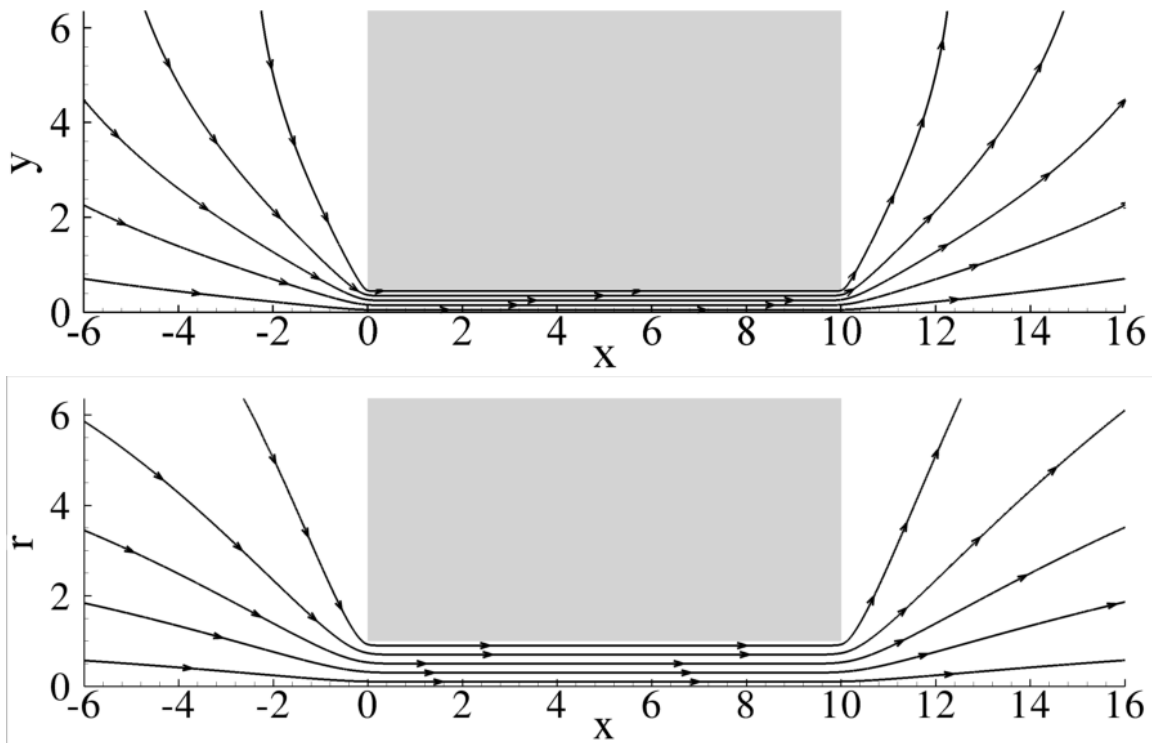


Figure 4.13: Streamlines for the plate (up) and tube (down) geometry with $L/L_0 = 10$ and $\delta = 10$

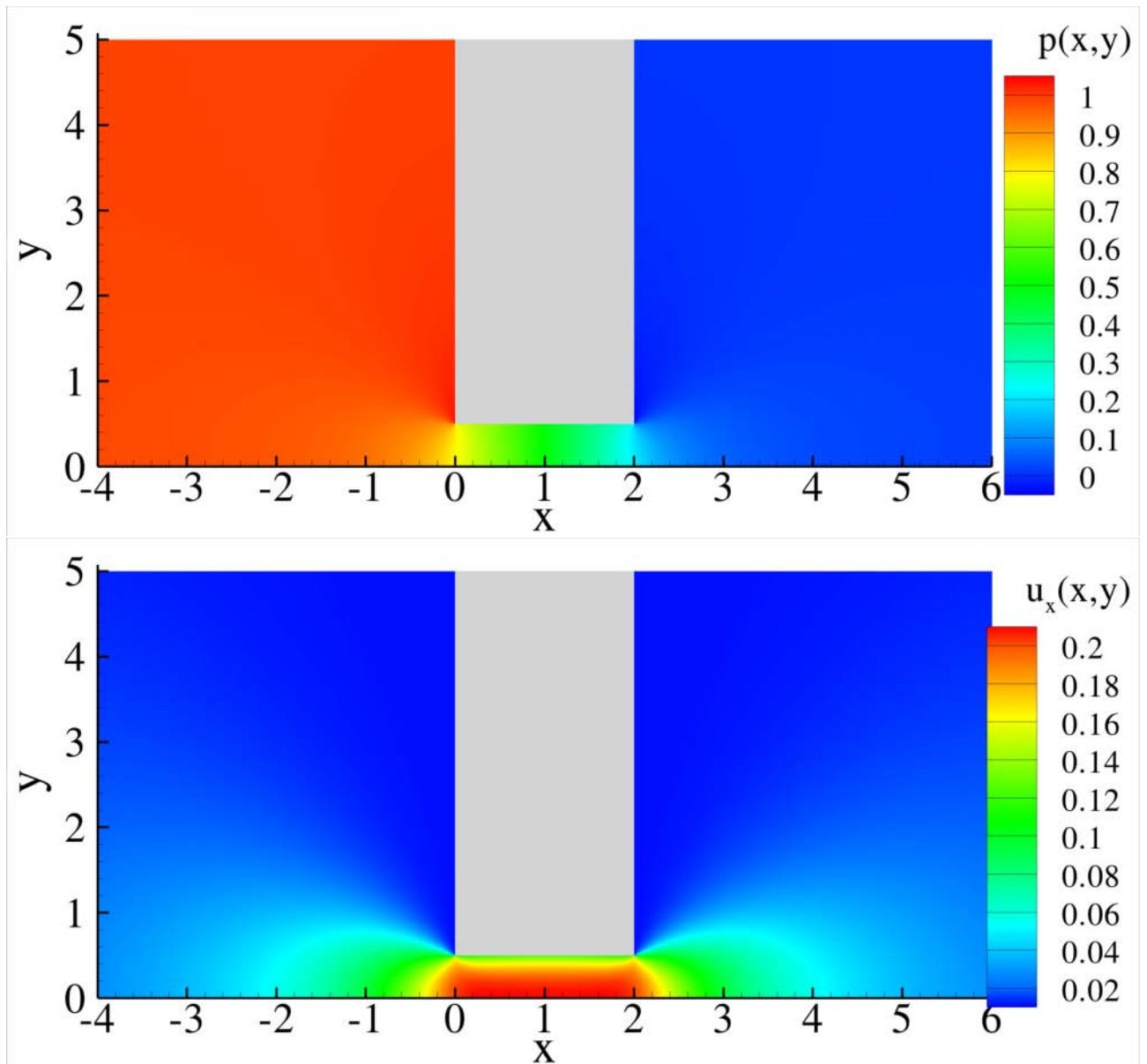


Figure 4.14: Pressure perturbation (up) and axial velocity (down) for the plate geometry with $L/H = 2$ and $\delta = 1$

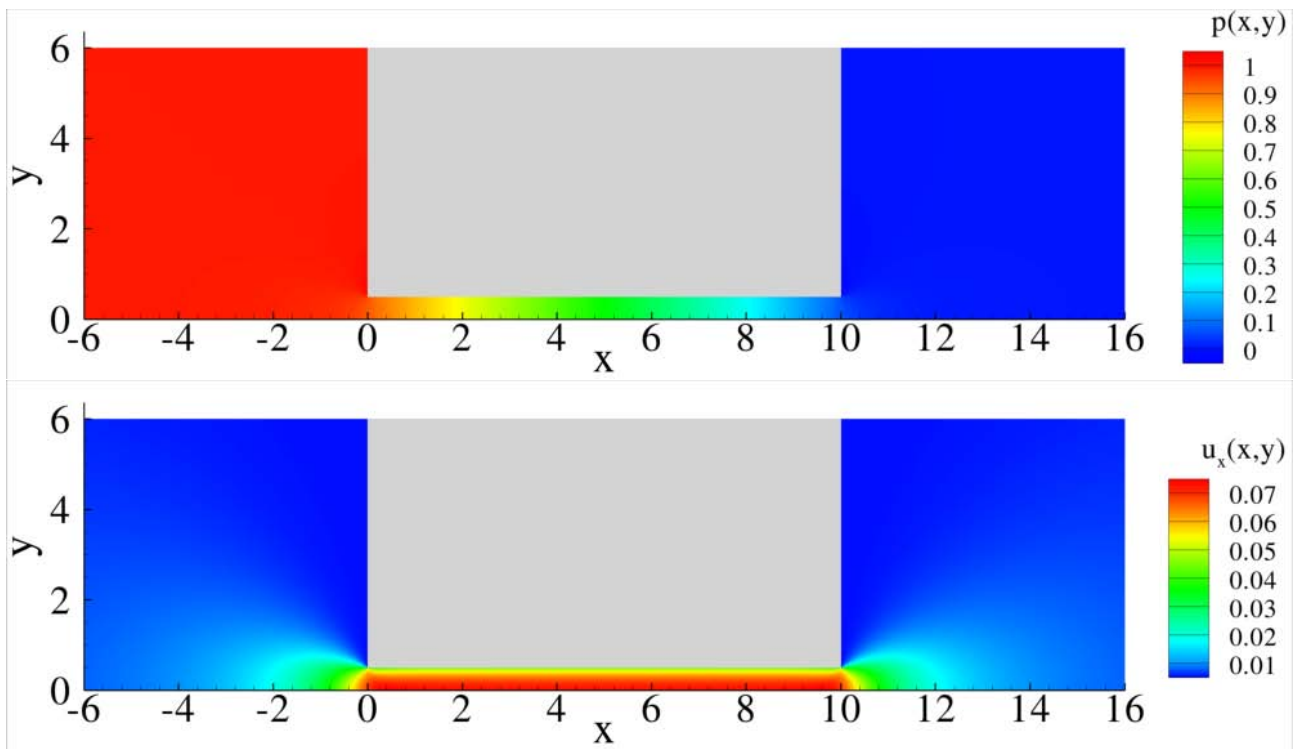


Figure 4.15: Pressure perturbation (up) and axial velocity (down) for the plate geometry with $L/H = 10$ and $\delta = 1$

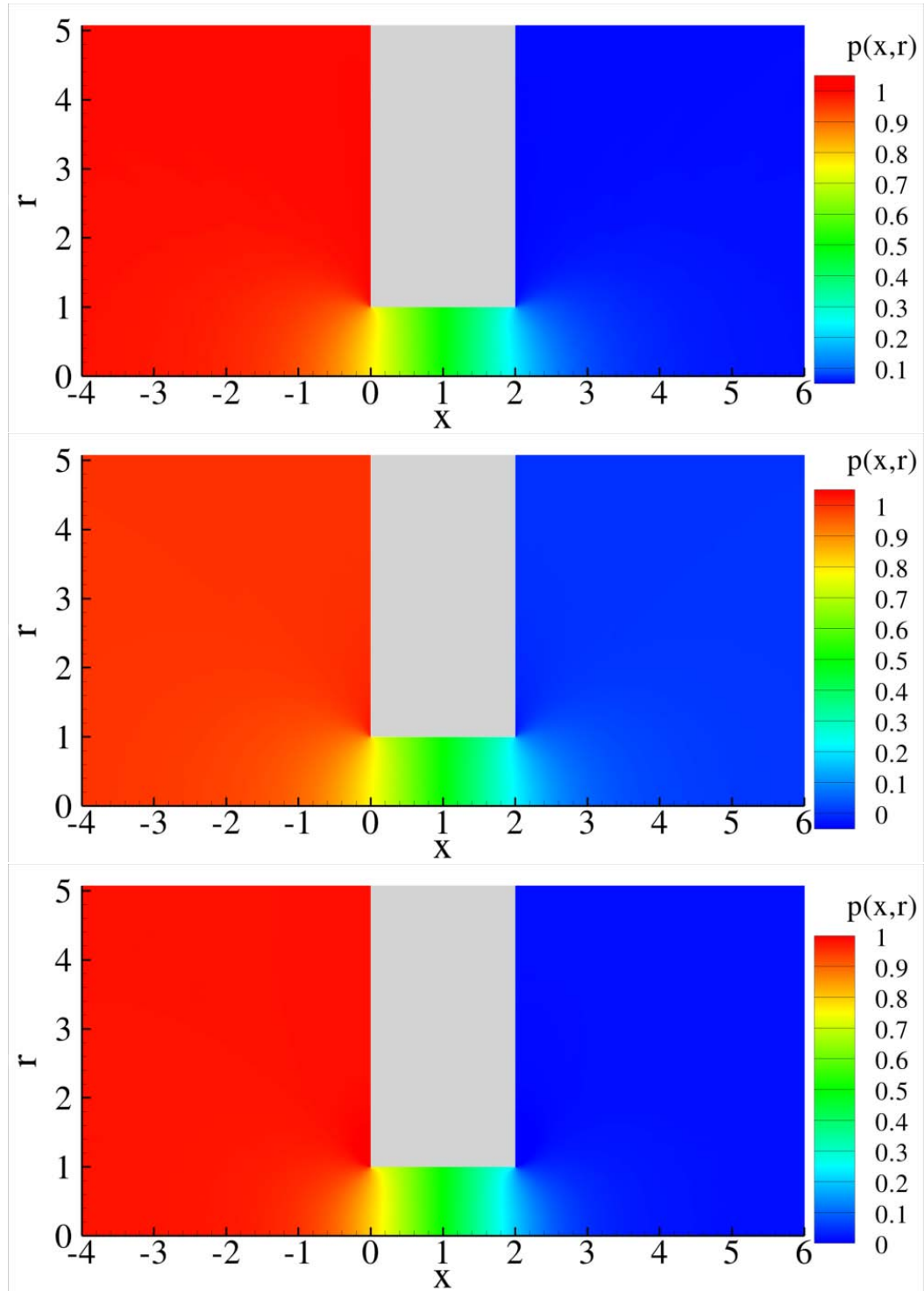


Figure 4.16: Pressure perturbation for the tube geometry with $L/L_0 = 2$ and $\delta = 0.1$ (up), $\delta = 1$ (middle), $\delta = 10$ (down)

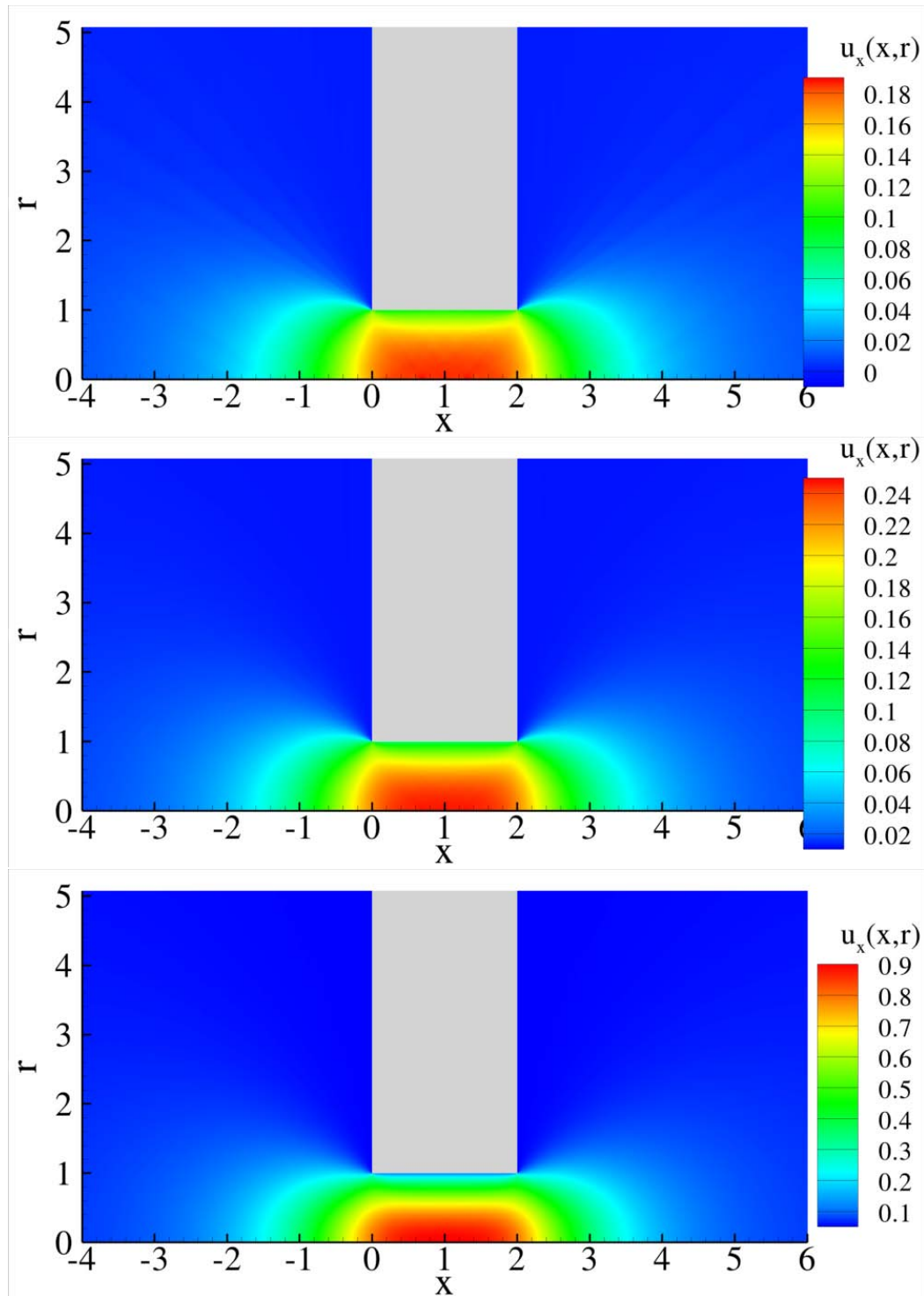


Figure 4.17: Axial velocity for the tube geometry with $L/L_0 = 2$ and $\delta = 0.1$ (up), $\delta = 1$ (middle), $\delta = 10$ (down)

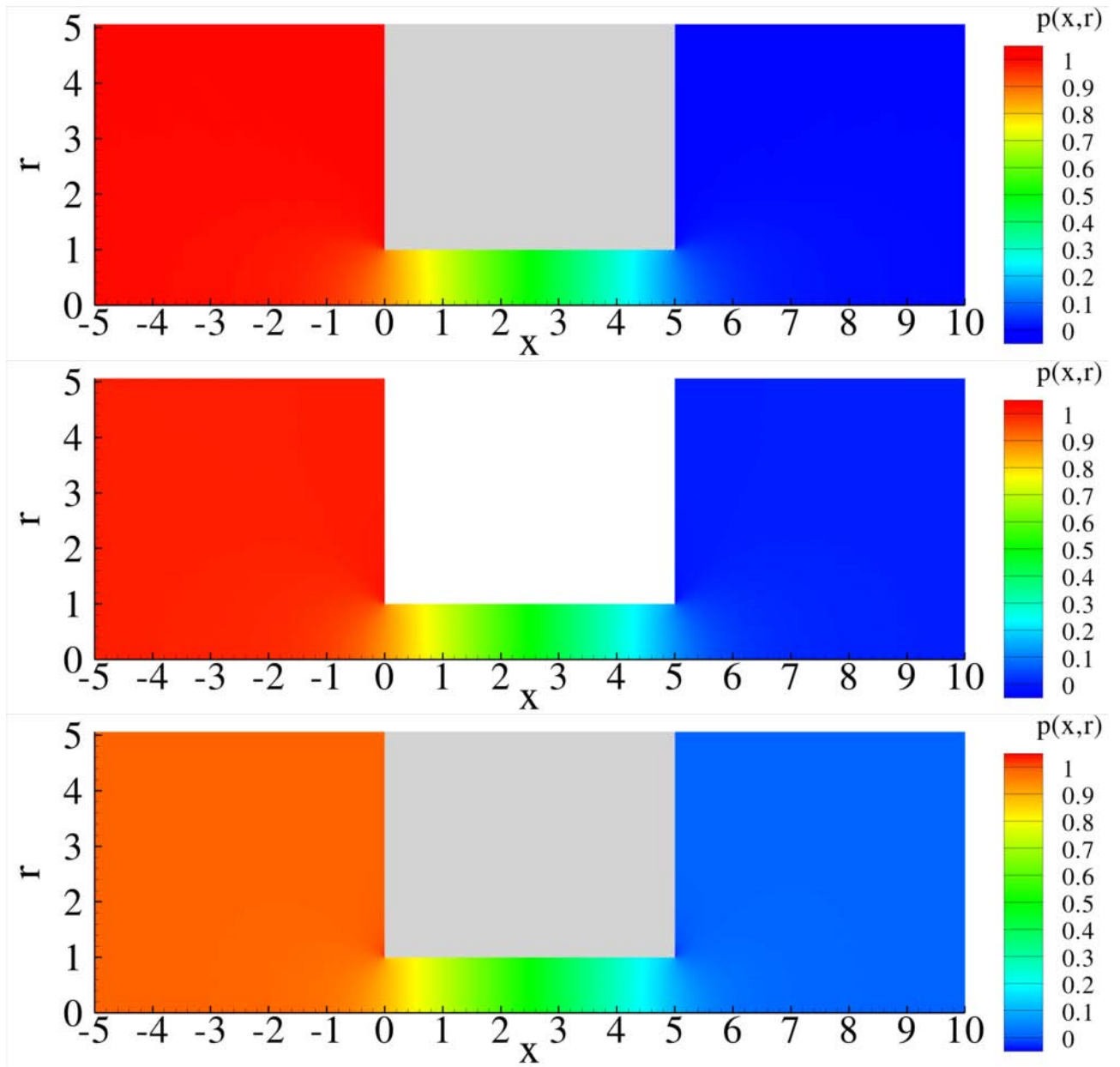


Figure 4.18: Pressure perturbation for the tube geometry with $L/L_0 = 5$ and $\delta = 0.1$ (up), $\delta = 1$ (middle), $\delta = 10$ (down)

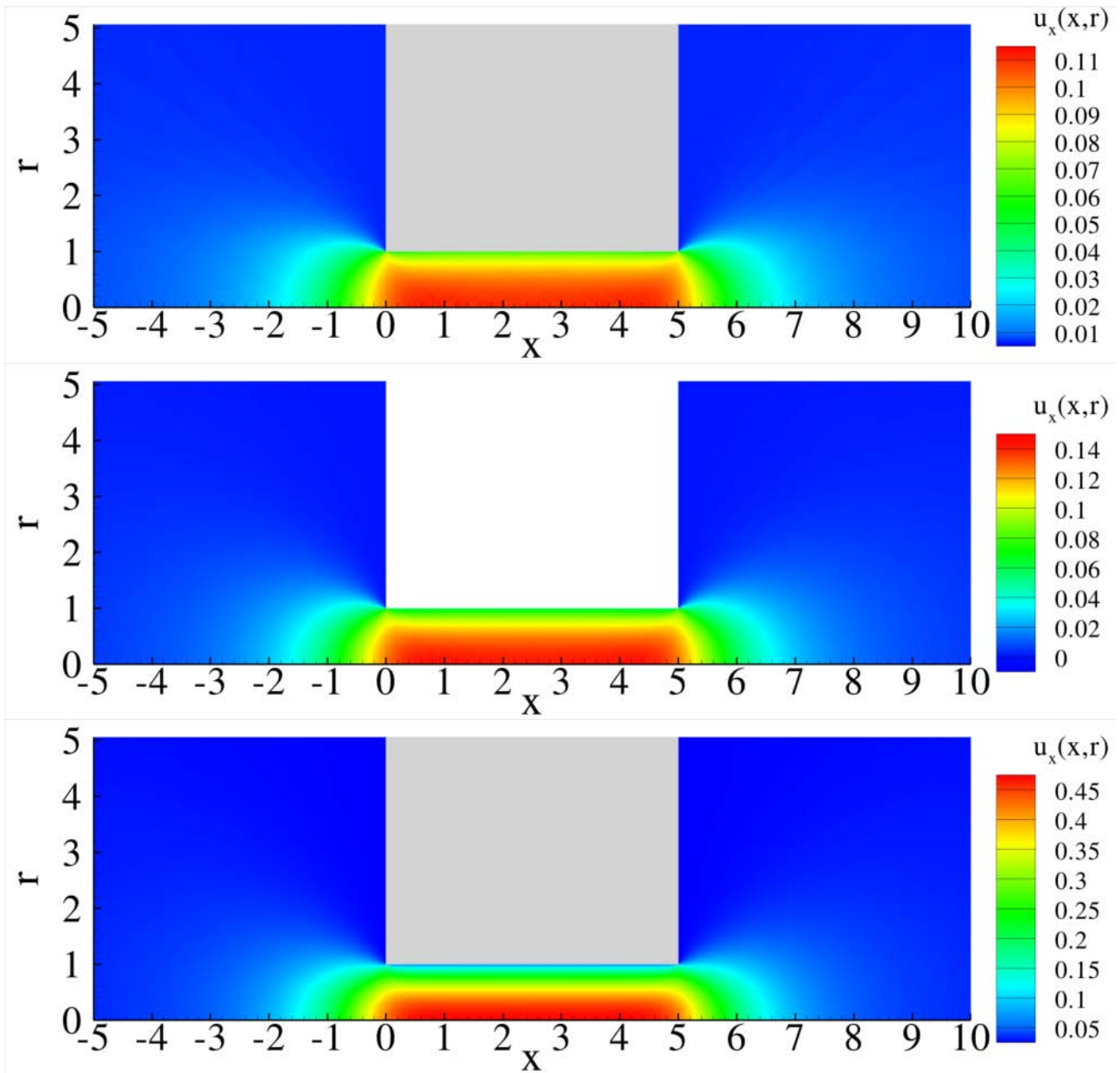


Figure 4.19: Axial velocity for the tube geometry with $L/L_0 = 5$ and $\delta = 0.1$ (up), $\delta = 1$ (middle), $\delta = 10$ (down)

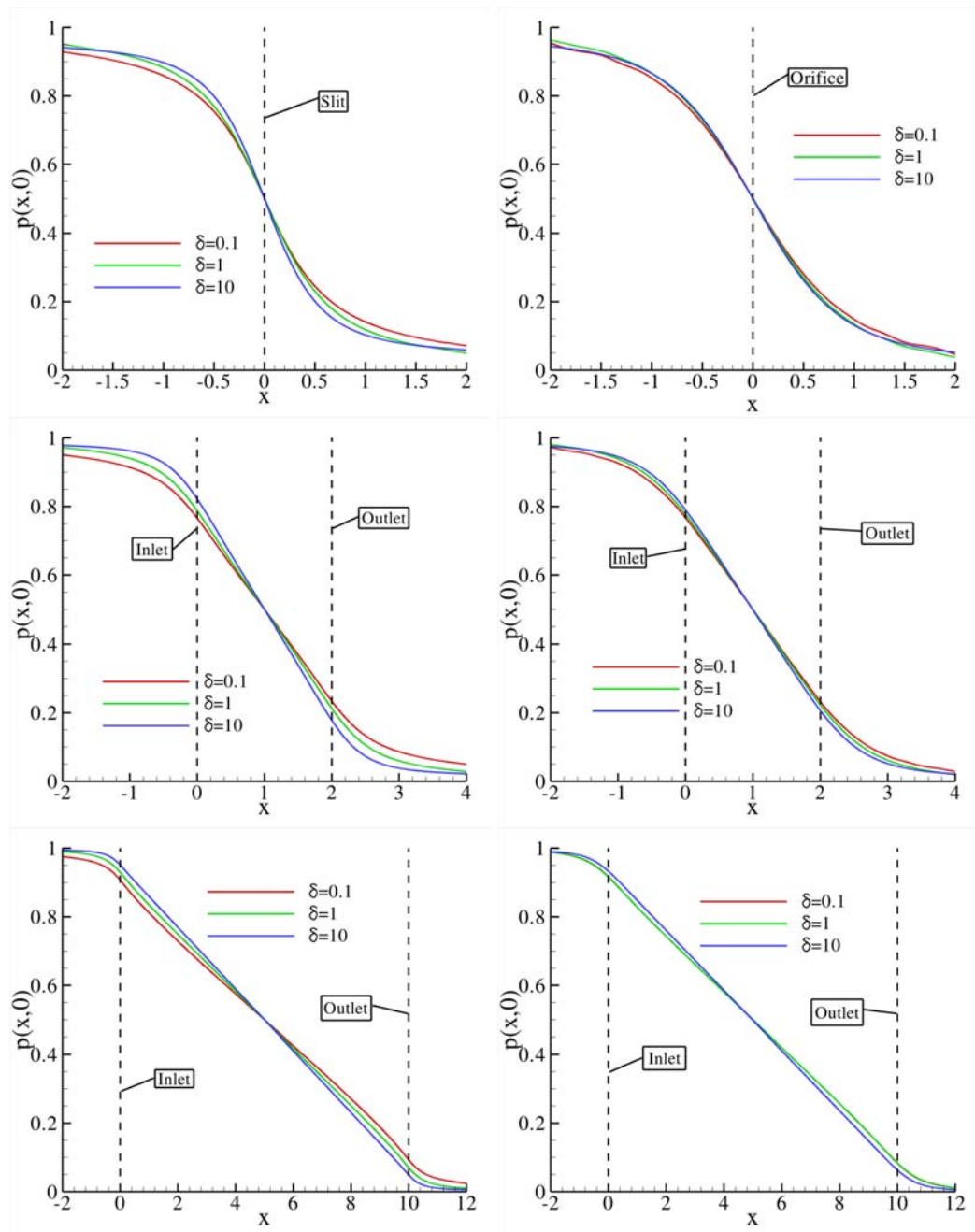


Figure 4.20: Pressure perturbation distribution at the symmetry axis for the plate (left) and tube (right) geometry with $L/L_0 = 0$ (up), $L/L_0 = 2$ (middle), $L/L_0 = 10$ (down)

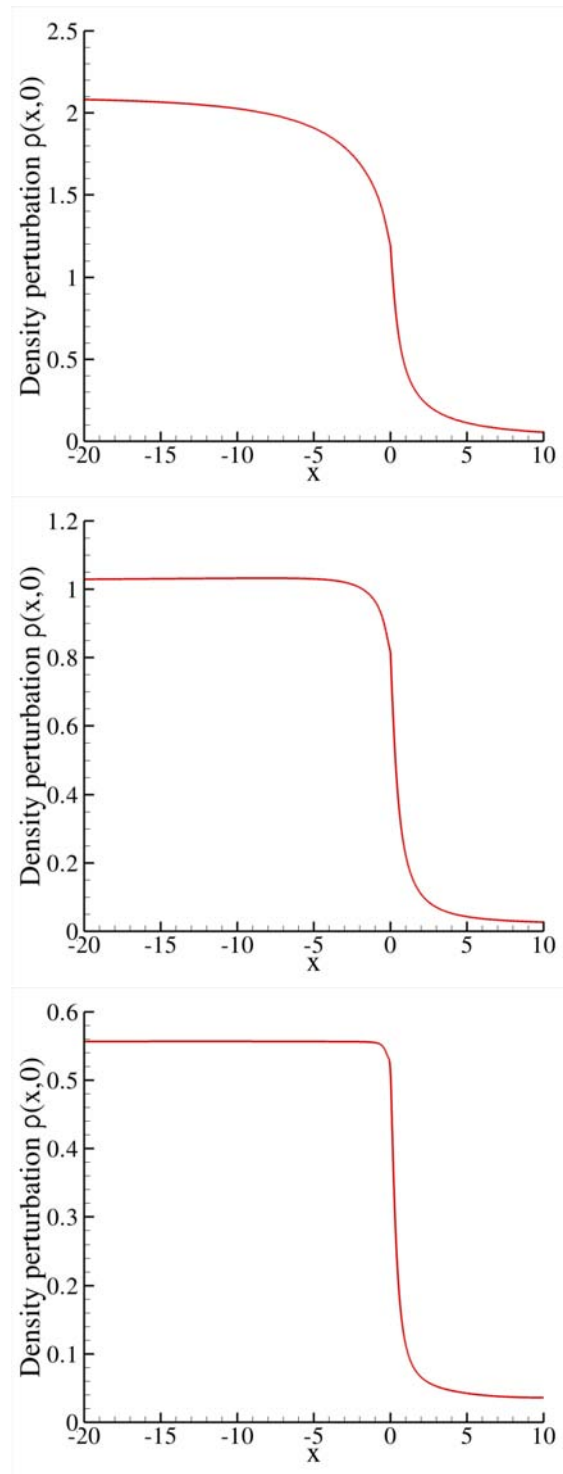


Figure 4.21: Density perturbation along the symmetry axis for the plate geometry and $\delta = 0.2$ (top), $\delta = 1$ (middle), $\delta = 10$ (bottom)

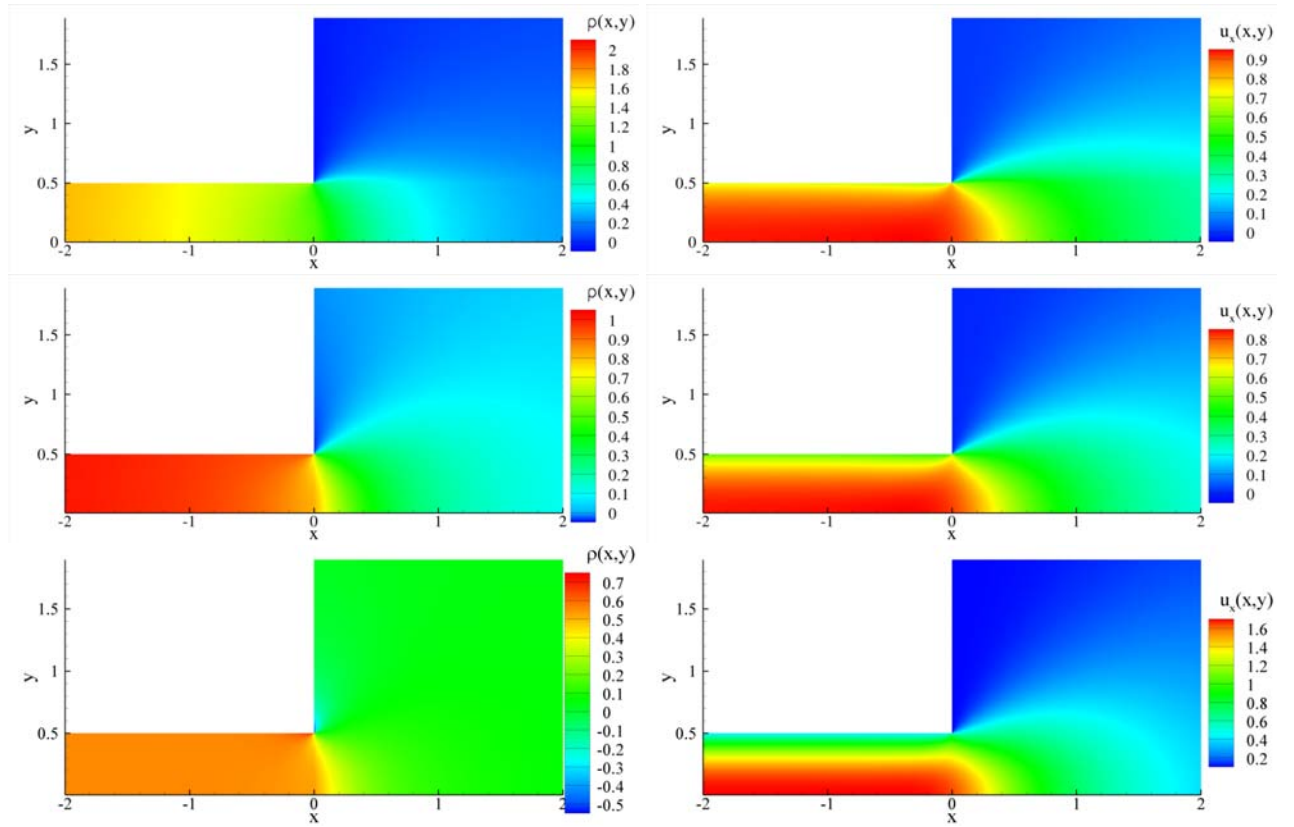


Figure 4.22: Density (left) and horizontal velocity (right) perturbation distributions for $\delta = 0.2$ (up), $\delta = 1$ (middle) and $\delta = 10$ (below)

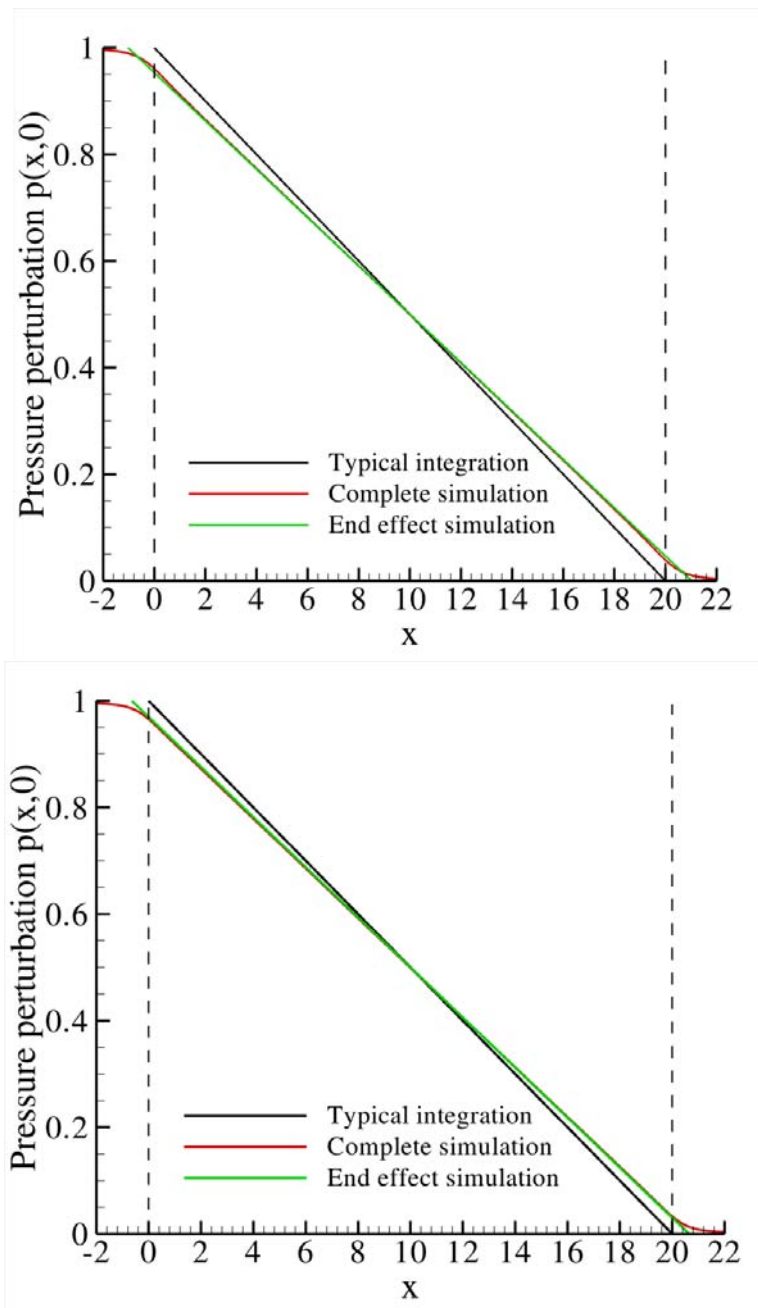


Figure 4.23: Comparison of results obtained by the end geometry formulation with linearized results for $\delta = 1$ (up) and $\delta = 10$ (down)

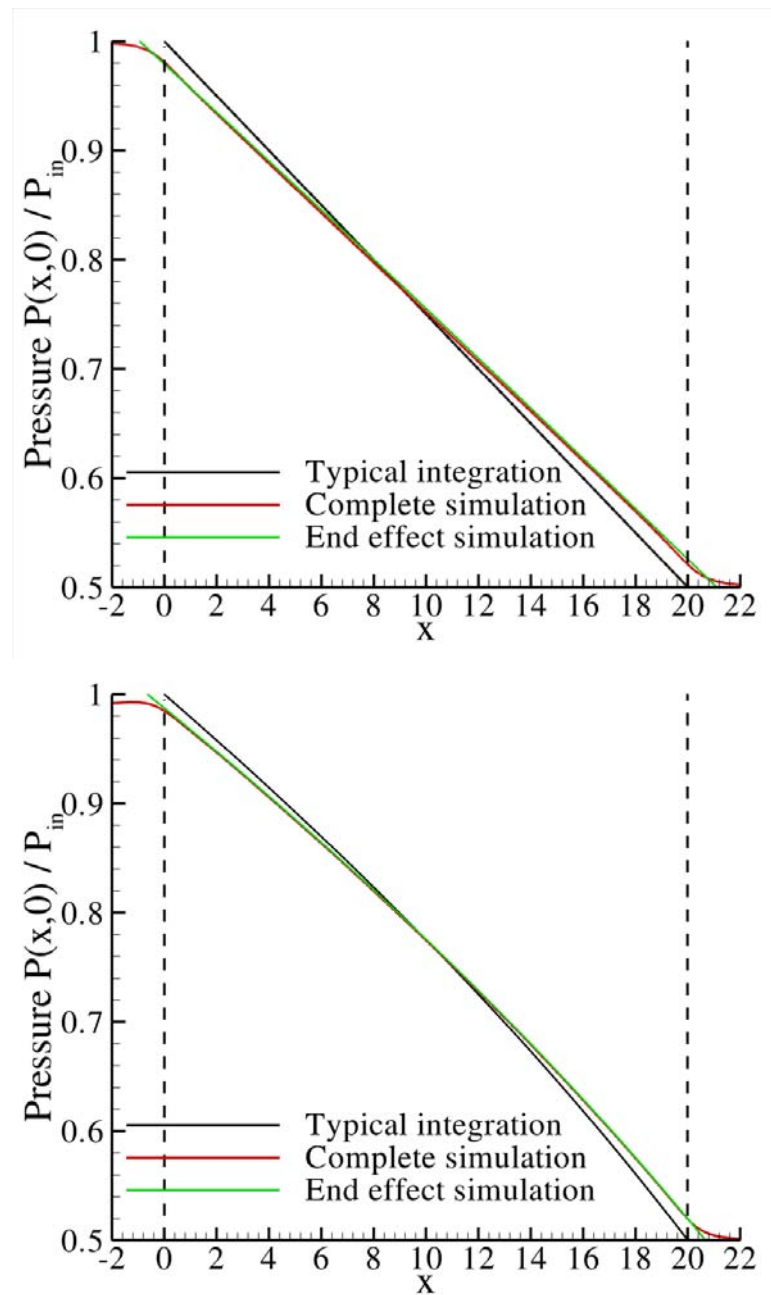


Figure 4.24: Comparison of results obtained by the end geometry formulation with non-linear results for $\delta = 1$ (up) and $\delta = 10$ (down)

Chapter 5

Non linear heat transfer

5.1 Introduction

The study of heat transfer phenomena in rarefied gases is important in several practical applications, as seen in Chapter 2, and have therefore been theoretically investigated by many researchers [187, 177, 179, 188, 113]. In most cases, only small values of the normalized temperature difference have been considered since the linearization of the distribution function leads to a more tractable mathematical formulation with a robust theoretical background. The corresponding works with a finite temperature difference are limited [188, 189, 190] and, in most cases, results are provided only within a certain range of the rarefaction, thermal and geometrical parameters involved in the problem. Questions arise on the range of applicability for the linearized formulation and the effect of higher temperature differences and different intermolecular potentials. Therefore, there is a need for a complete and accurate study of such phenomena.

A detailed investigation of the conductive heat transfer problem in a rarefied gas is performed here for a wide range of all involved parameters. The geometries of parallel plates and concentric cylinders are examined for simplicity, in order to focus on the physical aspects of the problem. A set of nonlinear kinetic equations subject to suitable boundary conditions is solved numerically for the unknown distribution function based on the discrete velocity method. Complete treatment of the heat transfer problems under consideration has been successfully applied in the literature only in the case of small temperature differences based on linearized kinetic theory [177, 175, 113].

In the present work, the nonlinear form of the Shakhov kinetic model [55] has been employed, subject to Cercignani-Lampis (CL) boundary conditions [101]. The Shakhov model, unlike the BGK model, provides simultaneously the correct expressions for the heat conduction and viscosity transport

coefficients. Intermolecular interactions are simulated based on the Inverse Power Law (IPL) [80]. By varying the viscosity dependence on temperature according to the IPL model, various intermolecular potentials have been considered. The two limiting cases of the IPL interaction, namely the Maxwell and the hard sphere interaction are examined in detail. The numerical solution is based on an advanced discrete velocity algorithm providing accurate results with modest computational effort. Macroscopic quantities, such as heat flux, density and temperature, are provided in the whole range of the Knudsen number for several values of the radius ratio and for small, moderate and large temperature differences. The influence of the intermolecular interaction model is also investigated. Based on this study the range of validity of the linearized kinetic analysis is discussed.

In the next section, the kinetic formulation is presented for the two problems in question. Then, the implemented computational scheme is described in detail. Finally the most important results are provided in the last section, where the effect of each parameter is discussed.

5.2 Formulation of the two problems

5.2.1 Introduction

In the following subsections, the kinetic modelling of two problems of non-linear heat conduction are presented. In particular, the geometries of interest here are

- two infinitely wide and long parallel plates at a distance H
- two concentric cylinders with radii R_A, R_B

The geometries are displayed in Figure 5.1. In both cases, an arbitrarily large temperature difference ΔT is imposed between the walls. The physical conditions are fully determined if the rarefaction state, the temperature difference and the radius ratio $\gamma = R_A/R_B$ (in the cylindrical case) are given.

5.2.2 Heat transfer between parallel plates

The task is to describe the state of a stationary monoatomic gas confined between two infinite parallel plates, fixed at $\hat{y}_i = \mp H/2$, $i = A, B$ as seen in Figure 5.1. The plates are maintained at

constant temperatures $T_i = T_0 \pm \Delta T/2$, $i = A, B$, while T_0 is a reference temperature. Then, the temperature ratio is defined as $T_A/T_B = (1 + \beta)/(1 - \beta)$, where $\beta = \Delta T/(2T_0)$ is the dimensionless temperature difference. In the kinetic approach applied here, the main unknown is the distribution function $f = f(\hat{y}, \boldsymbol{\xi})$, which for the specific configuration depends on the coordinate between the plates \hat{y} and the molecular velocity $\boldsymbol{\xi} = (\xi_x, \xi_y, \xi_z)$. Since the problem is non-isothermal, the Shakhov kinetic model equation

$$\xi_y \frac{\partial f}{\partial \hat{y}} = \frac{P}{\mu} \{f^S - f\} \quad (5.1)$$

is more suitable than the BGK model. The Shakhov model term is

$$f^S = f^M \left[1 + \frac{2m}{15n(k_B T)^2} \hat{q}_y \xi_y \left(\frac{m\xi^2}{2k_B T} - \frac{5}{2} \right) \right] \quad (5.2)$$

where the appropriate Prandtl number value for monatomic gases ($\text{Pr} = 2/3$) has been substituted and

$$f^M = n \left(\frac{m}{2\pi k_B T} \right)^{3/2} \exp \left[-\frac{m\xi^2}{2k_B T} \right] \quad (5.3)$$

is the local Maxwellian distribution. The number density $n(\hat{y})$, temperature $T(\hat{y})$ and heat flux $\hat{q}(\hat{y})$ are found by moments of the distribution function, i.e.

$$n(\hat{y}) = \int \int \int f d\xi_x d\xi_y d\xi_z \quad (5.4)$$

$$T(\hat{y}) = \frac{m}{3nk_B} \int \int \int \xi^2 f d\xi_x d\xi_y d\xi_z \quad (5.5)$$

$$\hat{q}(\hat{y}) = \hat{q}_y(\hat{y}) = \frac{m}{2} \int \int \int \xi^2 \xi_y f d\xi_x d\xi_y d\xi_z \quad (5.6)$$

By applying the conservation of energy (see Appendix 5) it is easily deduced that the heat flux is constant at any position between the plates ($\hat{q}(\hat{y}) = \text{constant}$). Finally, m and k_B denote the molecular mass and the Boltzmann constant respectively. At this stage it is convenient to introduce the dimensionless quantities

$$y = \frac{\hat{y}}{H}, \quad \mathbf{c} = \frac{\boldsymbol{\xi}}{v_0}, \quad g = \frac{fv_0^3}{n_0}, \quad \rho = \frac{n}{n_0}, \quad \tau = \frac{T}{T_0}, \quad q = q_y = \frac{\hat{q}_y}{P_0 v_0} \quad (5.7)$$

where H is the distance between the plates, $v_0 = \sqrt{2k_B T_0/m}$ is the most probable molecular velocity, $g = g(y, \mathbf{c})$ is the dimensionless distribution function, ρ , τ and q are the dimensionless number density, temperature and heat flux respectively, while $P_0 = n_0 k_B T_0$ is a reference pressure. The average number density

$$n_0 = \frac{1}{H} \int_{-H/2}^{H/2} n(\hat{y}) d\hat{y} \quad (5.8)$$

has been used to specify the density level. Even more,

$$\delta_0 = \frac{P_0 H}{\mu_0 v_0} = \frac{\sqrt{\pi}}{2} \frac{1}{\text{Kn}_0} \quad (5.9)$$

is the reference rarefaction parameter, while μ_0 is the gas viscosity at temperature T_0 . The rarefaction parameter is inversely proportional to the Knudsen number and therefore as δ_0 is increased the atmosphere becomes more dense (or less rarefied). The cases of $\delta_0 = 0$ and $\delta_0 \rightarrow \infty$ correspond to the free molecular and hydrodynamic limits respectively. Then, after employing the hard sphere law for the dependence of viscosity on temperature

$$\frac{\mu}{\mu_0} = \sqrt{\frac{T}{T_0}} \quad (5.10)$$

Equations (5.1)-(5.3) become

$$c_y \frac{\partial g}{\partial y} = \delta_0 \rho \sqrt{\tau} \{g^S - g\} \quad (5.11)$$

$$g^S = g^M \left[1 + \frac{4}{15} \frac{q c_y}{\rho \tau^2} \left(\frac{c^2}{\tau} - \frac{5}{2} \right) \right] \quad (5.12)$$

$$g^M = \frac{\rho}{(\pi \tau)^{3/2}} \exp \left[-\frac{c^2}{\tau} \right] \quad (5.13)$$

Furthermore, due to the symmetries of the configuration, it is possible to eliminate the two components of the molecular velocity in the x and z directions by taking appropriate moments of the distribution function to form the so-called projections. To eliminate the independent variables c_x and c_z we define

$$\varphi(y, c_y) = \int \int g(y, \mathbf{c}) dc_x dc_z \quad (5.14)$$

$$\psi(y, c_y) = \int \int (c_x^2 + c_z^2) g(y, \mathbf{c}) dc_x dc_z \quad (5.15)$$

and operate accordingly on Equation (5.11) to reduce after some routine manipulation the final coupled set of non-linear integro-differential equations

$$c_y \frac{\partial \varphi}{\partial y} = \delta_0 \rho \sqrt{\tau} \{ \varphi^S - \varphi \} \quad (5.16)$$

$$c_y \frac{\partial \psi}{\partial y} = \delta_0 \rho \sqrt{\tau} \{ \psi^S - \psi \} \quad (5.17)$$

where the S model terms are

$$\varphi^S = \varphi^M \left[1 + \frac{4}{15} \frac{q c_y}{\rho \tau^2} \left(\frac{c_y^2}{\tau} - \frac{3}{2} \right) \right] \quad (5.18)$$

$$\psi^S = \psi^M \left[1 + \frac{4}{15} \frac{q c_y}{\rho \tau^2} \left(\frac{c_y^2}{\tau} - \frac{1}{2} \right) \right] \quad (5.19)$$

Equations (5.16) and (5.17) must be solved for the unknown reduced distributions φ and ψ , which depend only on two independent variables, reducing significantly the required computational effort.

The projections of the Maxwellian distribution, φ^M and ψ^M , are

$$\varphi^M = \frac{\rho}{\sqrt{\pi \tau}} \exp \left[-\frac{c_y^2}{\tau} \right] \quad (5.20)$$

$$\psi^M = \frac{\rho \sqrt{\tau}}{\sqrt{\pi}} \exp \left[-\frac{c_y^2}{\tau} \right] \quad (5.21)$$

Finally, the dimensionless macroscopic quantities in terms of φ and ψ are

$$\rho(y) = \int \varphi dc_y \quad (5.22)$$

$$\tau(y) = \frac{2}{3\rho} \int (\psi + c_y^2 \varphi) dc_y \quad (5.23)$$

$$q(y) = q_y(y) = \int c_y (\psi + c_y^2 \varphi) dc_y \quad (5.24)$$

The interaction between the particles and the walls is modelled according to the Cercignani-Lampis boundary conditions. The final expressions are reproduced here from Section 3.2.3

$$\varphi^+ = -\frac{2}{\alpha_n \tau} \int_{c'_n < 0} \varphi^- c'_n \exp \left(-\frac{c_n^2 + (1 - \alpha_n) c_n'^2}{\tau \alpha_n} \right) I_0 \left(\frac{2\sqrt{1 - \alpha_n} c_n c'_n}{\tau \alpha_n} \right) dc'_n \quad (5.25)$$

$$\begin{aligned} \psi^+ = & -\frac{2}{\alpha_n \tau} \int_{c'_n < 0} [(1 - \alpha_t)^2 \psi^- + \tau \alpha_t (2 - \alpha_t) \varphi^-] c'_n \\ & \times \exp \left(-\frac{c_n^2 + (1 - \alpha_n) c_n'^2}{\tau \alpha_n} \right) I_0 \left(\frac{2\sqrt{1 - \alpha_n} c_n c'_n}{\tau \alpha_n} \right) dc'_n \end{aligned} \quad (5.26)$$

with c_n, c'_n being the positive and negative c_y values respectively for the lower wall and vice versa for the upper wall.

The problem is described by kinetic equations (5.16) and (5.17), coupled by the moments (5.22)-(5.24) and subject to boundary conditions (5.25) and (5.26). It is seen that the rarefaction parameter δ_0 and the temperature ratio β fully determine the physical conditions, if the accommodation coefficient values are known.

5.2.3 Heat transfer between coaxial cylinders

Consider two concentric stationary cylinders of infinite length, with radii R_A and R_B and the annular region $R_A < \hat{r} < R_B$ filled with a monoatomic gas at rest and at arbitrary density level. The cylinders are maintained at different temperatures T_A and T_B , with $T_A > T_B$. Due to the temperature difference $\Delta T = T_A - T_B$, which may be arbitrarily large in magnitude, there is a radial heat flux through the rarefied gas from the hot towards the cold cylinder. The problem is axially symmetric and its configuration is shown in Figure 5.1, where it is seen that the letters A and B refer to the inner (hot) and outer (cold) cylinders respectively. The objective is to estimate all macroscopic distributions in terms of the three parameters governing this heat transfer problem, namely the temperature difference between the cylindrical walls, the ratio of the two cylindrical radii and the degree of gas rarefaction.

It is convenient to introduce these three parameters in dimensionless form, taking the quantities at the outer cylinder as reference quantities. In particular

$$\beta = \frac{T_A - T_B}{T_B} \quad (5.27)$$

is the dimensionless temperature difference,

$$\gamma = \frac{R_A}{R_B} \quad (5.28)$$

is the radius ratio and

$$\delta_0 = \frac{R_B P_B}{\mu_B v_B} = \frac{\sqrt{\pi}}{2} \frac{1}{\text{Kn}_0} \quad (5.29)$$

is the reference rarefaction parameter. In the latter expression, P_B is the reference gas pressure, measured when the system is in equilibrium ($T_A = T_B$), μ_B is the gas viscosity at reference temperature T_B and $v_B = \sqrt{2k_B T_B / m}$, with k_B being the Boltzmann constant and m the molecular mass, is the most probable molecular velocity.

The governing equation is the nonlinear Shakhov kinetic model, which, taking into account the symmetries of the problem under consideration, is written as [55]

$$\xi_p \cos \theta \frac{\partial f}{\partial \hat{r}} - \frac{\xi_p \sin \theta}{\hat{r}} \frac{\partial f}{\partial \theta} = \frac{P}{\mu} \{f^S - f\} \quad (5.30)$$

with

$$f^S = f^M \left[1 + \frac{2m}{15n(k_B T)^2} \hat{q} \xi_p \cos \theta \left(\frac{m \xi^2}{2k_B T} - \frac{5}{2} \right) \right] \quad (5.31)$$

being the Shakhov model term and

$$f^M = n \left(\frac{m}{2\pi k_B T} \right)^{3/2} \exp \left(-\frac{m \xi^2}{2k_B T} \right) \quad (5.32)$$

being the local Maxwellian. Here, $f = f(\hat{r}, \boldsymbol{\xi})$ is the unknown distribution function, \hat{r} is the radial spatial coordinate and $\boldsymbol{\xi} = (\xi_r, \xi_\theta, \xi_z) = (\xi_p \cos \theta, \xi_p \sin \theta, \xi_z)$ is the molecular velocity vector, while $\boldsymbol{\xi}_p = (\xi_r, \xi_\theta)$, shown in Figure 5.1, is the planar velocity vector, with $\xi_p = |\boldsymbol{\xi}_p|$. Also, n , T and \hat{q} are the macroscopic distributions of number density, temperature and radial heat flow respectively, which may be obtained by the moments of the distribution function according to

$$n(\hat{r}) = \int \int \int f \xi_p d\xi_p d\theta d\xi_z \quad (5.33)$$

$$T(\hat{r}) = \frac{m}{3n(\hat{r}) k_B} \int \int \int (\xi_p^2 + \xi_z^2) f \xi_p d\xi_p d\theta d\xi_z \quad (5.34)$$

$$\hat{q}(\hat{r}) = \hat{q}_r(\hat{r}) = \frac{m}{2} \int \int \int (\xi_p^2 + \xi_z^2) (\xi_p \cos \theta) f \xi_p d\xi_p d\theta d\xi_z \quad (5.35)$$

Furthermore, μ is the viscosity of the gas at local temperature T , while P is the local pressure of the gas, given by the equation of state $P = nk_B T$.

It is noted that, even though the Shakhov model fulfils the collision invariants and provides correct expressions of the transport coefficients, there is no proof so far that it satisfies the H-theorem. This is a drawback for the Shakhov model. However, this unresolved issue produces no numerical problems or unphysical findings (e.g. negative distributions). Furthermore, it has been chosen between several nonlinear kinetic models, mainly due to the fact that the corresponding linearized solution for the specific heat transfer problem is available in the literature [113], allowing a direct comparison between the linear and nonlinear solutions at small temperature differences. This is important, in order to benchmark the nonlinear results in the linear limit and also to check the range of validity of the linearized theory. As mentioned before, all results are in good agreement with the corresponding nonlinear BGK results, provided that in the BGK model

$$\xi_p \cos \theta \frac{\partial f}{\partial \hat{r}} - \frac{\xi_p \sin \theta}{\hat{r}} \frac{\partial f}{\partial \theta} = \nu (f^M - f) \quad (5.36)$$

the collision frequency is chosen as $\nu = (2P)/(3\mu)$ in order to obtain the correct heat conduction transport coefficient.

The unknown distribution function introduced in the previous section depends on four independent variables (one in the physical space and three in the velocity space). Following a typical projection procedure, it is possible to eliminate the z -component of the molecular velocity vector. By reducing the number of independent variables from four to three the associated computational effort is significantly reduced. Also, for practical reasons all equations and quantities are non-dimensionalized. The following dimensionless quantities are introduced:

$$r = \frac{\hat{r}}{R_B}, \quad \mathbf{c} = \frac{\boldsymbol{\xi}}{v_B}, \quad g = \frac{f v_B^3}{n_B}, \quad \rho = \frac{n}{n_B}, \quad \tau = \frac{T}{T_B}, \quad \mathbf{q} = \frac{\hat{\mathbf{q}}}{P_B v_B}, \quad P = \frac{\hat{P}}{P_B} \quad (5.37)$$

All quantities with the subscript B are considered as reference quantities. Here, $g = g(r, \mathbf{c})$ is a dimensionless distribution function, with $\gamma \leq r \leq 1$ and $\mathbf{c} = (c_r, c_\vartheta, c_z)$ denoting the independent variables ($c_r = c_p \cos \theta$, $c_\vartheta = c_p \sin \theta$), while c_p denotes the magnitude of the dimensionless planar molecular velocity magnitude. Furthermore, ρ , τ , q , and p are the dimensionless distributions of number density, temperature, radial heat flow and gas pressure respectively.

Then, to proceed with the mathematical manipulation, molecular interaction must be specified. The IPL interaction, where the repulsive force between two molecules is proportional to the inverse of the n th power of the distance between their centers, is introduced. The IPL interaction yields a viscosity of the form [80, 51]

$$\mu = \mu_B (T/T_B)^\omega \quad (5.38)$$

where $\omega = 1/2 + [2/(n-1)]$. The parameter ω takes the values of 1/2 and 1 for the hard sphere ($n \rightarrow \infty$) and Maxwell ($n = 5$) interactions respectively, which are the two limiting cases. Based on the above, it is easily deduced that the local rarefaction parameter, defined as $\delta = (PR_B)/(\mu v)$, is given by

$$\delta = \delta_0 \rho \tau^{1-\omega} \quad (5.39)$$

where δ_0 is the reference rarefaction parameter defined in Equation (5.29).

The quantities given by Equations (5.38) and (5.39) are introduced into Equations (5.30) and (5.32) to yield the dimensionless nonlinear Shakhov kinetic model equation

$$c_p \cos \theta \frac{\partial g}{\partial r} - \frac{c_p \sin \theta}{r} \frac{\partial g}{\partial \theta} = \delta_0 \rho \tau^{1-\omega} \{g^S - g\} \quad (5.40)$$

where

$$g^S = g^M \left[1 + \frac{4}{15} \frac{1}{\rho \tau^2} q c_p \cos \theta \left(\frac{c^2}{\tau} - \frac{5}{2} \right) \right] \quad (5.41)$$

with

$$g^M = \frac{\rho}{(\pi \tau)^{3/2}} \exp \left(-\frac{c^2}{\tau} \right) \quad (5.42)$$

being the dimensionless local Maxwellian. Since the Shakhov collision model satisfies, as it should, the collisional invariants of mass, momentum and energy, the corresponding conservation equations may be obtained by operating accordingly on Equation (5.40). The detailed derivation is contained in Appendix 5. The mass equation implies that $u_r(r) = 0$ is always satisfied, while the energy equation yields that the product $q(r)r$ is constant at any position $\gamma \leq r \leq 1$ between the cylinders. Both conditions are implemented to benchmark the accuracy of the computed distribution function. Also,

from the r -momentum equation it is deduced that the gradient dp/dr is different than zero. Thus, there is a pressure gradient due to heat flow and not due to fluid flow. This is a non-equilibrium cross effect, which becomes stronger as the temperature difference between the cylinders and the gas rarefaction are increased, while it is completely eliminated in the hydrodynamic limit.

Next, the projection procedure is introduced by defining the reduced distribution functions

$$\varphi(r, c_p, \theta) = \int g dc_z \quad (5.43)$$

$$\psi(r, c_p, \theta) = \int c_z^2 g dc_z \quad (5.44)$$

Then, by operating successively on Equations (5.40)-(5.42) with the integral operators $\int (\cdot) dc_z$ and $\int (\cdot) c_z^2 dc_z$, the following two coupled integro-differential equations are obtained for the unknowns φ and ψ :

$$c_p \cos \theta \frac{\partial \varphi}{\partial r} - \frac{c_p \sin \theta}{r} \frac{\partial \varphi}{\partial \theta} = \delta_0 \rho \tau^{1-\omega} (\varphi^S - \varphi) \quad (5.45)$$

$$c_p \cos \theta \frac{\partial \psi}{\partial r} - \frac{c_p \sin \theta}{r} \frac{\partial \psi}{\partial \theta} = \delta_0 \rho \tau^{1-\omega} (\psi^S - \psi) \quad (5.46)$$

Here,

$$\varphi^S = \varphi^M \left[1 + \frac{4}{15} \frac{1}{\rho \tau^2} q c_p \cos \theta \left(\frac{c_p^2}{\tau} - 2 \right) \right] \quad (5.47)$$

$$\psi^S = \psi^M \left[1 + \frac{4}{15} \frac{1}{\rho \tau^2} q c_p \cos \theta \left(\frac{c_p^2}{\tau} - 1 \right) \right] \quad (5.48)$$

while

$$\varphi^M = \frac{\rho}{\pi \tau} \exp \left(-\frac{c_p^2}{\tau} \right) \quad (5.49)$$

$$\psi^M = \frac{\rho}{2\pi} \exp \left(-\frac{c_p^2}{\tau} \right) \quad (5.50)$$

are the local Maxwellians. The same non-dimensionalization and projection procedures are applied to the moments (5.33)-(5.35), to find that the macroscopic quantities are given, in terms of φ and ψ , according to

$$\rho(r) = \int_0^{2\pi} \int_0^\infty \varphi c_p dc_p d\theta \quad (5.51)$$

$$\tau(r) = \frac{2}{3\rho(r)} \int_0^{2\pi} \int_0^\infty (c_p^2 \varphi + \psi) c_p dc_p d\theta \quad (5.52)$$

$$q(r) = \int_0^{2\pi} \int_0^\infty (c_p \cos \theta) (c_p^2 \varphi + \psi) c_p dc_p d\theta \quad (5.53)$$

Also, gas pressure is given by $p(r) = \rho(r) \tau(r)$. Equations (5.45)-(5.50), along with the associated moments (5.51)-(5.53) constitute the basic set of equations to be solved.

Having established the set of governing equations, all that is left is to derive the appropriate boundary conditions for the outgoing distributions at the inner ($r = \gamma$) and outer ($r = 1$) walls. Since this has been done in detail in Section 3.2.4, we only reproduce the final equations here. At the inner wall $r = \gamma$, the Cercignani-Lampis boundary conditions read as

$$\begin{aligned} \varphi^+(\gamma, c_p, \theta) = & -\frac{2}{\alpha_n(1+\beta)^{3/2}\sqrt{\pi\alpha_t(2-\alpha_t)}} \int_{\pi/2}^{3\pi/2} \int_0^\infty (\dot{c}_p' \cos \theta') \varphi^-(\gamma, \dot{c}_p', \theta') \times \\ & \exp\left[-\frac{(c_p \cos \theta)^2 + (1-\alpha_n)(\dot{c}_p' \cos \theta')^2}{(1+\beta)\alpha_n}\right] \exp\left[-\frac{[(c_p \sin \theta) - (1-\alpha_t)(\dot{c}_p' \sin \theta')]^2}{(1+\beta)\alpha_t(2-\alpha_t)}\right] \times \\ & I_0\left[\frac{2\sqrt{1-\alpha_n}(\dot{c}_p' \cos \theta)(\dot{c}_p' \cos \theta')}{(1+\beta)\alpha_n}\right] \dot{c}_p' d\dot{c}_p' d\theta' \end{aligned} \quad (5.54)$$

$$\begin{aligned} \psi^+(\gamma, c_p, \theta) = & -\frac{2}{\alpha_n(1+\beta)^{3/2}\sqrt{\pi\alpha_t(2-\alpha_t)}} \int_{\pi/2}^{3\pi/2} \int_0^\infty (\dot{c}_p' \cos \theta') \times \\ & \left[(1-\alpha_t)^2 \psi^-(\gamma, \dot{c}_p', \theta') + \frac{1+\beta}{2} \alpha_t (2-\alpha_t) \varphi^-(\gamma, \dot{c}_p', \theta')\right] \times \\ & \exp\left[-\frac{(c_p \cos \theta)^2 + (1-\alpha_n)(\dot{c}_p' \cos \theta')^2}{(1+\beta)\alpha_n}\right] \exp\left[-\frac{[(c_p \sin \theta) - (1-\alpha_t)(\dot{c}_p' \sin \theta')]^2}{(1+\beta)\alpha_t(2-\alpha_t)}\right] \times \\ & I_0\left[\frac{2\sqrt{1-\alpha_n}(c_p \cos \theta)(\dot{c}_p' \cos \theta')}{(1+\beta)\alpha_n}\right] \dot{c}_p' d\dot{c}_p' d\theta' \end{aligned} \quad (5.55)$$

and are valid for $\theta \in [-\pi/2, \pi/2]$, while on the outer wall we impose diffuse boundary conditions

$$\varphi^+(1, c_p, \theta) = \frac{1}{\pi} \exp(-c_p^2) \quad (5.56)$$

$$\psi^+(1, c_p, \theta) = \frac{1}{2\pi} \exp(-c_p^2) \quad (5.57)$$

for the angles $\theta \in [\pi/2, 3\pi/2]$.

The nonlinear set of Equations (5.45)-(5.50) along with the boundary conditions (5.54)-(5.57) provide a theoretically well-established kinetic formulation for the heat transfer problem under consideration.

5.3 Numerical scheme

The computational scheme, based on the discrete velocity method, has been successfully applied in the past to solve linearized kinetic model equations describing several non-equilibrium systems [77, 74]. Here, it is extended to deal with non-linear kinetic equations in a very efficient and accurate manner. In the following discussion, the numerical scheme is presented for the cylindrical case, but a similar procedure is also followed for the plane case with c_y instead of c_p , while also omitting the streaming term containing the velocity angle θ .

Both the molecular velocity space (c_p, θ) , with $c_p \in [0, \infty)$ and $\theta \in [0, 2\pi]$, and the physical space $r \in [\gamma, 1]$ are discretized. The continuum spectrum of magnitudes of the molecular velocity vector is replaced by a set of discrete magnitudes $c_p^{(m)} \in [0, c_p^{max}]$, $m = 1, 2, \dots, M$, which are taken to be the roots of the Legendre polynomial of order M accordingly mapped from $[-1, 1]$ to $[0, c_p^{max}]$. It is obvious that the choice of this discrete set is directly connected to the implemented numerical integration over the molecular velocity space. Although, various discrete velocity sets may be applied, it has been found that the Gauss-Legendre integration provides reliable results with less computational effort in the whole range of the Knudsen number without changing the integration rule depending upon the gas rarefaction. The numerical parameters related to the choice of the discrete velocity magnitudes used in the present work are provided in Table 5.1. Also, by using a uniform grid, the angular space is divided into N intervals. Each of the angular intervals is defined by its angle θ_n , $n = 1, 2, \dots, N$. Finally, the distance between the two cylinders is divided into I equal segments, defined by r_i , $i = 1, 2, \dots, I + 1$.

The governing kinetic equations (5.45)-(5.50) are discretized in the variable c_p and the resulting equations are integrated over each spatial and angular interval, $[r_{i-1/2}, r_{i+1/2}]$ and $[\theta_{n-1/2}, \theta_{n+1/2}]$. The first and the second term at the left hand side of the kinetic equations are integrated analytically in terms of r and θ respectively and then the integration in terms of the remaining variable is performed based on the trapezoidal rule. The resulting discrete equation for φ is

$$\begin{aligned}
 & \varphi_{n+\frac{1}{2}, i+\frac{1}{2}}^{(m)} \left[\frac{c_p^{(m)} \cos \theta_n}{2\Delta r} - \frac{c_p^{(m)} \sin \theta_n}{2r_{i+\frac{1}{2}} \Delta \theta} + \frac{\delta_0}{4} \rho_{i+\frac{1}{2}} \tau_{i+\frac{1}{2}}^{1-\omega} \right] + \\
 & \varphi_{n-\frac{1}{2}, i+\frac{1}{2}}^{(m)} \left[\frac{c_p^{(m)} \cos \theta_n}{2\Delta r} + \frac{c_p^{(m)} \sin \theta_n}{2r_{i+\frac{1}{2}} \Delta \theta} + \frac{\delta_0}{4} \rho_{i+\frac{1}{2}} \tau_{i+\frac{1}{2}}^{1-\omega} \right] + \\
 & \varphi_{n+\frac{1}{2}, i-\frac{1}{2}}^{(m)} \left[-\frac{c_p^{(m)} \cos \theta_n}{2\Delta r} - \frac{c_p^{(m)} \sin \theta_n}{2r_{i-\frac{1}{2}} \Delta \theta} + \frac{\delta_0}{4} \rho_{i-\frac{1}{2}} \tau_{i-\frac{1}{2}}^{1-\omega} \right] + \\
 & \varphi_{n-\frac{1}{2}, i-\frac{1}{2}}^{(m)} \left[-\frac{c_p^{(m)} \cos \theta_n}{2\Delta r} + \frac{c_p^{(m)} \sin \theta_n}{2r_{i-\frac{1}{2}} \Delta \theta} + \frac{\delta_0}{4} \rho_{i-\frac{1}{2}} \tau_{i-\frac{1}{2}}^{1-\omega} \right] = \\
 & \frac{\delta_0}{4} \left[\rho_{i+\frac{1}{2}} \tau_{i+\frac{1}{2}}^{1-\omega} \left(\varphi_{n+\frac{1}{2}, i+\frac{1}{2}}^{S,(m)} + \varphi_{n-\frac{1}{2}, i+\frac{1}{2}}^{S,(m)} \right) + \rho_{i-\frac{1}{2}} \tau_{i-\frac{1}{2}}^{1-\omega} \left(\varphi_{n+\frac{1}{2}, i-\frac{1}{2}}^{S,(m)} + \varphi_{n-\frac{1}{2}, i-\frac{1}{2}}^{S,(m)} \right) \right]
 \end{aligned} \tag{5.58}$$

where

$$\varphi_{n,i}^{S,(m)} = \frac{\rho_i}{\pi \tau_i} \exp \left[-\frac{(c_p^{(m)})^2}{\tau_i} \right] \left\{ 1 + \frac{4}{15} \frac{1}{\rho_i \tau_i^2} q_i c_p^{(m)} \cos \theta_n \left[\frac{(c_p^{(m)})^2}{\tau_i} - 2 \right] \right\} \tag{5.59}$$

The corresponding equation for ψ is derived in a similar manner and is omitted here. Due to the trapezoidal integration, the error is of $O(\Delta r^2, \Delta \theta^2)$ and its form is known. Similar derivations on Equations (5.16)-(5.21) for the plane problem lead to

$$\begin{aligned}
 & \varphi_{i+1/2}^{(m)} \left[\frac{c_y^{(m)}}{\Delta y} + \frac{\delta_0}{2} \rho_{i+1/2} \sqrt{\tau_{i+1/2}} \right] + \varphi_{i-1/2}^{(m)} \left[-\frac{c_y^{(m)}}{\Delta y} + \frac{\delta_0}{2} \rho_{i-1/2} \sqrt{\tau_{i-1/2}} \right] \\
 & = \frac{\delta_0}{2} \left(\rho_{i+1/2} \sqrt{\tau_{i+1/2}} \varphi_{i+1/2}^{S,(m)} + \rho_{i-1/2} \sqrt{\tau_{i-1/2}} \varphi_{i-1/2}^{S,(m)} \right)
 \end{aligned} \tag{5.60}$$

with

$$\varphi_i^{S,(m)} = \frac{\rho_i}{\sqrt{\pi \tau_i}} \exp \left[-\frac{(c_y^{(m)})^2}{\tau_i} \right] \left\{ 1 + \frac{4}{15} \frac{1}{\rho_i \tau_i^2} q_y c_y^{(m)} \left[\frac{(c_y^{(m)})^2}{\tau_i} - 2 \right] \right\} \tag{5.61}$$

The discretized equations for $\varphi_{n,i}^{(m)}$ and $\psi_{n,i}^{(m)}$ and the associated discretized moments (5.51)-(5.53) for ρ_i , τ_i and q_i are solved in an iterative manner. Based on the computed values of ρ_i , τ_i and q_i of the previous iteration (or on a reasonable initial assumption at the beginning), the kinetic equations are solved for $\varphi_{n,i}^{(m)}$ and $\psi_{n,i}^{(m)}$. Then, updated values of ρ_i , τ_i and q_i are obtained by introducing in the moments the computed distribution functions. The new values of the bulk quantities are used to initiate the next iteration. This iteration process is terminated when some convergence criteria imposed on the macroscopic quantities is fulfilled and is named in this text the typical iteration algorithm. The flow diagram of this algorithm is shown in Figure 5.2. This algorithm is applied for the parallel plates, using $I = 401$ nodes and $M = 80$ discrete velocities. The convergence criterion, set as the average absolute residual per node, has been set equal to 10^{-8} and the results are considered accurate to all three significant figures.

For the cylindrical case, due to the slow convergence of the code for small radius ratios ($\gamma < 0.1$), some modifications are required to reach convergence faster. The typical iteration algorithm has been upgraded by implementing the Romberg integration rule and the Wynn-epsilon (We) acceleration algorithm [191, 192]. In particular, the Romberg rule provides very accurate estimates of integration in the macroscopic quantities and in the boundary conditions, even when coarse angle and spatial grids are used, while the We algorithm speeds up the slow convergence of the typical iteration scheme. Both methodologies result to a significant reduction of CPU time. The flow diagram of the upgraded algorithm is shown in Figure 5.3.

The Romberg integration rule is carried out by the expression

$$T_k(l) = \frac{4^k T_{k-1}(2l) - T_{k-1}(l)}{4^k - 1} \quad k = 1, 2, 3... \quad (5.62)$$

where $T_k(l)$ denotes the estimation of an integral with l intervals after k integration steps, while $T_0(l)$ is the original trapezoidal rule with l intervals. This treatment can be implemented in both the spatial and angular domains and the resulting accuracy is of $O(\Delta r^{2k+2}, \Delta \theta^{2k+2})$. The Romberg rule is applied twice. First, at the Cercignani-Lampis boundary conditions (5.54) and (5.55), when integration with respect to the angle θ , is performed. The trapezoidal estimates are obtained initially on a coarse grid of

n angles, which is doubled repeatedly until the total number of N angles is reached. Secondly, at the macroscopic quantities (5.51)-(5.53), where the computation is performed initially on a coarse spatial and angular grid and, after convergence has been reached, it is repeated in a refined mesh, where the grid parameters have been doubled. This refinement is repeated $k - 1$ times and the results are combined according to Equation (5.62) at each spatial point until the final number of N angles and I space nodes is reached.

It is also noted that in each grid refinement the results of the previous grid have been used as an initial condition to speed up convergence. This procedure has lead to an accurate solution with a moderately dense grid. In particular, the initial number of angular and spatial intervals are $N = 24$ and $I = 51$ respectively. Then, the Romberg rule is applied four times ($k = 5$) in the angular space and two times ($k = 3$) in the physical space, leading to the final values of $N = 192$ and $I = 201$. The above parameters are used for all values of the rarefaction parameter δ_0 .

The We acceleration is a strongly nonlinear sequence accelerator that can exhibit spectacular acceleration for some sequences and has been described as the most elegant of all convergence acceleration methods [192]. The convergence of a series $S_j, j = 1, \dots, J$, can be accelerated by forming a tableau whose even columns are estimations of the sequence limit

$$\varepsilon_{i+1}^{(j)} = \varepsilon_{i-1}^{(j+1)} + \left[\varepsilon_i^{(j+1)} - \varepsilon_i^{(j)} \right]^{-1} \quad (5.63)$$

with $\varepsilon_{-1}^{(j)} = 0$ and $\varepsilon_0^{(j)} = S_j$. This algorithm is imposed inside the typical iteration loop to all macroscopic quantities, ρ_i, τ_i and q_i . Thus, a value of each sequence is stored in regular intervals between the iterations and a transitional stage is allowed before each application of the algorithm. It is important to numerically monitor the values of each sequence and ensure that the series is converging. Then, the We acceleration is implemented. If the series is diverging then the We acceleration is not used within this iteration loop and the last estimation obtained by the typical iterative scheme is kept. Also, in general, the upgraded iterative method with the We acceleration scheme is stable and converges in the whole range of the δ . Attention is needed in the hydrodynamic regime, where the parameters of the We scheme must be chosen after some numerical trials in order to optimize performance. This is also

the regime where the largest reduction in the number of iterations has been observed (up to 75% for $\delta = 650$ [156]). In the calculations, a total of $J = 51$ terms have been used for $\delta_0 \leq 200$ and $J = 101$ for $\delta_0 > 200$.

Comparing the computational efficiency of the typical and the upgraded algorithms it has been found that while keeping the same accuracy in the results, the CPU time of the latter one is reduced by at least one order of magnitude. Furthermore, both Romberg and We schemes are easily applied in both linearized and nonlinear kinetic problems. Finally, it is noted that for more demanding problems the upgraded algorithm can be further improved by extending and optimizing the implementation of the Romberg rule.

5.4 Results and discussion

5.4.1 Introduction

Results in graphical and tabulated form are presented for the macroscopic quantities in terms of all parameters involved in the problem. In particular, in Section 5.4.3.1 the radial heat flow as well as the distributions of temperature, density and pressure are provided for various values of the normalized temperature difference β , the radius ratio γ and the reference rarefaction parameter δ_0 . Gas-surface interaction has been studied for these problems in Chapter 3 and thus is omitted here. The influence of the intermolecular collision models on the macroscopic quantities is examined in Section 5.4.3.2 respectively. Finally, in Section 5.4.3.3 the range of validity of the linear solution is considered by comparing the present nonlinear results with the corresponding linearized ones for various values of β .

The results presented here, are based on the discretization and the numerical parameters given in Section 5.3. This set of parameters ensures grid independent results to all three significant figures given in the tables below. Validation of the numerical solution and benchmarking of the results has been performed in several manners. The numerical results satisfy the conservation equations obtained in Appendix 5 with at least 0.01% accuracy, while in the free molecular and hydrodynamic limits,

they coincide with the analytical solutions presented in Appendix 6. Also, for all cases examined the obtained results based on the nonlinear Shakhov model are in very good agreement with the corresponding ones obtained by the nonlinear BGK model, provided that the proper collision frequency is implemented in the BGK model. In addition, for adequately small temperature differences the nonlinear solution provides identical results to several significant figures with the corresponding linearized ones. Finally, additional benchmarking has been performed by considering the limiting case of γ being very close to one, which corresponds to the problem of heat transfer between two parallel plates. Very good agreement has been obtained between the cylindrical results with the radius ratio $\gamma = 0.999$ and the corresponding ones for the plane heat transfer problem.

5.4.2 Heat transfer between parallel plates

In Table 5.2, numerical results for the dimensionless heat flux q defined by Equation (5.24) have been tabulated for $0 \leq \delta_0 \leq 150$ and for small, moderate and large values of the ratio T_A/T_B . It is seen that for $\delta_0 \leq 1.5$, as T_A/T_B is increased, the heat flux is also increased up to some value of T_A/T_B and then as T_A/T_B is further increased the heat flux is reduced. The ratio T_A/T_B at which the maximum heat flux is observed depends on δ_0 . This is an unexpected behaviour of q in terms of T_A/T_B and it is not easily justified physically. For $\delta_0 \geq 15$, the heat flux is increased monotonically with T_A/T_B . Next, in terms of δ_0 , it is seen that for $T_A/T_B \leq 7$ the heat flux is decreased as δ_0 is increased, i.e. as we are moving from the free molecular to the continuum regimes. This is expected and has been also observed in linear analysis with small temperature ratios. Here, however, for $T_A/T_B \geq 10$, as δ_0 is increased, the heat flux is initially increased and then at some δ_0 is reduced. It is noted that for $\delta_0 = 0$ and $\delta_0 = 150$, which correspond to the free molecular and hydrodynamic limits, the agreement with the corresponding analytical results presented in [179, 176] is at least two significant figures.

Results on the dimensionless heat flux, based on linear kinetic analysis, are presented in Table 5.3, for the same set of the parameters δ_0 and T_A/T_B . It is seen that for small and moderate T_A/T_B there is a qualitative agreement between linear and non-linear results. Also, for small values of T_A/T_B there is good quantitative agreement. Of course, for moderate and large T_A/T_B there are discrepancies and

as expected the linearized kinetic analysis is not capable of producing accurate results. In particular, at small δ_0 and large T_A/T_B the linear results are erroneous. Therefore, linear analysis can not capture the non-monotonic behaviour of q at large temperature ratios, which has been previously observed. However, it may be argued that the range of applicability of the linear analysis is wider than expected.

Temperature profiles, based on linear and nonlinear analysis, are presented in Figure 5.4 for $\delta_0 = 0, 1.5$ and 150 , with $T_A/T_B = 3$ ($\beta = 0.5$). The linear results are always symmetric about $y = 0$. This is not the case for the non-linear analysis. In the non-linear results the temperature jumps at the hot plate ($y = -1/2$) are much larger than the corresponding ones at the cold plate ($y = 1/2$). These results are indicative for other values of δ_0 and T_A/T_B . The drop in the temperature in the free molecular limit may be explained if we remember that the temperature is a second order moment, representing the variance of the molecular velocities. For a large temperature difference, the vast majority of molecules moves from the cold to the hot wall with a very low velocity (located in a narrow velocity range due to the Maxwellian form). The number of molecules moving in the opposite direction is much smaller, and even though their velocities are far larger, they are not able to increase the variance of molecular velocities. As a result, the complete normalized temperature profile is constant and lower than the mean temperature. On the other hand, the non-linear temperature profile near the hydrodynamic regime is not of constant gradient due to the dependence of the gas thermal conductivity on the temperature.

Finally, in Figure 5.5, typical profiles of the reduced distribution functions φ and ψ in terms of the molecular velocity c_y are provided at $y = \pm 1/2$ and $y = 0$ for $\delta_0 = 1.5$ and $T_A/T_B = 3$. The parts of the distribution for $c_y > 0$ and $c_y < 0$ correspond to particles moving from left to right (hot to cold) and vice versa respectively. The discontinuity at $c_y = 0$ is evident and it is much stronger at the walls than in the center of the slab. Also, in general the discontinuities become stronger as δ_0 is increased and/or T_A/T_B is increased.

Another unexpected feature here is that the required number of iterations for convergence shows a non-monotonic trend in terms of the rarefaction parameter δ_0 , as seen in Table 5.4. In particular, the minimum number of iterations is observed around $\delta_0 = 1$. It has also been seen that this

behaviour is observed only when the formulation of the problem is such that a normalization expression, such as (5.8), is included for the density.

5.4.3 Heat transfer between coaxial cylinders

5.4.3.1 Bulk quantities for hard sphere molecules with diffuse boundary conditions

In this subsection the study is focused on the dependency of the macroscopic quantities on δ_0 , γ and β . Therefore, only diffuse boundary conditions ($\alpha_t = \alpha_n = 1$) and hard sphere molecules ($\omega = 1/2$) are considered. The reference rarefaction parameter varies in the whole range of the Knudsen number ($0 \leq \delta_0 \leq 650$), the outer radius is 2 up to 65 times larger than the inner radius ($1/2 \leq \gamma \leq 1/65$), while the normalized temperature difference takes the values of $\beta = 0.1, 1$ and 10 . The temperature ratio is $T_A/T_B = 1 + \beta$. It may be stated that the values of $\beta = 0.1, 1$ and 10 correspond to linear, nonlinear and strongly nonlinear heat transfer configurations respectively.

First, results for the radial heat flow, a quantity with great practical interest defined by Equation (5.53), are presented. As it is noted before, if the radial heat flow is defined at some point $\gamma \leq r \leq 1$, then based on the energy conservation principal (the product $q(r)r$ remains constant), it may be easily calculated at any point along the radius using the relation $q(\gamma)\gamma = q(r)r = q(1)$. Therefore, most of the results and discussion are based on the estimation of $q(r)$ at $r = \gamma$.

The behaviour of the radial heat flow $q(r = \gamma)$ in terms of the reference rarefaction parameter δ_0 is shown in Figure 5.6 for $\gamma = 0.1, 0.2, 0.5$ and $\beta = 0.1, 10$. It is seen that in most cases as δ_0 is increased (i.e., the gas becomes more dense) the dimensionless radial heat flow is decreased monotonically. In particular, it is decreased very slowly for $\delta_0 < 1$, while the reduction becomes much faster for $\delta_0 > 1$. However, it is seen that in the case of $\beta = 10$ and $\gamma = 0.1$, starting from $\delta_0 = 10^{-2}$ the heat flow is slightly increased, reaching a peak in the transition regime around $\delta_0 \simeq 1$, and then it is decreased as δ_0 is increased. This is a nonlinear effect appearing at large β and small γ . Overall, it is obvious that the gas rarefaction strongly influences the radial heat flow for all values of β and γ .

The radius ratio effect can also be noticed in Figure 5.6. It is seen that in the free molecular

regime $0 \leq \delta_0 \leq 0.1$ the radial heat flow is independent of γ for both small and large temperature differences. Then, as δ_0 is increased the effect of γ on q becomes more evident. In particular, for $\delta_0 \geq 0.1$, q is decreased as γ is increased (i.e. as the annular region is decreased).

The behaviour of the radial heat flow $q(r = \gamma)$ in terms of β is shown in Table 5.5, covering a wide range of all three parameters determining the heat transfer problem. For small values of β the radial heat flow is increased proportionally to β . However, as β is increased and in particular for $\beta \geq 1$ the dependency is not linear any more and q is increased faster, following a power law of β . It is also seen that this nonlinear behaviour becomes stronger as the rarefied gas becomes denser, i.e. as δ_0 is increased. It may be useful to note that tabulated results are important in this type of research work since they can be easily accessed in the future for comparison purposes with experiments or as benchmarks for computations. In this framework, the results of Table 5.5 will be used in the next subsections in order to study the influence of the intermolecular interaction law. In addition, they will also be used to study the range of validity of the linear approximation by comparing with corresponding linear results previously reported in the literature. In order to provide this comparison in a direct manner, we have chosen to provide the heat flow results in Table 5.5 in terms of β, γ and the product $\delta_0 \gamma$. It is readily seen that the values of the rarefaction parameter in Table 5.5 vary in $0 \leq \delta_0 \leq 650$.

Next, the macroscopic quantities of number density and temperature, defined by Equations (5.51) and (5.52) respectively, are considered. In Figure 5.7, the temperature distributions $\tau(r)$ of the gas are presented along the radius $\gamma \leq r \leq 1$ for $\beta = 0.1, 1, 10$, $\gamma = 0.1, 0.5$ and various values of δ_0 . It is noted that the dimensionless temperature of the inner ($r = \gamma$) and outer ($r = 1$) cylindrical wall is $\tau_A = 1 + \beta$ and $\tau_B = 1$ respectively. It is clearly seen that the temperature jump at the walls is increased as δ_0 is decreased. It is also observed that the temperature jump at the inner wall is significantly larger than the corresponding jump at the outer wall. Evenmore, as β is increased the temperature jumps at both walls are increased. However, it is evident from the plotted results that the increase of β has a much stronger effect on the jump at the inner compared to that of the outer wall. To illustrate this significant impact of β on $\tau(\gamma)$ it is stated that in the free molecular limit ($\delta_0 = 0$) for

$\beta = 1$ the temperature of the wall is $\tau_A = 2$ and the temperature of the gas at the wall is $\tau(\gamma) = 1.4$. The corresponding values for $\beta = 10$ are $\tau_A = 11$ and $\tau(\gamma) = 3.3$. This behaviour may be explained by the fact that the gas becomes more rarefied as its temperature is increased. Beyond the quantitative differences, the qualitative behaviour of the temperature profiles with regard to β is similar. Comparing the temperature profiles for $\gamma = 0.5$ and 0.1 it is seen that the temperature is decreased more rapidly in the latter case.

The dimensionless number density distributions $\rho(r)$ are shown in Figure 5.8 for $\beta = 0.1, 1, 10$, $\delta_0 = 0, 2, 20$ and $\gamma = 0.5$. As expected, the values of the number density are low at the hot wall and high at the cold wall, while they are monotonically increased between the two walls. This is in agreement with the related characteristics of the temperature distributions discussed above. Also, in all cases the density distributions have the common S-shaped profile, except in the case of $\beta = 10$ and $\delta_0 = 20$. The latter behaviour is a nonlinear effect and it is present at large β and δ_0 . Since, according to Equation (5.39) in the cases of hard sphere and Maxwell molecules, $\delta = \delta_0 \rho \sqrt{\tau}$ and $\delta = \delta_0 \rho$ respectively, the variation of the local rarefaction parameter between the cylinders is qualitatively similar to that of the density profiles in Figure 5.8. Thus, moving from the hot towards the cold wall the rarefaction parameter is monotonically increased, i.e. the atmosphere becomes less rarefied.

The dimensionless pressure profile is also plotted in Figure 5.9 for $\beta = 0.1, 1, 10$, $\gamma = 0.1, 0.5$ and various values of δ_0 . Although the pressure distribution may be directly obtained by the density and temperature distributions, $p = \rho\tau$, it is plotted for completeness and clarity purposes. It is seen that, in all cases, there is a pressure variation along the radius of the annulus, which is increased as δ_0 is decreased and β is increased. This observation has been theoretically proven in Appendix 5 and it has been also observed by other researchers [193, 194]. The pressure variation is quite small for $\beta = 0.1$ and this is the reason that it has not been reported before in all related papers based on linear analysis. Of course for $\beta = 1$ and 10 the pressure variation is significant and there is no way to be due to numerical error. The build-up of a pressure gradient due to an imposed heat flow is sparked by non-equilibrium conditions and becomes more profound at large temperature differences and highly

rarefied atmospheres.

5.4.3.2 Influence of intermolecular interaction law

The influence of the intermolecular interaction on the heat transfer characteristics is studied through the variation of the IPL coefficient. The radial heat flow and temperature distributions are plotted in Figure 5.10 for hard spheres (“HS”) and Maxwell molecules (“MM”) characterized by $\omega = 0.5$ and $\omega = 1$ respectively. Results are provided for $\gamma = 0.5$, $\beta = 0.1, 10$ and $\delta_0 = 0, 2, 20$. As expected, the corresponding results are identical in the free molecular limit ($\delta_0 = 0$). For $\delta_0 > 0$ it is deduced that the variation between the “HS” and “MM” results is negligibly small at $\beta = 0.1$ even for large values of δ_0 . However, the discrepancies are significant at $\beta = 10$, particularly for $\delta_0 = 20$. Observing the heat flow distributions it is seen that the heat flow results of the “MM” are always higher than the corresponding ones for the “HS”. Comparing the temperature distributions of the two types of molecules it is deduced that at both walls the temperature jumps of the “MM” are always larger than the ones of the “HS”. Therefore, the corresponding distributions are crossing each other somewhere along the annular radius closer to the cold wall.

In addition, tabulated results of the radial heat flow $q(r = \gamma)$ for Maxwell molecules are given in Table 5.6 for a wide range of the involved parameters. The results of Table 5.6 can be compared directly with the ones in Table 5.5 for hard spheres. This comparison confirms that the deviation between corresponding “HS” and “MM” results is enlarged as β and δ_0 are increased and that it is also increased as γ is decreased (i.e. the annular region becomes larger). Indicatively, it is reported that for $\gamma = 0.1$ and $\delta_0 = 10$ ($\delta_0\gamma = 1$) the relative error is 4% at $\beta = 1$ and 14% at $\beta = 10$, while the maximum deviation between the reported results in Tables 5.5 and 5.6, which is 58%, occurs at $\beta = 10$, $\gamma = 1/65$ and $\delta_0 = 650$.

To extend this analysis beyond the limiting “HS” and “MM” molecules, in Figure 5.11, some dimensional radial heat flow results (W/m^2) in terms of the reference pressure P_B (Pa) are given for three different monoatomic gases, namely helium, argon and xenon having under standard conditions $\omega = 0.66, 0.81$ and 0.85 . These results are provided in dimensional form in order to facilitate

comparisons with experiments in the short future. The inner and outer diameters are $R_A = 1\text{cm}$ and $R_B = 10\text{cm}$, while the reference temperature is $T_B = 293\text{K}$. The reference pressure and the type of the gas are easily related to the reference rarefaction parameter δ_0 , while in order to keep these results as general as possible, the other two parameters β and γ are kept in dimensionless form. As expected, at highly rarefied atmospheres the heat flow is proportional to the gas pressure, while at dense atmospheres the heat flow becomes independent of the gas pressure. When the gas pressure is in the transition regime the relation is complex.

5.4.3.3 Range of validity of linear analysis

The numerical treatment of linear integro-differential equations compared to the nonlinear ones is much more tractable since it is based on a well-established theoretical basis. Therefore, it may be interesting to check the range of validity of the linear solution by comparing the corresponding linear and nonlinear results for various values of the normalized temperature difference parameter. According to theory, the linearization of this heat transfer problem is allowed provided that $\beta \ll 1$.

Results for the radial heat flow, denoted as q_L , based on the linearized Shakhov model and diffuse boundary conditions are provided for various values of δ_0 and γ in Table II of Reference [113]. A comparison can be made with the corresponding nonlinear “HS” results, presented here in Table 5.5, after multiplying the linear heat flows in Table II with the appropriate value of β . As β is increased significant deviations are observed. The maximum difference for $\beta = 1$ is about 16% and for $\beta = 10$ about 64%.

The percentage error between the nonlinear and linear heat flows, defined as $\epsilon = |(q - q_L)/q| \times 100\%$, is presented in Figure 5.12 for several values of δ_0 and $\gamma = 0.1, 0.5$. In highly and moderate rarefied atmospheres ($\delta_0 = 0.2, 2$) the introduced error for all $\beta = 0.1, 1, 10$ is less than 2%. In less rarefied atmospheres ($\delta_0 = 10, 20$) the error is increased. For example for $\beta = 10$ and $\delta_0 = 20$ the error is about 15%. However, it is seen that even for large temperature differences the discrepancies remain within reasonable margins. It may be argued that the range of applicability of the linear analysis is wider than expected and this might be quite useful in practical applications.

Furthermore, the nonlinear and linear profiles of the radial heat flux and temperature are plotted in Figure 5.13, for $\gamma = 0.5$, $\beta = 0.1, 1, 10$ and $\delta_0 = 0, 2, 20$. As expected, the discrepancies are very small for both quantities when $\beta = 0.1$ and then they gradually increase as β is increased. However, it is interesting to note that the discrepancies between the temperature distributions are significantly larger compared to the discrepancies of the heat flow distributions for the same set of parameters. For example, in the case of $\beta = 10$ and $\delta_0 = 20$ the deviation in the heat flow is about 15% and more or less remains constant along the radius, while the corresponding error for the temperature profiles varies along the radius and takes a maximum value of about 35% at $r = \gamma$. This is an unexpected observation, which may be important when linearized theory is applied to finite temperature differences.

5.5 Concluding remarks

The problem of nonlinear heat transfer through a rarefied gas confined between two coaxial cylinders is solved based on the nonlinear form of the Shakhov kinetic model, subject to Cercignani-Lampis boundary conditions, while intermolecular interactions are simulated based on the Inverse Power Law. The governing equations are discretized based on the discrete velocity method and a typical second order finite difference scheme. The numerical algorithm becomes computationally efficient by applying the Romberg integration rule and the Wynn-epsilon (We) acceleration algorithm.

The quantitative behaviour of all macroscopic quantities (radial heat flow, density, temperature and pressure) in terms of the rarefaction parameter, the radius ratio and the temperature difference is examined in detail. A pressure variation in the radial direction is detected and confirmed. Departure of the corresponding linear results has been observed as the temperature difference between the cylinders is increased and as the gas atmosphere becomes less rarefied. This deviation becomes significant at large temperature differences and small Knudsen numbers. However, it is concluded that linear analysis can capture the correct behaviour of the heat flow configuration even for moderate temperature differences and it is argued that the range of applicability of the linear analysis is wider than expected. By studying the cases of hard sphere and Maxwell particles it is verified that the type of

molecular interaction plays an important role when the heat transfer configuration becomes strongly nonlinear, while the influence of the gas-surface scattering law has similar effects both in linear and nonlinear conditions. Even more, although the formulation and most of the results are in dimensionless form, some dimensional results are also provided for specific gases in order to demonstrate in a more comprehensive manner the effect of the problem parameters on the radial heat flow.

The present work may be useful in engineering applications as well as in comparisons with experimental results which, as far as the authors are aware of, are not available for the case of large temperature differences at this stage.

Table 5.1: Number and range of discrete velocity magnitudes

β	M	c_p^{max}
0.1	20	5
1	20	6
10	24	14

Table 5.2: Non-linear dimensionless heat fluxes for the parallel plate geometry and various values of δ_0 , T_A/T_B
 $T_A/T_B = (1 + \beta) / (1 - \beta)$

δ_0	1.1	1.5	3	7	10	100
0	5.64×10^{-2}	2.22×10^{-1}	5.06×10^{-1}	6.14×10^{-1}	5.98×10^{-1}	2.83×10^{-1}
1.5×10^{-4}	5.64×10^{-2}	2.22×10^{-1}	5.06×10^{-1}	6.14×10^{-1}	5.98×10^{-1}	2.83×10^{-1}
1.5×10^{-1}	5.23×10^{-2}	2.06×10^{-1}	4.74×10^{-1}	5.89×10^{-1}	5.82×10^{-1}	3.20×10^{-1}
1.5	3.57×10^{-2}	1.41×10^{-1}	3.32×10^{-1}	4.38×10^{-1}	4.49×10^{-1}	3.68×10^{-1}
15	9.92×10^{-3}	3.95×10^{-2}	9.68×10^{-2}	1.39×10^{-1}	1.49×10^{-1}	1.64×10^{-1}
150	1.22×10^{-3}	4.86×10^{-3}	1.20×10^{-2}	1.77×10^{-2}	1.92×10^{-2}	2.24×10^{-2}

Table 5.3: Linearized dimensionless heat fluxes for the parallel plate geometry and various values of δ_0 , T_A/T_B
 $T_A/T_B = (1 + \beta) / (1 - \beta)$

δ_0	1.1	1.5	3	7	10	100
0	5.64×10^{-2}	2.26×10^{-1}	5.64×10^{-1}	8.46×10^{-1}	9.23×10^{-1}	1.11
1.5×10^{-4}	5.64×10^{-2}	2.26×10^{-1}	5.64×10^{-1}	8.46×10^{-1}	9.23×10^{-1}	1.11
1.5×10^{-1}	5.23×10^{-2}	2.09×10^{-1}	5.23×10^{-1}	7.85×10^{-1}	8.56×10^{-1}	1.03
1.5	3.57×10^{-2}	1.43×10^{-1}	3.57×10^{-1}	5.36×10^{-1}	5.84×10^{-1}	7.00×10^{-1}
15	9.92×10^{-3}	3.97×10^{-2}	9.92×10^{-2}	1.49×10^{-1}	1.62×10^{-1}	1.94×10^{-1}
150	1.22×10^{-3}	4.87×10^{-3}	1.22×10^{-2}	1.83×10^{-2}	1.99×10^{-2}	2.39×10^{-2}

Table 5.4: Number of iterations needed for some indicative cases with diffuse reflection

δ_0	$T_A/T_B = (1 + \beta) / (1 - \beta)$			
	1.1	1.5	3	7
0.15	87	87	86	81
1.5	54	53	52	48
15	610	698	779	849
150	28724	35502	41679	46378

Table 5.5: Radial heat flow $q_r(r = \gamma)$ for hard sphere molecules with diffuse boundary conditions

	$\delta_0\gamma$	$\gamma = 1/2$	$1/5$	$1/10$	$1/20$	$1/65$
$\beta = 0.1$	0	5.64×10^{-2}	5.64×10^{-2}	5.64×10^{-2}	5.64×10^{-2}	5.64×10^{-2}
	0.1	5.54×10^{-2}	5.45×10^{-2}	5.38×10^{-2}	5.31×10^{-2}	5.18×10^{-2}
	1	4.73×10^{-2}	4.05×10^{-2}	3.62×10^{-2}	3.24×10^{-2}	2.72×10^{-2}
	5	2.86×10^{-2}	1.78×10^{-2}	1.36×10^{-2}	1.10×10^{-2}	8.24×10^{-3}
	10	1.90×10^{-2}	1.02×10^{-2}	7.53×10^{-3}	5.94×10^{-3}	4.40×10^{-3}
$\beta = 1$	0	5.64×10^{-1}	5.64×10^{-1}	5.64×10^{-1}	5.64×10^{-1}	5.64×10^{-1}
	0.1	5.54×10^{-1}	5.46×10^{-1}	5.39×10^{-1}	5.31×10^{-1}	5.14×10^{-1}
	1	4.73×10^{-1}	4.02×10^{-1}	3.57×10^{-1}	3.18×10^{-1}	2.68×10^{-1}
	5	2.91×10^{-1}	1.86×10^{-1}	1.45×10^{-1}	1.19×10^{-1}	9.06×10^{-2}
	10	2.00×10^{-1}	1.12×10^{-1}	8.39×10^{-2}	6.69×10^{-2}	4.97×10^{-2}
$\beta = 10$	0	5.64	5.64	5.64	5.64	5.64
	0.1	5.58	5.61	5.61	5.53	5.18
	1	4.78	4.06	3.50	3.03	2.48
	5	3.04	2.04	1.63	1.37	1.10
	10	2.24	1.38	1.08	8.95×10^{-1}	7.02×10^{-1}

Table 5.6: Radial heat flow $q_r(r = \gamma)$ for Maxwell molecules with diffuse boundary conditions

	$\delta_0\gamma$	$\gamma = 1/2$	$1/5$	$1/10$	$1/20$	$1/65$
$\beta = 0.1$	0	5.64×10^{-2}	5.64×10^{-2}	5.64×10^{-2}	5.64×10^{-2}	5.64×10^{-2}
	0.1	5.54×10^{-2}	5.45×10^{-2}	5.38×10^{-2}	5.31×10^{-2}	5.18×10^{-2}
	1	4.78×10^{-2}	4.07×10^{-2}	3.64×10^{-2}	3.26×10^{-2}	2.74×10^{-2}
	5	2.89×10^{-2}	1.80×10^{-2}	1.38×10^{-2}	1.12×10^{-2}	8.40×10^{-3}
	10	1.93×10^{-2}	1.04×10^{-2}	7.69×10^{-3}	6.07×10^{-3}	4.49×10^{-3}
$\beta = 1$	0	5.64×10^{-1}	5.64×10^{-1}	5.64×10^{-1}	5.64×10^{-1}	5.64×10^{-1}
	0.1	5.55×10^{-1}	5.47×10^{-1}	5.41×10^{-1}	5.33×10^{-1}	5.16×10^{-1}
	1	4.82×10^{-1}	4.15×10^{-1}	3.71×10^{-1}	3.33×10^{-1}	2.83×10^{-1}
	5	3.12×10^{-1}	2.06×10^{-1}	1.63×10^{-1}	1.35×10^{-1}	1.04×10^{-1}
	10	2.21×10^{-1}	1.29×10^{-1}	9.75×10^{-2}	7.85×10^{-2}	5.89×10^{-2}
$\beta = 10$	0	5.64	5.64	5.64	5.64	5.64
	0.1	5.61	5.64	5.65	5.60	5.27
	1	5.09	4.52	3.99	3.50	2.91
	5	3.70	2.67	2.19	1.88	1.55
	10	2.94	1.98	1.60	1.36	1.11

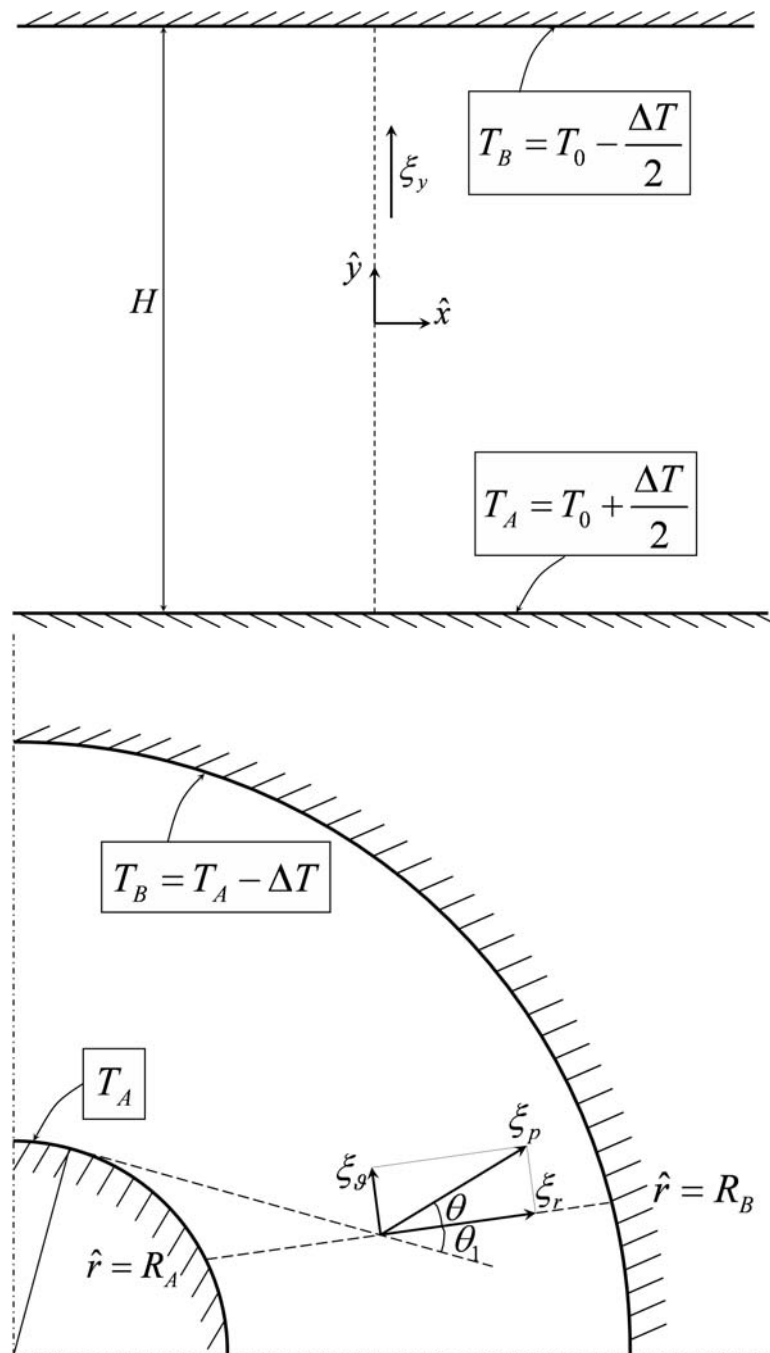


Figure 5.1: Geometry and coordinate system for the parallel plate (up) and coaxial cylinders (down) problems

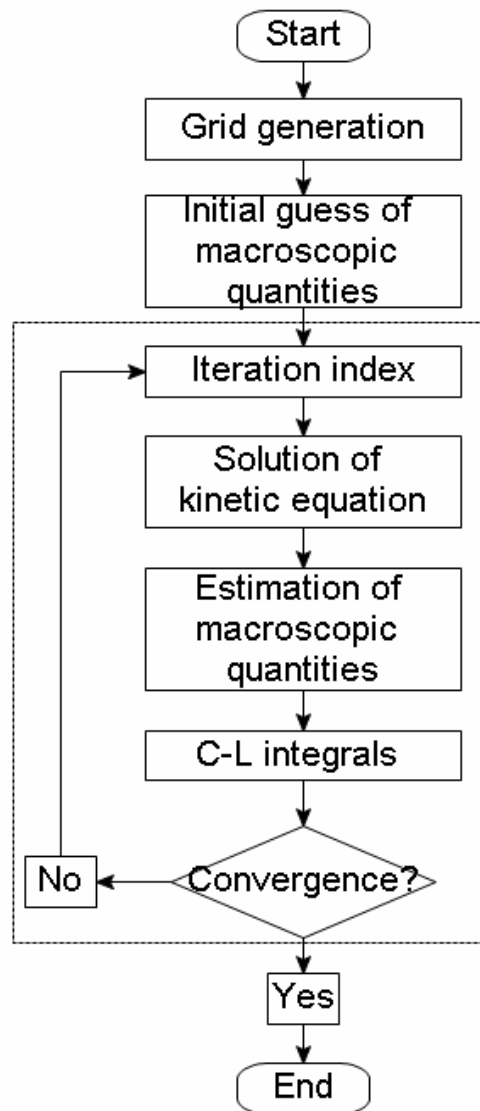


Figure 5.2: Flow diagram of the typical iteration algorithm

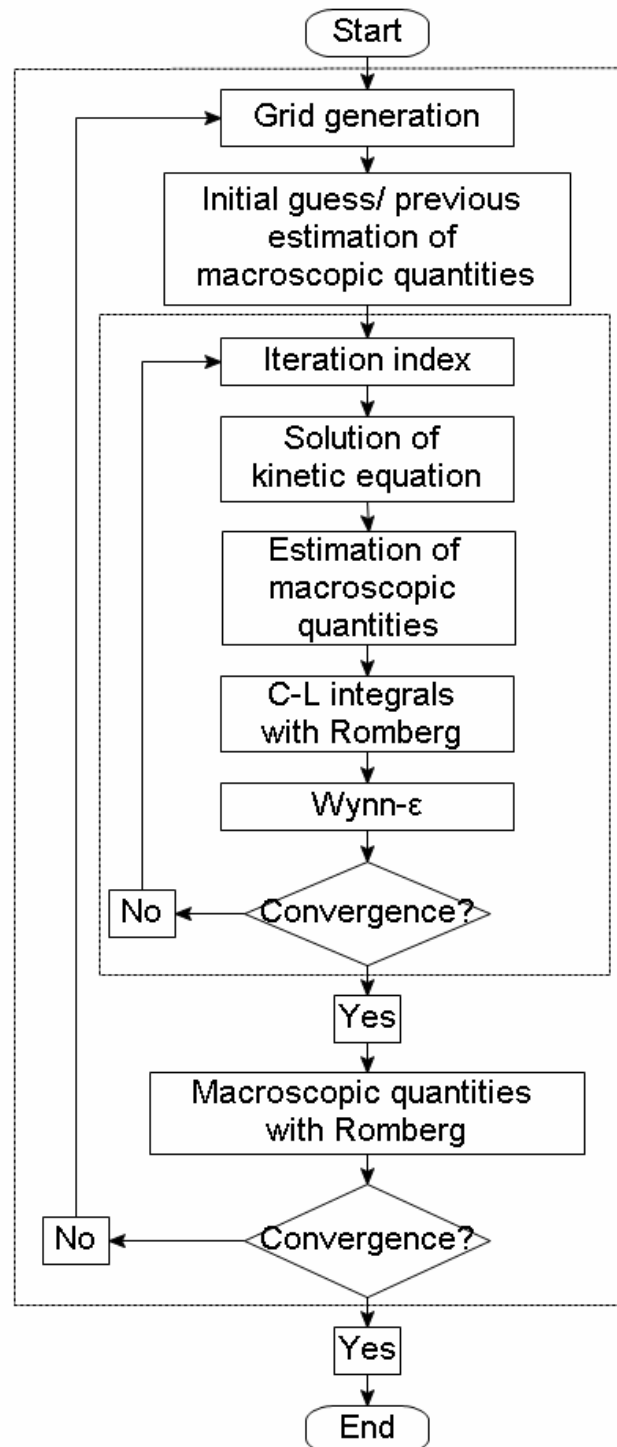


Figure 5.3: Flow diagram of the upgraded iteration algorithm

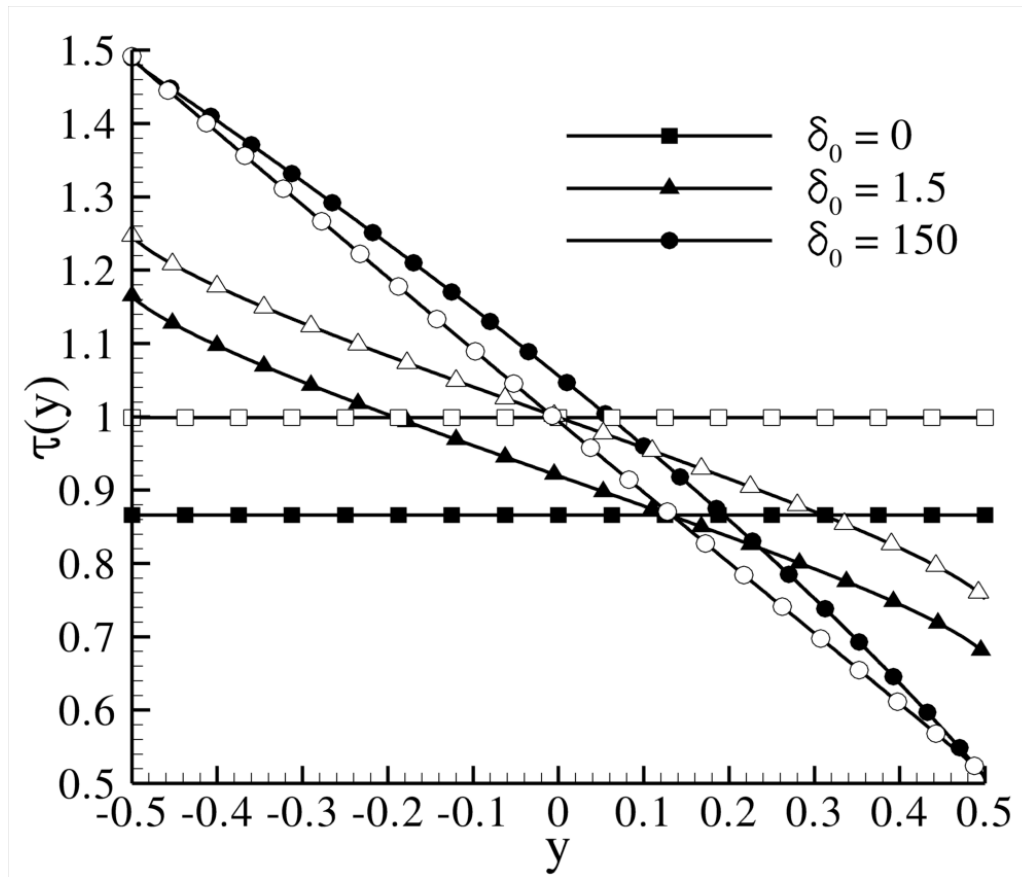


Figure 5.4: Linear (empty symbols) and non-linear (filled symbols) temperature profiles for various δ_0 with $T_A/T_B = 3$ ($\beta = 0.5$)

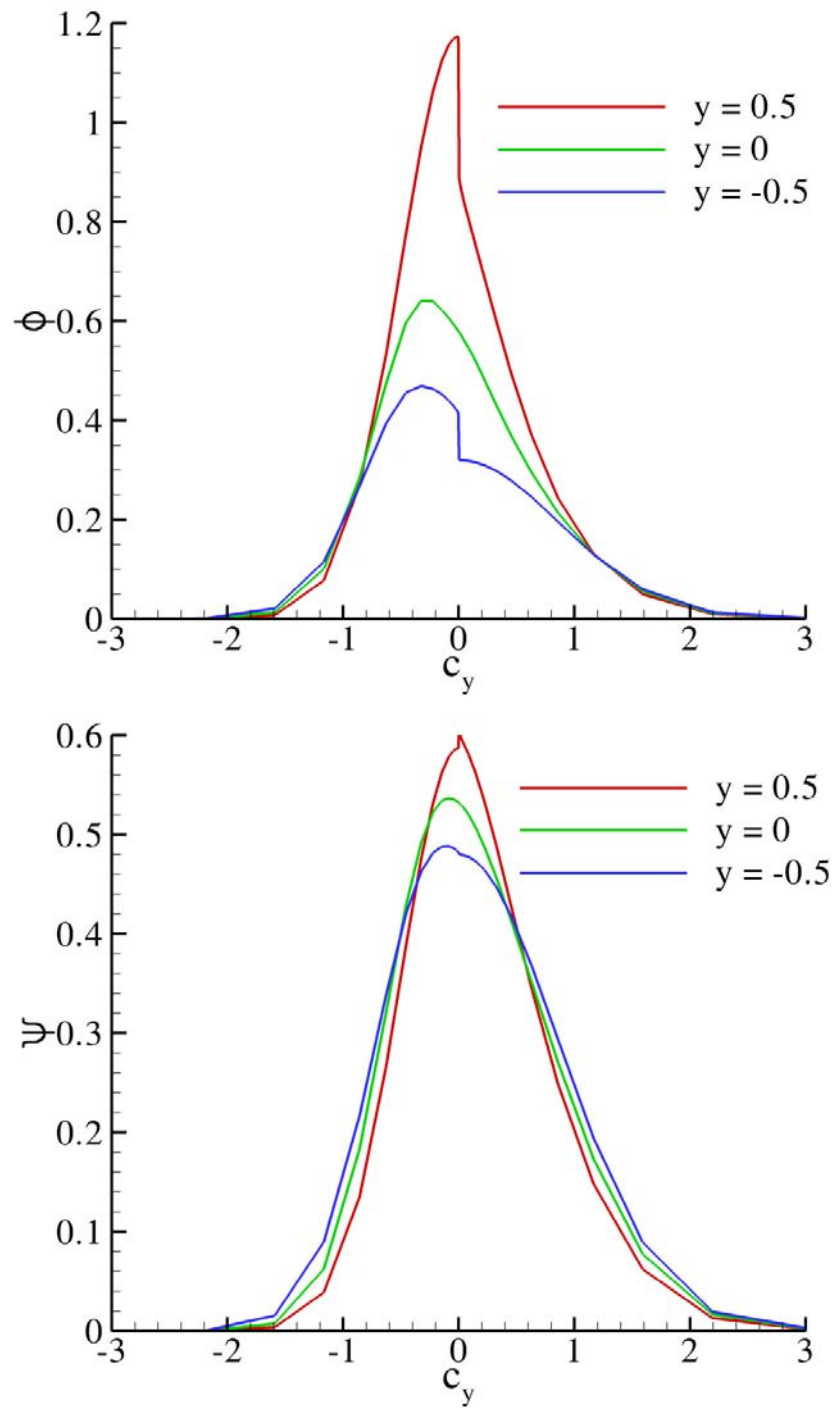


Figure 5.5: Reduced distribution functions φ (left) and ψ (right) in terms of the molecular velocity c_y at several locations between the plates for $\delta_0 = 1.5$ and $T_A/T_B = 3$ ($\beta = 0.5$)

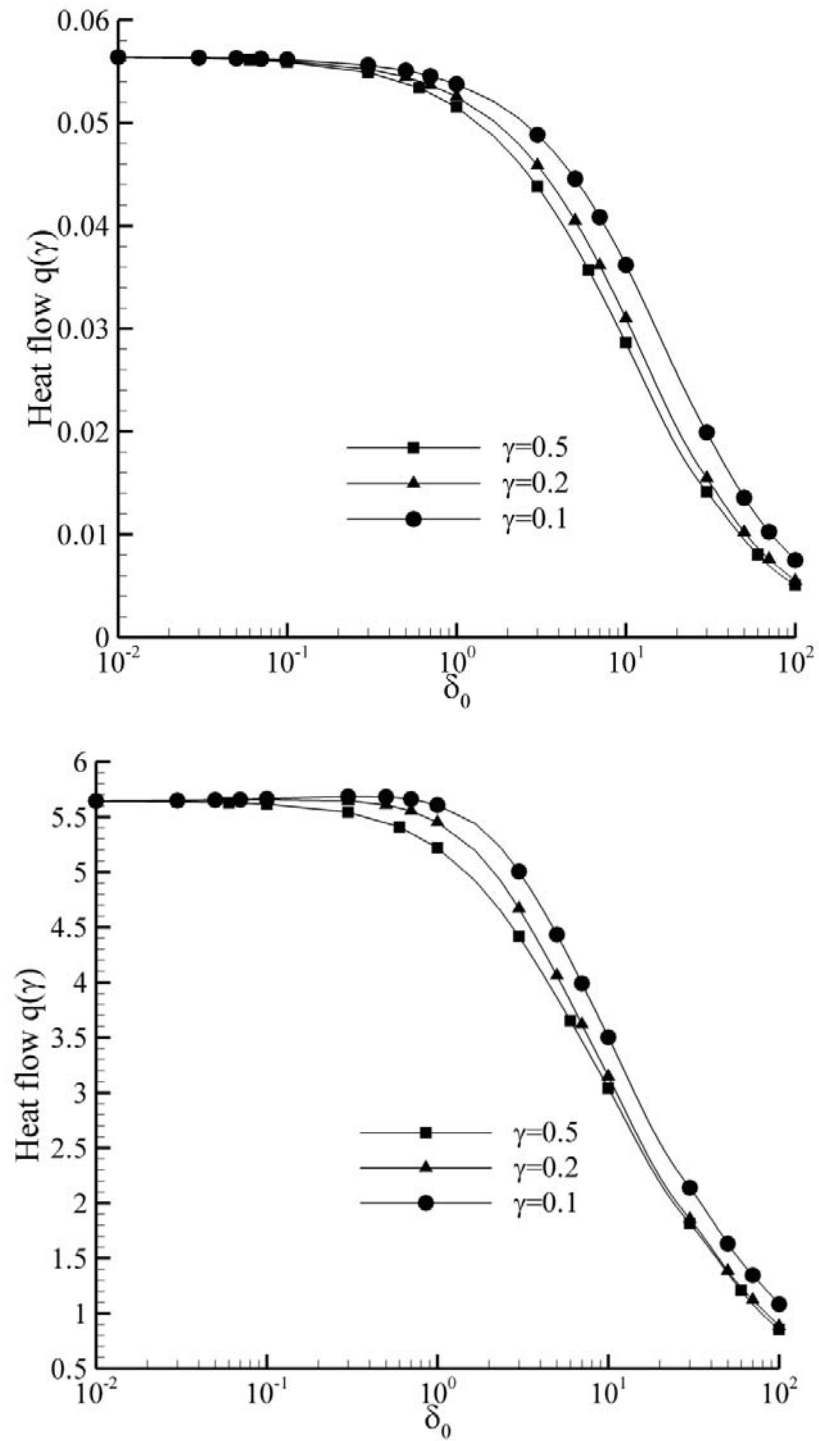


Figure 5.6: Dimensionless radial heat flow q_r at $r = \gamma$ in terms of δ_0 for various γ , with $\beta = 0.1$ (up) and $\beta = 10$ (down)

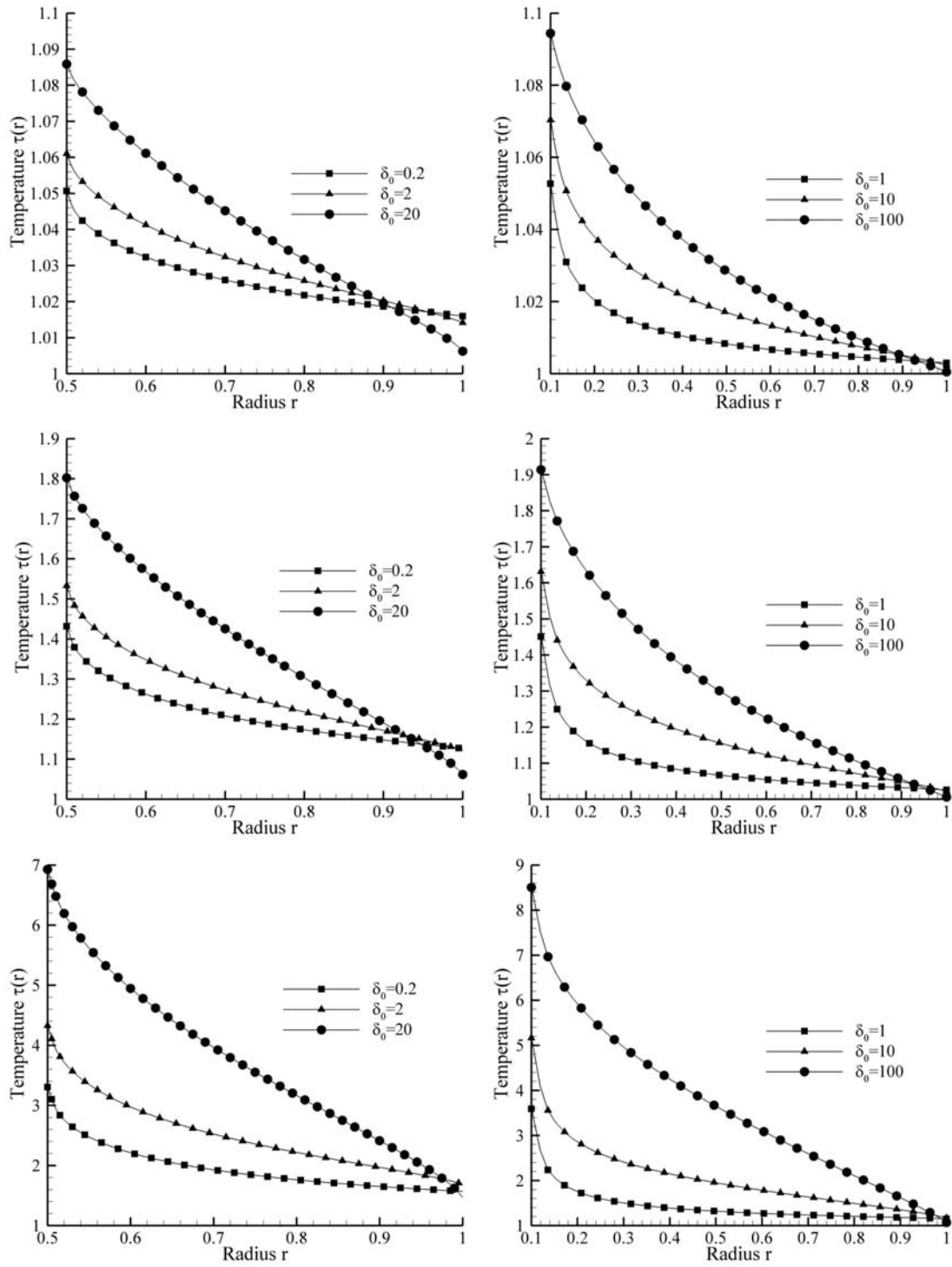


Figure 5.7: Dimensionless temperature profiles $\tau(r)$ for $\beta = 0.1$ (up), $\beta = 1$ (middle) and $\beta = 10$ (down), with $\gamma = 0.5$ (left) and $\gamma = 0.1$ (right)

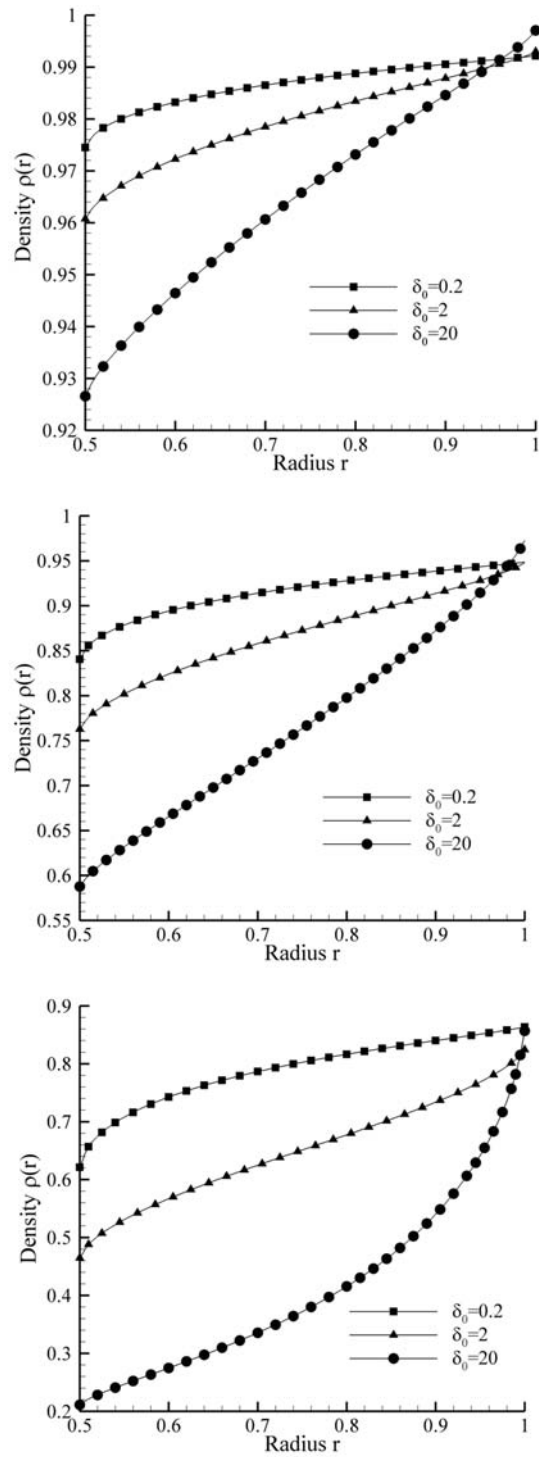


Figure 5.8: Dimensionless density profiles $\rho(r)$ for $\beta = 0.1$ (up), $\beta = 1$ (middle) and $\beta = 10$ (down), with $\gamma = 0.5$

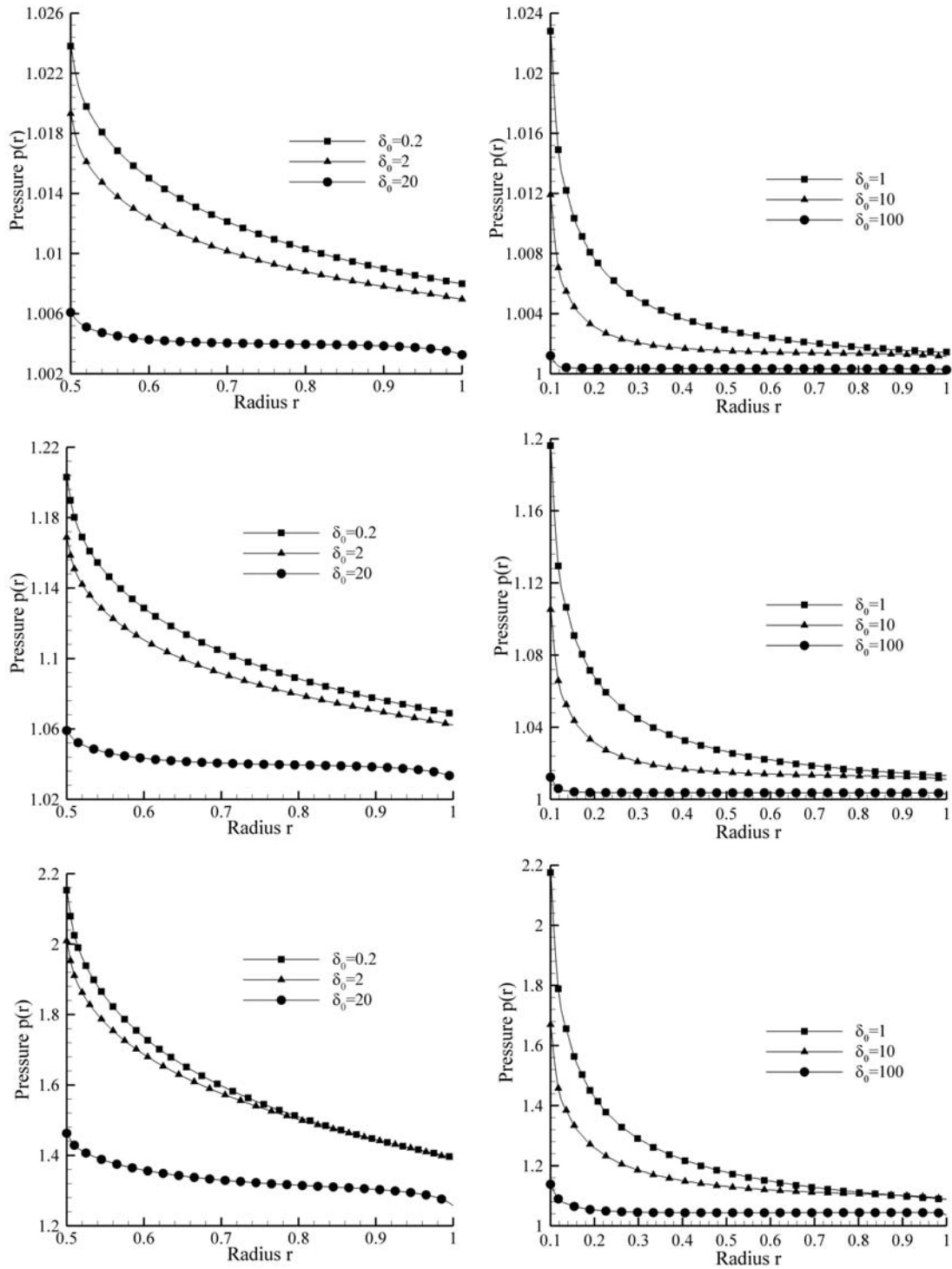


Figure 5.9: Dimensionless pressure profiles $p(r)$ for $\beta = 0.1$ (up), $\beta = 1$ (middle) and $\beta = 10$ (down), with $\gamma = 0.5$ (left) and $\gamma = 0.1$ (right)

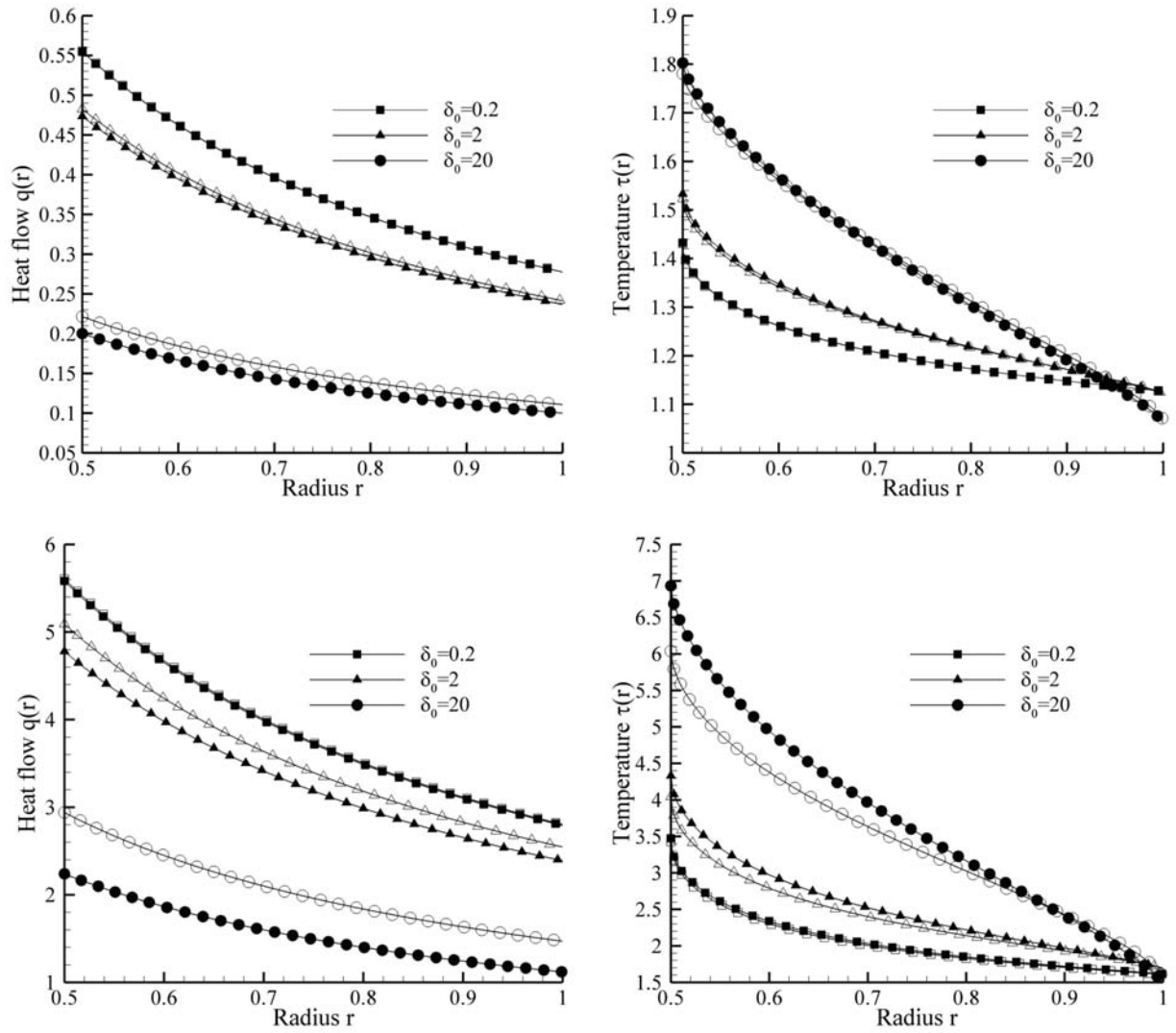


Figure 5.10: Dependence of the dimensionless radial heat flow and temperature distributions on the IPL coefficient ω for $\beta = 1$ (up) and $\beta = 10$ (down). Hard spheres ($\omega = 0.5$) are denoted with filled symbols and Maxwell molecules ($\omega = 1$) with empty symbols

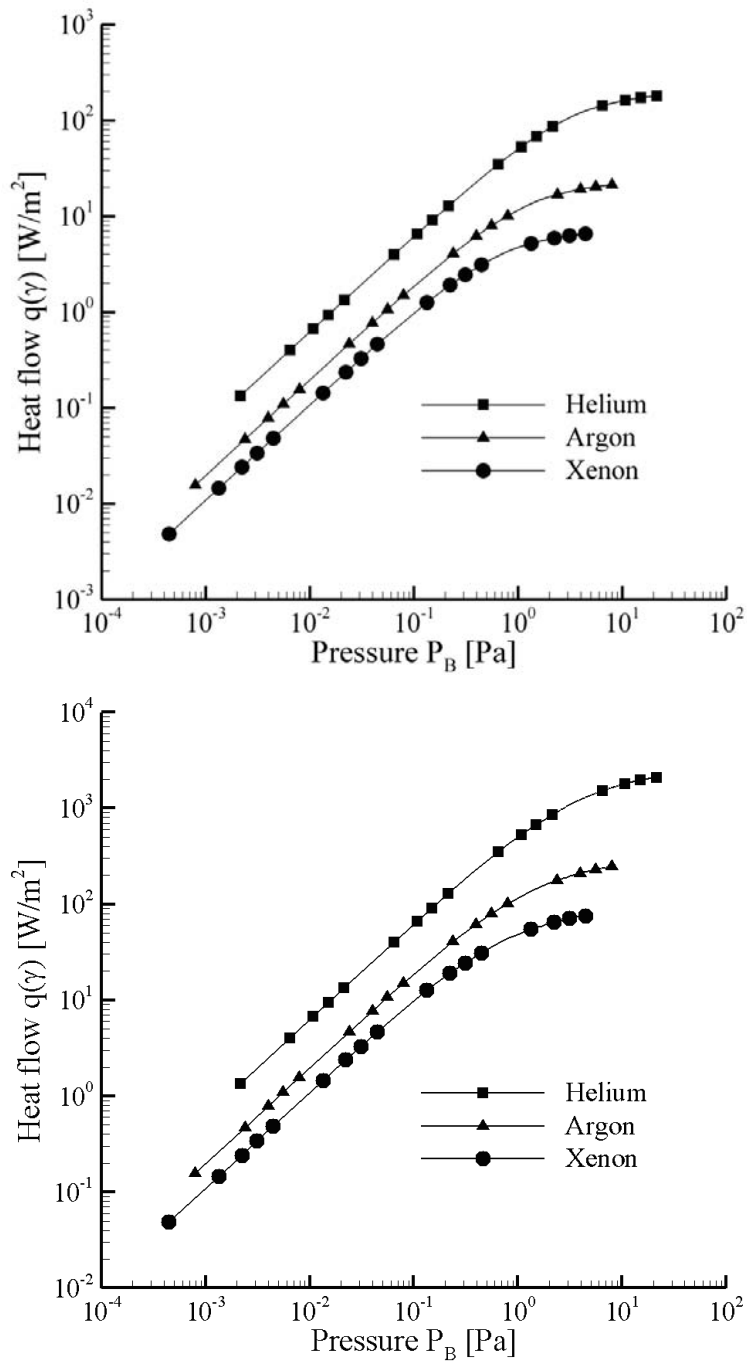


Figure 5.11: Dimensional radial heat flow through various gases in terms of the reference pressure P_B for $\gamma = 0.1$, with $\beta = 0.1$ (up) and $\beta = 1$ (down)

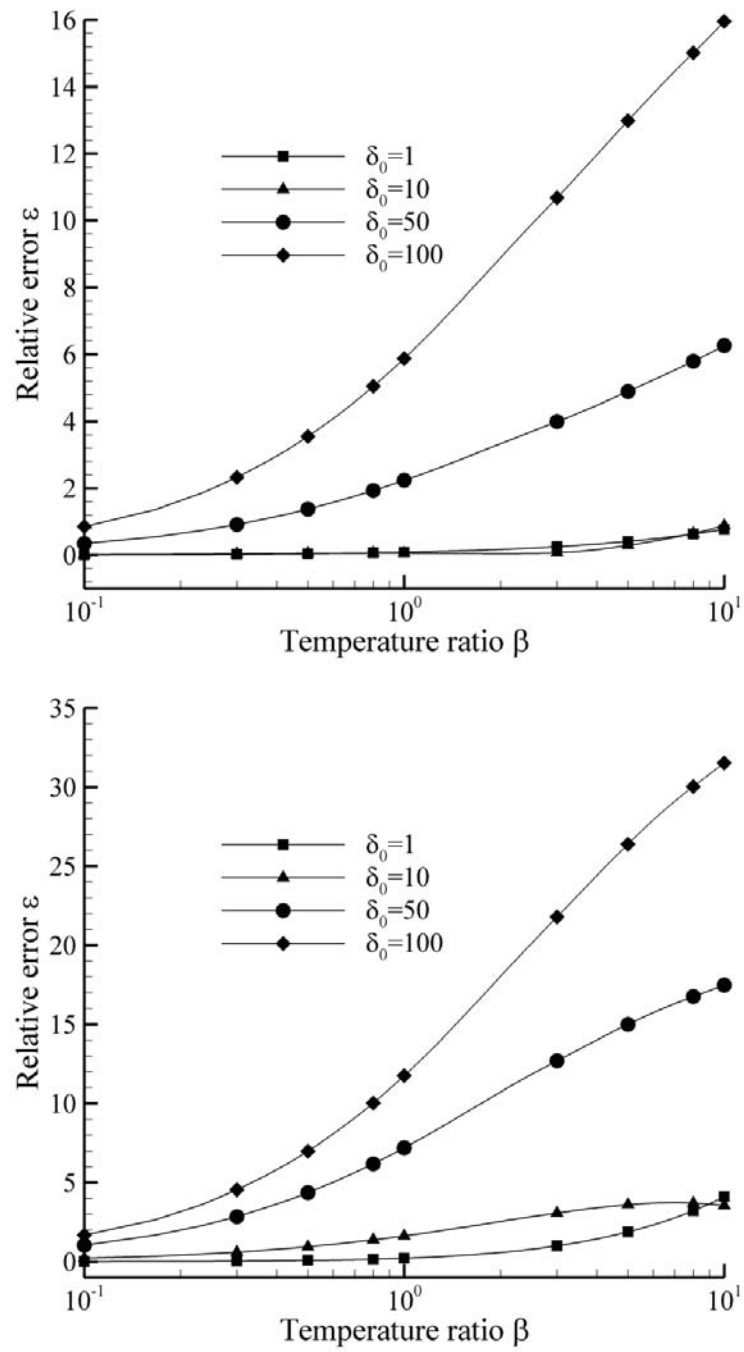


Figure 5.12: Relative error between nonlinear and linearized radial heat flow in terms of β for various δ_0 , with $\gamma = 0.5$ (up) and $\gamma = 0.1$ (down)

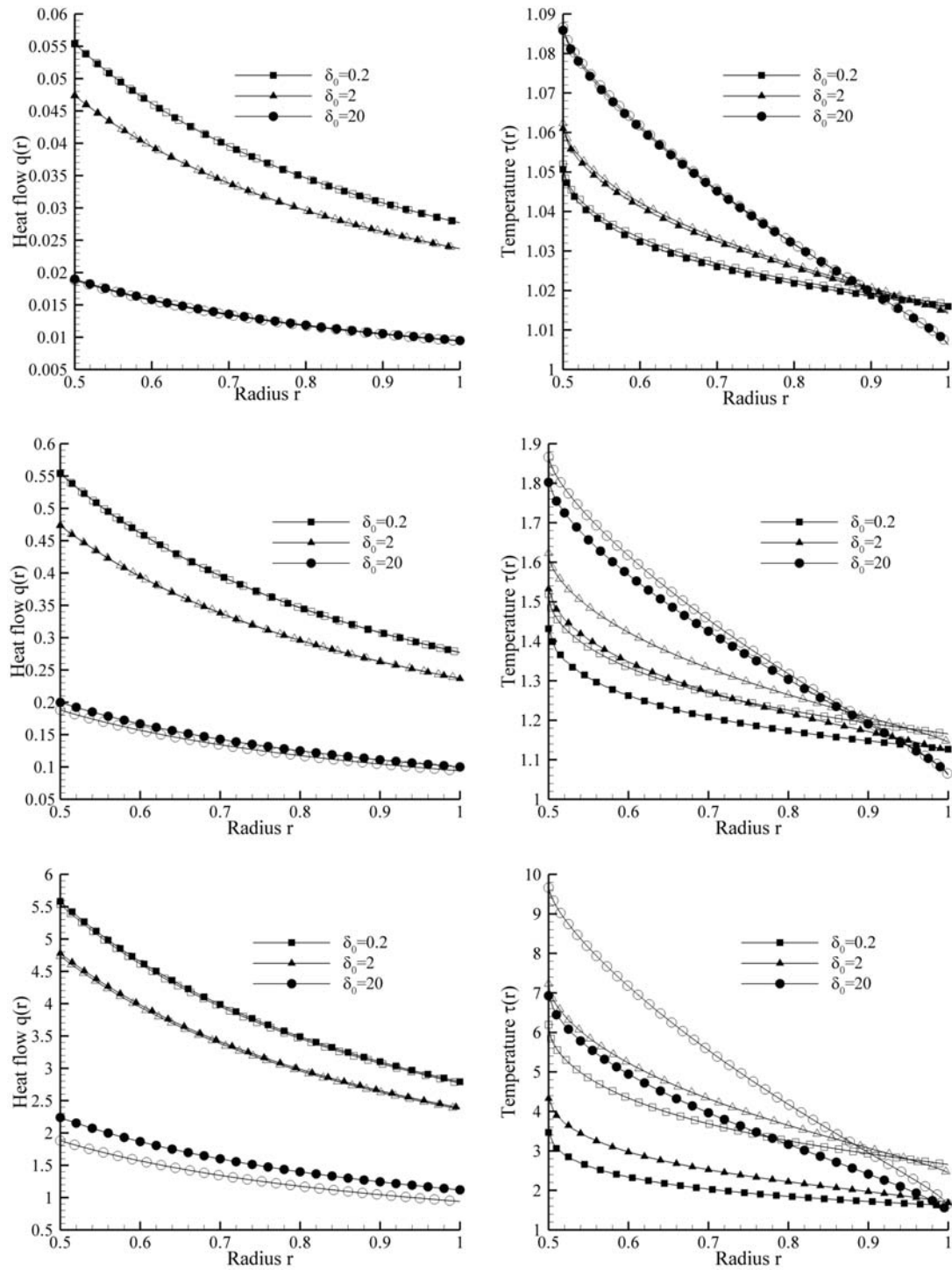


Figure 5.13: Dimensionless radial heat flow and temperature profiles using linearized (empty symbols) and nonlinear (filled symbols) analysis for $\beta = 0.1$ (up), $\beta = 1$ (middle) and $\beta = 10$ (down)

Chapter 6

Non linear flows

6.1 Introduction

The pressure driven flow problems examined in previous chapters concern only small pressure differences between the reservoirs or local gradients. These conditions allow the linearization of the kinetic equations, leading to a formulation of favourable mathematical properties. In order to simulate high speed flows, we must either use the non-linear form of the kinetic models or the DSMC method. In this chapter, both approaches have been used to study non-linear flow through short channel components, commonly found in micro-electro-mechanical systems and vacuum networks.

The ellipsoidal kinetic model equation, solved by the discrete velocity method, has been employed to tackle the problem of flow through a short cylindrical tube of isothermal or adiabatic walls. Even though this configuration has been considered in the past using the DSMC method [152], it would be useful to reexamine it under the scope of deterministic kinetic modelling to investigate for possible differences and their sources. We also provide an upgraded numerical scheme, significantly reducing memory consumption and computational effort. This is performed by an efficient marching scheme, similar to the one presented in Chapter 4 but augmented by Wynn- ε convergence acceleration, grid refinement and parallelization. A qualitative comparison with DSMC is also included for this problem, both in terms of flow rates and computational performance. Furthermore, another reason to consider this configuration is that a systematic study of non-linear transport is required in order to obtain a better understanding of the differences with the linearized formulation and the corresponding limitations. This is a key factor in developing a methodology which covers all possible physical conditions for the problem at hand.

Furthermore, the DSMC method has been used to simulate flow through an expansion/contraction

element, consisting of two consecutive tubes of different diameter connected in series. The existing in-house code has been adapted to the new geometry and new results are provided and compared with experiments. Our purpose is to examine the flow field produced for this configuration and high pressure differences and provide insight regarding the influence of each geometrical parameter. The DSMC method is chosen here since non-linear flow are more frequently encountered in practical applications for such geometries.

6.2 Kinetic formulation - Short tube flow

6.2.1 Introduction

In this section, we present the formulation for the non-linear, pressure driven, short tube flow. A detailed description of the problem is the following: Consider a monatomic rarefied gas stored in two large reservoirs connected by a cylindrical tube of radius R and length L , as shown in Figure 6.1. An arbitrarily large pressure difference is imposed between the two containers ($\hat{P}_{out} < \hat{P}_{in}$), causing flow of the gas through the tube. The walls and the gas in the container areas far from the tube are maintained at the same temperature T_0 .

In the following subsections, we present the derivation of the governing equations, the macroscopic moments and the boundary conditions. Their final forms are obtained in dimensionless form, using the ellipsoidal (ES) kinetic model equation. It is noted that the distribution function is five-dimensional for the current problem and no projection is possible. Finally, isothermal and adiabatic boundary conditions are formulated in the corresponding subsection.

6.2.2 Governing equations

The coordinate system in the physical space (\hat{r}, \hat{x}) and the molecular velocity coordinate system ($\xi_r, \xi_\vartheta, \xi_x$) coincides with the one given in Chapter 4 for the tube problem, given in Figure 4.2. The symbol ϑ denotes the direction perpendicular to the $\hat{r} - \hat{x}$ plane, while θ is the molecular velocity angle in the $\hat{r} - \vartheta$ plane. The computational domain includes a part of the containers upstream and downstream of the tube, since the channel is relatively short and the effects of flow entrance and exit

needs to be taken into account.

The starting point is the ES kinetic model equation [56], which has been found to exhibit significant advantages in comparison to its predecessor, the BGK model, such as the adjustment of the Prandtl number. In cylindrical coordinates it is expressed by

$$\xi_r \frac{\partial f}{\partial \hat{r}} - \frac{\xi_\vartheta}{\hat{r}} \frac{\partial f}{\partial \theta} + \xi_x \frac{\partial f}{\partial \hat{x}} = \nu (f^{ES} - f) \quad (6.1)$$

with $f = f(\hat{r}, \hat{x}, \xi_r, \xi_\vartheta, \xi_x)$ being the distribution function and ν is the collision frequency. The collision term is retained in its non-linear form with

$$f^{ES} = \frac{n}{\pi^{3/2}} \sqrt{|A|} \exp \left[- \sum_{i,j=1}^3 (\xi_i - \hat{u}_i) A_{ij} (\xi_j - \hat{u}_j) \right] \quad (6.2)$$

where

$$A = \left[(2k_B T \delta_{ij}) / (m \text{Pr}) - 2(1 - \text{Pr}) \hat{P}_{ij} / (nm \text{Pr}) \right]^{-1} \quad (6.3)$$

In the previous expression, Pr is the Prandtl number, k_B is the Boltzmann constant, m is the molar mass and δ_{ij} is the Kronecker delta. Also, n , T , $\hat{\mathbf{u}}$, \hat{P}_{ij} are the number density, temperature, gas bulk velocity and stress tensor components, respectively. By substituting $\text{Pr} = 1$ it can be seen that the BGK expression is retrieved. The characteristic value for monatomic gases, $\text{Pr} = 2/3$, has been used in the following calculations.

The left reservoir conditions, i.e. the number density n_{in} and pressure P_{in} , are chosen as reference quantities and are also denoted by n_0 , P_0 , with $P_0 = n_0 k_B T_0$ from the ideal gas law. Then, all quantities of interest are non-dimensionalized as follows:

$$\begin{aligned} r = \frac{\hat{r}}{R}, \quad x = \frac{\hat{x}}{R}, \quad \mathbf{c} = \frac{\boldsymbol{\xi}}{v_0}, \quad g = \frac{f v_0^3}{n_0}, \quad \rho = \frac{n}{n_0}, \quad \mathbf{u} = \frac{\hat{\mathbf{u}}}{v_0} \\ \tau = \frac{T}{T_0}, \quad \mathbf{q} = \frac{\hat{\mathbf{q}}}{P_0 v_0}, \quad P = \frac{\hat{P}}{P_0}, \quad P_{ij} = \frac{\hat{P}_{ij}}{P_0}, \quad i, j = r, \vartheta, x \end{aligned} \quad (6.4)$$

with $v_0 = \sqrt{2k_B T_0 / m}$ being the most probable molecular velocity and $\hat{\mathbf{q}}$ is the heat flux vector.

The collision frequency is given by the expression

$$\nu = \frac{P}{\mu} \text{Pr} \quad (6.5)$$

where μ is the dynamic viscosity. For hard sphere interaction, we may substitute $\mu_0/\mu = \sqrt{T_0/T}$, with μ_0 being the gas viscosity at reference temperature T_0 , and the ideal gas law $P = nk_B T$ to get

$$\nu = \delta_0 \rho \sqrt{\tau} \frac{v_0}{R} \text{Pr} \quad (6.6)$$

The reference rarefaction parameter δ_0 is also defined here as

$$\delta_0 = \frac{P_0 R}{\mu_0 v_0} = \frac{\sqrt{\pi}}{2} \frac{1}{\text{Kn}_0} \quad (6.7)$$

It is inversely proportional to the Knudsen number and therefore as δ_0 is increased the atmosphere becomes more dense (or less rarefied). The cases of $\delta_0 = 0$ and $\delta_0 \rightarrow \infty$ correspond to the free molecular and hydrodynamic limits respectively.

It is seen that the distribution function $g = g(x, r, c_r, c_\theta, c_x)$ can not be projected in the velocity space because all molecular velocity components are required. As a result, g depends on a total of five dimensions, similarly to the linearized tube problem of Chapter 4. The velocity vector is transformed into cylindrical coordinates $\mathbf{c} = (c_p, \theta, c_x)$ and the final form of the governing equation is

$$c_p \cos \theta \frac{\partial g}{\partial r} - \frac{c_p \sin \theta}{r} \frac{\partial g}{\partial \theta} + c_x \frac{\partial g}{\partial x} = \delta_0 \rho \sqrt{\tau} \text{Pr} (g^{ES} - g) \quad (6.8)$$

where the dimensionless ES model term becomes

$$g^{ES} = \frac{\rho}{\pi^{3/2}} \text{Pr}^{3/2} \sqrt{|K|} \exp \left[-\text{Pr} \sum_{i,j=1}^3 (c_i - u_i) K_{ij} (c_j - u_j) \right] \quad (6.9)$$

with

$$K = [\tau \delta_{ij} - (1 - \text{Pr}) P_{ij} / \rho]^{-1} \quad (6.10)$$

We only examine velocity angles in $\theta \in [0, \pi]$ since the distribution function is axisymmetrical.

For completeness purposes and since an indicative model comparison is presented in the results section, the BGK and S models, properly adjusted for the current problem, are also presented here.

The g^{ES} term in Equation (6.8) is substituted by

$$g^{BGK} = \frac{\rho}{(\pi \tau)^{3/2}} \exp \left[-\frac{(\mathbf{c} - \mathbf{u})^2}{\tau} \right] \quad (6.11)$$

$$g^S = g^{BGK} \left\{ 1 + \frac{4}{5\rho\tau^2} (1 - \text{Pr}) \mathbf{q} \cdot (\mathbf{c} - \mathbf{u}) \left[\frac{(\mathbf{c} - \mathbf{u})^2}{\tau} - \frac{5}{2} \right] \right\} \quad (6.12)$$

The collision frequency in these cases

$$\nu_{BGK,S} = \delta_0 \rho \sqrt{\tau} \frac{v_0}{R} \quad (6.13)$$

does not contain the Prandtl number.

6.2.3 Macroscopic quantity moments

The macroscopic quantities are also non-dimensionalized, leading to the following expressions:

$$\rho = 2 \int_0^\infty \int_0^\pi \int_{-\infty}^\infty c_p g dc_x d\theta dc_p \quad (6.14)$$

$$\tau = \frac{4}{3\rho} \int_0^\infty \int_0^\pi \int_{-\infty}^\infty c_p [(c_p \cos \theta - u_r)^2 + (c_p \sin \theta)^2 + (c_x - u_x)^2] g dc_x d\theta dc_p \quad (6.15)$$

$$u_x = \frac{2}{\rho} \int_0^\infty \int_0^\pi \int_{-\infty}^\infty c_p c_x g dc_x d\theta dc_p \quad (6.16)$$

$$u_r = \frac{2}{\rho} \int_0^\infty \int_0^\pi \int_{-\infty}^\infty c_p^2 \cos \theta g dc_x d\theta dc_p \quad (6.17)$$

$$P_{ij} = 2 \int_0^\infty \int_0^\pi \int_{-\infty}^\infty c_p (c_i - u_i) (c_j - u_j) g dc_x d\theta dc_p \quad (6.18)$$

$$q_x = 2 \int_0^\infty \int_0^\pi \int_{-\infty}^\infty c_p [(c_p \cos \theta - u_r)^2 + (c_p \sin \theta)^2 + (c_x - u_x)^2] (c_x - u_x) g dc_x d\theta dc_p \quad (6.19)$$

$$q_r = 2 \int_0^\infty \int_0^\pi \int_{-\infty}^\infty c_p [(c_p \cos \theta - u_r)^2 + (c_p \sin \theta)^2 + (c_x - u_x)^2] (c_p \cos \theta - u_r) g dc_x d\theta dc_p \quad (6.20)$$

Vector/tensor components containing the ϑ -direction once, i.e. $u_\vartheta, p_{r\vartheta}, p_{z\vartheta}, q_\vartheta$, are equal to zero, while $p_{\vartheta\vartheta}$ is not. Pressure can be obtained by $P = \rho\tau$.

The main quantity of interest is the mass flow rate through the tube \dot{M} and our aim is to calculate it for a wide range of the parameters characterizing the flow: the reference rarefaction parameter δ_0 , the channel aspect ratio L/R and the pressure ratio $P_{out} = \hat{P}_{out}/\hat{P}_{in}$. For the current problem, the mass flow rate is found by

$$\dot{M} = 2\pi \int_0^R [mn(\hat{x}, \hat{r})] \hat{u}_x(\hat{x}, \hat{r}) \hat{r} d\hat{r} \quad (6.21)$$

The flow rate is non-dimensionalized by the analytical free molecular solution for flow through an orifice

$$\dot{M}_{FM} = \frac{R^2 \sqrt{\pi} \hat{P}_{in}}{v_0} \quad (6.22)$$

which is obtained by the method of characteristics. Results are presented for the dimensionless flow rate

$$W = \frac{\dot{M}}{\dot{M}_{FM}} = 4\sqrt{\pi}G \quad (6.23)$$

where the reduced flow rate

$$G|_x = \int_0^1 u_x(x, r) r dr \quad (6.24)$$

is obtained from the numerical simulations. The analytical derivation of these expressions is found in Appendix 2.

6.2.4 Boundary conditions

The incoming boundary distributions at the free surfaces (A),(B),(F),(G) have a Maxwellian form, with a number density value obtained by the corresponding container conditions $\rho = P/\tau$ or the condition of no wall penetration. Incoming molecules from all non-specular boundary surfaces conform to

$$g^+ = \frac{C}{(\pi\tau)^{3/2}} \exp\left(-\frac{c^2}{\tau}\right) \quad (6.25)$$

In the following, we discern between the following situations:

- Isothermal flow

Due to the reference value selection, we have $\tau_{in} = \tau_{out} = 1$ for all boundary surfaces, leading to

$$C_{in} = \rho_{in} = 1 \quad (6.26)$$

for the left and

$$C_{out} = \rho_{out} = P_{out} \quad (6.27)$$

for the right container Maxwellian distributions. Furthermore, on the walls we have

$$C_w = \rho_w \quad (6.28)$$

where the ρ_w constants are found by imposing the impermeability condition ($u_{normal} = 0$) for diffuse boundary conditions. This condition leads to

$$\rho_w = -\frac{I_{impinging}}{I_{departing}} \quad (6.29)$$

with

$$I_{departing}|_a = \frac{1}{\pi^{3/2}} \int_{c_{x1a}}^{c_{x2a}} \int_{\pi-\theta_{2a}}^{\pi-\theta_{1a}} \int_0^\infty \exp(-c_p^2 - c_x^2) [c_p \phi_a(\theta, c_p, c_x)] dc_p d\theta dc_x \quad (6.30)$$

$$I_{impinging}|_a = \int_{-c_{x2a}}^{-c_{x1a}} \int_{\theta_{1a}}^{\theta_{2a}} \int_0^\infty g^- [c_p \phi_a(\theta, c_p, c_x)] dc_p d\theta dc_x \quad (6.31)$$

The subscript $a = C, D, E$ is used to discern between the wall surfaces, according to the letters shown in Figure 6.1. The possible values for the above quantities are

$$C : \theta_{1C} = 0, \theta_{2C} = \pi, c_{x1a} = -\infty, c_{x2a} = 0, \phi_C(\theta, c_p, c_x) = c_x$$

$$D : \theta_{1D} = 0, \theta_{2D} = \pi/2, c_{x1a} = -\infty, c_{x2a} = \infty, \phi_D(\theta, c_p, c_x) = c_p \cos \theta \quad (6.32)$$

$$E : \theta_{1E} = 0, \theta_{2E} = \pi, c_{x1a} = 0, c_{x2a} = \infty, \phi_E(\theta, c_p, c_x) = c_x$$

These expressions are obtained in a procedure very similar to the one used in Chapter 4 for the linearized equations, elaborated in Appendix 1.

- Adiabatic flow

The case of adiabatic flow can also be considered by imposing a second condition at the walls, besides the usual one of no wall penetration: the condition of zero normal heat flux. Since the temperature is unknown for adiabatic walls, we may consider it as an adjustable parameter. Therefore, we have two parameters (ρ_w, τ_w) for each wall, which we use to impose the desirable conditions ($u_{normal} = q_{normal} = 0$). In order to avoid solving numerically the resulting system of equations, which would lead to a considerable computational effort at each iteration, we solve the departing integrals analytically in this case. The resulting expressions are

$$\rho_{w,i} = \frac{4\sqrt{\pi}}{\sqrt{\tau_{w,i}}} s A_i, \tau_{w,i} = \frac{B_i - A_i u_t^2}{2A_i}, i = C, D, E \quad (6.33)$$

$$A_C = \int_0^\infty \int_0^\pi \int_0^\infty c_x c_p g^- dc_p d\theta dc_x \quad (6.34)$$

$$A_D = \int_{-\infty}^\infty \int_0^{\pi/2} \int_0^\infty c_p^2 \cos \theta g^- dc_p d\theta dc_x \quad (6.35)$$

$$A_E = \int_{-\infty}^0 \int_0^\pi \int_0^\infty c_x c_p g^- dc_p d\theta dc_x \quad (6.36)$$

$$B_C = \int_0^\infty \int_0^\pi \int_0^\infty c_p c_x (\mathbf{c} - \mathbf{u})^2 g^- dc_p d\theta dc_x \quad (6.37)$$

$$B_D = \int_{-\infty}^\infty \int_0^{\pi/2} \int_0^\infty c_p c_r (\mathbf{c} - \mathbf{u})^2 g^- dc_p d\theta dc_x \quad (6.38)$$

$$B_E = \int_{-\infty}^0 \int_0^\pi \int_0^\infty c_p c_x (\mathbf{c} - \mathbf{u})^2 g^- dc_p d\theta dc_x \quad (6.39)$$

where $s = 1$ for walls C,D, $s = -1$ for wall E and u_t is the wall tangential velocity (u_r for walls C,E and u_x for wall D). A detailed derivation is included in Appendix 1.

At all cases, specular reflection is imposed at the center due to the axial symmetry.

$$g^+(0, x, c_p, \theta, c_x) = g^-(0, x, c_p, \pi - \theta, c_x) \quad (6.40)$$

for angles in $\theta \in [0, \pi/2]$.

6.3 The Discrete Velocity numerical method and its optimization

6.3.1 Introduction

In the following subsections, we discuss the derivation of the discretized equation, the numerical algorithm and the modifications applied to complete the simulations more efficiently. In particular, we discuss the Wynn- ε algorithm and the technique of grid refinement, which reduce the total computational time by at least an order of magnitude. Other numerical details, such as the discretization parameters and convergence criteria are also given.

6.3.2 Numerical scheme

The discrete velocity method is applied in the molecular velocity space. The continuum spectra of c_p and c_x are discretized by the Legendre polynomial roots mapped in $[0, c_{p,max}]$ and $[0, c_{x,max}]$ respectively, while the molecular velocity angles are uniformly distributed in $[0, \pi]$.

A second order finite volume scheme has been applied here for the discretization of the governing equation (6.8) in the physical and angular spaces. The final expression is derived by integrating in r, θ, x for an arbitrary discretization interval, in the same way as in Appendix 3 for the linearized equations, and is displayed in Table 6.1. Note that the ES model terms $g_{i,j,k}^{ES,(l,m)}$, the local rarefaction parameter $\delta_0 \rho_{i,k} \sqrt{\tau_{i,k}}$ and the radius r_i depend on the physical coordinate indices of all nodes surrounding the discretization interval, in a manner occurring naturally through this procedure. The discretized expression is also usable at $r = 0$ after the application of the l'Hospital rule to eliminate $1/r$ terms.

The solution procedure is iterative, leading to the determination of the distribution function. The discrete velocity typical algorithm steps may be summarized as follows:

1. At first, a reasonable assumption is made for the distributions of various macroscopic quantities, such as ρ , \mathbf{u} , τ , \mathbf{q} and P_{ij} .
2. The kinetic model term is calculated from Equation (6.9) (or Equations (6.11) and (6.12) for the BGK and S models), using the macroscopic variables.
3. The discretized equations are solved, using a marching scheme and the macroscopic quantities.
4. The new values for the distribution function are used to generate new values for the bulk quantities via the corresponding moments, Equations (6.14) - (6.20).
5. Steps 2 - 4 are repeated until a proper convergence criterion, imposed on the bulk quantities, is satisfied.

The only difference with previously shown algorithms is the calculation of the kinetic model term at each point in the 5-dimensional phase space.

The advanced marching algorithm described in Chapter 4 for the linearized tube problem is identical to the one used here. Since it has been previously presented in detail, we will just outline its main characteristics here. The improved memory management leads to a reduction in the dimension of the distribution function array from five to two dimensions. The size of this array is determined by the height of the entrance/exit regions and the number of the molecular velocity angles. A small difference with the linearized tube scheme is that two additional temporary arrays need to be allocated for the calculation of the collisional model term in the current and previous columns. The code is also parallelized for the velocity magnitudes only, since the distribution function values of various velocity angles are not independent with each other as explained in Chapter 4, and each processor solves the kinetic equation for a group of velocities. Macroscopic quantities and impermeability constants are transmitted to all processors at the end of each iteration.

6.3.3 Further improvements in the numerical algorithm

The accuracy and convergence of the numerical method have been improved by using the Wynn- ε algorithm [156, 157]. The Wynn- ε algorithm is a strongly nonlinear sequence accelerator, applied in regular iteration intervals on the bulk quantities to obtain a converged solution faster. In particular, the macroscopic quantities at each physical point and the impermeability constants form sequences which gradually lead to the converged values. The convergence of a sequence S_j , $j = 1, \dots, J$, composed of an odd number of terms J , can be accelerated by inserting them in a table whose even columns are estimations of the sequence limit

$$\varepsilon_{l+1}^{(j)} = \varepsilon_{l-1}^{(j+1)} + \left[\varepsilon_l^{(j+1)} - \varepsilon_l^{(j)} \right]^{-1} \quad (6.41)$$

with $\varepsilon_{-1}^{(j)} = 0$ and $\varepsilon_0^{(j)} = S_j$. In this table, the even columns contain accelerated values and the best estimation is located in the element $\varepsilon_J^{(1)}$.

It is important to numerically monitor the values of each sequence and evaluate if it is appropriate to apply the acceleration method or not. For this purpose, we check if the minimum and maximum values of the sequence are the first and last terms (or the other way around), since a non-monotonic curve may lead to an erroneous result. Moreover, approximations of the first and second derivatives are found using points of the sequence and are used to ensure that it is converging. The absolute value of the second derivative must also be above a certain value to ensure that the trend is not exactly linear. In our calculations a quite low value is chosen for the second derivative ($10^{-8} - 10^{-11}$) since for large delta the changes in most macroscopic quantities are very slow, nearly linear with a very small gradient, even for a wide iteration interval. Finally, the sign of the estimated value is checked if density or temperature is considered.

The application of the above technique can greatly decrease the number of iterations near the hydrodynamic regime. Furthermore, *false convergence* effects appearing in large δ_0 are significantly reduced. Finally, another important feature of this method is that it can also be easily applied with linearized kinetic equations after minor modifications, or in fact with any numerical method which includes an iterative scheme.

Another technique that has to be used due to the very large computational effort is physical grid refinement. Initially, the physical mesh is uniformly distributed with only 5 intervals per unit length in every direction. The simulation is performed with this grid and, after convergence has been reached, it is repeated in a refined mesh, where the number of intervals at each physical direction has been doubled, using the previous solution as an initial condition. This procedure is repeated until the final number of nodes has been reached, in order to avoid a large number of iterations for the dense grid, leading to great savings for large values of δ_0 .

The discretization parameters used are displayed in Table 6.2. Finally, it is noted that the convergence criterion is the average residual per physical node, defined as in Chapter 4

$$\text{residual} = \frac{1}{4N_{total}} \sum_{i=1}^{N_{total}} [|\rho_i - \rho_i^{pr}| + |\tau_i - \tau_i^{pr}| + |u_{x,i} - u_{x,i}^{pr}| + |u_{r,i} - u_{r,i}^{pr}|] \quad (6.42)$$

where N_{total} is the total number of physical nodes and the pr superscript denotes quantities in the previous iteration.

6.4 DSMC formulation - Flow through an expansion/contraction element

6.4.1 Introduction and problem description

We also investigate the problem of flow through a channel with sudden expansion/contraction via the DSMC method. This is another application of DSMC in a more complex geometry. This work is useful in various configurations of vacuum engineering and design. It is motivated by the need of estimating the mass flow rate and pressure difference under conditions encountered in practical applications.

Consider a monatomic, rarefied gas, confined in two containers held at different pressures \hat{P}_{in} and \hat{P}_{out} , with $\hat{P}_{in} > \hat{P}_{out}$ and identical temperatures T_0 . The containers are connected by a contraction or expansion element, i.e. an element consisting of two cylindrical tubes of different diameters connected in series. Due to the pressure difference, there is gas flow through the element. The pressure gradient direction may be oriented either from the tube of the larger diameter towards the smaller one or vice versa, causing sudden contraction or expansion of the flow respectively. Since the channels

considered here are short, the finite length effect is considered by including virtual computational regimes at the entrance and exit of the element, representing a part of the reservoirs upstream and downstream. The geometry and coordinate system are displayed in Figure 6.2. Results include various bulk quantities of practical interest, such as channel conductances, as well as distributions of density, temperature and velocity.

6.4.2 The DSMC method

In the DSMC algorithm, the main hypothesis is that at each discrete time interval, particle motion and intermolecular collisions are considered as two independent, uncoupled steps. If the time interval is smaller than the mean free time between collisions, the method produces physically realistic results. The physical space domain is discretized into cells, which are used to track particles and calculate the bulk properties. The boundary conditions are imposed by properly adjusting the velocity of particles departing from the boundary surfaces, resulting to specular, diffuse or symmetry conditions. The intermolecular collision pairs are chosen randomly, with the probability being proportional to the collision cross-section and the relative velocity.

The steps of the DSMC algorithm can be briefly described as follows:

1. The geometrical characteristics (radii, lengths and region sizes), the numerical parameters (number of computational particles, time step, cell discretization) and the flow conditions (such as δ_0 , P_{out}) are provided as input to the numerical code.
2. The positions and velocities of molecules are assigned values according to an initial assumption of the macroscopic quantity fields. In particular, the molecules are placed uniformly inside each cell, their number being dependent on the pressure of the left container for $x < (L_1 + L_2)/R_1$ and the right container pressure for $x > (L_1 + L_2)/R_1$. The distribution of their velocities is a Maxwellian according to the reference temperature T_0 and the local density.
3. The free motion of particles is considered, using simple relations of the form

$$\mathbf{x} - \mathbf{x}_0 = \mathbf{c}\Delta t \quad (6.43)$$

where x_0, x are the initial and final positions, c is the velocity vector and Δt is the time interval. The boundary conditions are performed in the same step: molecules leave and enter the domain from the open boundaries, scatter at the walls according to the gas-surface interaction model of our choice or are projected in the $x - r$ plane to take into account the axisymmetry. The number of molecules entering the domain from each free surface is approximately

$$N_{free} = \frac{1}{4} A_{free} n_{free} v_m \Delta t \quad (6.44)$$

with A_{free} being the free surface area through which the molecules pass, n_{free} is the number density conditions at the corresponding container and $v_m = \sqrt{(8k_B T_0)/(m\pi)}$ is the mean molecular velocity. In the steady state of the problem, the total incoming flow of computational particles through the free surfaces is equal to the total outgoing flow.

4. The particles undergo a number of binary collisions, found by an appropriate model. The collision partners are selected randomly from the molecules located at the local area of the corresponding cell (also called a sub-cell), in order to ensure that only molecules in proximity to each other are selected as collision partners. The number of collisions is found by an appropriate model. The molecule pairs subject to the collision are chosen with a probability equal to

$$P_{coll} = F_N \sigma_T c_r \Delta t / V_{cell} \quad (6.45)$$

Thus, the number of collisions is proportional to the ratio of real to computational molecules F_N , the collision cross-section σ_T and the relative velocity c_r , the time step Δt and the volume of the cell V_{cell} . This probability is further divided by $P_{coll,max}$, which is the same quantity for the maximum value of $\sigma_T c_r$ inside each cell. The post-collision velocities are chosen so that the principles of momentum and energy equilibrium are satisfied.

5. The cell and sub-cell of each particle are registered in relative arrays, in order to be used in the collision and bulk quantity calculation steps.

6. Macroscopic quantities ϕ_{cell} are calculated at the center of each cell by properly combining the properties of computational particles. Since we are interested in the steady state of the flow, we can average the sample in time after ensuring that the macroscopic quantities do not change any more. This should not be performed in every time step in order to avoid correlations between consecutive time instances.
7. The computational time is advanced by an interval Δt and steps 3-6 are repeated, until we are certain that the steady state has been reached. This is measured by examining the statistical fluctuations of macroscopic flow rates.

Results include dimensionless flow rates and macroscopic quantity field contours, defined as in Equations (6.23) and (6.4) respectively. Also, the comparison with experimental data is performed in terms of the conductance, given by

$$C = \frac{R_u T_0}{m(P_{in} - P_{out})} \dot{M} \quad (6.46)$$

where R_u is the universal gas constant.

6.4.3 Numerical details

The DSMC numerical code developed for the solution of flow through a short tube [152] has been extended for the geometry of interest. The 3-level cell grid shown in Figure 6.3 has been adopted in the DSMC simulations to capture the large macroscopic gradients and possible vortices near the corner. The dimensions of the upstream and downstream computational regions have been taken equal to $8R_1 \times 8R_1$ for both containers.

In problems of this kind, due to the projection of the axisymmetrical domain on the $x - r$ plane and the large pressure drop, the number of computational particles in some cells may not be sufficiently high to obtain meaningful statistical quantities. For this reason, several weighting zones have been used both in the radial and axial directions to obtain a better distribution of model particles and a high degree of accuracy in the whole domain. When molecules pass through these virtual surfaces, they may be cloned or eliminated depending on the direction of their movement, in order to keep an

adequate number of particles per cell. The number and position of weighting zones, as well as other important numerical parameters such as the number of particles, are given in Table 6.3.

Moreover, in order to reduce the required simulation time to reach the steady state, the number of computational particles initially distributed in the domain was 25% of the final number. After a certain amount of time (10 dimensionless time units in our calculations), the number of particles is doubled and the sampling arrays are cleared. This procedure is repeated after another 10 dimensionless time units and finally, the sampling arrays are re-initialized once more after the same interval.

In our calculations, the non-time counter scheme (NTC) has been employed for the calculation of particle collision pairs. According to this model, the number of probable collision pairs is

$$N_{pairs} = \frac{1}{2} N \bar{N} F_N (\sigma_T c_r)_{max} \Delta t / V_{cell} \quad (6.47)$$

where \bar{N} is the time average of the molecules in the cell. After the determination of each collision pair, it is accepted or rejected according to Equation (6.45), divided by the maximum probability in that cell. Finally, the Hard-Sphere model is chosen for the intermolecular potential, while purely diffusive scattering is assumed at the walls.

6.5 Results

6.5.1 Introduction

In the following subsections, we present results on the bulk quantity fields, flow rates and conductances. Furthermore, the performance of the numerical codes is evaluated, by means of the number of iterations, parallelization speed-up and CPU time. In subsection 6.5.2 we discuss the problem of flow through a short tube, while subsection 6.5.3 concerns the contraction/expansion element. It is noted that the supercomputing facility of Juelich research center in Germany provided the necessary computational resources for the simulations with the non-linear scheme, while the DSMC calculations and single core non-linear runs have been performed in the cluster of the rarefied gas dynamics group of the department.

6.5.2 Flow through a tube

6.5.2.1 Flow rates and field distributions

The most important quantity for practical applications is the dimensionless flow rate W , shown in Table 6.4 for a wide range of the governing parameters. As seen in previous studies [152], the flow rate drops as the rarefaction parameter is decreased or as the length and pressure ratio are increased. The free molecular analytical solution (Appendix 6) is also obtained with very good accuracy. The Knudsen minimum is not observed for the length and pressure difference range examined here. It is also quite interesting to examine the similarities of the values for $P_{out} = 0.9$ with the linearized flow rates, presented in Chapter 4 (Table 4.5). In order to have a direct comparison, the values shown here must be multiplied with the conversion factor $1/(1 - P_{out}) = 10$. Even though they have been obtained using different kinetic models, the flow is nearly isothermal for such a slow flow and both models provide accurate results. The deviations between the values shown in the two tables drop significantly as the channel length increases or the rarefaction parameter decreases. This is to be expected, since the flow becomes more linearized and is another confirmation of the validity of both codes. Furthermore, this is another indication that the linearized formulation is valid for a linearization range larger than it may be expected by the strict mathematical limits.

A comparison with previous DSMC results shows some discrepancies. The flow rates of [149, 152], presented in Table 6.5 for $P_{out} = 0.1, 0.5, 0.9$ where they are available, display deviations between 0.7 % and 7.1%. It is important to note that the largest discrepancies occur in situations which are closer to equilibrium (such as when $P_{out} = 0.9$ or $L/R = 10$), where the DSMC method is highly affected by numerical noise and a great computational effort is required to get reliable results. In other cases, where the problem conditions are further away from thermodynamic equilibrium (such as $L/R \leq 1$), the maximum discrepancy is around 4 % in the transition regime. This is attributed to the limitations of the ellipsoidal kinetic model, since the post-collision distribution function probably does not conform to the prescribed modified Maxwellian for such non-linear flows. A second factor which may influence the results in this regime is the mis-treatment of the distribution function discontinuity. However, it has been seen in the past [195] (and it has been confirmed in our studies) that for

integrated quantities, such as the flow rate, the ray effects tend to cancel each other out and the integrated quantity is smooth if it is plotted along, say, the x-axis, even with no particular treatment. The two factors discussed here are estimated to be responsible for 1-2 %, while the remaining discrepancy may be due to the much smaller size of computational regions for the two containers in the DSMC studies. It must be noted that our purpose here is not to make a direct comparison with DSMC. Due to the existence of many variants of the DSMC algorithm and the stochastic nature of the method, it is difficult to ensure that the comparison will take place on the same basis.

In order to evaluate the differences between various kinetic models and justify our selection of the ES model, the dimensionless flow rate is given in Table 6.6 for the BGK and S model, in direct comparison with the values in Table 6.4. It is seen that the differences are relatively small (lower than 4%) and are based on the capability of each model to describe non-isothermal flows.

Some cases for the linearized flow through the cylindrical tube, presented in Chapter 4, have also been reproduced using the non-linear form of the BGK model. A pressure ratio value of $P_{out} = 0.99$ has been chosen to achieve the linearized state for two length values, namely $L/R = 1$ and 5. The resulting flow rates are shown in Table 6.7. In order to perform this comparison, the values shown here must be multiplied with $1/(1 - P_{out}) = 100$ in order to correspond to the flow rates shown in Table 4.5. A very good agreement is then observed, with the maximum deviation being 0.5 % for $\delta \leq 5$ and 2.3 % for $\delta_0 = 10$. An important note here is that the convergence criterion must be more strict in such pressure ratios, since it is based on absolute quantities. The general agreement observed here is another indication of validity for both codes. Furthermore, it is another important advantage of the non-linear model equations, since they are found to work very well even in this case, which is very difficult to simulate with the DSMC method. In fact, the non-linear kinetic solver works even better for small pressure ratios, since the initial conditions imposed here are very close to the final state: the density is nearly linear with a very small area affected in the containers, the temperature is practically equal to unity everywhere and the velocity is nearly zero. Thus, a very low number of iterations is required for the convergence of the code.

The density and axial velocity fields, as well as the streamlines, are also presented for some indicative cases. At first, the dependence on δ_0 is shown. In Figures 6.4 - 6.6, the values $\delta_0 = 0.1, 1, 10$ are examined for some highly non-linear cases, with a pressure ratio $P_{out} = 0.1$ and $L/R = 0$. It is seen that as the rarefaction parameter increases, the density field becomes unsymmetrical due to the increase of the Re number, found by $Re = Ma \times \delta$ from Equations (2.16) and (2.18), while also dropping slightly more abruptly. The axial velocity increases along with the rarefaction parameter and takes quite high values after the orifice ($L/R = 0$), up to $Ma = 0.92$. The ray effects are quite strong in the low rarefaction fields due to the large discontinuity of the distribution function. Concerning the streamlines, they also become less symmetric as the gas becomes denser and a vortex appears near the wall of the downstream container for $\delta_0 = 10$. On the other hand, some cases of slow flows are also given in Figures 6.7 - 6.9 for the same values of δ_0 , for $L/R = 10$ and $P_{out} = 0.9$. It is seen that they display symmetrical properties and close resemblance to the linearized field plots of Chapter 4. The density and streamline plots are nearly identical to each other and the only real difference is found on the magnitude of the gas velocity.

The dependence on the tube length is given in Figures 6.10-6.12, for $L/R = 0, 5, 10$, $P_{out} = 0.5$ and $\delta_0 = 10$. These cases are chosen here since the differences become more apparent, due to the high rarefaction parameter: as the tube becomes longer, the vortex becomes smaller, the velocity magnitude drops and the density isolines become nearly vertical inside the tube. The same characteristics are seen for increasing pressure ratio from 0.1 up to 0.9 in Figures 6.13 - 6.15 for $L/R = 1$ and $\delta_0 = 2$. The approach to symmetry is particularly apparent in these cases for the axial velocity contours.

Results on flow through a tube with adiabatic walls are also presented here. Some representative flow rate values are given in Table 6.8. The adiabatic flow rate is lower for the orifice geometry and higher for $L/R = 1$ in comparison to the isothermal values of Table 6.4. However, in most cases, the two tables present very similar values. Nearly all significant figures are the same for $\delta_0 \leq 0.1$, while the maximum deviation in the condition ranges examined appears for $\delta_0 = 20$ and $L/R = 1$ (around 1.3 %). Therefore, we limit this study to the similarities and differences observed in the fields.

An indicative plot for the normal heat flux along the tube boundary, in order to verify the correct application of the boundary conditions, is given in Figure 6.16 for $L/R = 1$, $\delta_0 = 20$, $P_{out} = 0.5$. It is seen that the heat flux is zero only for the adiabatic formulation, in the whole boundary except the two ends. The latter characteristic is easily explained if we consider that q_r is no longer perpendicular to the wall at the corners and is allowed to be non-zero along the vertical walls. Density and axial velocity field contours for the same case are given in Figures 6.17 and 6.18. It is seen that, in the case of the adiabatic tube, the density drops faster at the downstream container, the bulk velocity magnitude is lower and the vortex is significantly smaller. It has been seen that the wall heat permeability properties have a negligible effect on flows of small Re (i.e. small δ_0 or larger L/R) due to the already low heat fluxes.

6.5.2.2 Computational performance

The computational time ranged between few hours and few days, depending on the rarefaction parameter, the pressure ratio and the availability of processors. Several aspects of the numerical code performance are examined in this subsection, such as parallelization, memory consumption, acceleration, etc.

The speed-up S (CPU) obtained by the parallelization, defined here as

$$S \text{ (CPU)} = [\text{Time (8)} \times 8] / [\text{Time (CPU)} \times \text{CPU}] \quad (6.48)$$

with CPU being the number of processors, is displayed in Figure 6.19, using a number of CPUs varying from 16 to 256. The simulation time for eight processors has been taken as a reference, since this is the minimum number of processors that can be allocated in the Juelich supercomputing center. The scaling characteristics of the algorithm are quite good, considering the number of variables that have to be exchanged at each iteration. An average efficiency of about 94% for 64 processors and 75% for 256 processors is calculated. It is expected that a secondary parallelization in the spatial coordinates as well would further reduce the cost of exchanging information, since only a part of the domain would be stored (and transmitted) at each computational node. It is noted that Wynn- ε acceleration has not been

applied while timing the simulations in order to obtain a more accurate picture of the performance of the code.

The benefits of starting with a sparse grid and gradually refining it are seen in Table 6.9. The solution of each grid level is used as an initial condition for the simulation of the next level. Linear interpolation has been used here to connect the solutions of various grid levels as a first approximation. It is clear that the gain in the number of iterations for large values of δ_0 is significant and could further increase if a more advanced interpolation technique had been used. The iterations in dense grids are two orders of magnitude lower than the corresponding sparse grid number, leading to much lower simulation times.

The effect of Wynn- ε acceleration is demonstrated through an indicative case ($L/R = 1$, $\delta_0 = 10$, $P_{out} = 0.1$) shown in Figure 6.20. The evolution of the residual is plotted against the number of iterations for both a normal and an accelerated run. Both cases follow the same course for the first 500 iterations, to allow for a transitional stage before applying the acceleration scheme. Then, the sequence terms are collected every two iterations until 81 terms have been collected. Finally, Equation (6.41) is applied at iteration 660 as shown in Figure 6.20, causing an abrupt spike in the residual of the accelerated run. However, after this step, the residual of the accelerated run drops dramatically, leading to convergence in less than half the iterations required for a normal run. This improvement is also displayed in Table 6.9, where it can be seen that the application of the Wynn- ε scheme reduces the number of iterations for sparse grids up to 64 %.

The benefits of the algorithm modifications noted here are better appreciated by making a comparison of the computational time. The required CPU time in hours is presented in Table 6.10 for the execution of four different runs. In the first one, a single CPU is used and the modifications of parallelization, multiple grids and Wynn- ε are deactivated. Sixteen processors in parallel (MPI) are employed for the second run. The third column concerns runs with the grid refinement technique activated and in the fourth one the Wynn- ε acceleration has been additionally applied. The numerical parameters for this table are quite different than the normal simulations to ensure that the single core

runs would be executed in a realistic amount of time. The differences with Table 6.2 are $N_x = N_r = 100$, $M = 12$, $N_\theta = 100$. In cases 3 and 4, the physical grid is initially $N_x = N_r = 25$ and obtains its final resolution in two steps. Finally, the upstream/downstream regions had a size of 8×8 . It must also be stressed here that the specifications of the computer used in the single run (Case 1) are quite different than the ones used in the parallel runs (Cases 2,3,4). Therefore, this table only represents an indication on the efficiency of each approach, rather than the scaling and exact performance of the code. It is observed that the CPU time is drastically reduced from the single run when 16 processors are used, especially for large δ_0 . Furthermore, a dramatic improvement is also observed when multiple grid levels are considered: the total time is reduced by at least 76 %. Finally, the benefits of the Wynn- ε scheme are not so apparent for the cases shown here because it is mostly applied on the low grid levels. However, judging from corresponding cases for the problem of non-linear heat transfer between cylinders, it is expected that it would be much more useful near the hydrodynamic regime.

The number of iterations required for various δ_0 , L/R and P_{out} values are given in Figure 6.21 for five grid levels. Some fluctuations are to be expected in the sparse grid levels 1 and 2 due to the application of the Wynn- ε scheme. As it is expected, the number of iterations for the dense grid drops as the flow becomes more linear, i.e. as P_{out} increases because of the favourable selection of the initial conditions (linear density distribution along the tube, zero velocity, temperature equal to unity). However, it increases for longer tubes due to the larger number of impermeability constants that need to be stabilized. Furthermore, a large length to radius ratio practically means a narrow geometry, causing larger convergence times because of the difficulties in the transport of the gas from one vessel to the other. The increase of the reference rarefaction parameter δ_0 also leads to an increase of the number of iterations, as commonly seen in discrete velocity numerical codes.

An analysis on the total computational time required for each of the elementary parts of the algorithm is presented in Table 6.11. These values have been obtained by averaging the corresponding times in a variety of runs. It is seen that the calculation of the macroscopic quantities and the Maxwellian distribution are the most time-consuming parts due to the complicated exponential ex-

pressions they contain. The parallel communication cost is quite low here since the results concern 16 processors but may be increased for a very large number CPUs. The diffuse boundary conditions take up a very small part of the total time. Finally, miscellaneous computational work, including the allocation of arrays, the application of the Wynn- ε algorithm, the calculation of the residual, the temporary storage of the field to restore in case of unexpected shutdowns, etc. also takes up a relatively small part of the total effort.

Memory requirements for some indicative discretizations are shown in Table 6.12. A moderately long channel of $L/R = 10$ is taken as a test case with a relatively dense discretization. It is seen that memory consumption remains low as we modify the channel length and the number of discrete velocity magnitudes or angles, even to extremely large values such as $L/R = 200$. This is quite reasonable given the structure of the modified algorithm storage scheme. It is seen that it is significantly affected by the container region size and the number of physical nodes but in any case not in a restrictive degree, given the availability of computational resources today. This is a very important advantage of the code, leading to the conclusion that channels of any length can be simulated with it, especially if we consider that flow through long channels is low and thus the container regions can become even smaller.

6.5.2.3 Qualitative comparison with DSMC

It is hard to provide a definite conclusion regarding which numerical approach performs best, the DSMC or the DVM for non-linear kinetic equations. The reason is that there is a great deal of parameters that need to be fine-tuned in order to have numerical simulations corresponding exactly to one another and some who only exist in one of the two methodologies. Some examples of the variables that need to be adjusted are the fluctuation level, residual, number and position of weighting zones, time intervals of particle doubling or sampling array resetting, grid refinement parameters, Wynn- ε parameters, the number of discrete velocity angles and magnitudes, number and shape of cells, number of intervals per unit length, non-uniformity of mesh/cell grid, number of particles, time step, maximum value of the velocity magnitude. It is obvious that the two approaches are largely different and we can

only make a qualitative comparison.

Other difficulties arise in this effort to determine the fastest method: the memory requirements of the DSMC code can be very high for an accurate calculation, if computational regions of size 15×15 dimensionless units are used. Also, since the DSMC code is not yet parallelized (and even if it were, there would be significant difficulties in distributing the load evenly among the processors [85]), a comparison of this size would take up a significant amount of time. Thus, we restrain ourselves in the runs given in Table 6.10 while including the cases of $P_{out} = 0.9$ and $\delta_0 = 1, 10$.

In Figures 6.22 and 6.23 the evolution of the flow rate at the two ends is plotted against the computational time for the two methods. The abrupt changes for the DSMC code are due to the doubling of computational particles, shown explicitly in the Figures, performed to produce a rough estimation of the flow field. For the DVM, there are also changes in the flow rate, even though much smaller, due to the refinement of the grid. It is observed that both methods produce practically convergent values in comparable CPU times for $P_{out} = 0.1$. A conclusion on which method performs best in this case would be highly subjective, since several parameters such as the convergence criterion for each grid level and the doubling times are chosen rather intuitively. However, it is clear that the computational difficulties grow for DSMC when $P_{out} \geq 0.5$ is considered. On the other hand, the DVM works even better in this regime.

Thus, we may conclude that both methods work equally well for high pressure differences and short channels. The DSMC method may be slightly more accurate than the non-linear kinetic models as expansion into vacuum is approached, due to its equivalence with solving the Boltzmann equation and its ability to deal with discontinuities of the distribution function. As the pressure ratio becomes larger (say, $0.5 \leq P_{out} \leq 0.9$), the non-linear kinetic equations should be more reliable and much faster in convergence. Finally, in the case of very low pressure differences ($P_{out} \geq 0.9$) and highly rarefied flows ($\delta_0 \leq 10$), the Monte Carlo method is completely out of the question, unless some special treatment takes place [83], and the non-linear equations provide accurate results within even lower computational times. In the latter case, the linearized results of Chapter 4 can also be utilized to

avoid a complete simulation.

6.5.3 Flow through an expansion/contraction element

Due to the large number of parameters involved in this problem (δ , P_{out}/P_{in} , R_2/R_1 , L_1/R_1 , L_2/R_1), it would be very difficult to tabulate and present results for every possible parameter combination. Moreover, in many cases there are similarities with the flow through a simple tube, examined in detail before in previous sections. A qualitative analysis on the influence of each parameter may be inferred by examining some representative geometrical cases, given in Table 6.13. Indicative results are presented, demonstrating the applicability of the DSMC code, and will be extended in future work.

Field distributions of density and velocity, as well as streamlines, are shown in Figures 6.24 - 6.31 for both channel types. The gas behaviour is typical for the expansion of the gas to a lower pressure. A decrease in density and an increase in velocity are observed after the entrance of the channel at $x = 0$, returning to their equilibrium values after a short distance from the channel exit. In the first case, Figures 6.24 - 6.25, the field quantities are shown for the expanding channel element and a moderate radius ratio ($R_2/R_1 = 2$). The results are quite similar to the ones found for the single tube, with the exception of a small vortex forming at the corner of the expansion for large δ . Furthermore, if we compare these results with Figures 6.26 - 6.27, where the second case geometry with a higher radius ratio ($R_2/R_1 = 5$) is studied, we can see that only small differences exist regarding the density and axial velocity fields (even in terms of maximum values and contour levels). This practically means that the field is not affected in a large degree by adjusting the radius ratio to a value higher than 2. On the contrary, the streamlines are inevitably altered significantly by the change in geometry. The most striking difference lies in the shape of the vortex for $\delta = 10$, which spans at a much larger area and has a non-elliptic shape around the second tube exit. Regarding the contracting tube, the two geometrical cases 3,4 are shown in Figures 6.28 - 6.31 to describe the influence of the length increase on the flow field. It seems that as the length increases, the first (large) tube also does not play an important role on the flow field, since the left container equilibrium values are also observed in a large part of the first channel. The appearance of noise is strong in the most demanding cases, such as in the streamlines at

the left container part in Figure 6.31 due to the low pressure difference and the approach to equilibrium values in that area. A considerable computational effort would be required to reduce the noise in this case.

The flow rates W , defined by (6.23) but calculated as a function of molecules passing through the inlet and outlet cross-sections, are given for some indicative cases in Table 6.14. The similarities with corresponding values in Table 6.5 are evident for the expansion element and the agreement is even better as we further enlarge the second tube. This is not true in the contraction part, since it is the narrower tube part dimension that plays the most important role in the flow rate value. The trends are the same as the flow through a short tube, described earlier, regarding the pressure ratio, length and δ influence.

Typical conductance results shown below concern the geometry used in the experiments, where $R_1 = 10.4\text{mm}$, $L_1 = 9\text{mm}$, $R_2 = 20.7\text{mm}$, $L_2 = 14.9\text{mm}$. The upstream pressure P_{in} ranges in $0.003 - 30\text{ Pa}$ and nitrogen is used in average temperature $T_0 = 296\text{K}$. Conductance curves are displayed in Figure 6.32, obtained by both numerical and experimental approaches. Experimental measurements have been performed at the TRANSFLOW facility of KIT in Germany, described in section 3.3. It is seen that overall the agreement is good, with an average relative error below 10%, especially in the viscous regime (small Kn number). Larger discrepancies appear in the transition and free molecular regime, where the pressure is reduced and the accuracy of the measurements is strongly affected by the offset deviation of each flow device. This is probably a consequence of experimental inaccuracies and will be clarified in the near future.

Rathakrishnan and Sreekanth [164] have also studied this type of flow before experimentally for the case of the tube with a sudden expansion. However, the channels used in this particular investigation were relatively long (the geometrical parameters for the shortest one were $L_1/R_1 = 2$, $L_2/R_1 = 3.68$) and the Knudsen number is quite low for most cases (0.0026 to 1.75), leading to computational difficulties. Furthermore, the mass flow rate values were not presented in a tabulated form but in figures of low resolution. Thus, a comparison is not easily made with this work.

6.6 Concluding remarks

To sum up, an efficient discrete velocity algorithm has been presented and applied for the simulation of non-linear pressure driven flow through short, axisymmetrical channel elements. The flow rates and macroscopic quantities are in good agreement with previously reported results obtained by the DSMC method. Three kinetic models are applied for the collision term, namely the BGK, S and ES models. A new type of boundary conditions is introduced for adiabatic walls. The computational effort and memory demands are drastically reduced by the implementation of grid refinement, parallelization, Wynn- ε acceleration, and the usage of memory has been optimized. Overall, the performance of the non-linear code is similar to the performance of the DSMC code for high pressure differences while it is significantly faster as linearized flow is approached.

In the case of the channel with expansion/contraction, our goal is to extend our previous knowledge on flow through short tubes to the case of channel elements with more complicated geometries, frequently encountered in practical applications. Similarities are found and a comparison with experimental results shows good overall agreement, which degrades for low pressures due to experimental difficulties. The contracting channel seems to provide steeper gradients of pressure, temperature and velocity. This work will be continued to complete the study for a wide variety of channel geometries, such as tees, junctions, conical expansion and contraction elements. These can in turn be combined in a numerical code simulating flow networks as various components forming the complete vacuum/microflow system.

Table 6.1: Discretized equation for the problem of non-linear flow through a tube

$$\begin{aligned}
& g_{i+,j+,k+}^{(l,m)} \left(\frac{c_p^l \cos \theta_j}{4\Delta r_i} - \frac{c_p^l \sin \theta_j}{4\Delta \theta r_{i+}} + \frac{c_x}{4\Delta x_k} + \frac{\delta_0}{8} \rho_{i+,k+} \sqrt{\tau_{i+,k+}} \right) \\
& + g_{i+,j+,k-}^{(l,m)} \left(\frac{c_p^l \cos \theta_j}{4\Delta r_i} - \frac{c_p^l \sin \theta_j}{4\Delta \theta r_{i+}} - \frac{c_x}{4\Delta x_k} + \frac{\delta_0}{8} \rho_{i+,k-} \sqrt{\tau_{i+,k-}} \right) \\
& + g_{i+,j-,k+}^{(l,m)} \left(\frac{c_p^l \cos \theta_j}{4\Delta r_i} + \frac{c_p^l \sin \theta_j}{4\Delta \theta r_{i+}} + \frac{c_x}{4\Delta x_k} + \frac{\delta_0}{8} \rho_{i+,k+} \sqrt{\tau_{i+,k+}} \right) \\
& + g_{i+,j-,k-}^{(l,m)} \left(\frac{c_p^l \cos \theta_j}{4\Delta r_i} - \frac{c_p^l \sin \theta_j}{4\Delta \theta r_{i+}} - \frac{c_x}{4\Delta x_k} + \frac{\delta_0}{8} \rho_{i+,k-} \sqrt{\tau_{i+,k-}} \right) \\
& + g_{i-,j+,k+}^{(l,m)} \left(-\frac{c_p^l \cos \theta_j}{4\Delta r_i} - \frac{c_p^l \sin \theta_j}{4\Delta \theta r_{i-}} + \frac{c_x}{4\Delta x_k} + \frac{\delta_0}{8} \rho_{i-,k+} \sqrt{\tau_{i-,k+}} \right) \\
& + g_{i-,j+,k-}^{(l,m)} \left(-\frac{c_p^l \cos \theta_j}{4\Delta r_i} - \frac{c_p^l \sin \theta_j}{4\Delta \theta r_{i-}} - \frac{c_x}{4\Delta x_k} + \frac{\delta_0}{8} \rho_{i-,k-} \sqrt{\tau_{i-,k-}} \right) \\
& + g_{i-,j-,k+}^{(l,m)} \left(-\frac{c_p^l \cos \theta_j}{4\Delta r_i} + \frac{c_p^l \sin \theta_j}{4\Delta \theta r_{i-}} + \frac{c_x}{4\Delta x_k} + \frac{\delta_0}{8} \rho_{i-,k+} \sqrt{\tau_{i-,k+}} \right) \\
& + g_{i-,j-,k-}^{(l,m)} \left(-\frac{c_p^l \cos \theta_j}{4\Delta r_i} + \frac{c_p^l \sin \theta_j}{4\Delta \theta r_{i-}} - \frac{c_x}{4\Delta x_k} + \frac{\delta_0}{8} \rho_{i-,k-} \sqrt{\tau_{i-,k-}} \right) \\
& = \frac{\delta_0}{8} \left[\rho_{i+,k+} \sqrt{\tau_{i+,k+}} \left(g_{i+,j+,k+}^{ES,(l,m)} + g_{i+,j-,k+}^{ES,(l,m)} \right) \right. \\
& \quad + \rho_{i+,k-} \sqrt{\tau_{i+,k-}} \left(g_{i+,j+,k-}^{ES,(l,m)} + g_{i+,j-,k-}^{ES,(l,m)} \right) \\
& \quad + \rho_{i-,k+} \sqrt{\tau_{i-,k+}} \left(g_{i-,j+,k+}^{ES,(l,m)} + g_{i-,j-,k+}^{ES,(l,m)} \right) \\
& \quad \left. + \rho_{i-,k-} \sqrt{\tau_{i-,k-}} \left(g_{i-,j+,k-}^{ES,(l,m)} + g_{i-,j-,k-}^{ES,(l,m)} \right) \right]
\end{aligned}$$

Table 6.2: Discrete velocity algorithm numerical parameters

Initial number of nodes per unit length $N_x = N_r$	5-40
Number of grid levels	3-6
Final nodes per unit length $N_x = N_r$	80-160
Discrete angles N_θ in $(0, \pi)$	160
Discrete magnitudes M	16×16
Maximum value of velocity magnitude $c_{p,max} = c_{x,max}$	5
Convergence criterion	2.5×10^{-7}
Container sizes L_{left}, L_{right}	15×15

Table 6.3: DSMC numerical parameters

Number of particles	$20 - 30 \times 10^6$
Cells per unit length	20 - 80
Time step	$0.01R/v_0$
Maximum statistical fluctuation	0.1%
Axial weighting zones	6 ($r = 0.25, 0.5, 0.75, 1, 2, 3$)
Radial weighting zones	3 ($x = 0, L_1, L_1 + L_2$)

Table 6.4: Dimensionless flow rate W for the ES model

L/R	P_{out}	δ_0								
		0	0.01	0.1	0.5	1	2	5	10	20
0	0.1	0.900	0.903	0.923	1.00	1.07	1.18	1.35	1.45	1.50
	0.5	0.500	0.502	0.518	0.582	0.653	0.778	1.04	1.22	1.30
	0.9	0.100	0.100	0.105	0.121	0.140	0.176	0.280	0.432	0.584
1	0.1	0.605	0.606	0.619	0.666	0.713	0.788	0.931	1.06	1.17
	0.5	0.336	0.337	0.347	0.385	0.428	0.505	0.692	0.888	1.05
	0.9	0.672	0.675	0.0700	0.0798	0.0908	0.112	0.170	0.264	0.415
5	0.1	0.279	0.280	0.283	0.297	0.312	0.341	0.423	0.537	0.701
	0.5	0.155	0.156	0.158	0.169	0.182	0.207	0.280	0.398	0.581
	0.9	0.0310	0.0311	0.0318	0.0345	0.0378	0.0444	0.0641	0.0976	0.164
10	0.1	0.171	0.172	0.173	0.178	0.185	0.200	0.249	0.328	0.462
	0.5	0.0954	0.0955	0.0963	0.101	0.106	0.119	0.160	0.229	0.359
	0.9	0.0190	0.0191	0.0193	0.0204	0.0219	0.0253	0.0359	0.0543	0.0917

Table 6.5: Dimensionless flow rate W obtained by the DSMC method in previous works [149, 152]

L/R	P_{out}	δ_0								
		0	0.1	0.5	1	2	5	10		
0	0.1	-	0.910	-	1.03	-	-	1.44		
	0.5	-	0.509	-	0.613	-	-	1.19		
	0.9	-	0.103	-	0.130	-	-	0.402		
1	0.1	0.605	0.613	0.648	0.689	0.761	0.913	1.05		
	0.5	0.336	0.343	0.370	0.405	0.474	0.658	0.866		
	0.1	0.279	0.281	0.291	0.304	0.330	0.412	0.529		
5	0.5	0.155	0.156	0.163	0.175	0.197	0.271	0.388		
	0.1	0.170	-	0.171	-	0.192	-	0.321		
	0.5	0.0935	-	0.0934	-	0.114	-	0.223		

Table 6.6: Dimensionless flow rate W for the BGK and S models

L/R	P_{out}	δ_0					
		0.1			1		
		BGK	S	BGK	S	BGK	S
0	0.1	0.920	0.921	1.06	1.06	1.44	1.44
	0.5	0.515	0.516	0.635	0.641	1.21	1.21
	0.9	0.104	0.104	0.135	0.137	0.424	0.427
1	0.1	0.617	0.617	0.703	0.706	1.06	1.06
	0.5	0.345	0.346	0.417	0.422	0.885	0.886
	0.9	0.0695	0.0697	0.0881	0.0894	0.260	0.262

Table 6.7: Dimensionless flow rate W for the BGK model and $P_{out} = 0.99$

L/R	δ_0				
	0	0.1	1	5	10
1	6.72×10^{-3}	6.96×10^{-3}	8.94×10^{-3}	1.71×10^{-2}	2.69×10^{-2}
5	3.10×10^{-3}	3.15×10^{-3}	3.72×10^{-3}	6.45×10^{-3}	1.00×10^{-2}

Table 6.8: Dimensionless flow rate W for the ES model and adiabatic walls

L/R	P_{out}	δ_0			
		0	0.1	1	10
0	0.1	0.900	0.923	1.06	1.43
	0.5	0.500	0.518	0.650	1.20
1	0.1	0.605	0.620	0.718	1.07
	0.5	0.336	0.347	0.428	0.892

Table 6.9: Effect of grid refinement and the Wynn- ε scheme on the number of iterations

P_{out}	δ_0	Grid level	Nodes per unit length	Grid refinement	Wynn- ε
0.1	1	1	25	96	56
		2	50	20	20
		3	100	16	16
0.1	10	1	25	2340	837
		2	50	145	128
		3	100	94	88
0.5	1	1	25	96	53
		2	50	17	17
		3	100	14	14
0.5	10	1	25	2342	925
		2	50	200	163
		3	100	150	134

Table 6.10: Total CPU time [h] for various algorithm improvements

δ_0	P_{out}	Single CPU	16 CPUs	Multiple grid levels	Wynn- ε
1.00	0.1	169.09	14.84	3.54	3.33
1.00	0.5	168.96	14.86	3.14	2.92
10.00	0.1	>1591	360.46	30.72	26.10
10.00	0.5	>1849	360.60	41.00	38.25

Table 6.11: CPU time analysis [%] of the average time allocation for a typical run

Macroscopic quantities	53.2
Maxwellian distribution	26.2
Marching scheme	17.3
Parallel communication (MPI)	0.1
Boundary conditions	0.1
Miscellaneous	3.1

Table 6.12: Memory requirements for the non-linear DVM code

Parameter values	Test case	Parameter dependence				
		L/R	N_θ	M	L_{left}, L_{right}	N_x, N_r
Length ratio L/R	10	200	10	10	10	10
Nodes per unit length $N_x = N_r$	100	100	100	100	100	120
Discrete angles N_θ in $(0, \pi)$	160	160	400	160	160	160
Discrete magnitudes M	16×16	16×16	16×16	32×32	16×16	16×16
Container sizes L_{left}, L_{right}	15	15	15	15	10	15
Memory consumption [MBytes]	922	1300	933	922	423	1300

Table 6.13: DSMC expanding/contracting tube geometrical cases

Dimension	Case 1	Case 2	Case 3	Case 4
R_2/R_1	2.00	5.00	0.50	0.50
L_1/R_1	1.00	1.00	1.00	3.00
L_2/R_1	1.00	1.00	1.00	3.00

Table 6.14: DSMC expanding/contracting tube flow rate W

Parameters	δ				
	0.1	0.5	1	5	10
Case 1 , $P_{out} = 0.1$	0.606	0.641	0.682	0.909	1.05
Case 1 , $P_{out} = 0.5$	0.336	0.363	0.400	0.655	0.872
Case 2 , $P_{out} = 0.1$	0.612	0.612	0.689	0.915	1.05
Case 2 , $P_{out} = 0.5$	0.342	0.368	0.405	0.660	0.867
Case 3 , $P_{out} = 0.1$	0.113	0.116	0.120	0.146	0.172
Case 3 , $P_{out} = 0.5$	0.0624	0.0646	0.0681	0.0914	0.120
Case 4 , $P_{out} = 0.1$	0.0582	0.0592	0.0600	0.0714	0.0861
Case 4 , $P_{out} = 0.5$	0.0320	0.0328	0.0334	0.0430	0.0561

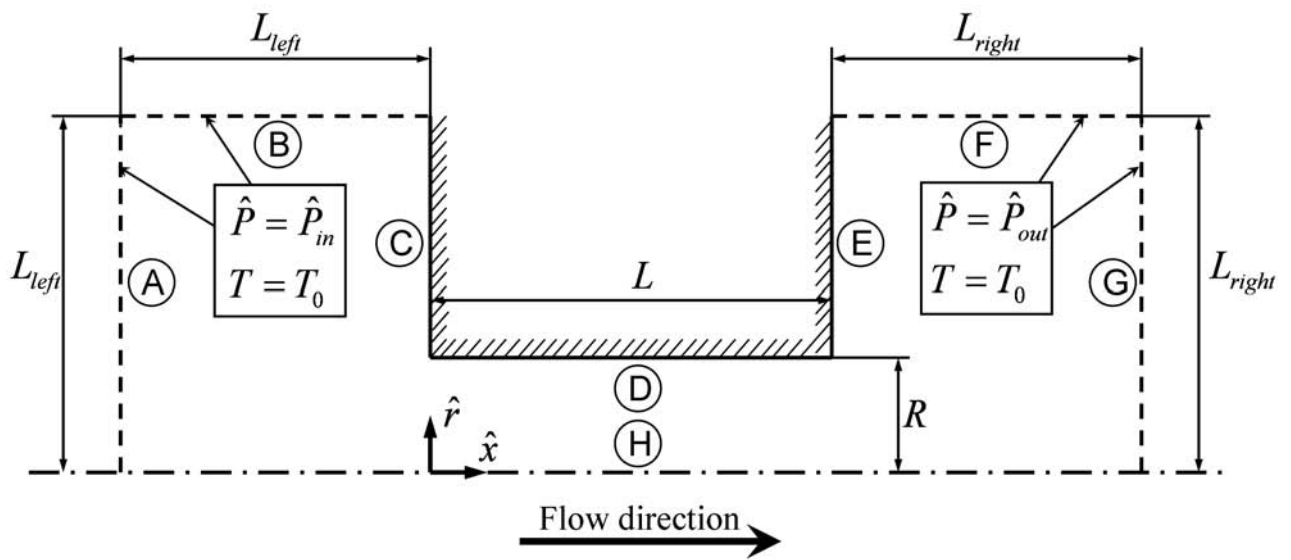


Figure 6.1: Cylindrical tube geometry

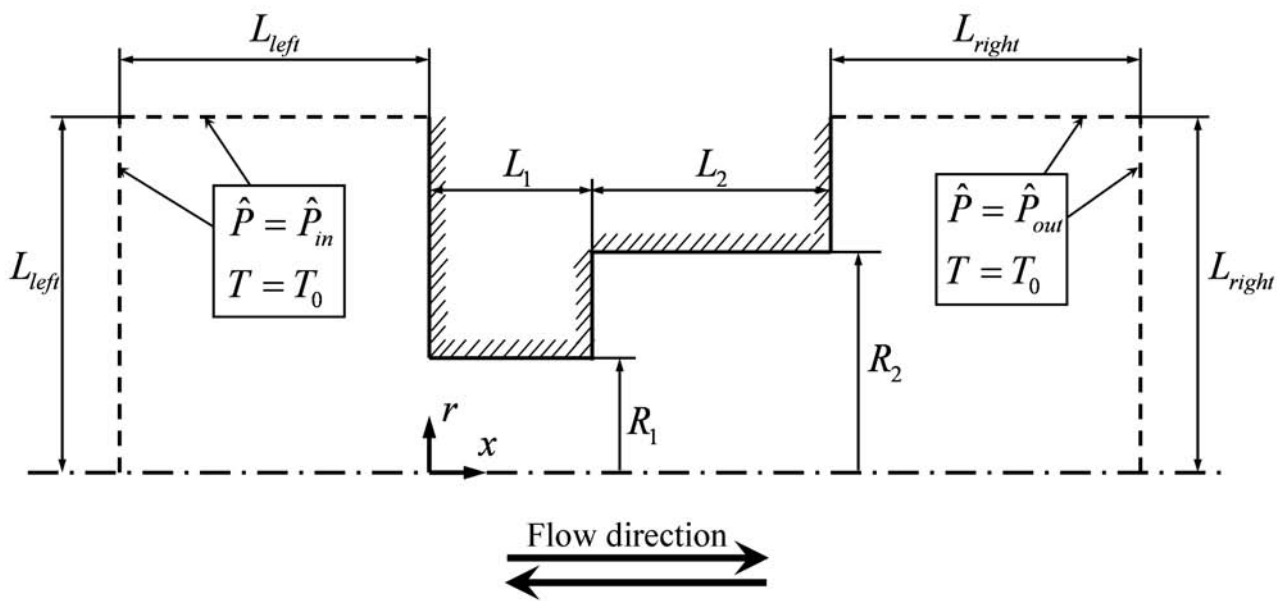


Figure 6.2: Expansion/contraction channel geometry

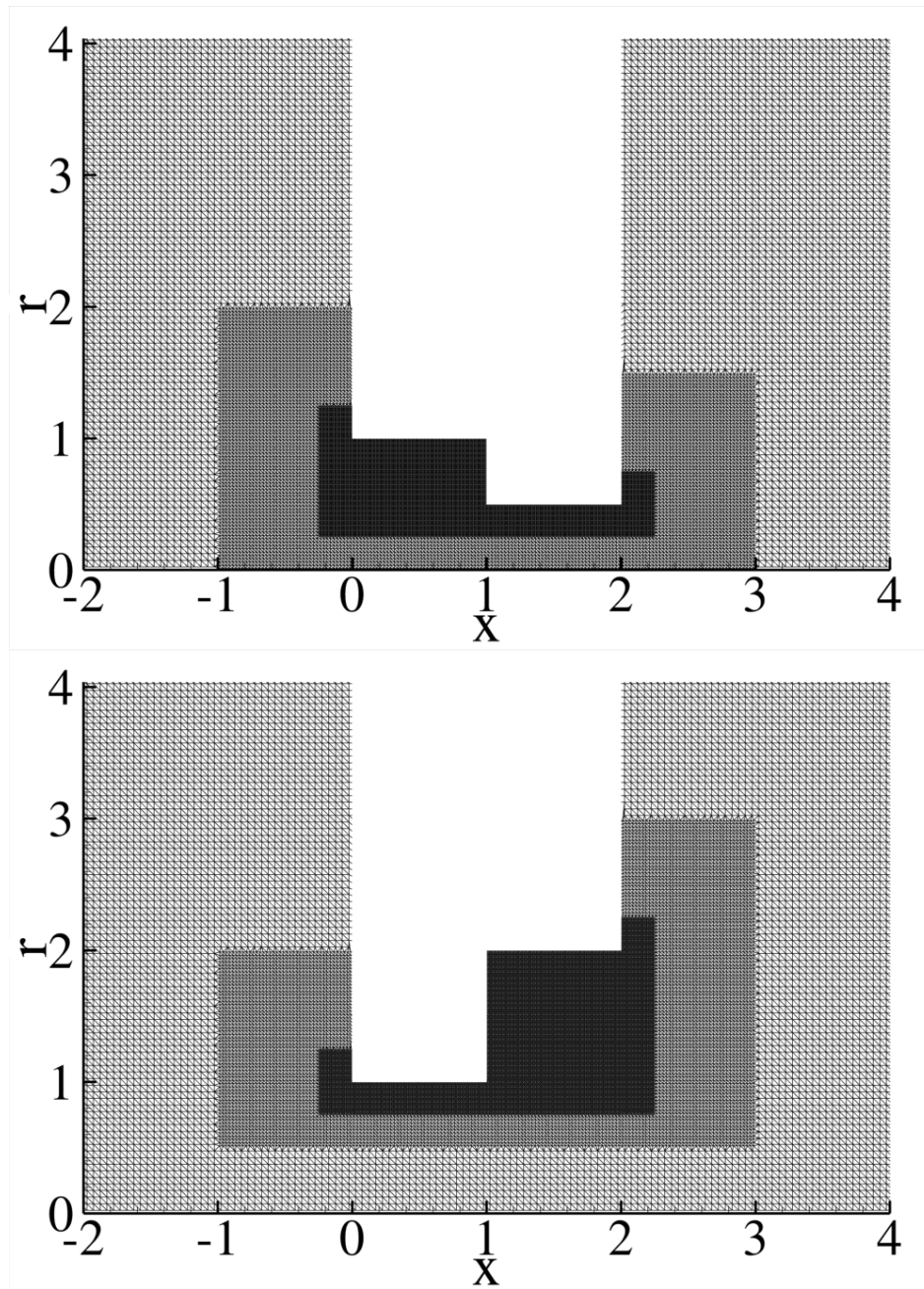


Figure 6.3: Expansion/contraction channel computational cell grid

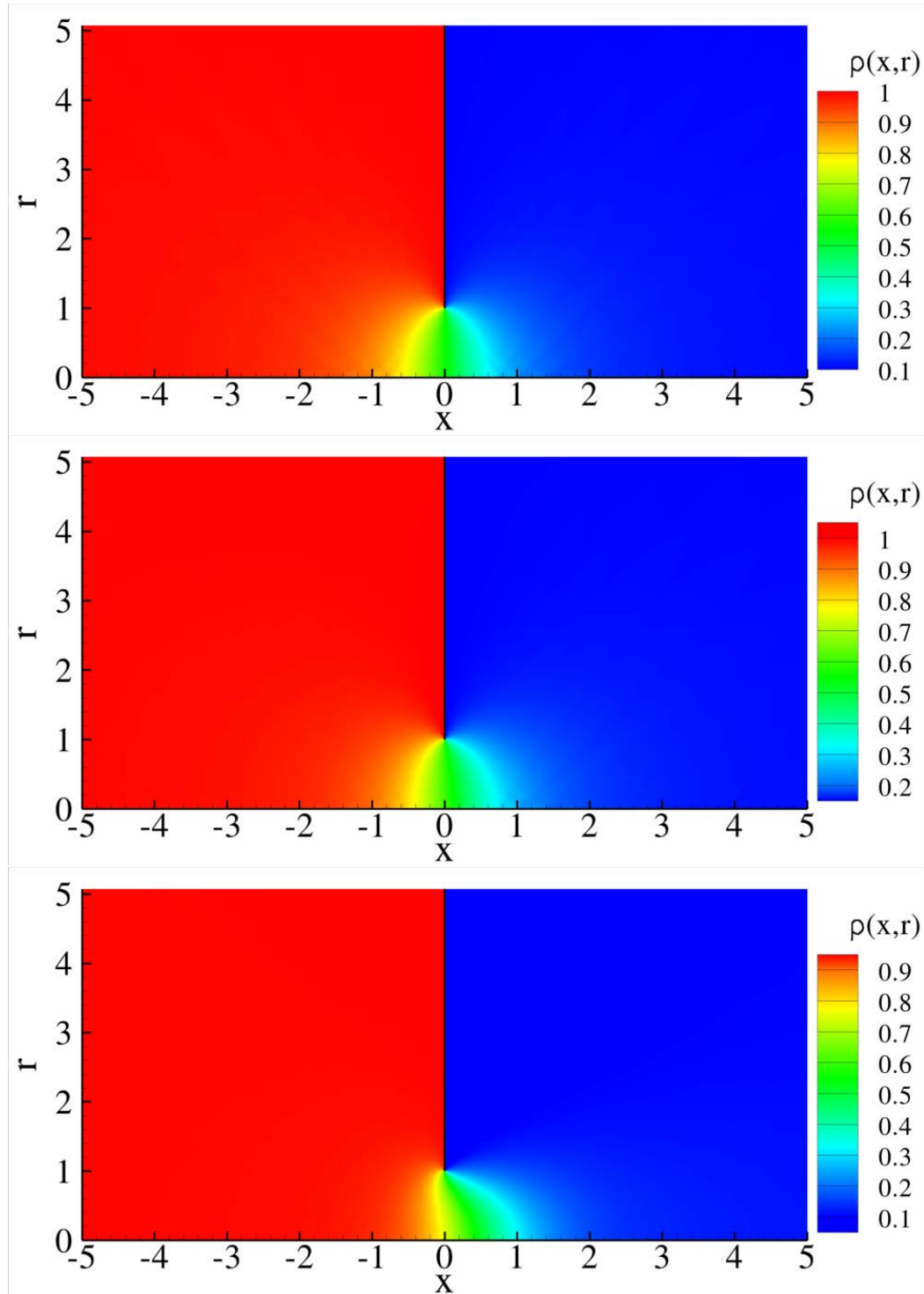


Figure 6.4: Density contour for the short tube geometry and $L/R = 0$, $P_{out} = 0.1$ with $\delta = 0.1$ (up), $\delta = 1$ (middle) and $\delta_0 = 10$ (down)

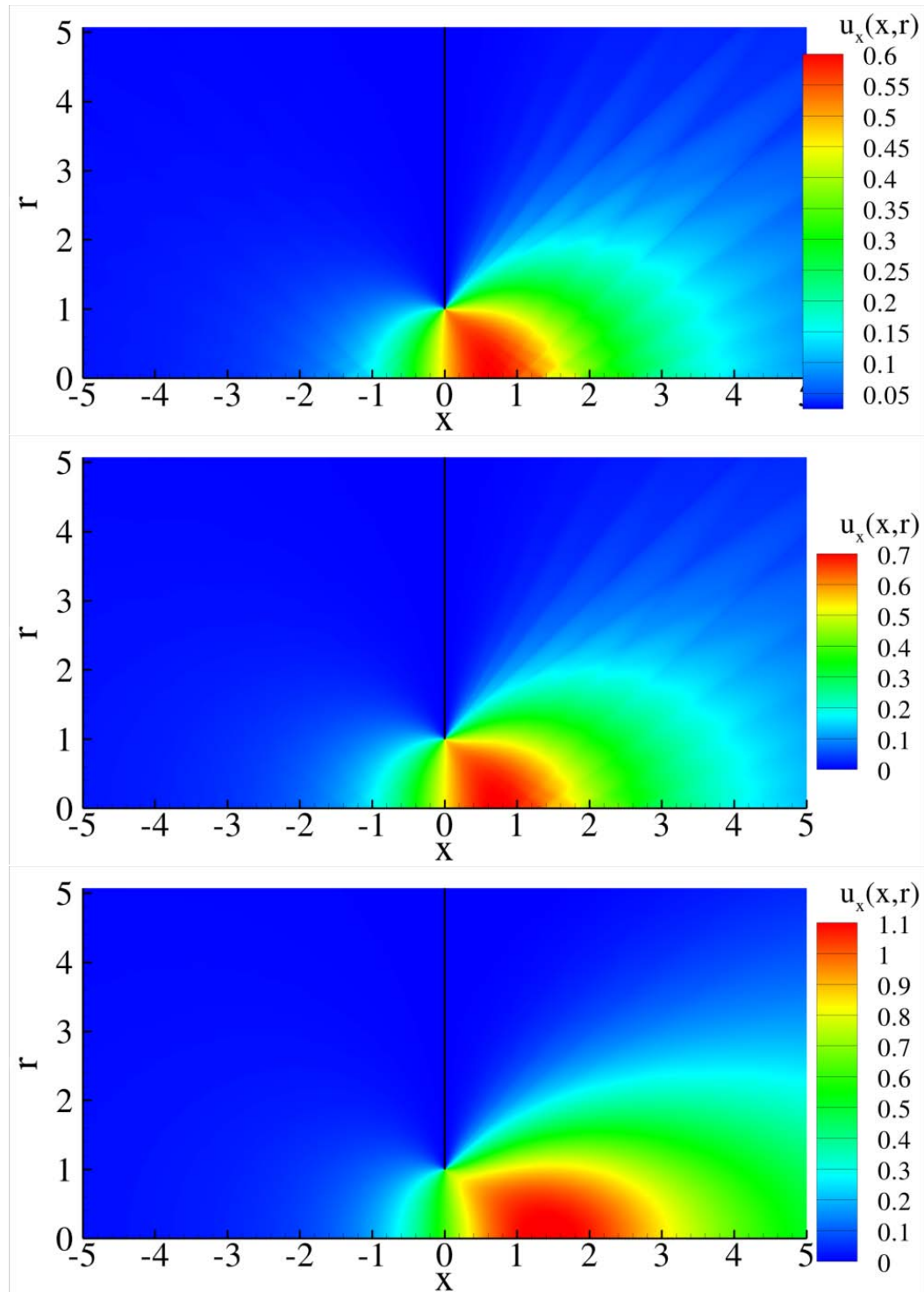


Figure 6.5: Axial velocity contour for the short tube geometry and $L/R = 0$, $P_{out} = 0.1$ with $\delta = 0.1$ (up), $\delta = 1$ (middle) and $\delta_0 = 10$ (down)

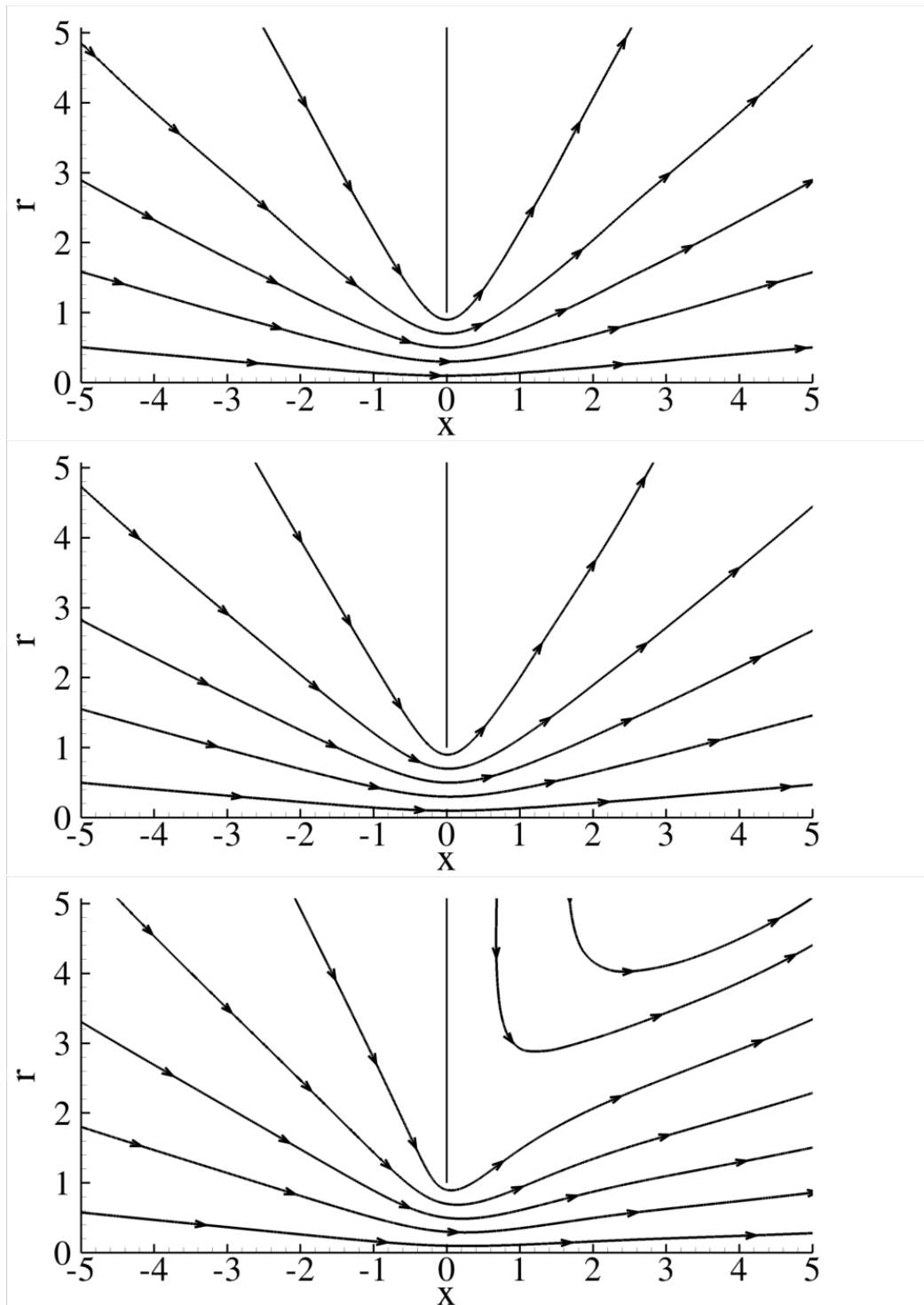


Figure 6.6: Streamlines for the short tube geometry and $L/R = 0$, $P_{out} = 0.1$ with $\delta = 0.1$ (up), $\delta = 1$ (middle) and $\delta_0 = 10$ (down)

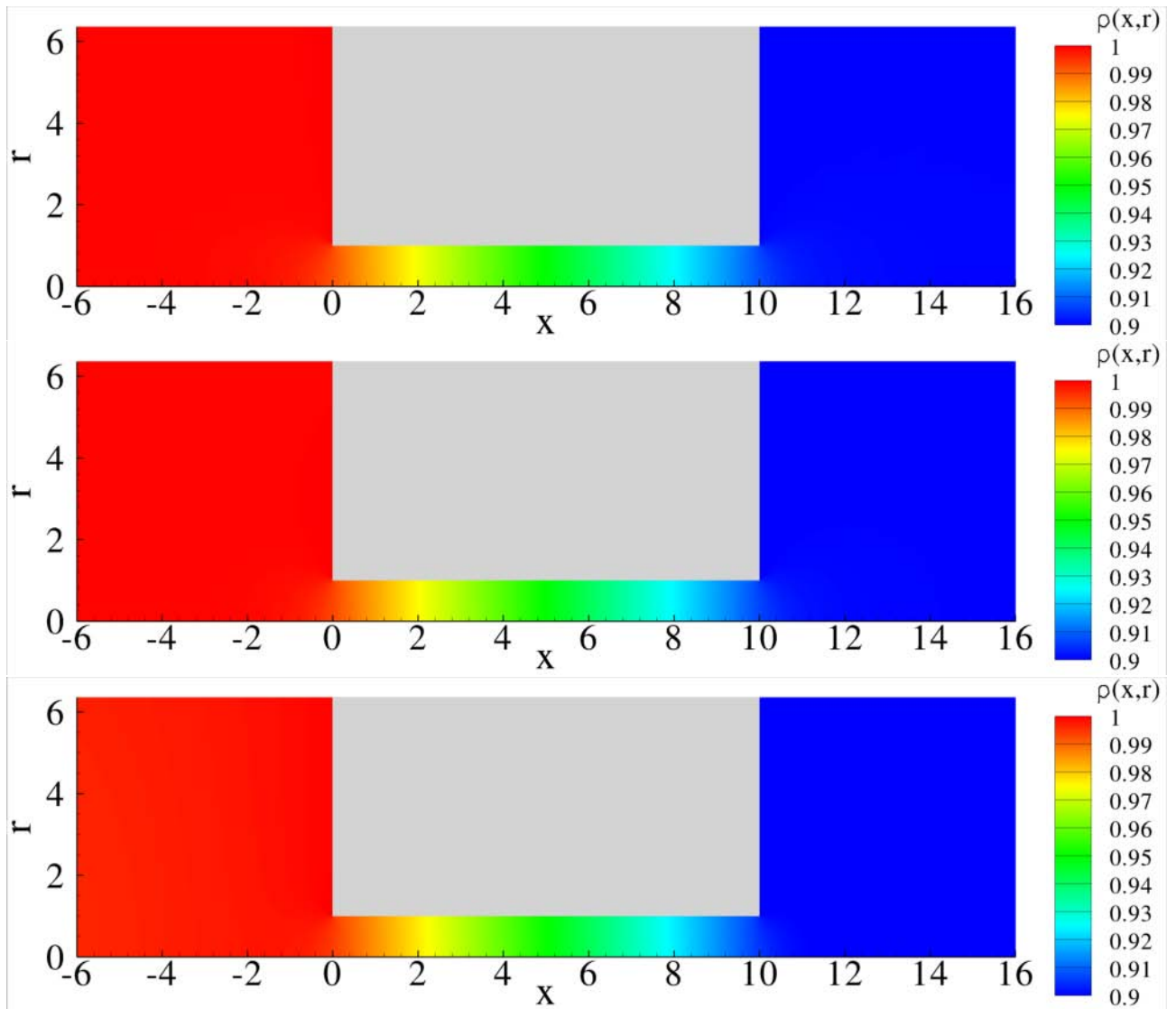


Figure 6.7: Density contour for the short tube geometry and $L/R = 10$, $P_{out} = 0.9$ with $\delta = 0.1$ (up), $\delta = 1$ (middle) and $\delta_0 = 10$ (down)

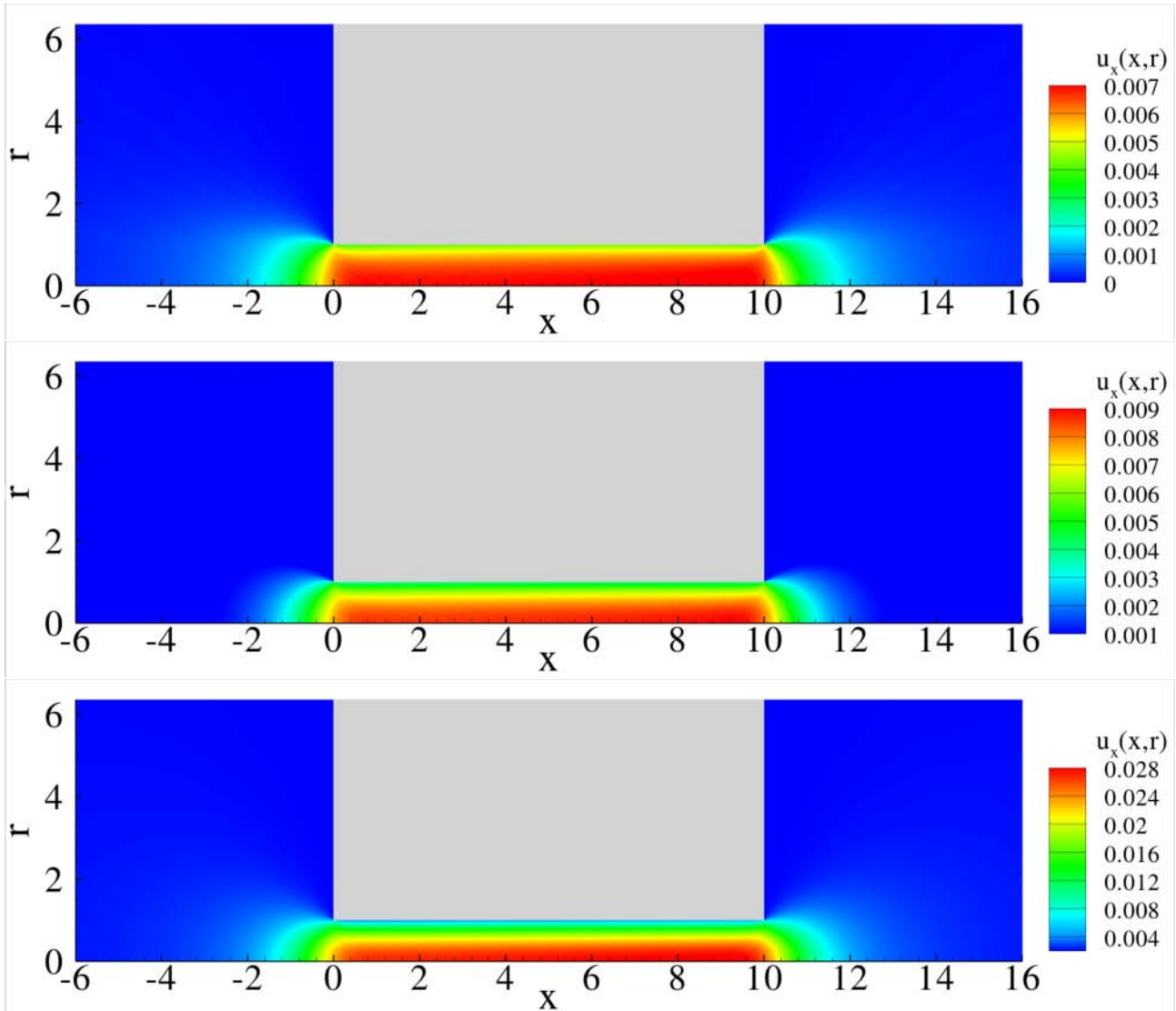


Figure 6.8: Axial velocity contour for the short tube geometry and $L/R = 10$, $P_{out} = 0.9$ with $\delta = 0.1$ (up), $\delta = 1$ (middle) and $\delta_0 = 10$ (down)

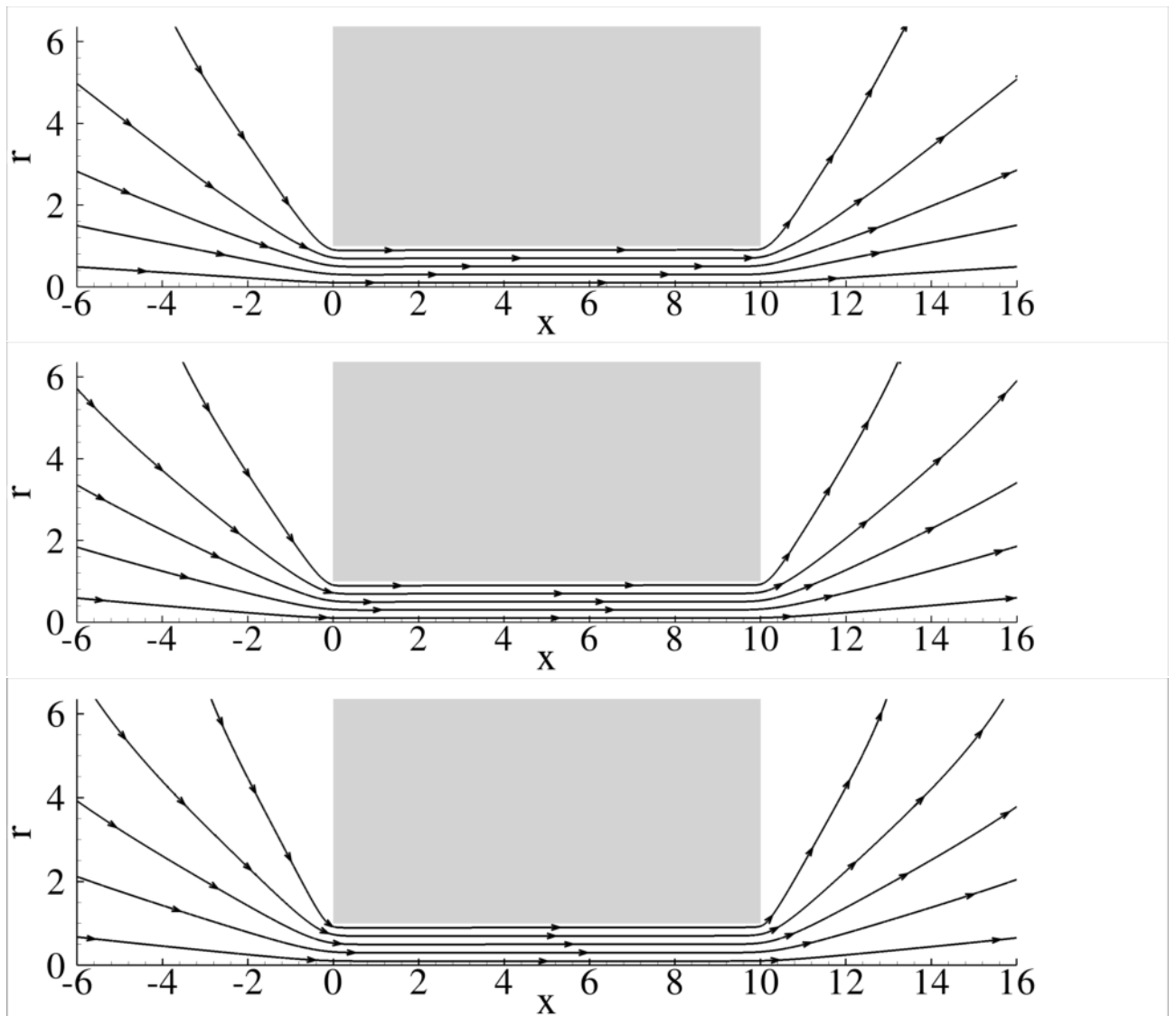


Figure 6.9: Streamlines for the short tube geometry and $L/R = 10$, $P_{out} = 0.9$ with $\delta = 0.1$ (up), $\delta = 1$ (middle) and $\delta_0 = 10$ (down)

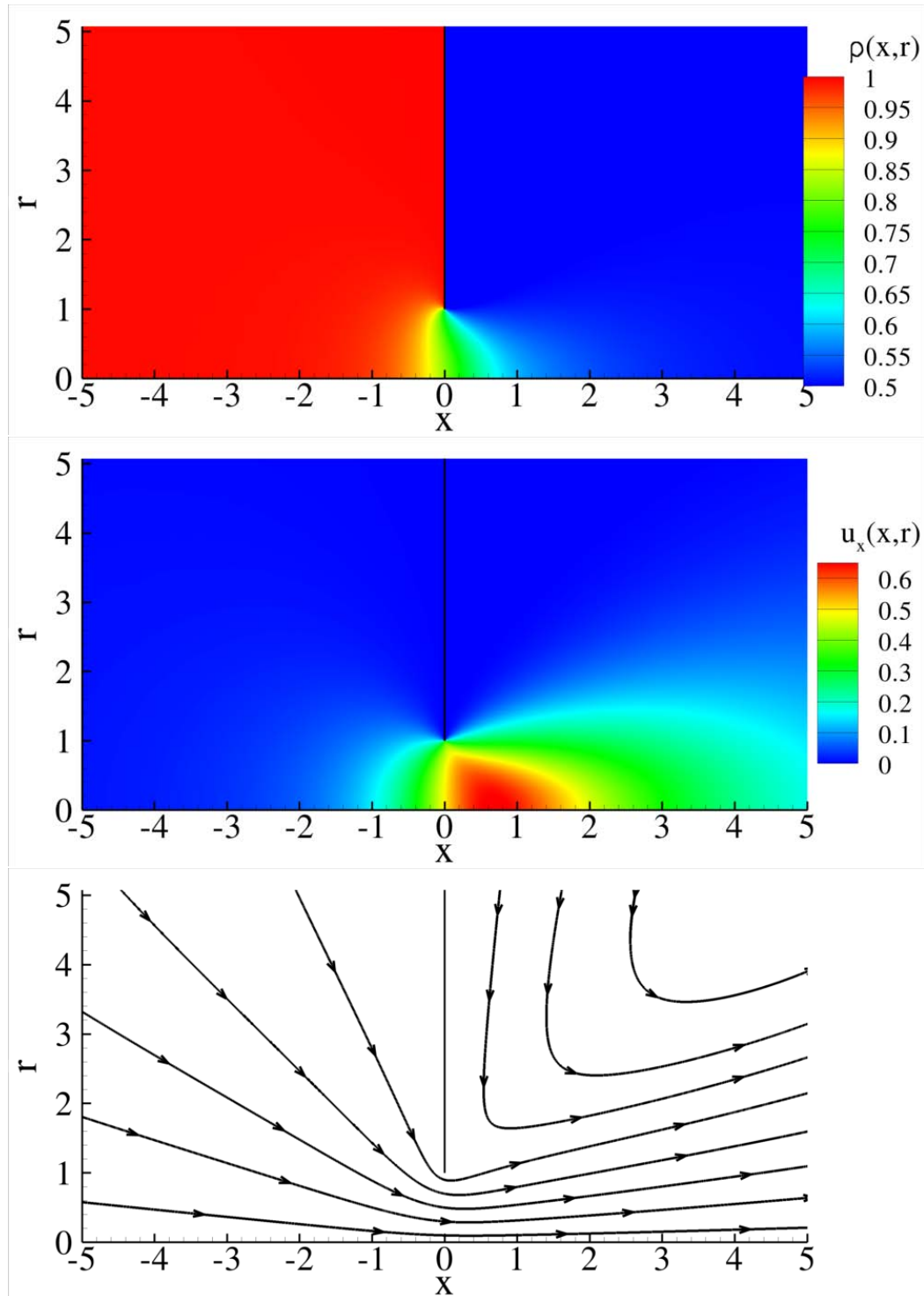


Figure 6.10: Density (up) and axial velocity (middle) contours, as well as streamlines (down) for the short tube geometry and $L/R = 0$, $P_{out} = 0.5$, $\delta_0 = 10$

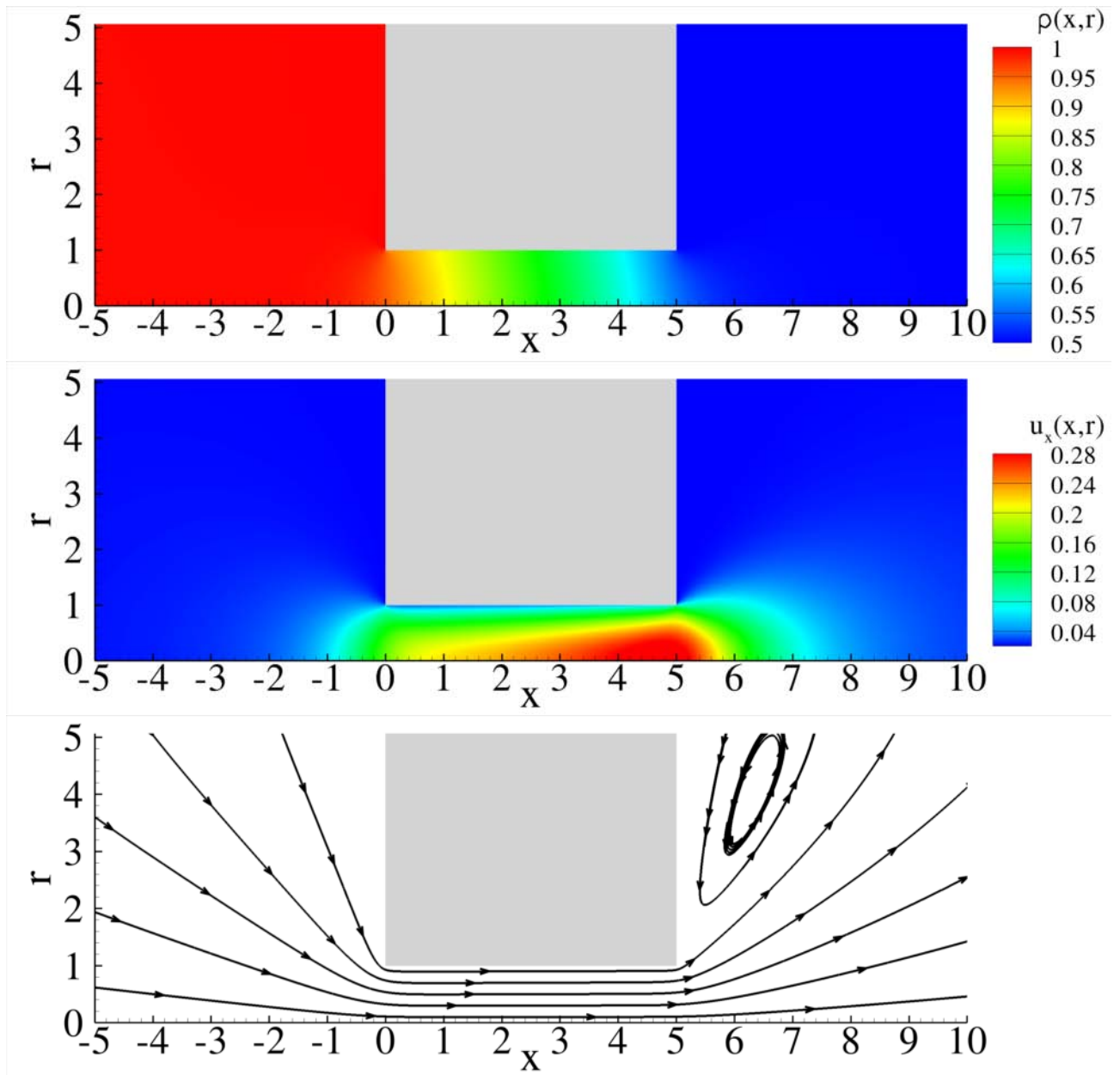


Figure 6.11: Density (up) and axial velocity (middle) contours, as well as streamlines (down) for the short tube geometry and $L/R = 5$, $P_{out} = 0.5$, $\delta_0 = 10$

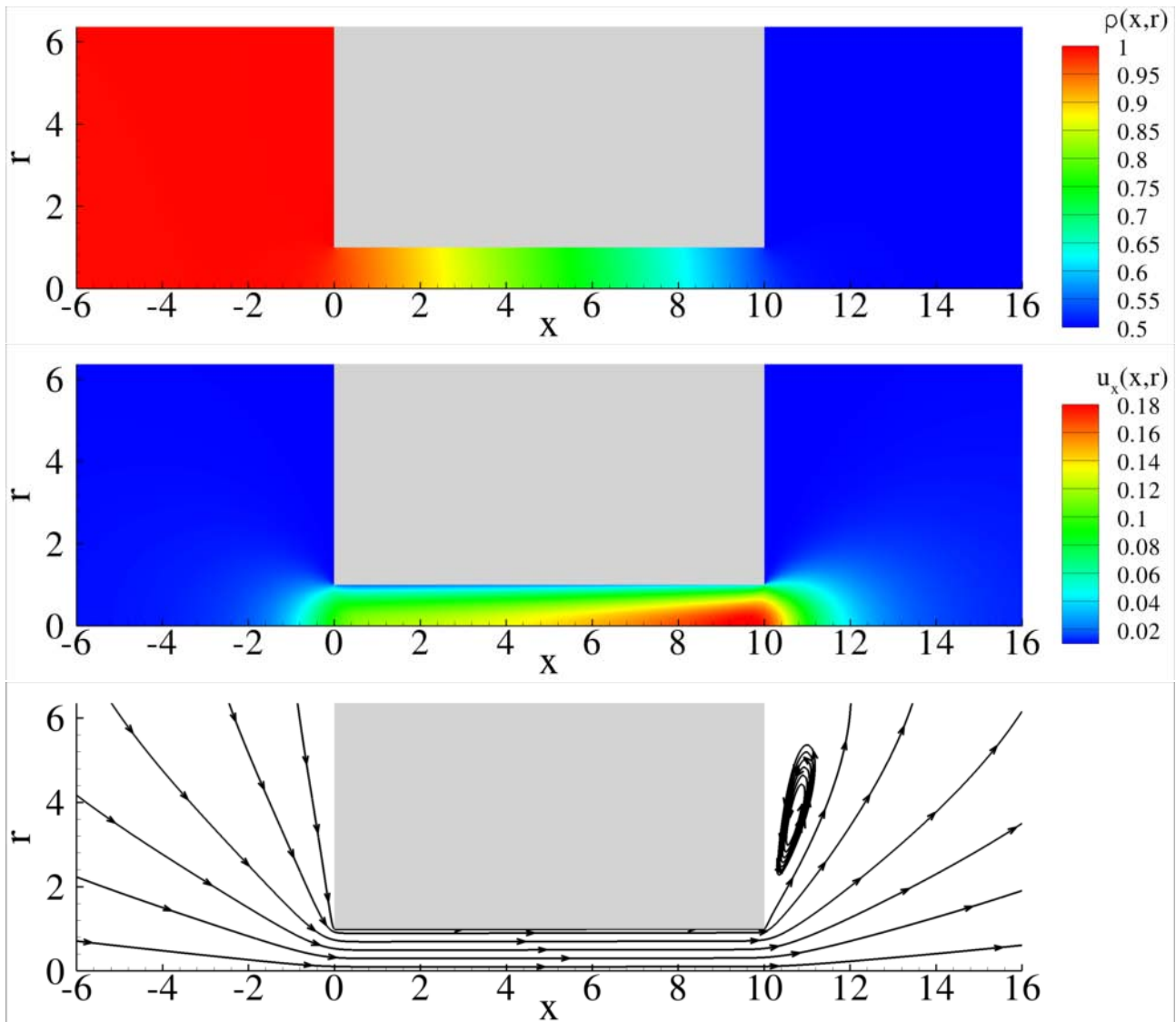


Figure 6.12: Density (up) and axial velocity (middle) contours, as well as streamlines (down) for the short tube geometry and $L/R = 10$, $P_{out} = 0.5$, $\delta_0 = 10$

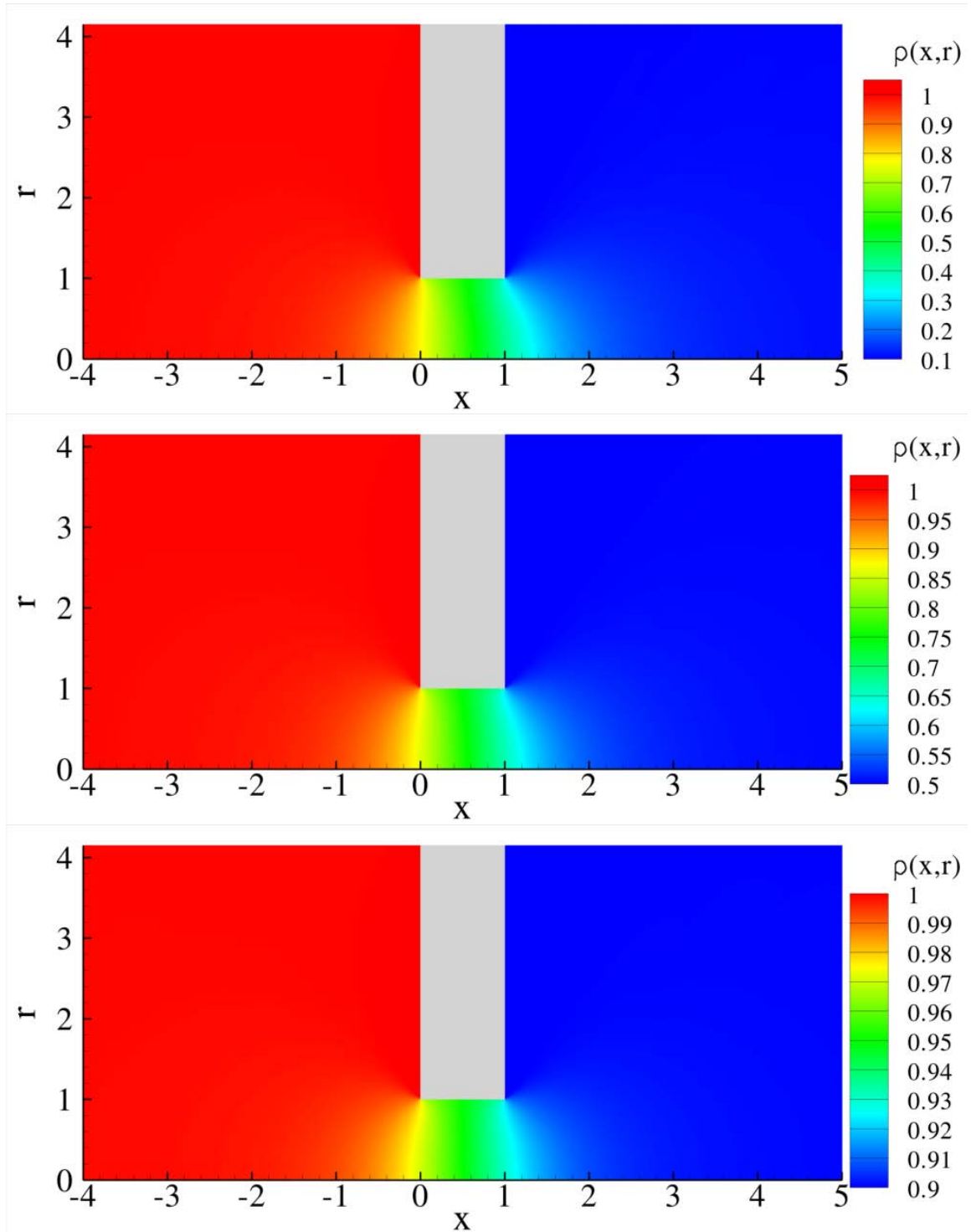


Figure 6.13: Density contour for the short tube geometry and $L/R = 1$, $\delta_0 = 2$ with $P_{out} = 0.1$ (up), $P_{out} = 0.5$ (middle) and $P_{out} = 0.9$ (down)

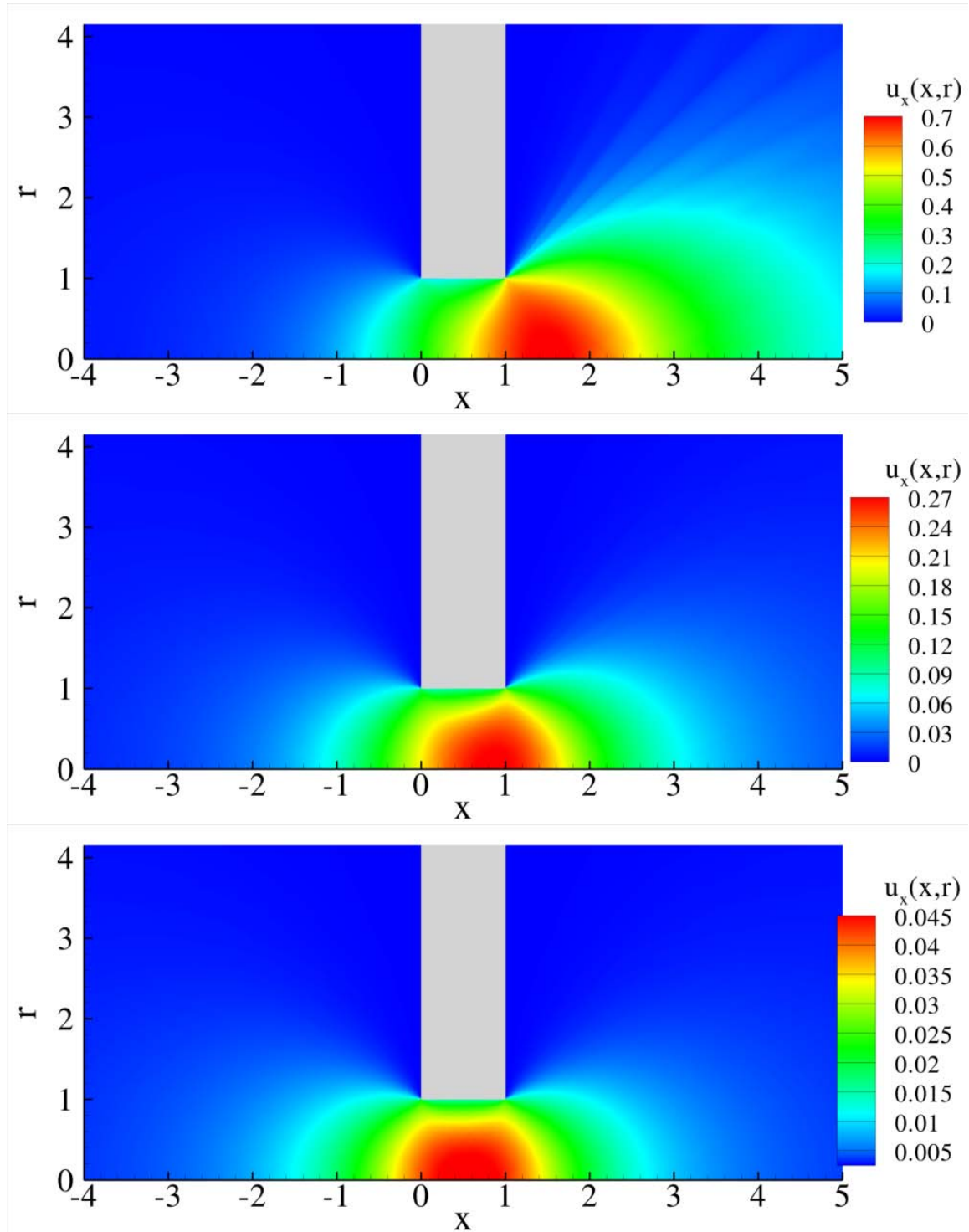


Figure 6.14: Axial velocity contour for the short tube geometry and $L/R = 1$, $\delta_0 = 2$ with $P_{out} = 0.1$ (up), $P_{out} = 0.5$ (middle) and $P_{out} = 0.9$ (down)

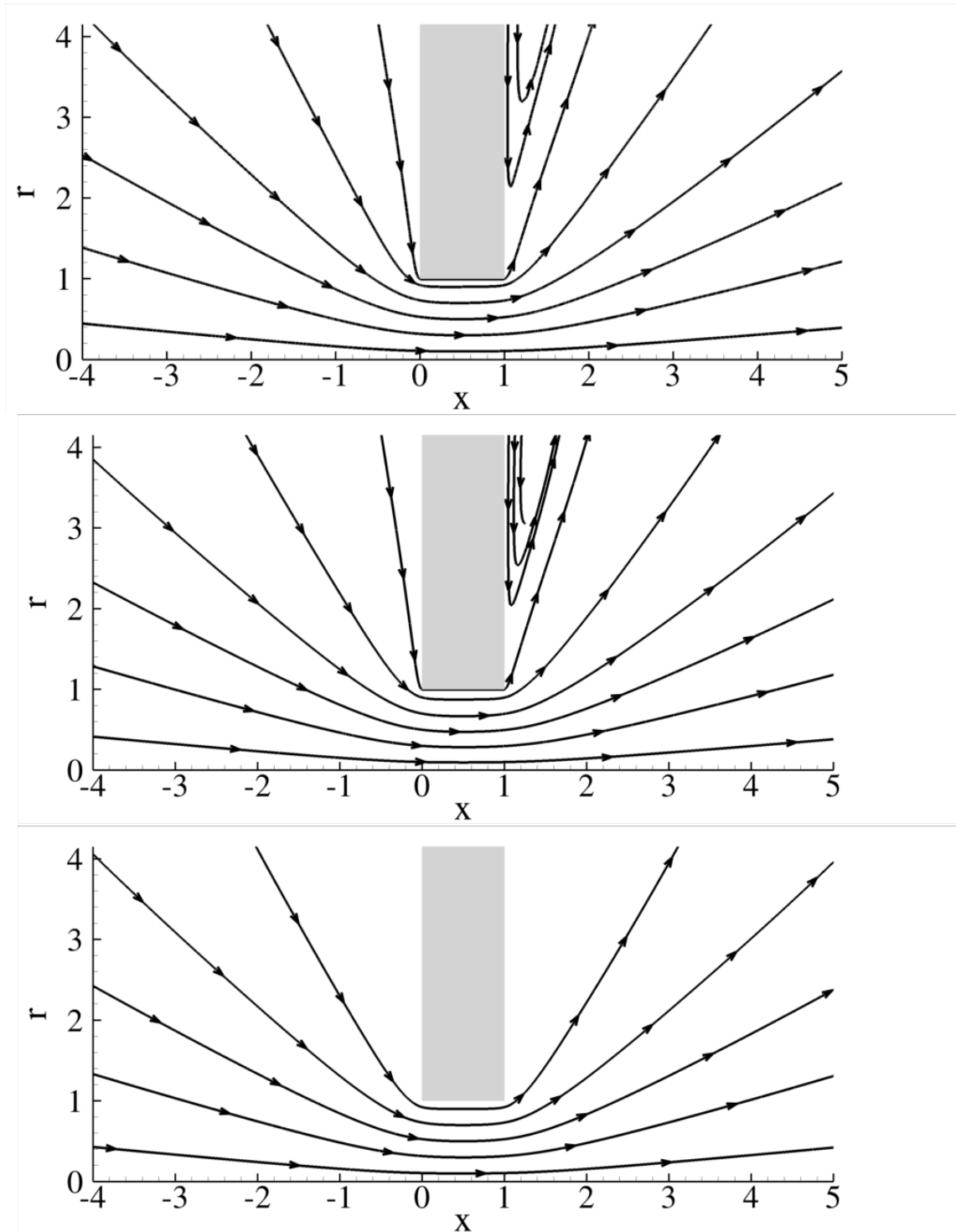


Figure 6.15: Streamlines for the short tube geometry and $L/R = 1$, $\delta_0 = 2$ with $P_{out} = 0.1$ (up), $P_{out} = 0.5$ (middle) and $P_{out} = 0.9$ (down)

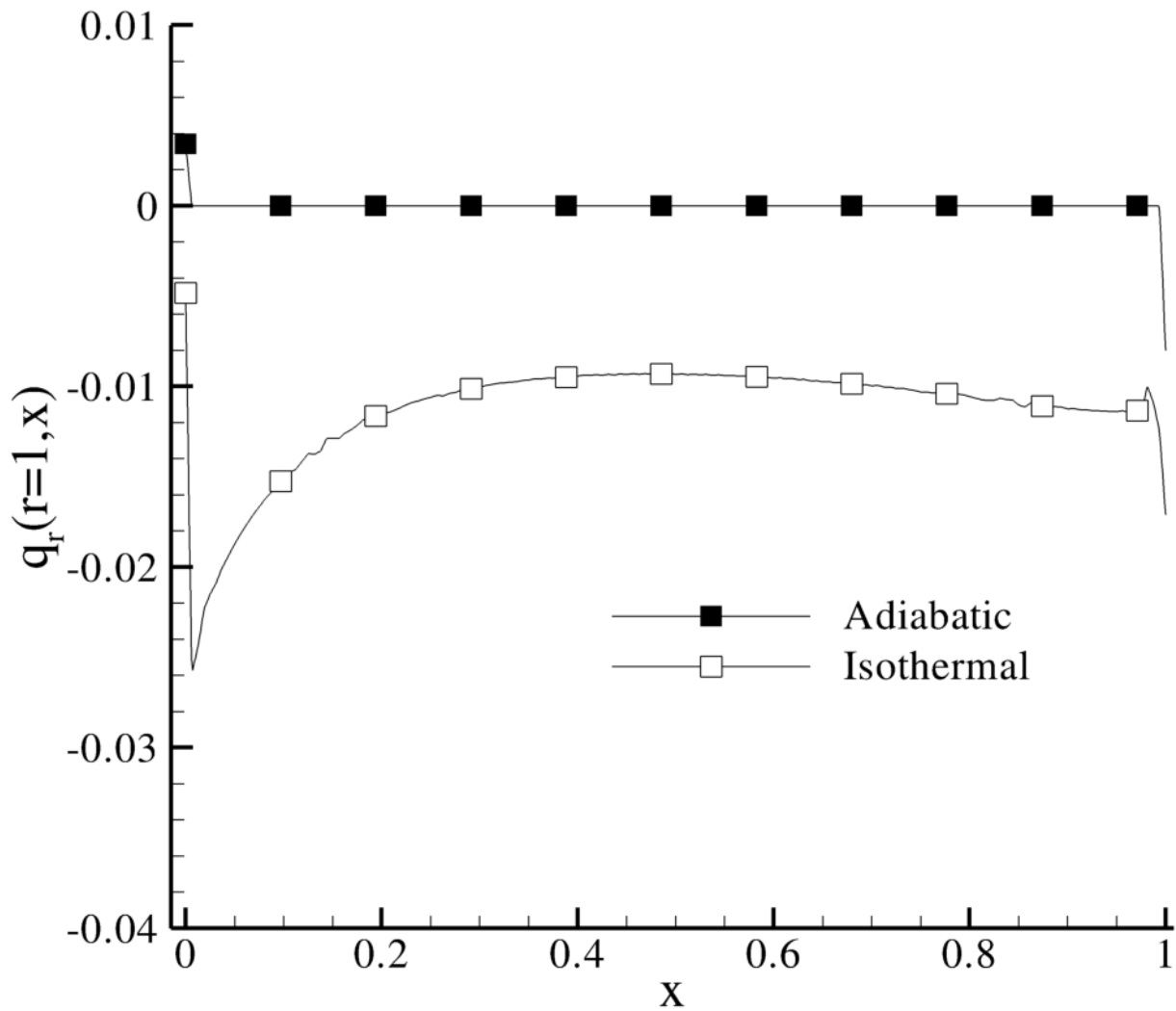


Figure 6.16: Heat flux in the direction normal to the wall for adiabatic and isothermal walls, with $L/R = 1$, $\delta_0 = 20$, $P_{out} = 0.5$

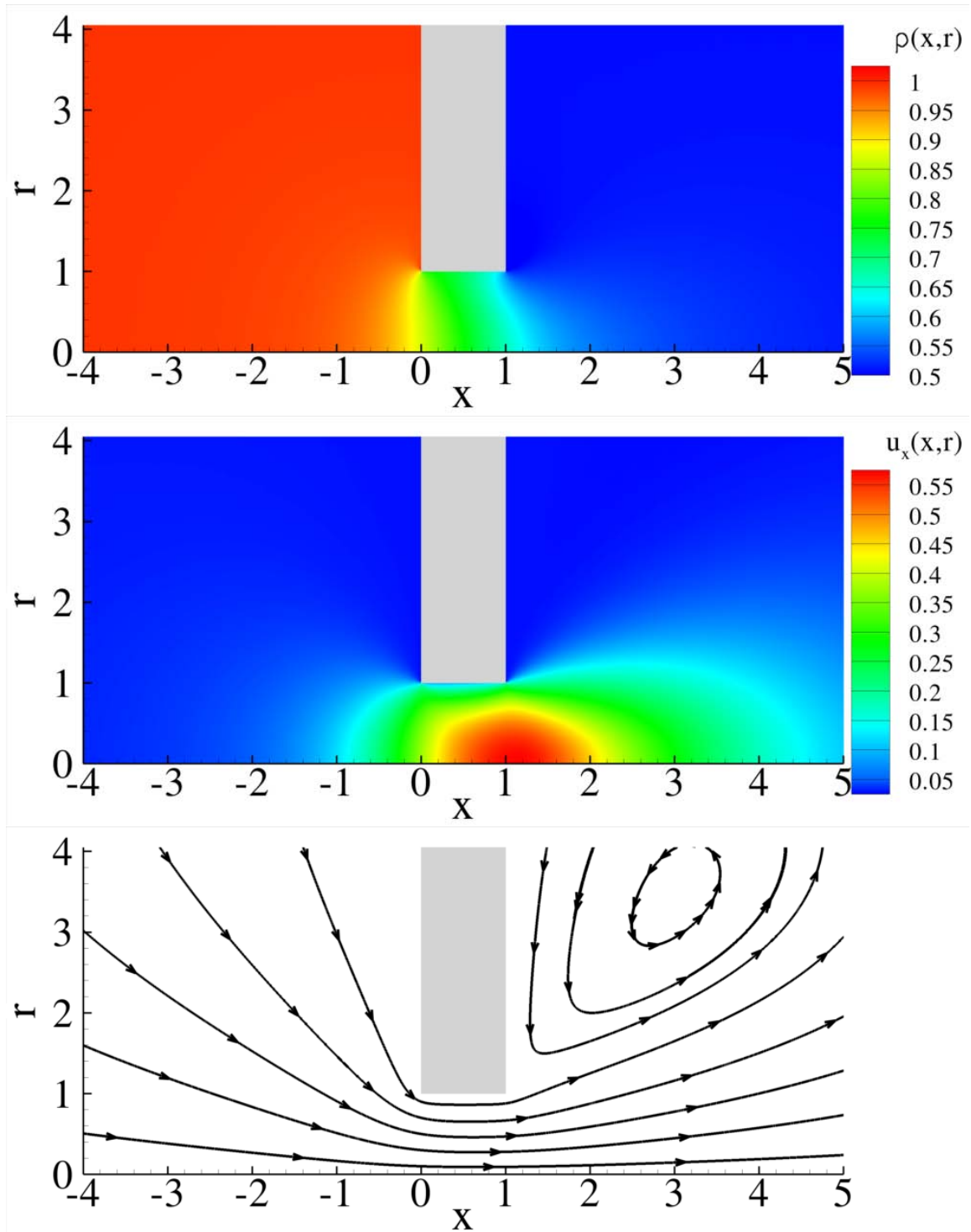


Figure 6.17: Density (up) and axial velocity (middle) contours, as well as streamlines (bottom) for flow through an adiabatic tube with $L/R = 1$, $P_{out} = 0.5$ with $\delta_0 = 20$

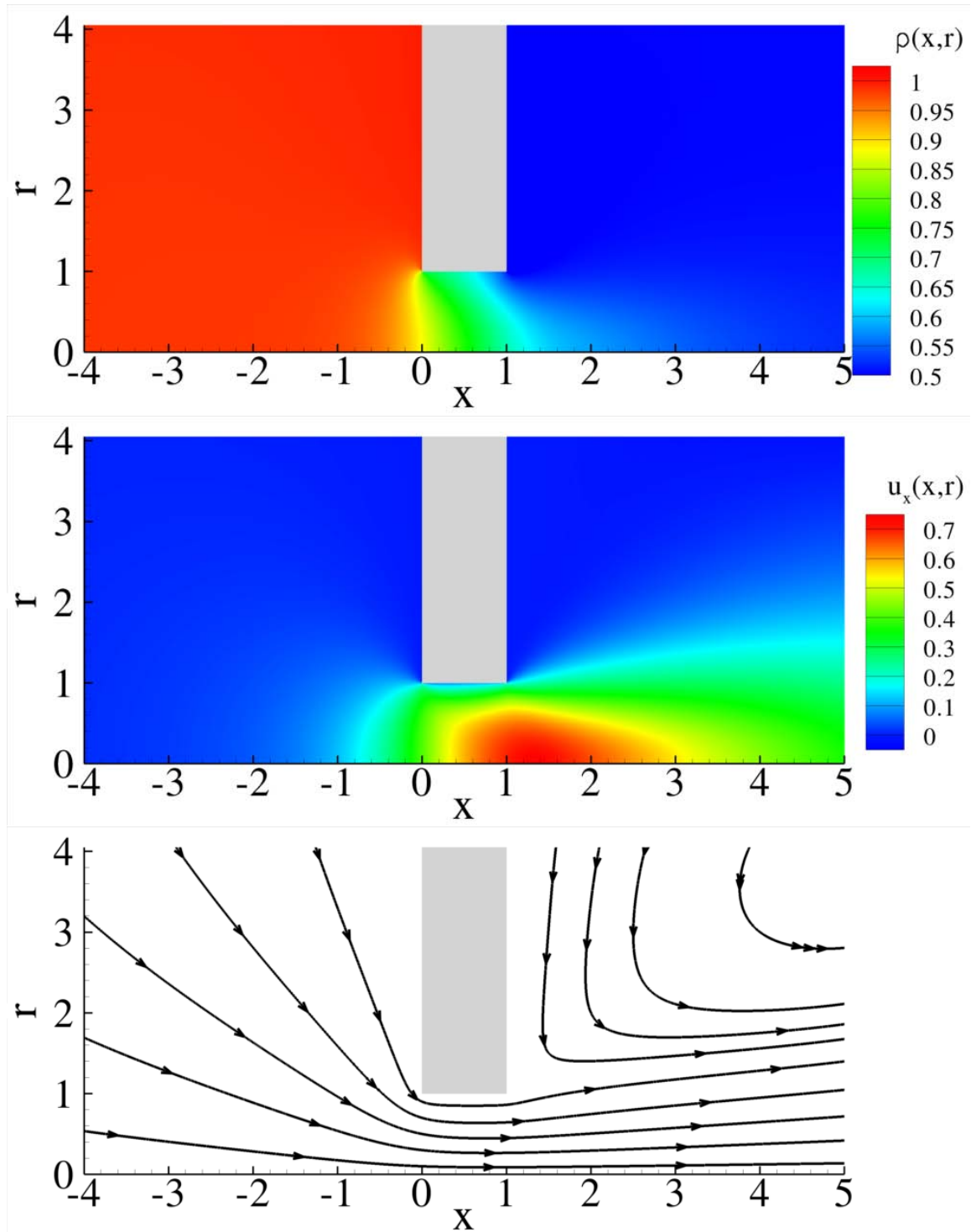


Figure 6.18: Density (up) and axial velocity (middle) contours, as well as streamlines (bottom) for flow through an isothermal tube with $L/R = 1$, $P_{out} = 0.5$ with $\delta_0 = 20$

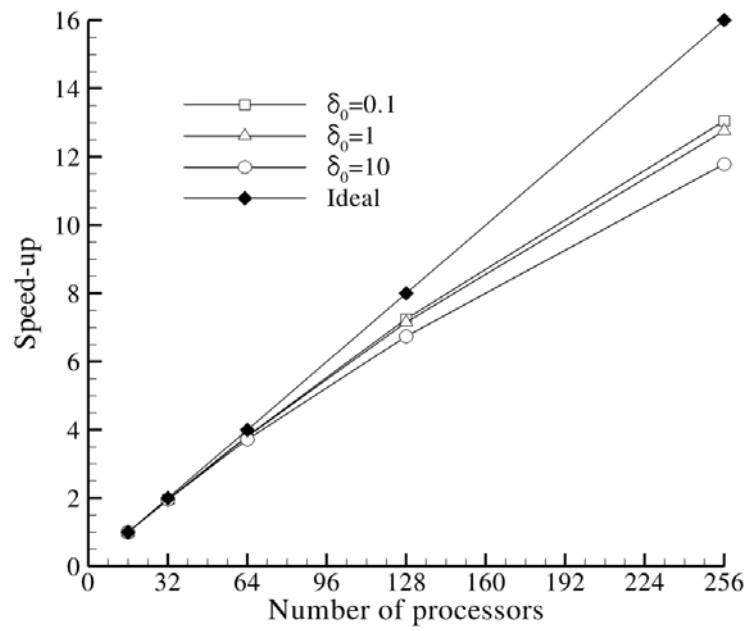


Figure 6.19: Speed up due to parallelization for various δ_0 and $P_{out} = 0.1$

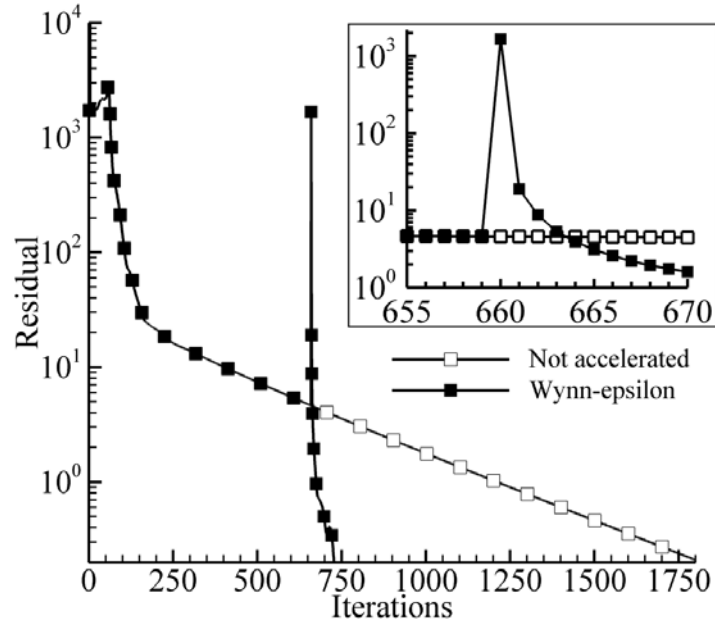


Figure 6.20: Wynn- ϵ effect on the residual for $\delta_0 = 10, P_{out} = 0.1$

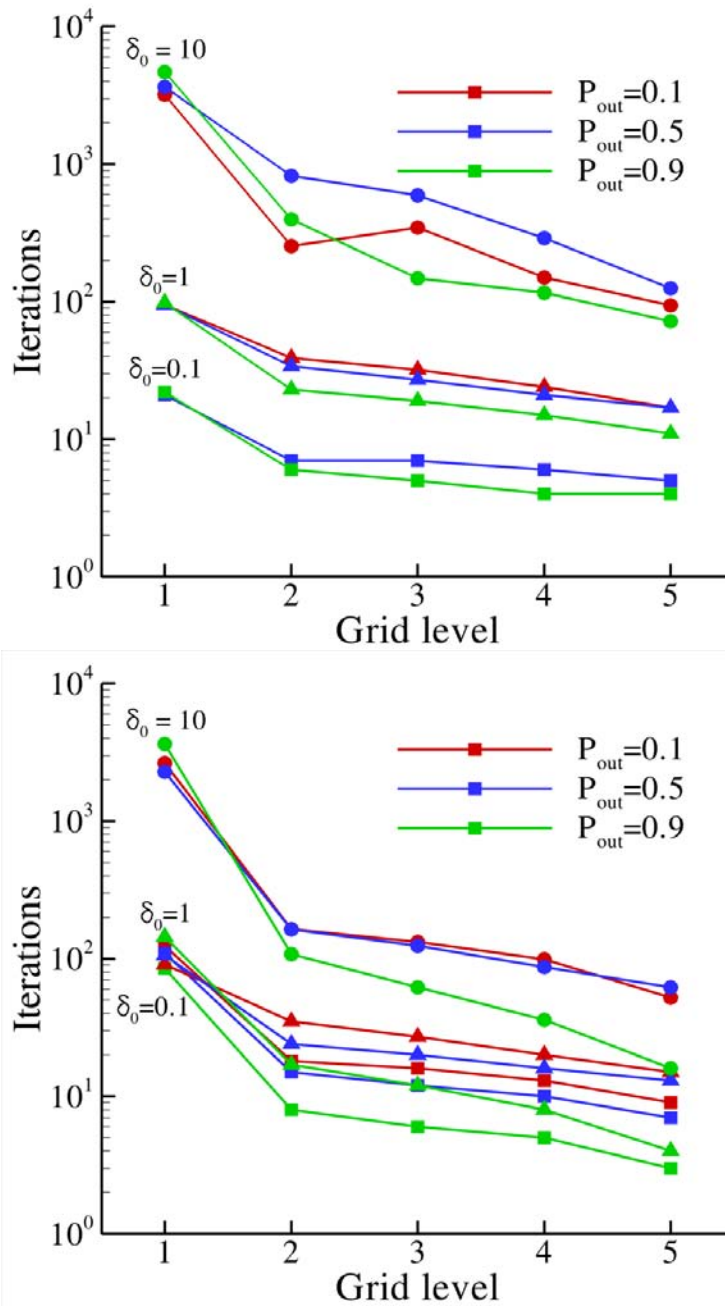


Figure 6.21: Iterations for various grid levels with $L/R = 1$ (up) and $L/R = 10$ (down) and for $\delta_0 = 0.1$ (square), $\delta_0 = 1$ (triangle), $\delta_0 = 10$ (circle)

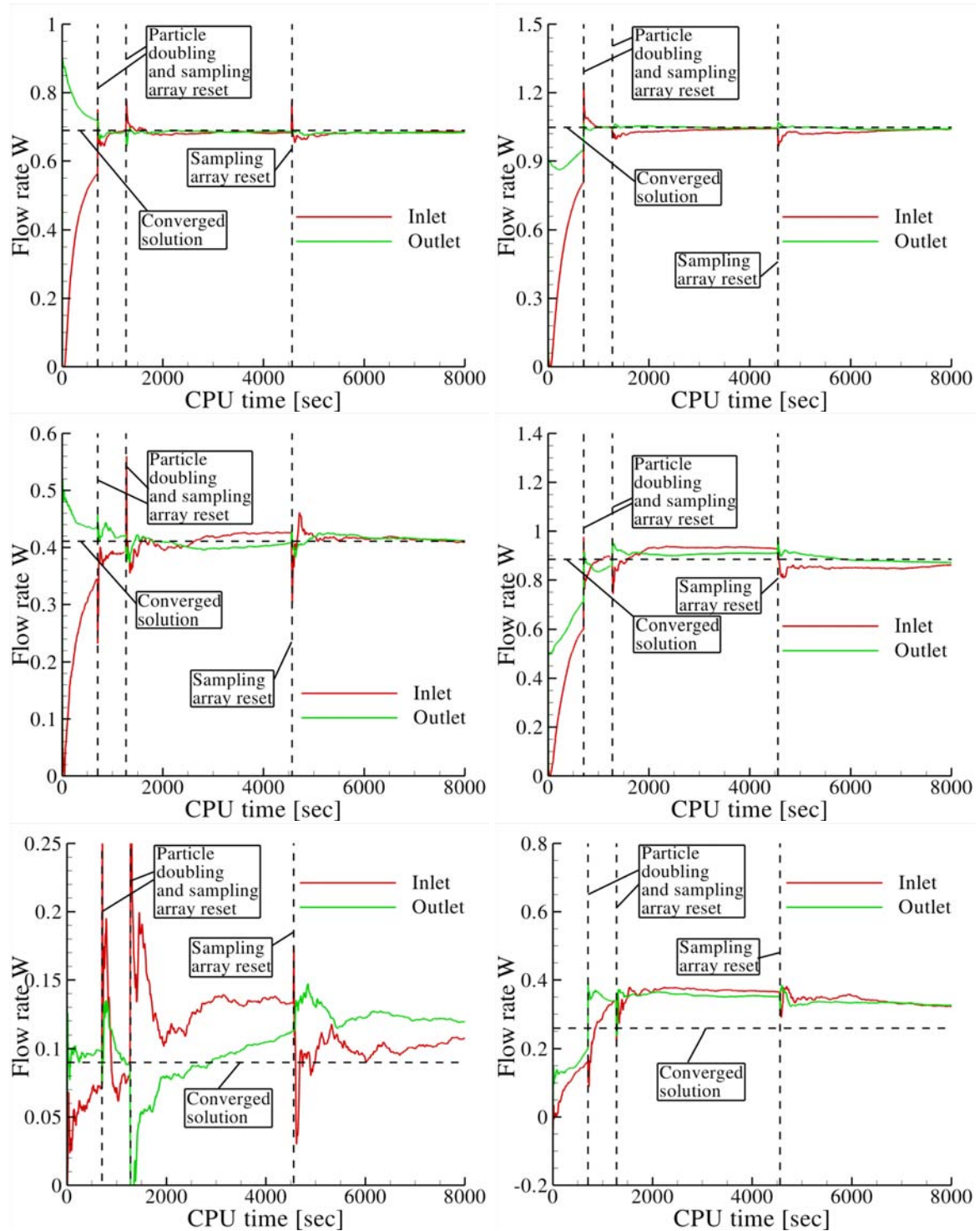


Figure 6.22: Evolution of the dimensionless flow rate W from DSMC against CPU time at the inlet and outlet cross-sections of a tube with $L/R = 1$, for $\delta_0 = 1$ (left), $\delta_0 = 10$ (right) and for $P_{out} = 0.1$ (up), $P_{out} = 0.5$ (middle), $P_{out} = 0.9$ (down)

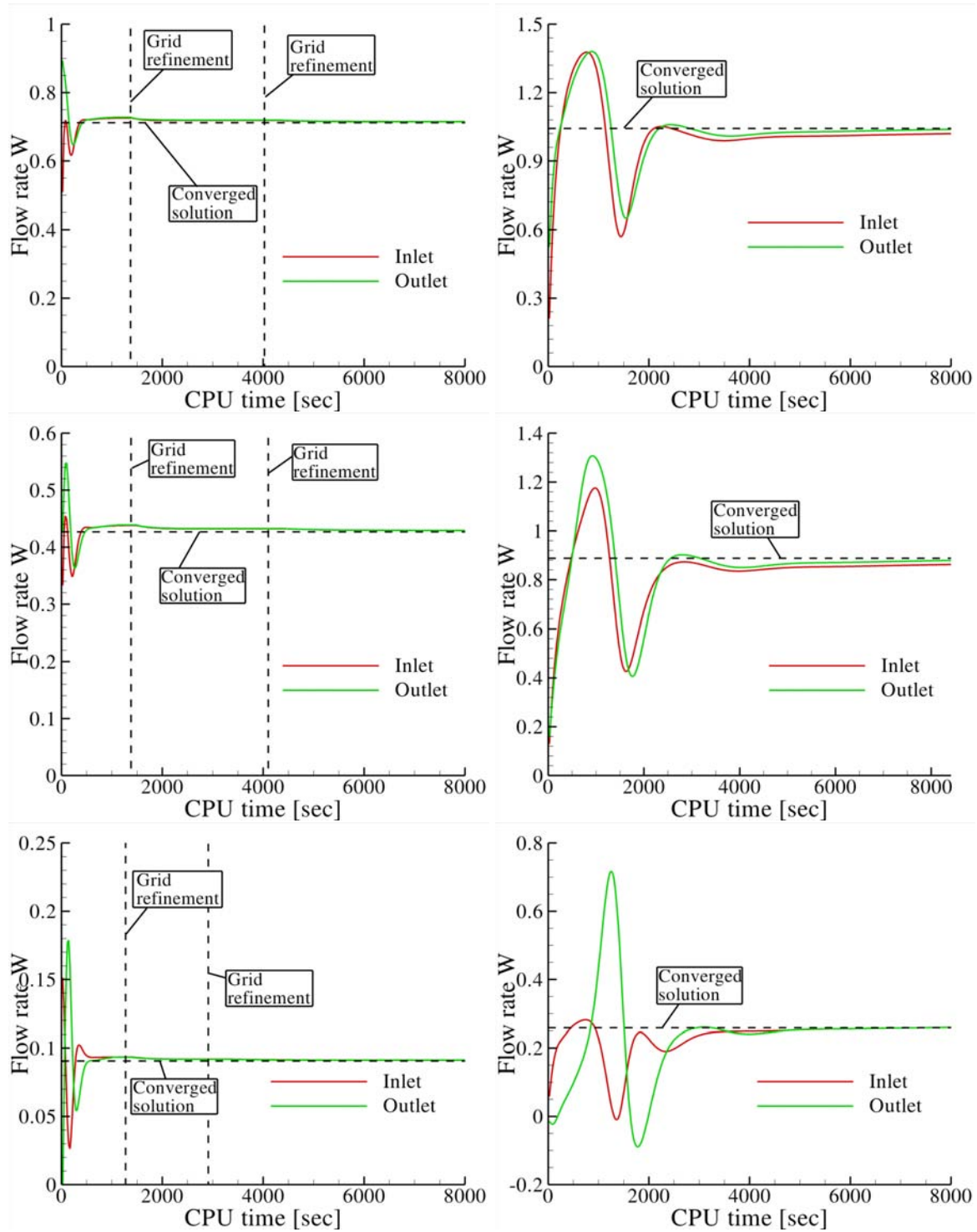


Figure 6.23: Evolution of the dimensionless flow rate W from DVM against CPU time at the inlet and outlet cross-sections of a tube with $L/R = 1$, for $\delta_0 = 1$ (left), $\delta_0 = 10$ (right) and for $P_{out} = 0.1$ (up), $P_{out} = 0.5$ (middle), $P_{out} = 0.9$ (down)

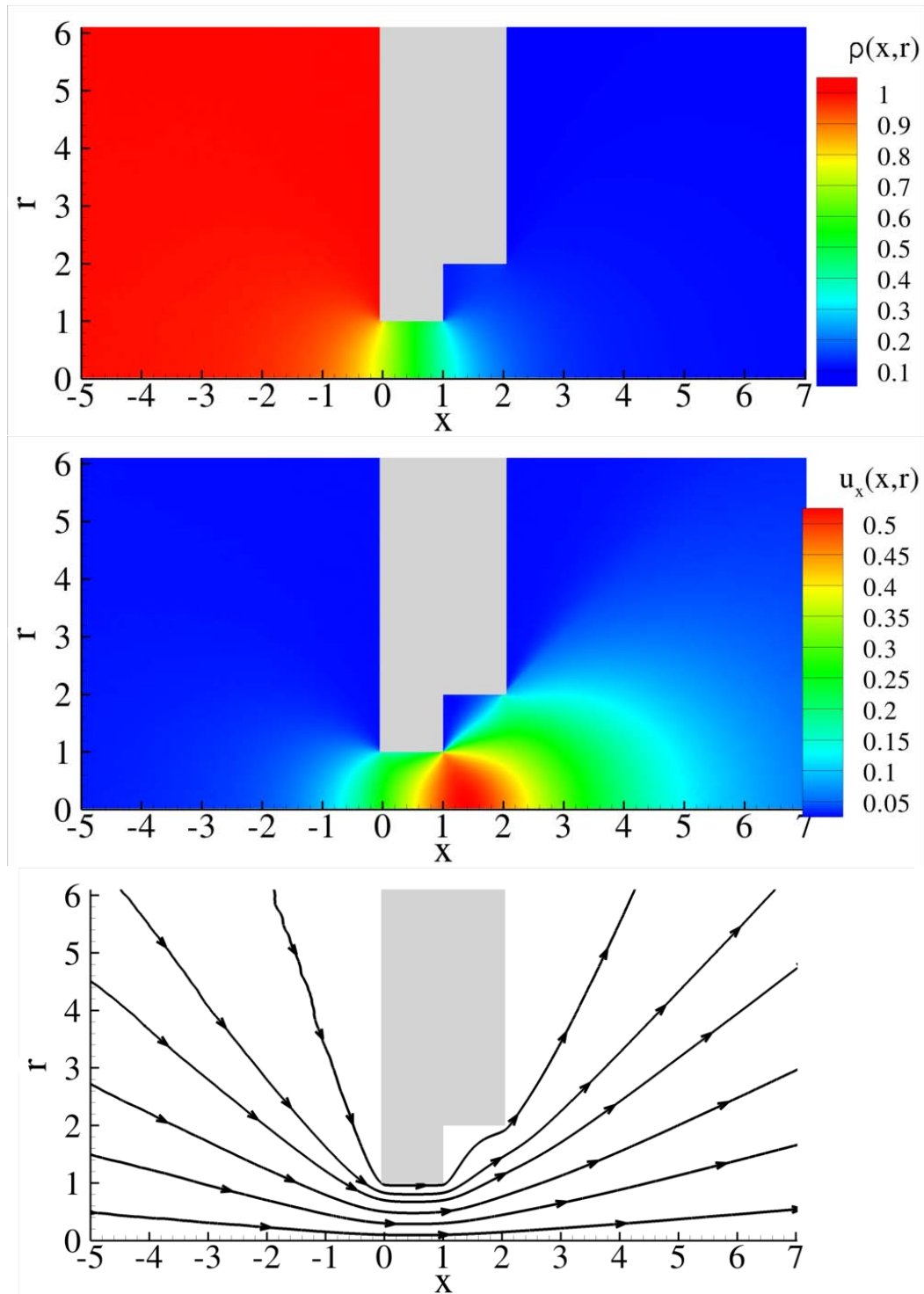


Figure 6.24: Density (up) and axial velocity (middle) contour, as well as streamlines (down) for the expanding tube geometry (Case 1) with $P_{out} = 0.1$, $\delta = 0.1$

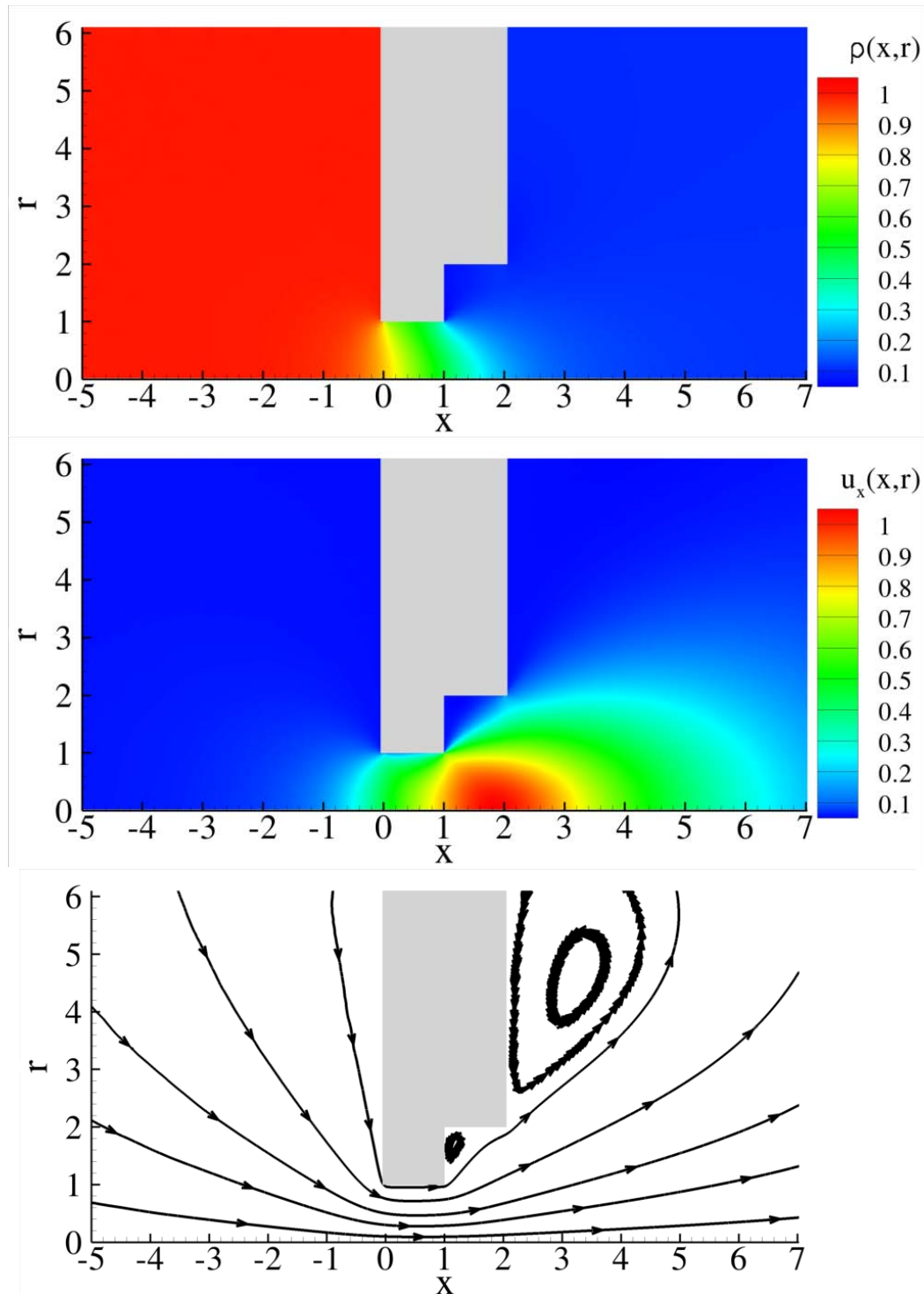


Figure 6.25: Density (up) and axial velocity (middle) contour, as well as streamlines (down) for the expanding tube geometry (Case 1) with $P_{out} = 0.1$, $\delta = 10$

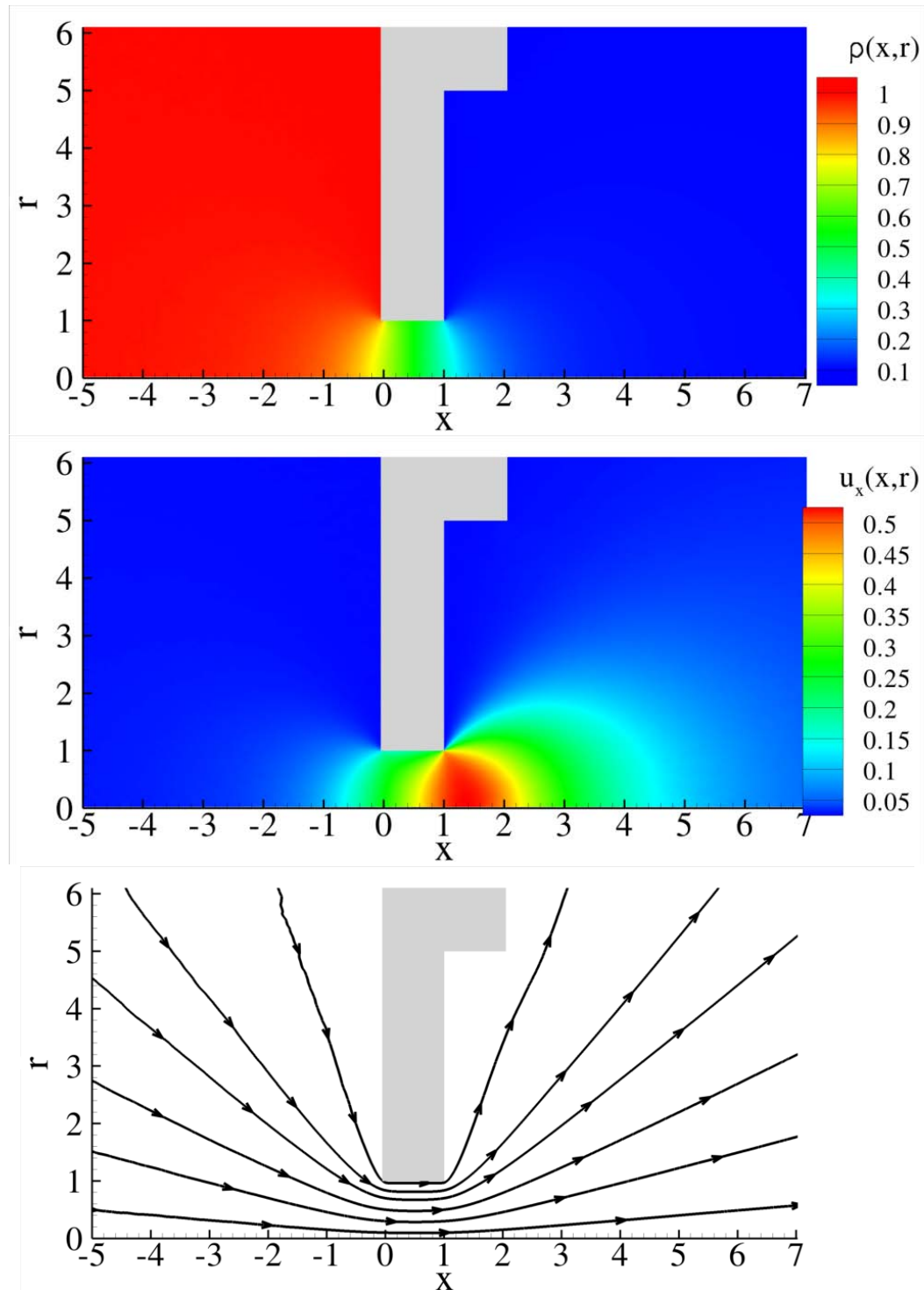


Figure 6.26: Density (up) and axial velocity (middle) contour, as well as streamlines (down) for the expanding tube geometry (Case 2) with $P_{out} = 0.1$, $\delta = 0.1$

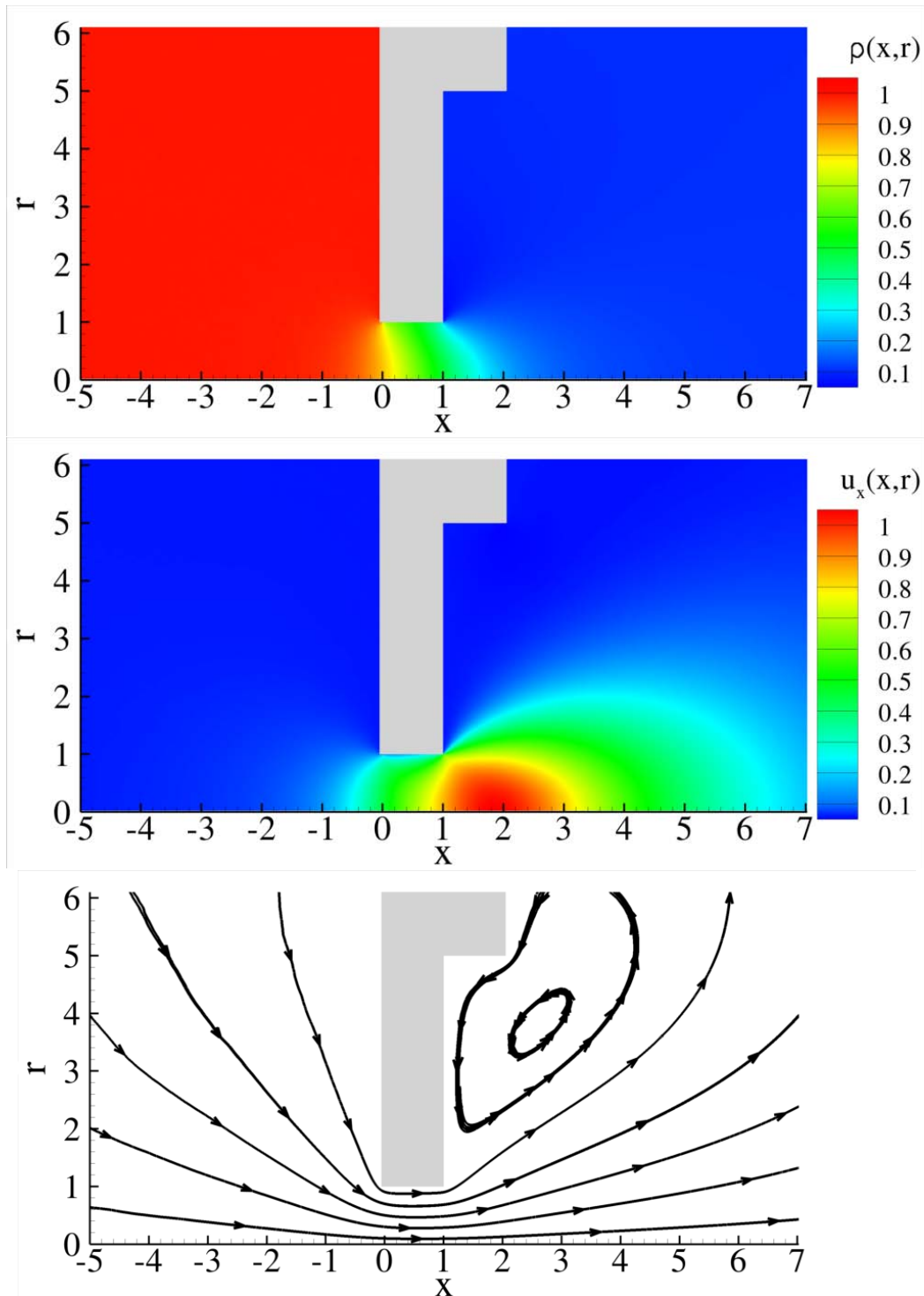


Figure 6.27: Density (up) and axial velocity (middle) contour, as well as streamlines (down) for the expanding tube geometry (Case 2) with $P_{out} = 0.1$, $\delta = 10$

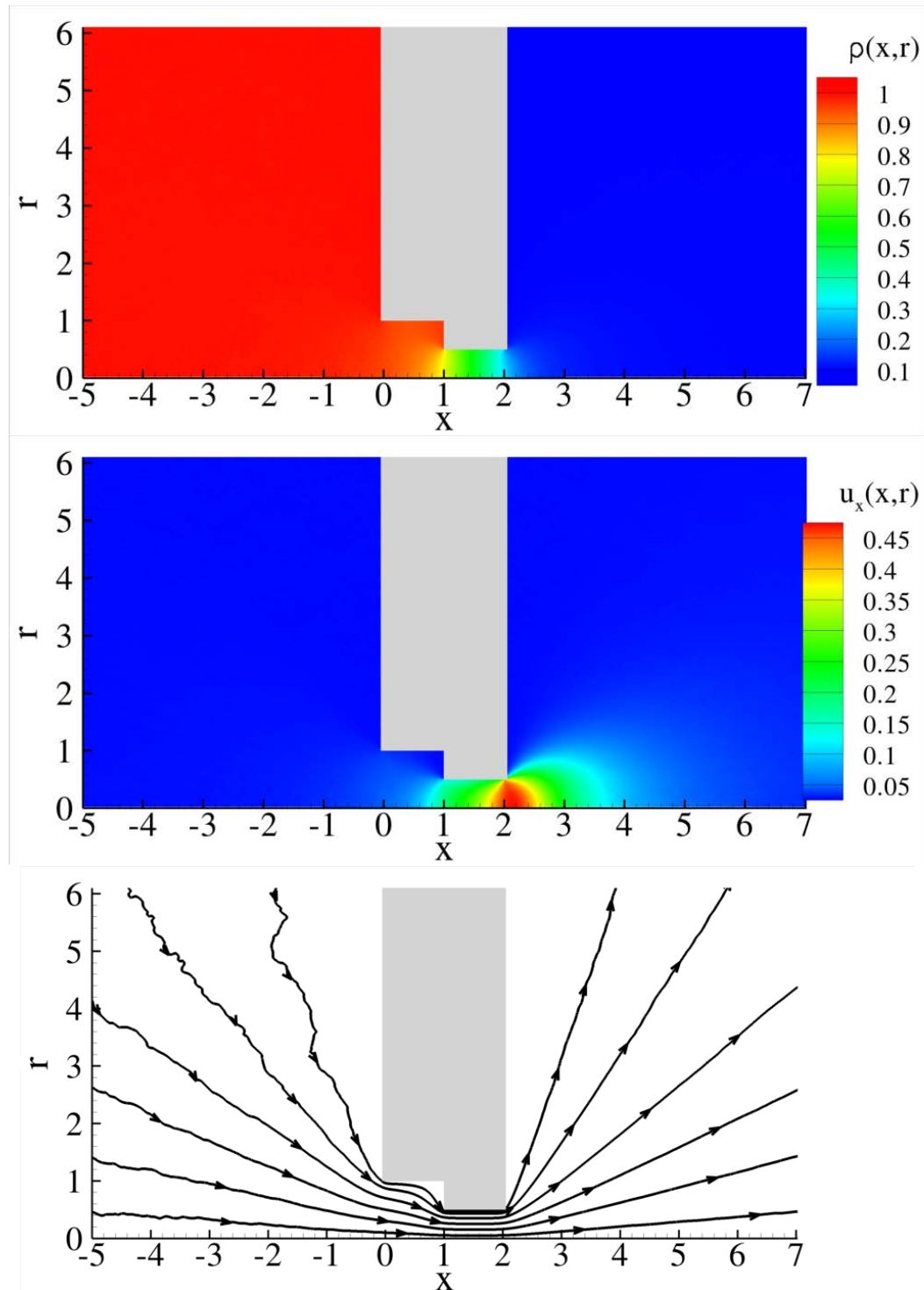


Figure 6.28: Density (up) and axial velocity (middle) contour, as well as streamlines (down) for the contracting tube geometry (Case 3) with $P_{out} = 0.1$, $\delta = 0.1$

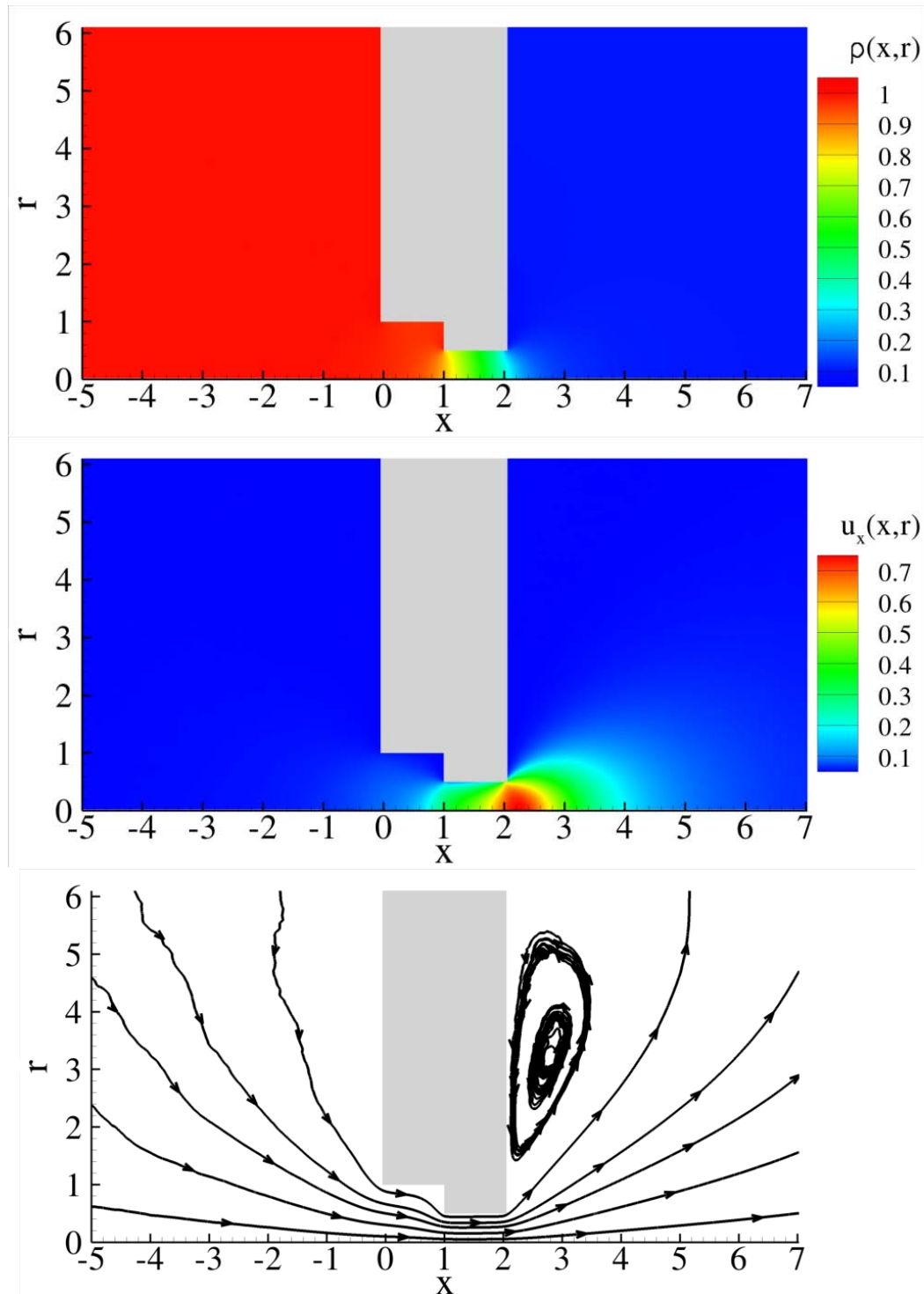


Figure 6.29: Density (up) and axial velocity (middle) contour, as well as streamlines (down) for the contracting tube geometry (Case 3) with $P_{out} = 0.1$, $\delta = 10$

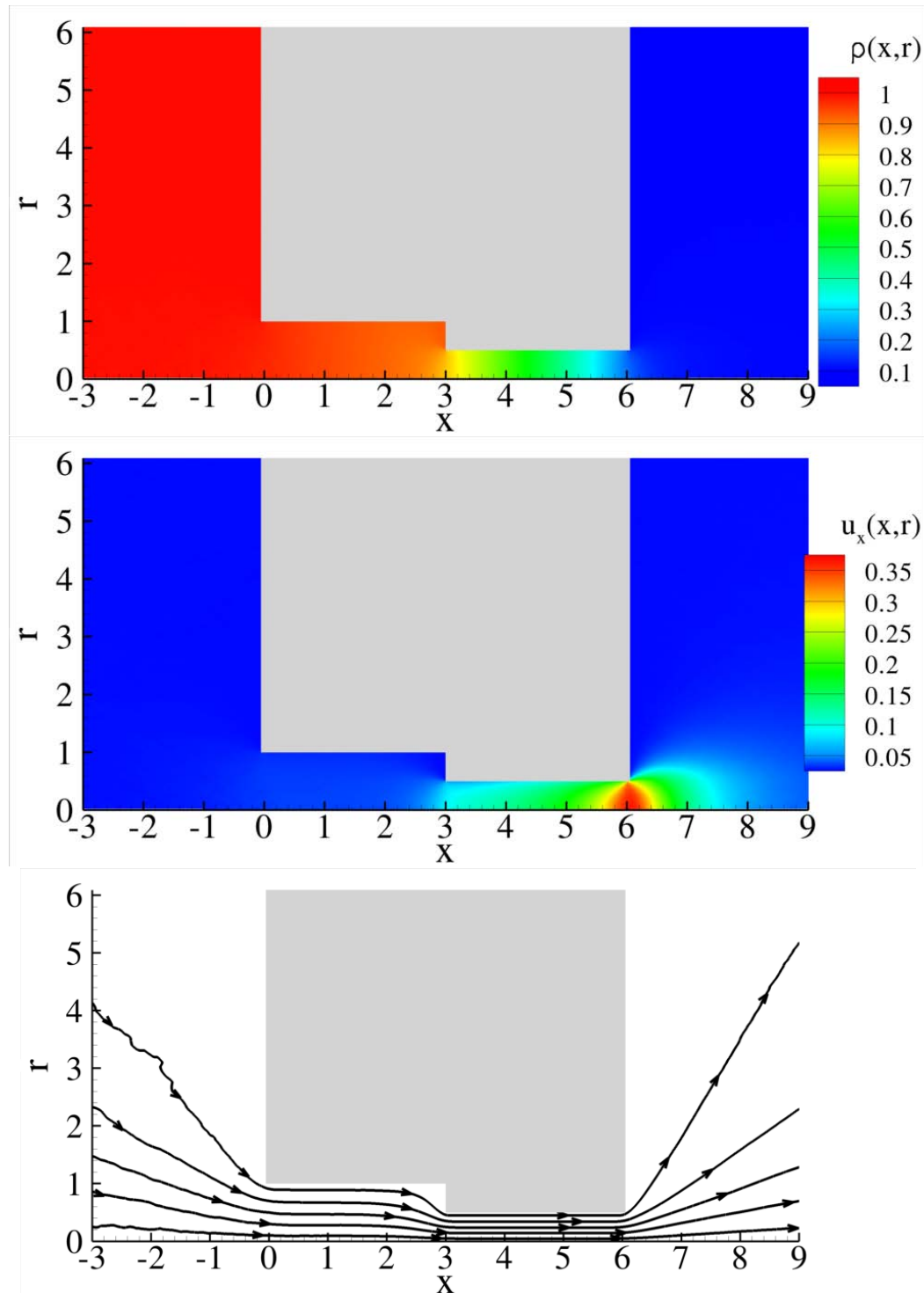


Figure 6.30: Density (up) and axial velocity (middle) contour, as well as streamlines (down) for the contracting tube geometry (Case 4) with $P_{out} = 0.1$, $\delta = 0.1$

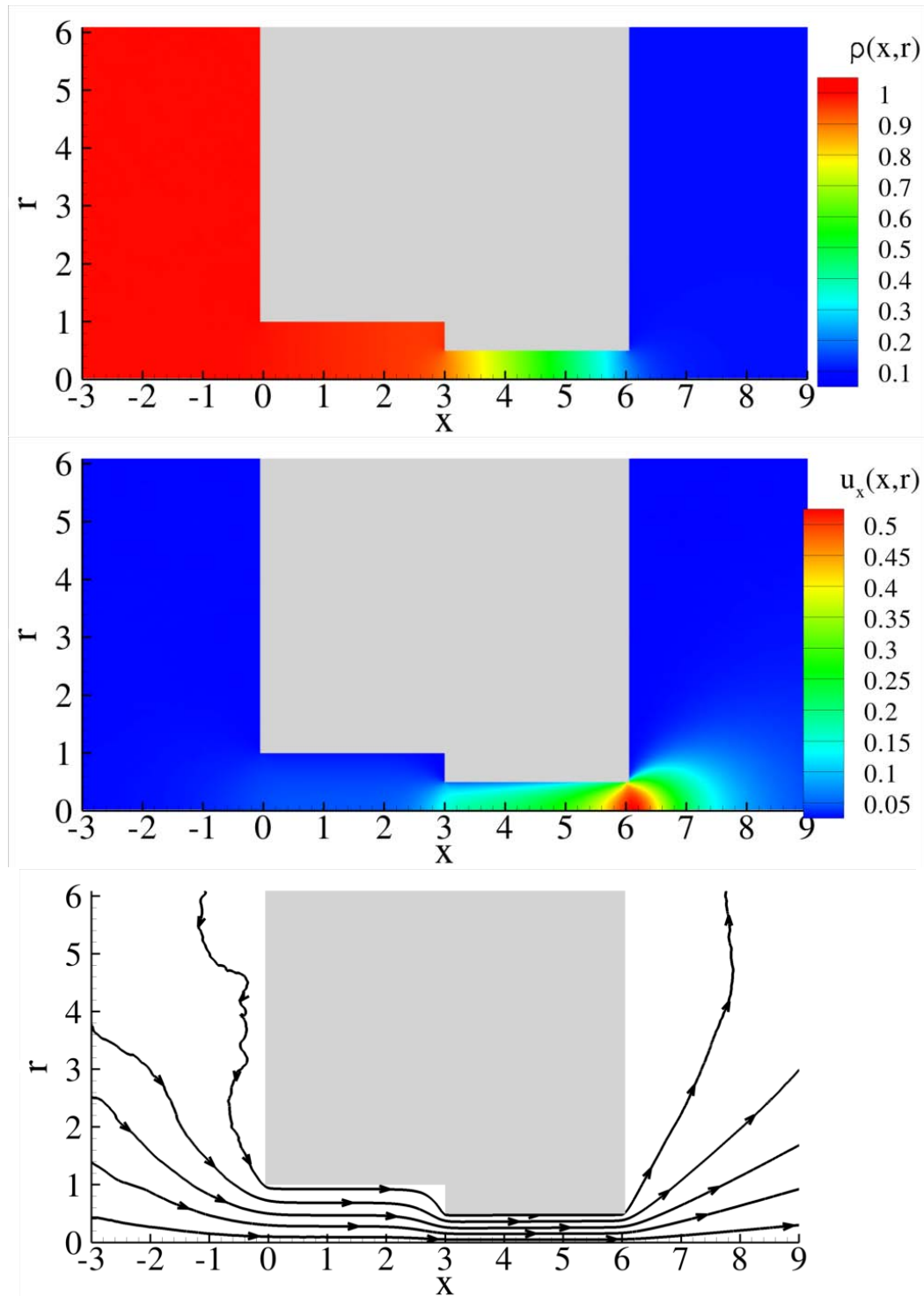


Figure 6.31: Density (up) and axial velocity (middle) contour, as well as streamlines (down) for the contracting tube geometry (Case 4) with $P_{out} = 0.1$, $\delta = 10$

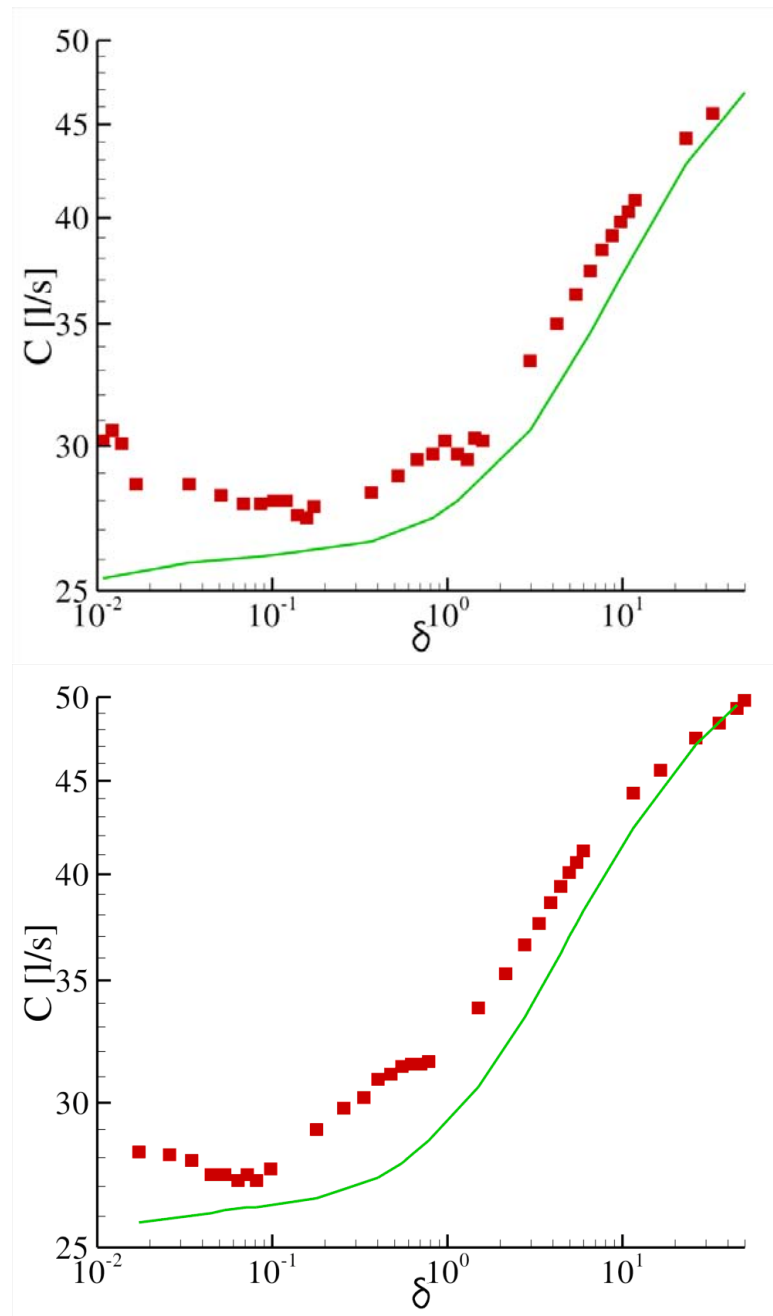


Figure 6.32: Numerical and experimental conductances for the contraction (up) and expansion (down) elements

Chapter 7

Concluding remarks

7.1 Summary and contributions

Several topics have been discussed in this dissertation, involving non-equilibrium transport phenomena in the whole range of the Knudsen number. Kinetic model equations have been solved deterministically and solutions of the Boltzmann equation have been obtained by stochastic approaches. The most important numerical methods, the Discrete Velocity method and the Direct Simulation Monte Carlo, have been applied and compared. This comparison involved not only results in terms of bulk quantities, such as flow rates, but also a qualitative analysis about the computational efficiency of each approach.

The application of advanced boundary conditions and in particular the ones derived using the Cercignani-Lampis scattering kernel, has been discussed for both flow and heat transfer configurations. This work not only provides a physical intuition regarding the influence of gas-surface interaction on the quantities of practical interest for the particular problems but may also lead to the calculation of the accommodation coefficients through a comparison with experimental results. The Cercignani-Lampis boundary conditions have been applied for the first time in several problems: linearized and non-linear heat transfer between parallel plates, non-linear heat transfer between coaxial cylinders and linearized flow in a rectangular duct. The non-linear form of the scattering kernel has not been used before for any problem in the literature and the differences in the formulation and the macroscopic quantities are highlighted. A comparison with experimental results is performed for flow through a rectangular duct and leads to a reasonable estimation of the tangential momentum accommodation coefficient, around $\alpha_t = 1.02 - 1.06$ for technical surfaces and various gases. Similarities and differences are discussed for the linear and non-linear heat transfer between plates problem. The

symmetry in terms of α_t of the heat flux for the cylindrical geometry are explained by the form of the boundary distribution function.

The problem of linearized flow in a parallel plate channel and a cylindrical tube, not considered before in the literature, have been studied here. The flow is due to a small pressure difference and linearized kinetic equations provide flow rates and macroscopic fields in a regime where other approaches, such as the DSMC method, have great difficulties. A comparison with DSMC indicates that a maximum deviation of around 7.7% is to be expected for any length with $\delta \leq 10$ and $\hat{P}_{out}/\hat{P}_{in} = 0.9$, indicating that this may be a useful limit in determining our simulation choice between the two approaches. It is also found that accommodation effects are negligible for the case of zero length and considerably stronger for moderate lengths, as expected. Moreover, the end effect is considered for long channels of both plane and cylindrical geometries. Results for both the axial pressure distribution and the dimensionless flow rate are compared between the typical integration scheme, the linearized (or the non-linear) formulation for the complete geometry and the end effect approach, and it is seen that the end effect approach greatly reduces discrepancies for moderately long channels ($10 \leq L/L_0 \leq 80$) in comparison to the typical scheme. It is believed that this method is an important contribution that can be easily applied in engineering calculations, significantly improving accuracy.

The study of heat transfer phenomena in problems of lower dimensionality, that is in the geometries of parallel plates and concentric cylinders, lead to a more complete understanding of differences between the linearized and non-linear formulation. It is seen that for small values of the rarefaction parameter δ_0 or the temperature ratio β the two approaches provide results very close to each other. Thus, a reliable estimation on the range of applicability of the linearized method has been provided, which is larger than the one expected by the strict mathematical limits. Non-linear effects due to departure from equilibrium, such as non-constant pressure profiles due to temperature differences, have been discovered. Different types of intermolecular interaction have been tested and differences in the temperature and heat flux profiles have been pointed out.

Even though the problem of non-linear flow in a cylindrical tube has been considered before

with DSMC, its treatment in this work based on the deterministic solution of kinetic model equations is beneficial for several reasons. First, the non-linear formulation is equally efficient for the simulation of flows in any pressure ratio, thus avoiding the obstacle of noise for moderate to low pressure differences which prohibits the usage of the DSMC method. Second, performance aspects of the code have been studied and compared qualitatively with the corresponding “in-house” version of the DSMC code for several values of the pressure ratio. Also, various kinetic models have been tested in this realistic configuration and this allowed the evaluation of the behaviour of various kinetic models. Finally, results extracted here serve as further validation of previously given results and strengthen our confidence towards their values.

The investigations described above for the linearized and non-linear formulations has lead to a significant outcome: the limits of the linearized formulation have been determined, in the search for a complete methodology covering all possible flow conditions. In this context, the above heat transfer and pressure driven flow problems have been examined and the interfaces separating the regimes where each methodology produces the most accurate results have been determined.

A study of adiabatic walls also does not exist in the literature to our knowledge. This new type of boundary conditions is applied in the non-linear pressure driven tube problem. Results show that for the particular flow configuration, the flow rate found for isothermal conditions is nearly identical to the adiabatic one for the range of parameters examined here. Some deviations are found for the macroscopic quantity fields. It is expected that this type of boundary conditions will receive more attention in the future due to the materials involved in the fabrication of MEMS.

Short channel elements of contraction/expansion geometrical characteristics have also been examined. Various different geometrical parameter combinations have been considered, indicating the dependence of the flow on each quantity. The DSMC algorithm included various techniques for the accurate and efficient simulation of the flow, such as weighting zones and particle doubling. A comparison with experiments shows good agreement. The extended study of these elements could be very beneficial for the simulation of realistic flow networks, where such geometries are frequently

encountered.

Memory optimization has been applied on all channel/tube codes involving the complete simulation of flow the flow field, allowing the use of very large computational domains. Various numerical techniques, such as the Wynn- ε acceleration, Romberg integration, grid refinement and parallelization, have been developed or applied for the efficient calculation of the most demanding non-linear problems. It is found that these techniques greatly benefit convergence time, reducing it by 1-2 orders of magnitude.

The current dissertation includes the upgrade and advancement of kinetic algorithms and models, the investigation of non-equilibrium transport phenomena and the extraction of results for linear and non-linear heat transfer and flow problems, including comparisons with experimental data and other numerical methods. To sum up, the most important contributions of this dissertation are outlined below:

- The non-linear form of the Cercignani-Lampis scattering kernel, which has not been applied before in the literature, has been used. Furthermore, the linearized form has also been employed for both flow and heat transfer problems. Comparisons with relevant experiments has lead to surface characterization with respect to argon and helium flows.
- An advanced and computationally efficient discrete velocity scheme has been developed for the numerical treatment of linear and non-linear flow and heat transfer configurations. Through this algorithm, memory and CPU time requirements have been significantly reduced.
- Linearized flow through orifices and tubes of finite length due to small pressure differences has been studied, providing results for the first time in the literature.
- The effect of the channel ends on the flow field and mass flow rate has been investigated for the geometries of rectangular channels with large aspect ratios and cylindrical tubes. A novel methodology is proposed to extend the well known fully developed flow analysis, applied in

infinitely long channels, to channels of finite length. These results may be used to avoid the complete numerical solution, greatly reducing the computational effort.

- Non-linear flow through orifices and tubes of finite length has been solved and compared with DSMC results. A qualitative comparison between the two numerical methods has also been performed and solid remarks about the effectiveness of the proposed discrete velocity algorithm have been drawn.
- A boundary condition model has been developed for adiabatic walls, which have not been considered before in the literature.
- The range of validity of linearized theory has been investigated through the problems of heat transfer between parallel plates and coaxial cylinders, as well as through flow through a cylindrical tube. It has been found that the linearized formulation results can be applied well beyond their theoretical limits with sufficient accuracy.
- Non-linear flow through a contraction/expansion pipe element, consisting of two cylindrical tubes connected in series, has been simulated via the DSMC method.

7.2 Future work

There are several possibilities for future work, concerning both theoretical and practical aspects of the current work.

- Further application of the Cercignani-Lampis scattering kernel in more complicated geometries and extension of comparison with experimental data. Other scattering kernels may also be applied to evaluate the validity of several models in a variety of physical conditions. Direct comparison with molecular beam data can also be attempted.
- Investigation of the limits of linearized theory and search for a methodology able to deal with any condition. For example, if the range of applicability of the linearized formulation has been

studied extensively, we could reach a conclusion on its limits and argue that all other problems may be solved by non-linear kinetic equations or DSMC.

- Simulation of the end effect geometry in a wider range of conditions and publication for engineering purposes. This is expected to lead to significantly better results than the simple integration scheme for moderately long channels with only minor modifications of the corresponding numerical codes.
- Numerical stability analysis and investigation of more effective acceleration schemes for non-linearized kinetic model equations. Even though the computational effort has been significantly reduced with the schemes shown here, it would be highly desirable to examine the possibility of acceleration methodologies similar to the ones applied before in the linearized problems [76].
- Use of the non-linear code for temperature driven flows. These physical conditions have already been integrated in the numerical code and simulations are under way.
- Study of mixture flow with linear and non-linear kinetic models in various configurations. The study of mixtures is obviously very important for nearly all practical applications and non-linear effects have not been studied extensively.
- Modification of the parallelized numerical codes in order to be executed by the GPU with CUDA. This new technology is becoming very popular for the numerical solution of problems in all scientific fields and generally delivers high performance improvements.
- Extension of the DSMC or non-linear DVM codes in more complicated geometries, with particular interest in various network elements such as junctions, curves and so on. This kind of work may be realized relatively easily due to the flexibility of the DSMC method and the related experience in this work.

It is hoped that the current work will stimulate more research in the related fields of non-linear kinetic equations, DSMC, as well as related experimental studies.

Bibliography

- [1] J.A. McLennan, *Introduction to non-equilibrium statistical mechanics*, Prentice-Hall, 1996.
- [2] C.M. Ho, Y.C. Tai, *Micro-electro-mechanical systems (MEMS) and fluid flows*, Annual Review of Fluid Mechanics, 30, 579-612, 1998.
- [3] J.M. Reese, M.A. Gallis, D.A. Lockerby, *New directions in fluid dynamics: non-equilibrium aerodynamic and microsystem flows*, Philosophical Transactions of the Royal Society A, 361, 2967-2988, 2003.
- [4] W. Jitschin, S. Ludwig, *Dynamical behaviour of the Pirani sensor*, Vacuum, 75(2), 169-176, 2004.
- [5] Chr. Day, D. Murdoch, *The ITER Vacuum Systems*, Journal of Physics: Conference Series, 114, 2008.
- [6] P.A. Gnoffo, *Planetary-entry gas dynamics*, Annual Review of Fluid Mechanics, 31, 459-494, 1999.
- [7] K. Moe, M.M. Moe, S.D. Wallace, *Improved Satellite Drag Coefficient Calculations from Orbital Measurements of Energy Accommodation*, Journal of Spacecraft and Rockets, 35, 266-272, 1998.
- [8] W. Umrath, *Fundamentals of Vacuum Technology*, Leybold, Cologne, 1998.
- [9] M.S. Ivanov, S.F. Gimelshein, *Computational hypersonic rarefied flows*, Annual Review of Fluid Mechanics, 30, 469-505, 1998.
- [10] R.A. East, *A reusable space-rescue vehicle: re-entry simulation*, Philosophical Transactions of the Royal Society A, 357, 2177-2195, 1999.

- [11] F. Sharipov, *Hypersonic flow of rarefied gas near the Brazilian satellite during its reentry into atmosphere*, Brazilian Journal of Physics, 33, 398-405, 2003.
- [12] G.J. LeBeau, F.E. Lumpkin III, *Application highlights of the DSMC Analysis Code (DAC) software for simulating rarefied flows*, Computer Methods in Applied Mechanics and Engineering, 191, 595-609, 2001.
- [13] Z. Chavis, R. Wilmoth, *Plume Modeling and Application to Mars 2001 Odyssey Aerobraking*, Journal of Spacecraft and Rockets, 42, 450-456, 2005.
- [14] H. Katsurayama, T. Abe, *Particle simulation of electromagnetic aerobraking in a hypersonic rarefied regime*, 27th International Symposium on Rarefied Gas Dynamics, 2010.
- [15] A.A. Alexeenko, D.A. Levin, S.F. Gimelshein, M.S. Ivanov, A.D. Ketsdever, *Numerical and Experimental Study of Orifice Flow in the Transitional Regime*, AIAA Paper 2001, 3072, 2001.
- [16] F. Sharipov, P. Fahrenbach, A. Zippa, *Numerical modeling of the Holweck pump*, Journal of Vacuum Science and Technology A, 23(5), 2005.
- [17] S. Giors, E. Colombo, F. Inzoli, F. Subba, R. Zanino, *Computational fluid dynamic model of a tapered Holweck vacuum pump operating in the viscous and transition regimes. I. Vacuum performance*, Journal of Vacuum Science Technology A: Vacuum, Surfaces and Films, 24(4), 1584 -1591, 2006.
- [18] G.A. Bird, *Effect of inlet guide vanes and sharp blades on the performance of a turbomolecular pump*, Journal of Vacuum Science and Technology A, 29(1), 011016, 2011.
- [19] S. Takata, H. Sugimoto, S. Kosuge, *Gas separation by means of the Knudsen compressor*, European Journal of Mechanics - B/Fluids, 26(2), 155-181, 2007.
- [20] P.J. Sun, J.Y. Wu, P. Zhang, L. Xu, M.L. Jiang, *Experimental study of the influences of degraded vacuum on multilayer insulation blankets*, Cryogenics, 49(12), 719-726, 2009.

- [21] A. Venkattraman, A. Alexeenko, *Molecular models for DSMC simulations of metal vapors in vacuum deposition systems*, 27th International Symposium on Rarefied Gas Dynamics, 2010.
- [22] A.R. Jha, *Cryogenic technology and applications*, Elsevier, Oxford, 2006.
- [23] X. Luo, Chr. Day, V. Hauer, O.B. Malyshev, R.J. Reid, F. Sharipov, *Monte Carlo simulation of gas flow through the KATRIN DPS2-F differential pumping system*, Vacuum, 80(8), 864-869, 2006.
- [24] O.B. Malyshev, Chr. Day, X. Luo, F. Sharipov, *Tritium gas flow dynamics through the source and transport system of the Karlsruhe tritium neutrino experiment*, Journal of Vacuum Science Technology A, 27(1), 73-81, 2009.
- [25] *Vacuum in Accelerators*, CERN Accelerator School (CAS), Platja d'Aro, Spain, 2006.
- [26] M. Houry, L. Gargiulo, C. Balorin, V. Bruno, D. Keller, H. Roche, N. Kammerer, Y. Meas-son, F. Carrel, V. Schoepff, *Diagnostics carried by a light multipurpose deployer for vacuum vessel interventions*, Fusion Engineering and Design, In Press, Corrected Proof, doi: 10.1016/j.fusengdes.2010.11.004, 2010.
- [27] M. Bao, H. Yang, *Squeeze film air damping in MEMS*, Sensors and Actuators A, 136(1), 3-27, 2007.
- [28] R. Legtenberg, A.W. Groeneveld, M. Elwenspoek, *Comb-drive actuators for large displace-ments*, Journal of Micromechanics and Microengineering, 6(3), 1996.
- [29] S.H. Oh, K.C. Lee, J. Chun, M. Kim, S.S. Lee, *Micro heat flux sensor using copper electroplat-ing in SU-8 microstructures*, Journal of Micromechanics and Microengineering, 11(3), 2001.
- [30] K. Tomarikawa, S. Yonemura, T. Tokumasu, T. Koido, *Numerical analysis of gas flow in porous media with surface reaction*, 27th International Symposium on Rarefied Gas Dynamics, 2010.

- [31] G.E. Karniadakis, A. Beskok, *Micro flows: Fundamentals and simulation*, Springer-Verlag, New York, 2002.
- [32] I.N. Ivchenko, S.K. Loyalka, R.V. Thompson Jr., *Analytical methods for problems of molecular transport*, Springer, Dordrecht, The Netherlands, 2007.
- [33] D.G. Coronell, K.F. Jensen, *Monte Carlo simulations of very low pressure chemical vapor deposition*, Journal of Computer-Aided Materials Design, 1, 3-26, 1993.
- [34] K. Jousten, G. Messer, D. Wandrey, *A precision gas flowmeter for vacuum metrology*, Vacuum, 44(2), 135-141, 1993.
- [35] M. Gad-el-Hak, *The MEMS handbook*, The Mechanical engineering handbook series, CRC Press, 2002.
- [36] K. Jousten, *Handbook of Vacuum Technology*, Wiley-VCH, Berlin, 2008.
- [37] E.P. Muntz, *Rarefied Gas Dynamics*, Annual Review of Fluid Mechanics, 21, 387-422, 1989.
- [38] W.D. Niven, *Scientific Papers of James Clerk Maxwell*, Dover Publications, Inc., New York, 1965.
- [39] L. Boltzmann, *Lectures on Gas Theory*, University of California Press, Berkeley, Translated by S.G. Brush, 1964.
- [40] R. Balescu, *Equilibrium and nonequilibrium statistical mechanics*, John Wiley and sons, New York, 1975.
- [41] J.H. Ferziger, H.G. Kaper, *Mathematical Theory of Transport Processes in Gases*, North-Holland, Amsterdam, 1972.
- [42] D. Hilbert, *Grundzuege einer allgemein Theorie der linearen Integralgleichungen*, Teubner, Leipzig, 1912.

- [43] H. Grad, *On the kinetic theory of rarefied gases*, Communications on Pure and Applied Mathematics, 2(4), 331-407, 1949.
- [44] M. Knudsen, *Die Molekularstroemung der Gase durch Offnungen und die Effusion*, Annalen der Physik, 333(5), 999-1016, 1909.
- [45] F. Sharipov, V. Seleznev, *Data on internal rarefied gas flows*, Journal of Physical and Chemical Reference Data, 27(3), 657-706, 1998.
- [46] R.G. Deissler, *An analysis of second-order slip flow and temperature-jump boundary conditions for rarefied gases*, International Journal of Heat and Mass Transfer, 7(6), 681-694, 1964.
- [47] D.A. Lockerby, J.M. Reese, *Near wall scaling of the Navier-Stokes constitutive relations for accurate micro gas flow simulations*, 5th International Conference on Nanochannels, Microchannels and Minichannels (ICNMM), June, 2007.
- [48] Y. Sone, *Kinetic Theory and Fluid Dynamics*, Birkhaeuser, Boston, 2002.
- [49] S. Chapman, *On the law of distribution of molecular velocities and on the theory of viscosity and thermal conduction, in a non-uniform simple monoatomic gas*, Philosophical Transactions of the Royal Society of London, 216, 279-341, 1916.
- [50] D. Enskog, *Bermerkungen zu einer Fundamentalgleichung in der kinetischen Gastheorie*, Phys. Z., 12, 533-539, 1911.
- [51] C. Shen, *Rarefied Gas Dynamics: Fundamentals, Simulations and Micro Flows*, Springer, 2005.
- [52] X. Zhong, R.W. MacCormack, D.R. Chapman, *Stabilization of the Burnett Equations and Application to Hypersonic Flows*, AIAA Journal, 31(6), 1036-1043, 1993.
- [53] P.L. Bhatnagar, E.P. Gross, M. Krook, *A model for collision processes in gases. I. Small amplitude processes in charged and neutral one-component systems*, Physical Review, 94(3), 511-525, 1953.

- [54] P. Welander, *On the temperature jump in a rarefied gas*, Arkiv for fysik, 7, 507-553, 1954.
- [55] E.M. Shakhov, *Generalization of the Krook kinetic equation*, Fluid Dynamics, 3(95), 1968.
- [56] L.H. Holway, *New statistical models for kinetic theory: methods of construction*, Physics of fluids, 9(9), 1966.
- [57] P. Andries, P. Le Tallec, J.P. Perlat, B. Perthame, *The Gaussian-BGK model of Boltzmann equation with small Prandtl number*, European Journal of Mechanics - B/Fluids, 19, 813-830, 2000.
- [58] Y. Zheng, H. Struchtrup, *Ellipsoidal statistical Bhatnagar-Gross-Krook model with velocity-dependent collision frequency*, Physics of Fluids, 17(12), 2005.
- [59] L. Mieussens, H. Struchtrup, *Numerical comparison of Bhatnagar-Gross-Krook models with proper Prandtl number*, Physics of Fluids, 16(8), 2797-2813, 2004.
- [60] G. Liu, *A method for constructing a model form for the Boltzmann equation*, Physics of Fluids A, 2(2), 277-280, 1990.
- [61] T.F. Morse, *Kinetic Model Equations for a Gas Mixture*, Physics of Fluids, 7(12), 2012-2013, 1964.
- [62] B.B. Hamel, *Kinetic Model for Binary Gas Mixtures*, Physics of Fluids, 8(3), 418-425, 1965.
- [63] F.J. McCormack, *Construction of linearized kinetic models for gaseous mixtures and molecular gases*, Physics of Fluids, 16(12), 2095-2105, 1973.
- [64] S. Kosuge, *Model Boltzmann equation for gas mixtures: Construction and numerical comparison*, European Journal of Mechanics - B/Fluids, 28(1), 170-184, 2009.
- [65] C. Cercignani, F. Sharipov, *Gaseous mixture slit flow at intermediate Knudsen numbers*, Physics of Fluids A, 4(6), 1283-1289, 1992.

- [66] S. Naris, D. Valougeorgis, F. Sharipov, D. Kalempa, *Discrete velocity modelling of gaseous mixture flows in MEMS*, Superlattices and Microstructures, 35(3-6), 629-643, 2004.
- [67] S. Chapman, T.G. Cowling, *The mathematical theory of non-uniform gases*, Cambridge University Press, Cambridge, 1970.
- [68] J.O. Hirschfelder, C.F. Curtiss, R.B. Bird, *The molecular theory of gases and liquids*, Wiley, New York, 1964.
- [69] T. Ohwada, Y. Sone, K. Aoki, *Numerical analysis of the Poiseuille and thermal transpiration flows between two parallel plates on the basis of the Boltzmann equation for hard-sphere molecules*, Physics of Fluids A, 1(12), 2042-2049, 1989.
- [70] P. Kowalczyk, A. Palczewski, G. Russo, Z. Walenta, *Numerical solutions of the Boltzmann equation: comparison of different algorithms*, European Journal of Mechanics - B/Fluids, 27(1), 62-74, 2008.
- [71] F. Sharipov, G. Bertoldo, *Numerical solution of the linearized Boltzmann equation for an arbitrary intermolecular potential*, Journal of Computational Physics, 228(9), 3345-3357, 2009.
- [72] A.B. Huang, D.L. Hartley, *Nonlinear Rarefied Couette Flow with Heat Transfer*, Physics of Fluids, 11(6), 1321-1326, 1968.
- [73] S. Naris, D. Valougeorgis, *Rarefied gas flow in a triangular duct based on a boundary fitted lattice*, European Journal of Mechanics - B/Fluids, 27, 810-822, 2008.
- [74] S. Varoutis, S. Naris, V. Hauer, Chr. Day, D. Valougeorgis, *Computational and experimental study of gas flows through long channels of various cross sections in the whole range of the Knudsen number*, Journal of Vacuum Science and Technology A, 27(1), 2009.
- [75] S. Pantazis, S. Varoutis, V. Hauer, Chr. Day, D. Valougeorgis, *Gas-surface scattering effect on vacuum gas flows through rectangular channels*, to appear in Vacuum.

- [76] D. Valougeorgis, S. Naris, *Acceleration schemes of the discrete velocity method: Gaseous flows in rectangular microchannels*, SIAM Journal of Scientific Computing, 25(2), 534-552, 2003.
- [77] S. Naris, D. Valougeorgis, *The driven cavity flow over the whole range of the Knudsen number*, Physics of Fluids, 17(9), 907106, 2005.
- [78] S. Pantazis, D. Valougeorgis, *Efficient simulation of rarefied gas flows through tubes of finite length based on kinetic model equations*, 27th International Symposium on Rarefied Gas Dynamics, 2010.
- [79] S. Misdanitis, S. Pantazis, D. Valougeorgis, *Rarefied flow between plates of finite length via an efficient fully deterministic nonlinear algorithm*, 2nd European Conference on Microfluidics, 2010.
- [80] G.A. Bird, *Molecular Gas Dynamics and the Direct Simulation of Gas Flows*, Oxford University Press, Oxford, 1994.
- [81] M.A. Gallis, J.R. Torczynski, D.J. Rader, G.A. Bird, *Convergence behavior of a new DSMC algorithm*, Journal of Computational Physics, 228(12), 4532-4548, 2009.
- [82] W. Wagner, *A convergence proof for Bird's direct simulation Monte Carlo method for the Boltzmann equation*, Journal of Statistical Physics, 66(3), 1011-1044, 1992.
- [83] L.L. Baker, N.G. Hadjiconstantinou, *Variance-reduced Monte Carlo solutions of the Boltzmann equation for low-speed gas flows: A discontinuous Galerkin formulation*, International Journal for Numerical Methods in Fluids, 58, 381-402, 2008.
- [84] G.A. Radtke, N.G. Hadjiconstantinou, W. Wagner, *Low-noise Monte Carlo simulation of the variable hard sphere gas*, Physics of Fluids, 23(3), 030606, 2011.

- [85] P. Cremonesi, M. Ferrari, A. Frezzotti, R. Pavani, *Parallel algorithms applied to direct simulation methods*, Euromicro Workshop on Parallel and Distributed Processing, 239-246, January 1993.
- [86] S. Naris, D. Valougeorgis, F. Sharipov, D. Kalempa, *Flow of gaseous mixtures through rectangular microchannels driven by pressure, temperature, and concentration gradients*, Physics of Fluids, 17(10), 100607, 2005.
- [87] G.P. Ghiroldi, *GPU Acceleration of Rarefied Gas Dynamic Simulations*, Politecnico di Milano - Dipartimento di Matematica, Milano, Italy 2010.
- [88] R.R. Nourgaliev, T.N. Dinh, T.G. Theofanous, D. Joseph, *The lattice Boltzmann equation method: theoretical interpretation, numerics and implications*, International Journal of Multiphase Flow, 29(1), 117-169, 2003.
- [89] T. Abe, *Derivation of the Lattice Boltzmann Method by Means of the Discrete Ordinate Method for the Boltzmann Equation*, Journal of Computational Physics, 131(1), 241-246, 1997.
- [90] Q. Sun, I.D. Boyd, J. Fan, *Development of an information preservation method for subsonic, micro-scale gas flows*, AIP Conference Proceedings, edited by T.J. Bartel and M.A. Gallis, 585(1), 547-553, 2001.
- [91] C. Scherer, J. Prolo Filho, L. Barichello, *An analytical approach to the unified solution of kinetic equations in rarefied gas dynamics. I. Flow problems*, Zeitschrift für Angewandte Mathematik und Physik (ZAMP), 60(1), 70-115, 2009.
- [92] D. Valougeorgis, *An analytical solution of the S-model kinetic equations*, Zeitschrift für Angewandte Mathematik und Physik (ZAMP), 54(1), 112-124, 2003.
- [93] H. Struchtrup, M. Torrilhon, *Regularization of Grad's 13 moment equations: Derivation and linear analysis*, Physics of Fluids, 15(9), 2668-2680, 2003.

- [94] S. Varoutis, D. Valougeorgis, F. Sharipov, *Application of the integro-moment method to steady-state two-dimensional rarefied gas flows subject to boundary induced discontinuities*, Journal of Computational Physics, 227(12), 6272-6287, 2008.
- [95] C. Cercignani, C.D. Pagani, *Variational Approach to Boundary-Value Problems in Kinetic Theory*, Physics of Fluids, 9(6), 1167-1173, 1966.
- [96] A. Frezzotti, G.P. Ghiroldi, L. Gibelli, *Solving the Boltzmann Equation on GPU*, <http://arxiv.org/abs/1005.5405>, 2010.
- [97] Y.Y. Kloss, P.V. Shuvalov, F.G. Tcheremissine, *Solving Boltzmann equation on GPU*, Procedia Computer Science, 1(1), 1083-1091, 2010.
- [98] P. Bassanini, C. Cercignani, C.D. Pagani, *Influence of the accommodation coefficient on the heat transfer in a rarefied gas*, International Journal of Heat Mass Transfer, 11, 1359-1369, 1968.
- [99] J.R.Jr. Thomas, T.S. Chang, C.E. Siewert, *Heat transfer between parallel plates with arbitrary surface accommodation*, Physics of Fluids, 16(12), 2116-2120, 1973.
- [100] M. Epstein, *A model of the wall boundary condition in kinetic theory*, AIAA Journal, 5, 1797-1800, 1967.
- [101] C. Cercignani, M. Lampis, *Kinetic models for gas-surface interactions*, Transport theory and statistical physics, 1(2), 101-114, 1971.
- [102] M.M.R. Williams, *A phenomenological study of gas-surface interactions*, Journal of Physics D: Applied Physics, 4, 1315-1319, 1971.
- [103] I. Kuscer, J. Mozina, F. Krizanic, *The Knudsen model of thermal accommodation*, 7th International Symposium on Rarefied Gas Dynamics, 1974.

- [104] T.G. Cowling, *On the Cercignani-Lampis formula for gas-surface interactions*, Journal of Physics D: Applied Physics, 7, 781-785, 1974.
- [105] F. Sharipov, *Application of the Cercignani-Lampis scattering kernel to calculations of rarefied gas flows. I. Plane flow between two parallel plates*, European Journal of Mechanics - B/Fluids, 21, 113-123, 2002.
- [106] F. Sharipov, *Application of the Cercignani-Lampis scattering kernel to calculations of rarefied gas flows. II. Slip and jump coefficients*, European Journal of Mechanics - B/Fluids, 22, 133-143, 2003.
- [107] F. Sharipov, *Application of the Cercignani-Lampis scattering kernel to calculations of rarefied gas flows. III. Poiseuille flow and thermal creep through a long tube*, European Journal of Mechanics - B/Fluids, 22, 145-154, 2003.
- [108] C. Cercignani, M. Lampis, S. Lorenzani, *Plane Poiseuille flow with symmetric and nonsymmetric gas-wall interactions*, Transport theory and statistical physics, 33, 545-561, 2004.
- [109] W.F.N. Santos, *Gas-Surface Interaction Effect on Round Leading Edge Aerothermodynamics*, Brazilian Journal of Physics, 37, 337-348, 2006.
- [110] A. Frezzotti, *Numerical simulation of supersonic rarefied gas flow past a flat plate: effects of the Gas-Surface interaction model on the flow field*, Rarefied Gas Dynamics: Theoretical and computational techniques, Progress in Astronautics and Aeronautics, 118, edited by E.P.Muntz, D.P. Weaver, D.H. Campbell, AIAA, Washington DC, 1989.
- [111] R.G. Lord, *Some extensions to the Cercignani-Lampis gas-surface scattering kernel*, Physics of Fluids A, 3(4), 706-710, 1991.
- [112] R.G. Lord, *Some further extensions to the Cercignani-Lampis gas-surface scattering kernel*, Physics of Fluids, 7(5), 1159-1161, 1995.

- [113] F. Sharipov, G. Bertoldo, *Heat transfer through a rarefied gas confined between two coaxial cylinders with high radius ratio*, Journal of Vacuum Science and Technology A, 24(6), 2087-2093, 2006.
- [114] A. Frezzotti, S.V. Nedeia, A.J. Markvoort, P. Spijker, L. Gibelli, *Comparison of molecular dynamics and kinetic modeling of gas-surface interaction*, 26th International Symposium on Rarefied Gas Dynamics, 2008.
- [115] O.A. Aksenova, I.A. Khalidov, *Molecular dynamics simulation of gas molecules reflected from rough surface*, 27th International Symposium on Rarefied Gas Dynamics, 2010.
- [116] J.P. Toennies, *Scattering of molecular beams from surfaces*, Applied Physics, 3, 91-114, 1974.
- [117] C.T. Rettner, H.A. Michelsen, D.J. Auerbach, C.B. Mullins, *Dynamics of recombinative desorption: Angular distributions of H₂, HD, and D₂ desorbing from Cu(111)*, Journal of Chemical Physics, 94, 7499-7501, 1991.
- [118] P. Tiwald, A. Schueller, H. Winter, K. Toekesi, F. Aigner, S. Graefe, C. Lemell, J. Burgdoerfer, *Interaction potentials for fast atoms in front of Al surfaces probed by rainbow scattering*, Physical Review B, 82, 125453, 2010.
- [119] C. Aubert, S. Colin, *High-order boundary conditions for gaseous flows in rectangular microducts*, Microscale Thermophysical Engineering, 5, 41-54, 2001.
- [120] S. Colin, P. Lalonde, R. Caen, *Validation of a Second-Order Slip Flow Model in Rectangular Microchannels*, Heat Transfer Engineering, 25(3), 23-30, 2004.
- [121] J. Pitakarnnop, S. Varoutis, D. Valougeorgis, S. Geoffroy, L. Baldas, S. Colin, *A novel experimental setup for gas microflows*, Microfluid Nanofluid, 8, 57-72, 2009.
- [122] N. Yamanishi, Y. Matsumoto, K. Shobatake, *Multistage gas-surface interaction model for the direct simulation Monte Carlo method*, Physics of Fluids, 11, 3540-3552, 1999.

- [123] D. Bruno, M. Cacciatore, S. Longo, M. Rutigliano, *Gas-surface scattering models for particle fluid dynamics: a comparison between analytical approximate models and molecular dynamics calculations*, Chemical Physics Letters, 320, 245-254, 2000.
- [124] K. Yamamoto, H. Takeuchi, T. Hyakutake, *Scattering properties and scattering kernel based on the molecular dynamics analysis of gas-wall interaction*, Physics of Fluids, 19, 087102, 2007.
- [125] S. Borisov, O. Sazhin, O. Gerasimova, *The Monte Carlo and molecular dynamics simulation of gas-surface interaction*, Lecture Notes in Computer Science, 3516, 143-146, 2005.
- [126] H.W. Liepmann, *Gas kinetic and gas dynamics of orifice flow*, Journal of Fluid Mechanics, 10, 65-79, 1961.
- [127] W. Jitschin, M. Ronzheimer, S. Khodabakhshi, *Gas flow measurement by means of orifices and Venturi tubes*, Vacuum, 53, 181-185, 1999.
- [128] O. Aktas, N.R. Aluru, U. Ravaioli, *Application of a parallel DSMC technique to predict flow characteristics in microfluidic filters*, Journal of Microelectromechanical systems, 10(4), 538-549, 2001.
- [129] G.D. Danilatos, M.R. Phillips, J.V. Nailon, *Electron beam current loss at the high-vacuum-high-pressure boundary in the enviromental scanning electron microscope*, Microscopy and Microanalysis, 7, 397-406, 2001.
- [130] G.A. Bird, *Transition regime behavior of supersonic beam skimmers*, Physics of Fluids, 19(10), 1486-1491, 1976.
- [131] K. Waichman, *Kinetic study of the effects of boundary geometry on rarefied vapor flow*, Physics of Fluids, 8(5), 1321-1329, 1996.
- [132] C. Cercignani, *Rarefied gas flow through long slots*, Zeitschrift fuer angewandte Mathematik und Physik (ZAMP), 30, 943-951, 1979.

- [133] F. Sharipov, V. Seleznev, *Rarefied gas flow through a long tube at any pressure ratio*, Journal of Vacuum Science and Technology A, 12(5), 2933-2935, 1994.
- [134] G. Breyannis, S. Varoutis, D. Valougeorgis, *Rarefied gas flow in concentric annular tube: Estimation of the Poiseuille number and the exact hydraulic diameter*, European Journal of Mechanics - B/Fluids, 27(5), 2008.
- [135] F. Sharipov, I. Graur, *Gas flow through an elliptical tube over the whole range of the gas rarefaction*, European Journal of Mechanics - B/Fluids, 27, 335-345, 2007.
- [136] S. Pantazis, S. Varoutis, V. Hauer, Chr. Day, D. Valougeorgis, *Gas-surface scattering effect on vacuum gas flows through rectangular channels*, 11th European Vacuum Conference, 2010.
- [137] V. Titarev, E. Shakhov, *High-order accurate conservative method for computing the poiseuille rarefied gas flow in a channel of arbitrary cross section*, Computational Mathematics and Mathematical Physics, 50(3), 537-548, 2010.
- [138] G.M. Alder, *The numerical solution of choked and supercritical ideal gas flow through orifices and convergent conical nozzles*, Journal of Mechanical Engineering Science, 21, 197-203, 1979.
- [139] A.K. Sreekanth, *Transition flow through short circular tubes*, Physics of Fluids, 8(11), 1951-1956, 1965.
- [140] T. Fujimoto, M. Usami, *Rarefied gas flow through a circular orifice and short tubes*, Journal of Fluids Engineering, 106, 367-373, 1984.
- [141] L. Marino, *Experiments on rarefied gas flows through tubes*, Microfluid Nanofluid, 6, 109-119, 2009.
- [142] S. Varoutis, V. Hauer, Chr. Day, S. Pantazis, D. Valougeorgis, *Experimental and numerical investigation in flow configurations related to the vacuum systems of fusion reactors*, Fusion Engineering and Design, 85(10-12), 1798-1802, 2010.

- [143] D.R. Willis, *Mass flow through a circular orifice and a two-dimensional slit at high Knudsen numbers*, Journal of Fluid Mechanics, 21(1), 21-31, 1965.
- [144] J.D. Stewart, *Mass flow rate for nearly-free molecular slit flow*, Journal of Fluid Mechanics, 35(3), 599-608, 1969.
- [145] R. Narasimha, *Orifice flow at high Knudsen numbers*, Journal of Fluid Mechanics, 10, 371-384, 1961.
- [146] F. Sharipov, D.V. Kozak, *Rarefied gas flow through a thin slit into vacuum simulated by the Monte Carlo method over the whole range of the Knudsen number*, Journal of Vacuum Science and Technology A, 27(3), 479-484, 2009.
- [147] O. Sazhin, *Gas molecule-molecule interaction and the gas-surface scattering effect on the rarefied gas flow through a slit into a vacuum*, Journal of Experimental and Theoretical Physics, 108(5), 874-879, 2009.
- [148] D.G. Wadsworth, D.A. Erwin, *Numerical simulation of rarefied flow through a slit. Part I: Direct simulation Monte Carlo results*, Physics of Fluids A, 5(1), 235-242, 1993.
- [149] F. Sharipov, *Numerical simulation of rarefied gas flow through a thin orifice*, Journal of Fluid Mechanics, 518, 35-60, 2004.
- [150] H. Taniguchi, M. Ota, M. Aritomi, *Effects of surface boundary conditions on transmission probabilities through circular tubes*, Vacuum, 47(6-8), 787-790, 1996.
- [151] H. Shinagawa, H. Setyawan, T. Asai, Y. Sugiyama, K. Okuyama, *An experimental and theoretical investigation of rarefied gas flow through circular tube of finite length*, Chemical Engineering Science, 57(19), 4027-4036, 2002.

- [152] S. Varoutis, D. Valougeorgis, F. Sharipov, *Simulation of gas flow through tubes of finite length over the whole range of rarefaction for various pressure drop ratios*, Journal of Vacuum Science and Technology A, 27(6), 2009.
- [153] E.M. Shakhov, *Solution of axisymmetric problems of rarefied gas theory by a finite difference method*, Zhurnal Vychislitel'noi Matematiki i Matematicheskoi Fiziki, 14(4), 970-981, 1974.
- [154] P. Raghuraman, D.R. Willis, *Kinetic theory analysis of rarefied gas flow through finite length slots*, Physics of Fluids, 20(6), 895-902, 1977.
- [155] D. Bergers, *Kinetic model solution for axisymmetric flow by the method of discrete ordinates*, Journal of Computational Physics, 57(2), 285-302, 1985.
- [156] S. Pantazis, D. Valougeorgis, *Heat transfer through rarefied gases between coaxial cylindrical surfaces with arbitrary temperature difference*, European Journal of Mechanics B/Fluids, 29(6), 494-509, 2010.
- [157] B.D. Ganapol, *Mining the discrete velocity method for high quality solutions for one-dimensional Poiseuille flow*, Zeitschrift fuer angewandte Mathematik und Physik (ZAMP), 57, 1011-1024, 2006.
- [158] S.F. Borisov, I.G. Neudachin, B.T. Porodnov, P.E. Suetin, *Flow of rarefied gases through an orifice for small pressure drop (In Russian)*, Zhurnal Tekhnicheskoi Fiziki, 43, 1735-1739, 1973.
- [159] B.T. Porodnov, P.E. Suetin, S.F. Borisov, V.D. Akinshin, *Experimental investigation of rarefied gas flow in different channels*, Journal of Fluid Mechanics, 64, 417-437, 1974.
- [160] V.D. Akin'shin, V.D. Seleznev, F.M. Sharipov, *Non-isothermal rarefied gas flow through a narrow slit*, Translated from Mekhanika Zhidkosti i Gaza, 4, 171-175, 1991.
- [161] M. Hasegawa, Y. Sone, *Rarefied gas flow through a slit*, Physics of Fluids A, 3(3), 466-477, 1990.

- [162] F. Sharipov, *Rarefied gas flow through a slit. Influence of the boundary conditions*, Physics of Fluids, 8(1), 262-268, 1996.
- [163] F. Sharipov, *Non-isothermal rarefied gas flow through a slit*, Physics of Fluids, 9(6), 1804-1810, 1997.
- [164] E. Rathakrishnan, A.K. Sreekanth, *Rarefied flow through sudden enlargements*, Fluid Dynamics Research, 16(2-3), 131-145, 1995.
- [165] T.P. Chiang, T.W.H. Sheu, *A numerical revisit of backward-facing step flow problem*, Physics of Fluids, 11(4), 862-874, 1999.
- [166] A. Agrawal, L. Djenidi, R.A. Antonia, *Simulation of gas flow in microchannels with a sudden expansion or contraction*, Journal of Fluid Mechanics, 530, 135-144, 2005.
- [167] F.B. Bao, J.Z. Lin, *Continuum Simulation of the Microscale Backward-Facing Step Flow in a Transition Regime*, Numerical Heat Transfer, Part A: Applications: An International Journal of Computation and Methodology, 59(8), 616-632, 2011.
- [168] A. Gat, I. Frankel, D. Weihs, *Compressible flows through micro-channels with sharp edged turns and bifurcations*, Microfluidics and Nanofluidics, 8(5), 2010.
- [169] A. Beskok, *Validation of a new velocity-slip model for separated gas microflows*, Numerical Heat Transfer, Part B: Fundamentals: An International Journal of Computation and Methodology, 40(6), 451-471, 2001.
- [170] S. Misdanitis, D. Valougeorgis, *Design of gas distribution systems consisting of long tubes in the whole range of the Knudsen number*, submitted in Journal of Vacuum Science and Technology A.
- [171] E.P. Gross, S. Ziering, *Heat flow between parallel plates*, Physics of Fluids, 2(6), 701-712, 1959.

- [172] M.L. Lavin, J.K. Haviland, *Application of a moment method to heat transfer in rarefied gases*, Physics of Fluids, 5(3), 274-279, 1962.
- [173] K. Frankowski, Z. Alterman, C.L. Pekeris, *Heat transport between parallel plates in a rarefied gas of rigid sphere molecules*, Physics of Fluids, 8(2), 245-258, 1964.
- [174] S.K. Loyalka, J.R. Thomas, *Heat transfer in a rarefied gas enclosed between parallel plates: Role of boundary conditions*, Physics of Fluids, 25(7), 1162-1164, 1982.
- [175] J.R. Thomas, D. Valougeorgis, *The FN method in kinetic theory: II. Heat transfer between parallel plates*, Transport Theory and Statistical Physics, 14, 497-512, 1985.
- [176] F. Sharipov, L.M.G. Cumin, D. Kalempa, *Heat flux between parallel plates through a binary gaseous mixture over the whole range of the Knudsen number*, Physica A, 378, 183-193, 2007.
- [177] P. Bassanini, C. Cercignani, C.D. Pagani, *Comparison of kinetic theory analyses of linearized heat transfer between parallel plates*, International Journal of Heat Mass Transfer, 10, 447-460, 1967.
- [178] P.J. Clause, M. Mareschal, *Heat transfer in a gas between parallel plates: Moment method and molecular dynamics*, Physical Review A, 38(8), 4241-4252, 1988.
- [179] D.R. Willis, *Heat transfer in a rarefied gas between parallel plates at large temperature ratios*, 1st International Symposium on Rarefied Gas Dynamics, Academic Press, New York-London, 1963.
- [180] C. Cercignani, *The Boltzmann equation and its applications*, Springer, New York, 1988.
- [181] B.T. Porodnov, A.N. Kulev, F.T. Tukhvetov, *Thermal transpiration in a circular capillary with a small temperature difference*, Journal of Fluid Mechanics, 88, 609-622, 1978.
- [182] F. Sharipov, *Rarefied gas flow through a long rectangular channel*, Journal of Vacuum Science and Technology A, 17(5), 3062-3066, 1999.

- [183] S. Varoutis, *Flows through channels of various cross sections in the whole range of the Knudsen number using deterministic and stochastic approaches (Ph.D. dissertation, in Greek)*, University of Thessaly - Department of Mechanical Engineering, Volos, Greece, 2008.
- [184] P. Perrier, I.A. Graur, T. Ewart, J.G. Meolans, *Mass flow rate measurements in microtubes: From hydrodynamic to near free molecular regime*, Physics of Fluids, 23(4), 2011.
- [185] V.D. Akinshin, A.M. Makarov, V.D. Seleznev, F.M. Sharipov, *Rarefied gas motion in a short planar channel over the entire Knudsen number range*, Journal of Applied Mechanics and Technical Physics, 30(5), 713-717, 1988.
- [186] F. Sharipov, *Rarefied gas flow through a long tube at arbitrary pressure and temperature drops*, Journal of Vacuum Science Technology A, 15(4), 2434-2436, 1997.
- [187] L. Lees, C.Y. Liu, *Kinetic Theory Description of Conductive Heat Transfer from a Fine Wire*, Physics of Fluids, 10(5), 1137-1148, 1962.
- [188] C.L. Su, R.W. Springer, *A modified discrete ordinate approach to nonlinear cylindrical heat transfer*, International Journal of Heat and Mass Transfer, 13(10), 1611-1621, 1970.
- [189] Y.S. Lou, T.K. Shih, *Nonlinear Heat Conduction in Rarefied Gases Confined between Concentric Cylinders and Spheres*, Physics of Fluids, 15(5), 785-788, 1972.
- [190] F.M. Sharipov, G.M. Kremer, *On the frame dependence of constitutive equations. I. Heat transfer through a rarefied gas between two rotating cylinders*, Continuum Mechanics and Thermodynamics, 7(1), 57-71, 1995.
- [191] B.D. Ganapol, *Analytical Benchmarks for Nuclear Engineering Applications - Case Studies in Neutron Transport Theory*, Nuclear Energy Agency Organization for Economic Co-operation and Development, OECD, NEA No. 6292, Oxford, 2008.

- [192] F. Bornemann, D. Laurie, S. Wagon, J. Waldvogel, R. David, Reviewed by H. Bailey, *The SIAM 100-digit challenge, a study in high-accuracy numerical computing*, <http://www-m3.ma.tum.de/m3old/bornemann/challengebook/index.html>, 2004.
- [193] C.L. Su, *Variational Principles for the Heat Flux in a Rarefied Gas between Concentric Cylinders*, *Physics of Fluids*, 11(10), 2144-2147, 1968.
- [194] B.T. Yeh, A. Frohn, *Heat conduction in binary gas mixtures between concentric cylinders*, *Physics of Fluids*, 16(6), 801-805, 1973.
- [195] E.E. Lewis, W.F.Jr. Miller, *Computational Methods of Neutron Transport Theory*, Wiley, New York, 1984.
- [196] R. Roscoe, *The flow of viscous fluids round plane obstacles*, *Philosophical Magazine Series*, 40(302), 338-351, 1949.
- [197] H. Hasimoto, *On the Flow of a Viscous Fluid past a thin Screen at Small Reynolds Numbers*, *Journal of the Physical Society of Japan*, 13, 1958.

Appendices

Appendix 1

Derivation of boundary conditions

1.1 Impermeability condition

The impermeability condition at the walls is imposed by setting the density constant of the departing distribution in a value such that the velocity component normal to the wall is equal to zero. An example is given here for linearized flow through a parallel plate channel examined in Chapter 4 for the vertical wall (C), as seen in Figure 4.1. The normal velocity component in this case is found from Equation (4.13)

$$u_x = \frac{1}{\pi} \int_0^{2\pi} \int_{-\infty}^{\infty} V c_p^2 \cos \theta \exp(-c_p^2) dc_p d\theta = 0 \quad (\text{A.1.1})$$

The integral may be split in two parts: the one containing distributions departing from the wall V^+ and another one for those impinging on the wall V^-

$$\int_{-\infty}^{\infty} \left[\int_{-\pi/2}^{\pi/2} V^- c_p^2 \cos \theta \exp(-c_p^2) d\theta + \int_{\pi/2}^{3\pi/2} V^+ c_p^2 \cos \theta \exp(-c_p^2) d\theta \right] dc_p = 0 \quad (\text{A.1.2})$$

Diffuse boundary conditions are imposed, i.e. the perturbation from the Maxwellian is substituted for the departing distribution V^+ , but since the wall is isothermal and stationary, it simply leads to $V^+ = \rho_w$ where $\rho_w = \rho_w(y)$ is a constant which must be adjusted to keep the velocity equal to zero. Thus, we get

$$I_{impinging} + \rho_w I_{departing} = 0 \quad (\text{A.1.3})$$

where

$$I_{impinging}|_a = \int_{-\pi/2}^{\pi/2} \int_0^{\infty} V^- [c_p^2 \cos \theta] \exp(-c_p^2) dc_p d\theta \quad (\text{A.1.4})$$

$$I_{departing}|_a = \int_{\pi/2}^{3\pi/2} \int_0^{\infty} [c_p^2 \cos \theta] \exp(-c_p^2) dc_p d\theta \quad (\text{A.1.5})$$

1.2 Fully developed flow boundary conditions

Another point that needs to be addressed is the derivation of unprojected distributions (4.57) and (4.58). Since the distribution function does not change in terms of x_1 when fully developed conditions are met, as seen in (4.50), the deviation from the Maxwellian is not caused by a dependence on x_1 and we expect that it can be described by

$$V_{in}(-L_{dev}, y, c_x, c_y) = Y(y, c_y) A(c_x) + B(y) \quad (\text{A.1.6})$$

The first function $A(c_x)$ is found by substituting this expression in the projection equation (4.53)

$$Y(y, c_y) = \frac{1}{\sqrt{\pi}} \int_{-\infty}^{\infty} [Y(y, c_y) A(c_x) + B(y)] c_x \exp(-c_x^2) dc_x \quad (\text{A.1.7})$$

and simplifying to get $A(c_x) = 2c_x$. Then, Equation (A.1.6) is inserted in the governing equation for the boundary (4.51) and, after subtracting Equation (4.55) multiplied by $2c_x$, we obtain

$$c_y \frac{B(y)}{\partial y} + \delta B(y) = \delta \rho_{in} \quad (\text{A.1.8})$$

which directly leads to $B(y) = \rho_{in}$ if we take into account that $d\rho_{in}/dy = 0$. The whole procedure can be repeated for the tube end geometry, substituting

$$h_{in}(-L_{dev}, r, c_p, \theta, c_z) = Z(r, c_p, \theta) A(c_z) + B(r) \quad (\text{A.1.9})$$

and working similarly with the projection (4.54) and the governing equation (4.52).

1.3 Adiabatic wall condition

In the case of adiabatic walls, we must impose the conditions of no penetration ($u_{normal} = 0$) and zero heat flux ($q_{normal} = 0$) simultaneously. Therefore, from Equation (6.16) we get

$$u_x = \frac{2}{\rho} \int_0^{\infty} \int_0^{\pi} \int_{-\infty}^{\infty} c_p c_x g dc_x d\theta dc_p = 0 \quad (\text{A.1.10})$$

and due to the boundary conditions

$$\int_0^\infty \int_0^\pi \int_0^\infty c_p c_x g^- dc_x d\theta dc_p + \int_0^\infty \int_0^\pi \int_{-\infty}^0 c_p c_x \frac{\rho_{w,C}}{(\pi \tau_{w,C})^{3/2}} \exp\left(-\frac{c_p^2 + c_x^2}{\tau_C}\right) dc_x d\theta dc_p = 0 \quad (\text{A.1.11})$$

Solving the second integral analytically leads to

$$\int_0^\infty \int_0^\pi \int_0^\infty c_p c_x g^- dc_x d\theta dc_p + \frac{\rho_{w,C}}{\pi^{3/2}} \sqrt{\tau_C} (\pi) \left(\frac{1}{2}\right) \left(-\frac{1}{2}\right) = 0 \quad (\text{A.1.12})$$

Finally, solving for $\rho_{w,C}$ yields

$$\rho_{w,C} = \frac{4\sqrt{\pi}}{\sqrt{\tau_C}} A \quad (\text{A.1.13})$$

where

$$A = \int_0^\infty \int_0^\pi \int_0^\infty c_p c_x g^- dc_x d\theta dc_p \quad (\text{A.1.14})$$

In the same way, the starting point for the imposition of zero heat flux is the corresponding moment, Equation (6.19)

$$q_x = 2 \int_0^\infty \int_0^\pi \int_{-\infty}^\infty c_p c_x [(c_p \cos \theta - u_r)^2 + (c_p \sin \theta)^2 + c_x^2] g dc_x d\theta dc_p = 0 \quad (\text{A.1.15})$$

where we have substituted $u_x = 0$. After the use of the boundary conditions, it becomes

$$\begin{aligned} & \int_0^\infty \int_0^\pi \int_0^\infty c_p c_x [(c_p \cos \theta - u_r)^2 + (c_p \sin \theta)^2 + c_x^2] g^- dc_x d\theta dc_p \\ & + \int_0^\infty \int_0^\pi \int_{-\infty}^0 c_p c_x [(c_p \cos \theta - u_r)^2 + (c_p \sin \theta)^2 + c_x^2] \frac{\rho_{w,C}}{(\pi \tau_C)^{3/2}} \exp\left(-\frac{c_p^2 + c_x^2}{\tau_C}\right) dc_x d\theta dc_p = 0 \end{aligned} \quad (\text{A.1.16})$$

We can solve the second integral analytically and obtain

$$\int_0^\infty \int_0^\pi \int_0^\infty c_p c_x [(c_p \cos \theta - u_r)^2 + (c_p \sin \theta)^2 + c_x^2] g^- dc_x d\theta dc_p - \frac{\rho_{w,C} \sqrt{\tau_C} (u_r^2 + 2\tau_C)}{4\sqrt{\pi}} = 0 \quad (\text{A.1.17})$$

Finally, we solve for $\rho_{w,C}$ again to get

$$\rho_{w,C} = \frac{4\sqrt{\pi}}{\sqrt{\tau_C}(u_r^2 + 2\tau_C)} B \quad (\text{A.1.18})$$

where

$$B = \int_0^\infty \int_0^\pi \int_0^\infty c_p c_x [(c_p \cos \theta - u_r)^2 + (c_p \sin \theta)^2 + c_x^2] g^- dc_x d\theta dc_p \quad (\text{A.1.19})$$

By combining Equations (A.1.13) and (A.1.18) we finally obtain the expression for $\tau_{w,C}$

$$\tau_{w,C} = \frac{B - Au_r^2}{2A} \quad (\text{A.1.20})$$

and $\rho_{w,C}$ is given by (A.1.13).

Appendix 2

Derivation of mass flow rate equation

2.1 Linearized flow

The mass flow rate through channels is obtained by associating it to the corresponding dimensionless numerical results. The complete procedure is shown here analytically for the case of the linearized flow through a parallel plate channel. The flow rate is defined by Equation (4.35)

$$\dot{M} = \int_{-H/2}^{H/2} [mn(\hat{x}, \hat{y})] \hat{u}_x(\hat{x}, \hat{y}) d\hat{y} \quad (\text{A.2.1})$$

and the pressure is substituted by the ideal gas law $P = mnRT = mnv_0^2/2$

$$\dot{M} = \int_{-H/2}^{H/2} \left[\frac{2\hat{P}(\hat{x}, \hat{y})}{v_0^2} \right] \hat{u}_x(\hat{x}, \hat{y}) d\hat{y} \quad (\text{A.2.2})$$

Then, it is non-dimensionalized according to (4.3)

$$\dot{M} = (v_0 \frac{\Delta P}{P_0})(H) \frac{2P_0(1 + h\Delta P/P_0)}{v_0^2} \int_{-1/2}^{1/2} u_x(x, y) dy \quad (\text{A.2.3})$$

and terms of order $(\Delta P/P_0)^2$ are omitted

$$\dot{M} = \frac{2\Delta PH}{v_0} \int_{-1/2}^{1/2} u_x(x, y) dy \quad (\text{A.2.4})$$

Furthermore, due to the symmetry of the field we get

$$\dot{M} = \frac{4\Delta PH}{v_0} \int_0^{1/2} u_x(x, y) dy \quad (\text{A.2.5})$$

Dividing by the free molecular solution for flow through a slit $\dot{M}_{FM} = (H\Delta P) / (v_0\sqrt{\pi})$ we finally obtain the dimensionless flow rate

$$W = \frac{\dot{M}}{\dot{M}_{FM}} = 4\sqrt{\pi}G \quad (\text{A.2.6})$$

with the reduced flow rate defined as

$$G|_x = \int_0^{1/2} u_x(x, y) dy \quad (\text{A.2.7})$$

The quantity G is obtained by the numerical results and W is tabulated in the previous chapters of this work. When results in dimensional form must be provided, the quantity W in Equation (A.2.6) is multiplied by the free molecular solution for the conditions of interest, that is

$$\dot{M} = W \frac{H\Delta P}{v_0\sqrt{\pi}} \quad (\text{A.2.8})$$

2.2 Non-linear flow

Similar derivations are given here for non-linear flow through a tube. The flow rate definition (6.21)

$$\dot{M} = 2\pi \int_0^R [mn(\hat{x}, \hat{r})] \hat{u}_x(\hat{x}, \hat{r}) \hat{r} d\hat{r} \quad (\text{A.2.9})$$

is non-dimensionalized according to (6.4)

$$\dot{M} = 2\pi (mn_0)(v_0)(R^2) \int_0^1 \rho(x, r) u_x(x, r) r dr \quad (\text{A.2.10})$$

Then, we multiply and divide with $v_0 = \sqrt{2(k_B/m)T_0}$ and use the ideal gas law $P_0 = n_0 k_B T_0$ to get

$$\dot{M} = 2\pi R^2 \frac{2P_0}{v_0} \int_0^1 \rho(x, r) u_x(x, r) r dr \quad (\text{A.2.11})$$

Finally, dividing by the free molecular solution $\dot{M}_{FM} = R^2 \sqrt{\pi} \hat{P}_{in} / v_0$, we get the dimensionless flow rate

$$W = \frac{\dot{M}}{\dot{M}_{FM}} = 4\sqrt{\pi}G \quad (\text{A.2.12})$$

where the reduced flow rate is defined as the integral

$$G|_x = \int_0^1 \rho(x, r) u_x(x, r) r dr \quad (\text{A.2.13})$$

Appendix 3

Derivation of discretized equations

The procedure of the finite difference equation derivation consists of integrating to remove all derivatives and using the trapezoidal rule when the remaining integrals can not be calculated analytically. In particular, for the case of Equation (4.46)

$$c_p \cos \theta \frac{\partial h}{\partial r} - \frac{c_p \sin \theta}{r} \frac{\partial h}{\partial \theta} + c_x \frac{\partial h}{\partial x} + \delta h = \delta \left[\rho + \tau \left(c^2 - \frac{3}{2} \right) + 2\mathbf{c} \cdot \mathbf{u} \right] + g(x, c_x) \quad (\text{A.3.1})$$

we can apply the operator (4.71)

$$A = \int_{x_k - \frac{\Delta x_k}{2}}^{x_k + \frac{\Delta x_k}{2}} \int_{\theta_j - \frac{\Delta \theta_j}{2}}^{\theta_j + \frac{\Delta \theta_j}{2}} \int_{r_i - \frac{\Delta r_i}{2}}^{r_i + \frac{\Delta r_i}{2}} (\cdot) dr d\theta dx \quad (\text{A.3.2})$$

on both sides to get

$$\begin{aligned} & \int_{x_k - \frac{\Delta x_k}{2}}^{x_k + \frac{\Delta x_k}{2}} \int_{\theta_j - \frac{\Delta \theta_j}{2}}^{\theta_j + \frac{\Delta \theta_j}{2}} \int_{r_i - \frac{\Delta r_i}{2}}^{r_i + \frac{\Delta r_i}{2}} \left[c_p \cos \theta \frac{\partial h}{\partial r} - \frac{c_p \sin \theta}{r} \frac{\partial h}{\partial \theta} + c_x \frac{\partial h}{\partial x} + \delta h \right] dr d\theta dx = \\ & \int_{x_k - \frac{\Delta x_k}{2}}^{x_k + \frac{\Delta x_k}{2}} \int_{\theta_j - \frac{\Delta \theta_j}{2}}^{\theta_j + \frac{\Delta \theta_j}{2}} \int_{r_i - \frac{\Delta r_i}{2}}^{r_i + \frac{\Delta r_i}{2}} \left\{ \delta \left[\rho + \tau \left(c^2 - \frac{3}{2} \right) + 2\mathbf{c} \cdot \mathbf{u} \right] + g(x, c_x) \right\} dr d\theta dx \end{aligned} \quad (\text{A.3.3})$$

and if we calculate some integrals analytically we obtain

$$\begin{aligned} & c_p \cos \theta_j \int_{x_k - \frac{\Delta x_k}{2}}^{x_k + \frac{\Delta x_k}{2}} \int_{\theta_j - \frac{\Delta \theta_j}{2}}^{\theta_j + \frac{\Delta \theta_j}{2}} [h_{i+} - h_{i-}] d\theta dx - c_p \sin \theta_j \int_{x_k - \frac{\Delta x_k}{2}}^{x_k + \frac{\Delta x_k}{2}} \int_{r_i - \frac{\Delta r_i}{2}}^{r_i + \frac{\Delta r_i}{2}} \left[\frac{1}{r} (h_{j+} - h_{j-}) \right] dr dx \\ & + c_x \int_{\theta_j - \frac{\Delta \theta_j}{2}}^{\theta_j + \frac{\Delta \theta_j}{2}} \int_{r_i - \frac{\Delta r_i}{2}}^{r_i + \frac{\Delta r_i}{2}} [h_{k+} - h_{k-}] dr d\theta + \delta \int_{x_k - \frac{\Delta x_k}{2}}^{x_k + \frac{\Delta x_k}{2}} \int_{\theta_j - \frac{\Delta \theta_j}{2}}^{\theta_j + \frac{\Delta \theta_j}{2}} \int_{r_i - \frac{\Delta r_i}{2}}^{r_i + \frac{\Delta r_i}{2}} h dr d\theta dx = \end{aligned} \quad (\text{A.3.4})$$

$$\delta(\Delta\theta_j) \int_{x_k - \frac{\Delta x_k}{2}}^{x_k + \frac{\Delta x_k}{2}} \int_{r_i - \frac{\Delta r_i}{2}}^{r_i + \frac{\Delta r_i}{2}} \left[\rho + \tau \left(c^2 - \frac{3}{2} \right) + 2\mathbf{c} \cdot \mathbf{u} \right] dr dx + g(x, c_x) (\Delta x_k \Delta \theta_j \Delta r_i)$$

where for example $h_{i\pm} = h(r_i \pm \frac{\Delta r_i}{2})$, $h_{j\pm} = h(\theta_j \pm \frac{\Delta \theta_j}{2})$, $h_{k\pm} = h(z_k \pm \frac{\Delta z_k}{2})$ and so on. We have also substituted $\cos \theta_j = \frac{1}{2} [\cos(\theta_j + \Delta \theta_j/2) + \cos(\theta_j - \Delta \theta_j/2)]$ and $\sin \theta_j = \frac{1}{2} [\sin(\theta_j + \Delta \theta_j/2) + \sin(\theta_j - \Delta \theta_j/2)]$ from trigonometric equalities, since $\cos(\Delta \theta_j/2) \cong 1$ is a very good approximation because of the relatively dense angular grid.

Finally, we apply the trapezoidal rule on Equation (A.3.4)

$$\begin{aligned} & \frac{c_p \cos \theta_j \Delta \theta_j \Delta x_k}{4} (h_{i+,j+,k+} + h_{i+,j-,k+} - h_{i-,j+,k+} - h_{i-,j-,k+} \\ & \quad + h_{i+,j+,k-} + h_{i+,j-,k-} - h_{i-,j+,k-} - h_{i-,j-,k-}) \\ & - \frac{c_p \sin \theta_j \Delta r_i \Delta x_k}{4} \left[\frac{1}{r_{i+}} (h_{i+,j+,k+} - h_{i+,j-,k+} + h_{i+,j+,k-} - h_{i+,j-,k-}) \right. \\ & \quad \left. + \frac{1}{r_{i-}} (h_{i-,j+,k+} - h_{i-,j-,k+} + h_{i-,j+,k-} - h_{i-,j-,k-}) \right] \\ & + \frac{c_x \Delta r_i \Delta \theta_j}{4} (h_{i+,j+,k+} + h_{i+,j-,k+} + h_{i-,j+,k+} + h_{i-,j-,k+} \\ & \quad - h_{i+,j+,k-} - h_{i+,j-,k-} - h_{i-,j+,k-} - h_{i-,j-,k-}) \\ & + \frac{\delta \Delta r_i \Delta \theta_j \Delta x_k}{8} (h_{i+,j+,k+} + h_{i+,j-,k+} + h_{i-,j+,k+} + h_{i-,j-,k+} \\ & \quad + h_{i+,j+,k-} + h_{i+,j-,k-} + h_{i-,j+,k-} + h_{i-,j-,k-}) \\ & = \frac{\delta \Delta r_i \Delta \theta_j \Delta x_k}{4} \{ (\rho_{i+,k+} + \rho_{i-,k+} + \rho_{i+,k-} + \rho_{i-,k-}) \\ & \quad + \left[(c_p)^2 + (c_z)^2 - \frac{3}{2} \right] (\tau_{i+,k+} + \tau_{i-,k+} + \tau_{i+,k-} + \tau_{i-,k-}) \\ & \quad + 2c_p \cos \theta_j (u_{r,i+,k+} + u_{r,i-,k+} + u_{r,i+,k-} + u_{r,i-,k-}) \\ & \quad + 2c_x (u_{x,i+,k+} + u_{x,i-,k+} + u_{x,i+,k-} + u_{x,i-,k-}) \} - g_{tb}(x_k, c_x) \Delta r_i \Delta \theta_j \Delta x_k \end{aligned}$$

Finally, after dividing with $\Delta r_i \Delta \theta_j \Delta x_k$ and applying the discretization in the velocity magnitudes, i.e. $c_p \rightarrow c_p^l$, $c_x \rightarrow c_x^m$, $h_{i+,j+,k+} \rightarrow h_{i+,j+,k+}^{(l,m)}$, we obtain the finite difference equation shown in Table 4.1.

Appendix 4

Grid description

The discretization in the physical space is dense near the corner points and gets sparser as we move away into the tube or in the inlet/outlet containers. The intervals vary according to

$$\begin{aligned}\Delta x_i &= \begin{cases} \Delta x_{i+1} (1 + \eta) & , \hat{x} < \hat{0} \\ \Delta x_{i-1} (1 + \eta) & , \hat{x} > \hat{0} \end{cases} \\ \Delta r_i &= \begin{cases} \Delta r_{i+1} (1 + \eta) & , \hat{r} < \hat{R} \\ \Delta r_{i-1} (1 + \eta) & , \hat{r} > \hat{R} \end{cases}\end{aligned}\quad (\text{A.4.1})$$

for the left corner and

$$\begin{aligned}\Delta x_i &= \begin{cases} \Delta x_{i+1} (1 + \eta) & , \hat{x} < \hat{L}_{channel} \\ \Delta x_{i-1} (1 + \eta) & , \hat{x} > \hat{L}_{channel} \end{cases} \\ \Delta r_i &= \begin{cases} \Delta r_{i+1} (1 + \eta) & , \hat{r} < \hat{R} \\ \Delta r_{i-1} (1 + \eta) & , \hat{r} > \hat{R} \end{cases}\end{aligned}\quad (\text{A.4.2})$$

for the right corner. The minimum intervals $\Delta x_0, \Delta r_0$ are chosen according to

$$\sum_0^{N_x-1} \Delta x_0 (1 + \eta)^i = 1 \quad (\text{A.4.3})$$

$$\sum_0^{N_r-1} \Delta r_0 (1 + \eta)^i = 1 \quad (\text{A.4.4})$$

and remain constant when we enlarge the computational domain (e.g. when L_{left}/L_0 is increased) for a constant number of nodes in the first unit length N_x , in order to ensure that changes in the quantities of interest are only due to the domain size modification.

Appendix 5

Conservation principles

5.1 Introduction

All conservation principles are easily deduced by taking appropriate moments of the governing equations. The right hand side (collision) terms are always eliminated, since this is a property that all collisional models must possess (collisions can not create or destroy mass, momentum or energy).

5.2 Non-linear heat transfer

For plate geometry, mass, momentum and energy conservation principles are obtained by operating on Equation (5.11) with

$$\int_{-\infty}^{\infty} \int_{-\infty}^{\infty} \int_{-\infty}^{\infty} (\cdot) dc_x dc_y dc_z \quad (\text{A.5.1})$$

$$\int_{-\infty}^{\infty} \int_{-\infty}^{\infty} \int_{-\infty}^{\infty} (\cdot) c_y dc_x dc_y dc_z \quad (\text{A.5.2})$$

$$\int_{-\infty}^{\infty} \int_{-\infty}^{\infty} \int_{-\infty}^{\infty} (\cdot) (c_x^2 + c_y^2 + c_z^2) dc_x dc_y dc_z \quad (\text{A.5.3})$$

to get

$$\frac{\partial u_y}{\partial y} = 0 \quad (\text{A.5.4})$$

$$\frac{\partial P_{yy}}{\partial y} = 0 \quad (\text{A.5.5})$$

$$\frac{\partial q_y}{\partial y} = 0 \quad (\text{A.5.6})$$

For the cylindrical case, we apply the operators

$$\int_{-\infty}^{\infty} \int_0^{\infty} \int_0^{2\pi} (\cdot) c_p d\theta dc_p dc_z \quad (\text{A.5.7})$$

$$\int_{-\infty}^{\infty} \int_0^{\infty} \int_0^{2\pi} (\cdot) c_p^2 \cos \theta d\theta dc_p dc_z \quad (\text{A.5.8})$$

$$\int_{-\infty}^{\infty} \int_0^{\infty} \int_0^{2\pi} (\cdot) (c_p^2 + c_z^2) c_p d\theta dc_p dc_z \quad (\text{A.5.9})$$

on Equation (5.40) and take into account that

$$\frac{c_p \sin \theta}{r} \frac{\partial g}{\partial \theta} = \frac{1}{r} \frac{\partial}{\partial \theta} [(c_p \sin \theta) g] - \frac{g}{r} (c_p \cos \theta) \quad (\text{A.5.10})$$

$$\frac{c_p^2 \cos \theta \sin \theta}{r} \frac{\partial g}{\partial \theta} = \frac{1}{r} \frac{\partial}{\partial \theta} [(c_p^2 \cos \theta \sin \theta) g] - \frac{(c_p \cos \theta)^2}{r} g + \frac{(c_p \sin \theta)^2}{r} g \quad (\text{A.5.11})$$

$$\frac{(c_p \sin \theta)^2}{r} \frac{\partial g}{\partial \theta} = \frac{1}{r} \frac{\partial}{\partial \theta} [(c_p \sin \theta)^2 g] - 2 \frac{(c_p^2 \cos \theta \sin \theta)}{r} g \quad (\text{A.5.12})$$

The conservation principles are

$$\frac{\partial(r u_r)}{\partial r} = 0 \quad (\text{A.5.13})$$

$$\frac{\partial P_{rr}}{\partial r} - \frac{1}{r} [P_{\vartheta\vartheta} - P_{rr}] = 0 \quad (\text{A.5.14})$$

$$\frac{\partial P_{r\vartheta}}{\partial r} + \frac{2P_{r\vartheta}}{r} = 0 \quad (\text{A.5.15})$$

$$\frac{\partial(r q_r)}{\partial r} = 0 \quad (\text{A.5.16})$$

The continuity equation, associated with the no penetration condition at the cylindrical walls, yields $u(r) = 0$, while the energy equation results to $q(r)r = \text{constant}$. Finally, since $p_{rr} \neq p_{\theta\theta}$, the r -momentum equation implies that $\partial p_{rr} / \partial r \neq 0$.

5.3 Linearized flow through a channel

In the case of linearized flows, the mass flow conservation is found by acting on equations (4.9) and (4.11) with

$$\int_{-\pi}^{\pi} \int_0^{\infty} (\cdot) c_p dc_p d\theta \quad (\text{A.5.17})$$

and

$$\int_{-\infty}^{\infty} \int_{-\pi}^{\pi} \int_0^{\infty} (\cdot) dc_p d\theta dc_x \quad (\text{A.5.18})$$

to obtain

$$\frac{\partial u_x}{\partial x} + \frac{\partial u_y}{\partial y} = 0 \quad (\text{A.5.19})$$

and

$$\frac{1}{r} \frac{\partial (ru_r)}{\partial r} + \frac{\partial u_x}{\partial x} = 0 \quad (\text{A.5.20})$$

since the right hand side terms are eliminated, as expected.

5.4 Non-linear flow through an axisymmetric channel element

The mass conservation principle is found by acting on the governing equation (6.8) with

$$\int_{-\infty}^{\infty} \int_{-\pi}^{\pi} \int_0^{\infty} (\cdot) dc_p d\theta dc_x \quad (\text{A.5.21})$$

and results in

$$\frac{1}{r} \frac{\partial (r\rho u_r)}{\partial r} + \frac{\partial (\rho u_x)}{\partial x} = 0 \quad (\text{A.5.22})$$

which is quite similar to the expression for linear flow through a cylindrical channel.

Appendix 6

Analytical solutions

6.1 Introduction

In some cases, it is possible to derive analytical solutions in the two limits of the Knudsen number: the free molecular regime ($Kn \rightarrow \infty$) and the hydrodynamic regime ($Kn \rightarrow 0$). Sometimes, we are also able to extend the hydrodynamic approach up to the slip regime ($Kn < 0.1$) if appropriate boundary conditions are taken into account. Closed form expressions are provided in this chapter, serving as benchmarking criteria for our numerical methods.

6.2 Free molecular regime

In the collisionless regime ($\delta \rightarrow 0$), the right hand side of the Boltzmann equation vanishes and the problem can be solved analytically by the method of characteristics.

- Non-linear heat transfer between parallel plates

Since there are no collisions, the distribution function remains constant for every \hat{y} and equal to the boundary conditions. Therefore, the distribution function is

$$f = \frac{n_2}{(2\pi k_B T_2)^{3/2}} e^{-\frac{\xi^2}{2k_B T_2}} \quad \text{for } \xi_y > 0 \quad (\text{A.6.1})$$

$$f = \frac{n_1}{(2\pi k_B T_1)^{3/2}} e^{-\frac{\xi^2}{2k_B T_1}} \quad \text{for } \xi_y < 0 \quad (\text{A.6.2})$$

where n_1, n_2, T_1, T_2 are the densities and temperatures on the right and left wall respectively. Using the above, we find that the density remains constant and equal to $n_0 = (n_1 + n_2)/2$, the impermeability condition at the walls ($u_y = 0$) gives $n_1/n_2 = \sqrt{T_2/T_1}$ and we obtain

$$n_1 = 2n_0 \sqrt{T_2} / \left(\sqrt{T_2} + \sqrt{T_1} \right) \quad (\text{A.6.3})$$

$$n_2 = 2n_0\sqrt{T_1}/\left(\sqrt{T_2} + \sqrt{T_1}\right) \quad (\text{A.6.4})$$

Then, the heat flux can be found by its definition, Equation (5.6), along with Equations (A.6.1) and (A.6.2). After non-dimensionalizing, the heat flux is

$$q_{fm} = \frac{2}{\sqrt{\pi}} \left(\sqrt{1 + \beta - \beta^2 - \beta^3} - \sqrt{1 - \beta - \beta^2 + \beta^3} \right) = \frac{2}{\sqrt{\pi}} \sqrt{\tau_1 \tau_2} (\sqrt{\tau_2} - \sqrt{\tau_1}) \quad (\text{A.6.5})$$

The temperature profile is calculated by

$$\tau_{fm} = \sqrt{1 - \beta^2} = \sqrt{\tau_1 \tau_2} \quad (\text{A.6.6})$$

- Linearized heat transfer between parallel plates

For the linear problem, the boundary conditions are

$$h^+|_{y=\pm\frac{1}{2}} = \rho_{wall}|_{y=\pm\frac{1}{2}} \pm \frac{1}{2} \left(c^2 - \frac{3}{2} \right) \quad (\text{A.6.7})$$

In a similar manner, this leads to

$$\rho_{fm,lin} = \rho_0 = \frac{1}{2} \left(\rho_{wall}|_{y=\frac{1}{2}} + \rho_{wall}|_{y=-\frac{1}{2}} \right) \quad (\text{A.6.8})$$

$$\rho_{wall}|_{y=\pm\frac{1}{2}} = \rho_0 \pm \frac{1}{4} \quad (\text{A.6.9})$$

$$q_{fm,lin} = \frac{1}{\sqrt{\pi}} \quad (\text{A.6.10})$$

$$\tau_{fm,lin} = 0 \quad (\text{A.6.11})$$

- Non-linear heat transfer between coaxial cylinders

The right hand side of Equations (5.45) and (5.46) becomes zero and in the case of Maxwell diffuse boundary conditions ($\alpha_t = \alpha_n = 1$) the reduced distribution functions are given for $\theta \in [-\pi/2, \pi/2]$ by

$$\varphi(\gamma, c_p, \theta) = \frac{\rho_w}{\pi(1+\beta)} \exp\left(-\frac{c_p^2}{1+\beta}\right) \quad (\text{A.6.12})$$

$$\psi(\gamma, c_p, \theta) = \frac{\rho_w}{2\pi} \exp\left(-\frac{c_p^2}{1+\beta}\right) \quad (\text{A.6.13})$$

and for $\theta \in [\pi/2, 3\pi/2]$ by

$$\varphi(1, c_p, \theta) = \frac{1}{\pi} \exp(-c_p^2) \quad (\text{A.6.14})$$

$$\psi(1, c_p, \theta) = \frac{1}{2\pi} \exp(-c_p^2) \quad (\text{A.6.15})$$

where the impermeability parameter ρ_w is obtained by the no penetration condition according to

$$\rho_w = -\frac{2\sqrt{\pi}}{\sqrt{1+\beta}} \int_{\pi/2}^{3\pi/2} \int_0^{\infty} (c_p \cos \theta) \varphi c_p dc_p d\theta \quad (\text{A.6.5})$$

Finally, by substituting these expressions into Equations (A.6.5) and (5.51)-(5.53) it is found that

$$\rho_w = \frac{1}{\sqrt{1+\beta}} \quad (\text{A.6.16})$$

$$\rho(r) = \frac{1}{\pi} \left(\theta_1 \frac{1}{\sqrt{1+\beta}} + \pi - \theta_1 \right) \quad (\text{A.6.17})$$

$$\tau(r) = \frac{1}{\rho(r)} \frac{1}{\pi} \left[\theta_1 \sqrt{1+\beta} + (\pi - \theta_1) \right] \quad (\text{A.6.18})$$

and

$$q(r) = \frac{\beta\gamma}{r\sqrt{\pi}} \quad (\text{A.6.19})$$

The discontinuity angle $\theta_1 = \sin^{-1}(\gamma/r)$ is displayed in Figure 5.1. This problem can also be solved when the Cercignani-Lampis boundary conditions are imposed on the inner cylinder. It is found that in this case the heat flux is given by

$$q(r) = \frac{\beta\gamma(\alpha_n + 2\alpha_t - \alpha_t^2)}{2r\sqrt{\pi}} \quad (\text{A.6.20})$$

which is similar to the linearized case appearing in [113]. It is seen that, although the distribution function is independent of r in the free molecular limit, the macroscopic quantities still depend on the space variable. The numerical solution for $\delta_0 = 0$ is in excellent agreement with the analytical results of Equations (A.6.17)-(A.6.20).

- Flow through a slit/orifice

At each point on the cross-section of a zero length opening, the distribution function is the Maxwellian at the upstream vessel conditions for positive axial velocities

$$f_{in} = \frac{n_{in}}{(2\pi k_B T_0)^{3/2}} e^{-\frac{\xi_x^2}{2k_B T_0}} \quad \text{for } \xi_x > 0 \quad (\text{A.6.21})$$

and the Maxwellian at the downstream vessel conditions for negative axial velocities

$$f_{out} = \frac{n_{out}}{(2\pi k_B T_0)^{3/2}} e^{-\frac{\xi_x^2}{2k_B T_0}} \quad \text{for } \xi_x < 0 \quad (\text{A.6.22})$$

By substituting these expressions in the definition of the macroscopic velocity and integrating along the opening, one can calculate the flow rate.

1. Linearized flow through a slit

After the linearizing according to Equation (4.1), non-dimensionalizing with (4.3) and projecting with (4.7) and (4.8), Equations (A.6.21) and (A.6.22) read as

$$V_{in} = 1 \quad X_{in} = 0 \quad \text{for } \xi_x > 0 \quad (\text{A.6.23})$$

$$V_{out} = 0 \quad X_{out} = 0 \quad \text{for } \xi_x < 0 \quad (\text{A.6.24})$$

and using Equation (4.13) we obtain that

$$u_x = \frac{1}{2\sqrt{\pi}} \quad (\text{A.6.25})$$

Substituting this result in Equation (A.2.4) we reach the final result

$$\dot{M}_{FM} = \frac{H \Delta P}{v_0 \sqrt{\pi}} \quad (\text{A.6.26})$$

2. Linearized flow through an orifice

Similarly to the previous case, the upstream/downstream distribution functions are

$$h_{in} = 1 \quad \text{for } \xi_x > 0 \quad (\text{A.6.27})$$

$$h_{out} = 0 \quad \text{for } \xi_x < 0 \quad (\text{A.6.28})$$

and the macroscopic velocity definition, Equation (4.18), leads to

$$u_x = \frac{1}{2\sqrt{\pi}} \quad (\text{A.6.29})$$

Integrating in the surface of the opening and dimensionalizing, we obtain

$$\dot{M}_{FM} = \frac{\sqrt{\pi} R^2 \Delta P}{v_0} \quad (\text{A.6.30})$$

3. Non-linear flow through an orifice

After non-dimensionalizing Equations (A.6.21) and (A.6.22) with Equation (6.4)

$$g_{in} = \frac{1}{\pi^{3/2}} e^{-c^2} \quad \text{for } \xi_x > 0 \quad (\text{A.6.31})$$

$$g_{out} = \frac{P_{out}}{\pi^{3/2}} e^{-c^2} \quad \text{for } c_x < 0 \quad (\text{A.6.32})$$

Using the definition of the dimensionless macroscopic velocity, Equation (6.16), we obtain

$$\rho u_x = \frac{1}{2\sqrt{\pi}} (1 - P_{out}) \quad (\text{A.6.33})$$

Then, the reduced flow rate G can be calculated from Equation (A.2.13)

$$G = \frac{1}{4\sqrt{\pi}} (1 - P_{out}) \quad (\text{A.6.34})$$

and the final free molecular solution for an orifice and an arbitrary pressure drop is

$$\dot{M}_{FM} = \frac{\sqrt{\pi} R^2 \hat{P}_{in}}{v_0} (1 - P_{out}) \quad (\text{A.6.35})$$

6.3 Hydrodynamic regime

In the continuum regime ($\delta \rightarrow \infty$), we can apply the hydrodynamic equations, as well as the constitutive relations. We can also extend our study to the slip regime by including appropriate velocity slip/temperature jump boundary conditions.

- Non-linear heat transfer between parallel plates

For the hydrodynamic limit we have

$$\frac{d}{d\hat{y}} \left(k \frac{dT}{d\hat{y}} \right) = 0 \quad (\text{A.6.36})$$

where k is the thermal conductivity, with

$$\frac{k}{k_0} = \left(\frac{T}{T_0} \right)^\omega \quad (\text{A.6.37})$$

and boundary conditions $T(-\frac{1}{2}) = T_0 + \Delta T/2$ and $T(\frac{1}{2}) = T_0 - \Delta T/2$. After integrating twice, we obtain

$$T^{\omega+1} = \frac{T_0^\omega (\omega + 1)}{k_0} [c_1 \hat{y} + c_2] \quad (\text{A.6.38})$$

where the two constants are determined by

$$\left[T_0 + \frac{\Delta T}{2} + \zeta_T \lambda \frac{c_1 T_0^\omega}{k_0 T_1^\omega} \right]^{\omega+1} + \left[T_0 - \frac{\Delta T}{2} - \zeta_T \lambda \frac{c_1 T_0^\omega}{k_0 T_2^\omega} \right]^{\omega+1} = \frac{2T_0^\omega (\omega + 1)}{k_0} c_2 \quad (\text{A.6.39})$$

$$\left[T_0 + \frac{\Delta T}{2} + \zeta_T \lambda \frac{c_1 T_0^\omega}{k_0 T_1^\omega} \right]^{\omega+1} - \left[T_0 - \frac{\Delta T}{2} - \zeta_T \lambda \frac{c_1 T_0^\omega}{k_0 T_2^\omega} \right]^{\omega+1} = -\frac{HT_0^\omega (\omega + 1)}{k_0} c_1 \quad (\text{A.6.40})$$

If we set $\zeta_T = 0$ we obtain

$$T = \left[\frac{T_2^{3/2} - T_1^{3/2}}{2H} + \frac{T_2^{3/2} + T_1^{3/2}}{2} \right]^{2/3} \quad (\text{A.6.41})$$

for the case of hard spheres ($\omega = 1/2$) and

$$T = \sqrt{-\frac{2\Delta T T_0}{H} + \frac{\Delta T^2 + 4T_0^2}{4}} \quad (\text{A.6.42})$$

for Maxwell molecules.

- Linearized heat transfer between parallel plates

The heat transfer equation in the slip regime is

$$\frac{d^2 T}{d\hat{y}^2} = 0 \rightarrow T = a\hat{y} + b \quad (\text{A.6.43})$$

Using the boundary conditions containing temperature jump terms

$$T|_{\hat{y}=\mp\frac{H}{2}} = T_0 \pm \frac{\Delta T}{2} \pm \zeta_T \lambda \frac{dT}{d\hat{y}} \quad (\text{A.6.44})$$

we obtain

$$T = -\frac{\Delta T}{H} \left(1 + \frac{2\zeta_T}{\delta}\right)^{-1} \hat{y} + T_0 \quad (\text{A.6.45})$$

where ζ_T is the temperature jump coefficient, equal to 1.954 for the S model. The corresponding heat flux is equal to

$$\hat{q} = k \frac{\Delta T}{H} \left(1 + \frac{2\zeta_T}{\delta}\right)^{-1} = \hat{q}_{fm} \frac{15\sqrt{\pi}}{8\delta} \left(1 + \frac{2\zeta_T}{\delta}\right)^{-1} \quad (\text{A.6.46})$$

$$q_L = \frac{15}{8\delta} \left(1 + \frac{2\zeta_T}{\delta}\right)^{-1} \quad (\text{A.6.47})$$

The results are in very good agreement with numerical results for $\delta = 150$, while they also remain relatively close for $\delta = 15$.

- Non-linear heat transfer between coaxial cylinders

The Fourier law is introduced into the energy equation to give

$$\frac{\partial}{\partial \hat{r}} \left[k(T) \frac{\partial T}{\partial \hat{r}} \right] = 0 \quad (\text{A.6.48})$$

where, based on the IPL interaction, we have

$$k(T) = k(T_B) \left(\frac{T}{T_B} \right)^\omega \quad (\text{A.6.49})$$

Substituting Equation (A.6.49) into (A.6.48) and nondimensionalizing the resulting equation according to Equation (5.37), leads to the temperature distribution

$$\tau(r) = \left\{ [(1 + \beta)^{\omega+1} - 1] \frac{\ln r}{\ln \gamma} + 1 \right\}^{1/(\omega+1)} \quad (\text{A.6.50})$$

For hard sphere molecules, following the calculations carried out in [36] it is deduced that

$$q(r) = -\frac{5}{4r} \frac{[(1 + \beta)^{3/2} - 1]}{\delta_0 \ln \gamma} \quad (\text{A.6.51})$$

Expressions (A.6.50) and (A.6.51) are in very good agreement with numerical results for large values of δ_0 but only in cases with small temperature difference. For large β the temperature gradient at the wall becomes important and temperature jump boundary conditions must be introduced. However, the jump solution is not provided here, since the mathematical derivation becomes complex when $k = k(T)$ and ω is involved, and more importantly does not really support further benchmarking of the present work. In the linear case, the solution is much simpler and is given in [36].

- Linearized flow through a slit

Roscoe [196] and Hasimoto [197] studied the problem of linearized slit flow in the hydrodynamic regime. Their result is

$$W = \frac{\pi^{3/2}}{16} \delta \quad (\text{A.6.52})$$

Numerical simulations with the linearized BGK for $\delta = 20$ have indicated that the analytical solution is achieved with a deviation smaller than 2%.

- Linearized flow through an orifice

The same authors [196, 197] studied the problem of linearized orifice flow in the hydrodynamic regime and obtained

$$W = \frac{2}{3\sqrt{\pi}} \delta \quad (\text{A.6.53})$$

There are deviations with the dimensionless flow rate shown here and values of δ closer to the hydrodynamic regime need to be considered.